ABSTRACT

Title of dissertation: MEASUREMENT OF ATMOSPHERIC NEUTRINO OSCILLATION PARAMETERS USING THREE YEARS OF ICECUBE DEEPCORE DATA

Yee Lam Elim Cheung
Doctor of Philosophy, 2018

Dissertation directed by: Professor Gregory Sullivan
Department of Physics

The story of neutrinos began in 1930 when Pauli proposed a hypothesized particle as a "desperate remedy" to rescue quantum theory. Although Pauli was pessimistic about the detectability of his new particle, Reins and Cowan first discovered (anti) neutrinos in 1956. Soon after, neutrinos became a puzzle for particle physicists due to a persistent deficit in observed rates by multiple experiments. This mystery was partly answered by Pontecorvo who first proposed the idea of neutrino oscillations in 1957. In 1998, the Super-Kamiokande (SK) collaboration provided the first definitive evidence of neutrino oscillations, for which both the SK and the Sudbury Neutrino Observatory (SNO) collaborations were awarded the Nobel Prize in Physics 2015.

While measuring oscillation parameters has long been a focus for numerous neutrino experiments, the IceCube Neutrino Observatory with DeepCore provides a unique window to measure atmospheric oscillation parameters. With an effective volume $\sim$ 300 times larger than SK, DeepCore can detect atmospheric neutrinos between a few and 100 GeV. In addition, IceCube acts as a thick veto shield for DeepCore to better identify atmospheric muon backgrounds. Given that the ampli-

tude of atmospheric neutrino oscillations is expected to be maximal at $\sim$ 25 GeV, IceCube-DeepCore is well suited for studying atmospheric neutrino oscillations by probing this energy window for the first time.

Using three years of IceCube-DeepCore data from 2012 to 2014, this work measures atmospheric neutrino oscillation parameters from the disappearance of muon neutrinos. The standard three neutrino mixing and matter effect due to Earth are considered. Under the assumption of a unitary mixing matrix, a binned analysis using a modified χ^2 is performed, and sixteen systematics are taken into account. Preferring a normal neutrino mass ordering, this analysis measures the mass squared difference, $\Delta m^2_{23} = 2.55^{+0.12}_{-0.11} \times 10^{-3}$ eV^2, and the mixing angle, $\sin^2\theta_{23} = 0.58^{+0.04}_{-0.13}$. The measurement from this work is comparable to the latest measurements from other long baseline neutrino experiments.

Measurement of Atmospheric Neutrino Oscillation Parameters Using Three Years of IceCube-DeepCore Data

by

Yee Lam Elim Cheung

Dissertation submitted to the Faculty of the Graduate School of the
University of Maryland, College Park in partial fulfillment
of the requirements for the degree of
Doctor of Philosophy
2018

Advisory Committee:
Dr. Gregory Sullivan, Chair/Advisor
Dr. Kara Hoffman
Dr. Drew Baden
Dr. Colman Miller
Dr. Rabindra Mohapatra

Acknowledgments

Since the first year of my graduate study, I never thought I could actually finish this dissertation. Without the love and supports from my family, friends, and colleagues, my pursuit of a degree in physics would not be successful.

First, I thank my family. Without the mental and financial supports from my parents, I could never come to the United States and work on subjects I am passionate for. Used to be the dumbest kid in classes, I was taught that rewards are given to those who work hard. Thank you my mom and my dad for your love and wisdom, and I hope you are proud of me for what I have accomplished. I also thank my husband, who gives me unconditional love and supports. Despite my workaholism, he made sure I had enough rest when I did not sleep for days. My husband is always here with me for my tears and happiness. I am also grateful to have my heart-warming family in-laws within a four-hour drive.

Second, I thank my friends and colleagues in the local IceCube group. I am extremely lucky to have Dr Greg Sullivan as my advisor, who gives me useful advice so I can keep moving forward and making progress. Thank you for giving me a chance to learn hardware and getting me to the Pole! I will never forget the cold but amazing experience. I also thank Dr Erik Blaufuss, who helped me whenever I was confused about technical details related to my analysis and the detector; he has always been a great mentor who gave me timely advice when I needed. Thank you Dr. Kara Hoffman for your permission to let me help with ARA deployment, which added lots of fun in my final years. I am also grateful to work with Don La Dieu, who recovered my analysis scripts when I did **$ rm ~/*** and makes sure our local cluster is running for my endless jobs. I cannot express my gratitude through words to our post doc, John Felde, and my fellow graduate students. Although I am the odd one out working on neutrino oscillations, I have never felt left out in a

group of GRB experts. I am fortunate to be friends with Mike Richman, Robert Hellauer, and Ryan Maunu. Besides happy hours, we had lots of fun skiing and tubing at Alberta, going to Washington Nationals games, and hanging out during collaboration meetings. It is my pleasure to get to know Liz Friedman and John Evans. Going to the Pole with Liz brought the fun to a whole new level. Of course, without the efficient staff members, Naomi, Pauline, and Paulina, taking care of all my paperworks, my life as a graduate student would have been much more difficult. And, I am also grateful for the financial support provided by the University of Maryland.

Third, I thank my friends and colleagues in the IceCube collaboration. I am glad to work with Michael Larson in Copenhagen. Though sometimes we got frustrated with each other, we always communicated and came to agreements on numbers and decisions on how to move forwards. I wish him, his wife Almut, and their son Henning all the best. I am also thankful to the people in the working group, who have pushed me to do better in all aspects. Special thanks to Martin Leuermann, JP de André, Moriah Tobin, and Melanie Day. Besides the working group, I got to meet friendly professors from other institutes. In particular, thank you, Dr Tom Gaisser, for letting me randomly stop by so I can ask questions related to neutrino fluxes. Thank you, Dr Naoko Kurahashi, for being super supportive throughout my graduate years. Thank you, Dr Albrecht Karle, for allowing me to work at Madison and for teaching me how to tape at the Pole. Last, I could not complete this analysis without the IceCube detector proposed by Dr Francis Halzen, funded by the National Science Foundation, and constructed by hard-working and smart physicists, engineers, and drillers in the extreme environment.

The list of people whom I am grateful for is endless. I apologize for not naming every person who has helped me get to this point of my life. With all the knowledge and experience I have earned, I am excited to move forward to my next chapter.

Table of Contents

List of Tables

List of Figures

Chapter 1: Introduction

The existence of neutrinos was first proposed by Wolfgang Pauli in his famous letter [2] on 4th December 1930 as a hypothesis to rescue the law of energy and momentum conservation in β decay. Naming his new particle *neutrons*, Pauli was worried about its detectability, as he commented [3]

> "I have done a terrible thing, I have postulated a particle that cannot be detected."

Two years later, James Chadwick discovered the neutron we know today with a mass as heavy as a proton [4]. Clearly too heavy, Pauli's new particle was renamed as *neutrinos*, meaning the little neutral one in Italian, by Enrico Fermi. Fermi included neutrinos in his theory of β decay published in 1933 [5], which is the basis of the currently known weak interaction. Fermi's paper also provided an experimental method to accurately measure the neutrino mass from a β decay. Hanna *et al.* performed the proposed experiment in 1949 and concluded that "our initial assumption of a zero neutrino mass is correct, within our limits of error" [6].

Back then, it was difficult to detect neutral particles, let alone particles with (nearly) zero masses and small cross sections. In 1953, Cowan and Reines attempted to detect neutrinos from reactors located at Hanford, Washington, via inverse β decay [7]. In this experiment, a tank of liquid scintillator was prepared. When an anti-neutrino from nuclear fission activities interacts with a target proton, energetic positrons are produced and annihilate with nearby electrons, giving out photons.

The liquid scintillator also contained cadmium salts to capture neutrons from the inverse β decays, producing more light. With only a few hours of data, Cowan and Reines measured the difference between counts when reactor was on and counts when reactor was off. They concluded that the observed difference in counts agreed, within the error bar, with the prediction from the hypothesis of the existence of anti-neutrinos [7]. To provide a more definitive result, Cowan and Reines re-designed their experiments to better identify neutrino signal events by moving the detector underground and introducing veto layers. In a few years, Cowan and Reines re-confirmed that they detected anti-neutrinos [8, 9].

At around the same time, Bruno Pontecorvo proposed that an incoming neutrinos could be detected via the conversion of Chlorine-37 to Argon-37 [10]. This method was adapted by Ray Davis [11] in 1955 to detect neutrinos from a reactor at the Brookhaven National Laboratory, but the neutrino flux was too low to draw a convincing conclusion [12]. By burying the same apparatus underground, Davis also attempted to detect any potential neutrinos from the Sun [11]. In 1964, John Bahcall, a theoretical physicist who studied solar nuclear activities, and Davis proposed the theoretical [13] and experimental [14] possibilities to detect solar neutrinos above 0.97 MeV at the Homestake Gold Mine in South Dakota. In particular, based on the understanding of the ^8B reaction in the Sun, Bahcall predicted that high energy ($\sim$ MeV) neutrinos from the ^8B reaction would have an observed flux on Earth of $1.4 \pm 0.6 \times 10^7$ cm^{-2} s^{-1} [12] . Closely working with Bahcall, Davis was optimistic about his proposed experiment, which is now known as the Homestake experiment.

With the discovery of anti-neutrinos by Cowan and Reines, Pontecorvo proposed a hypothesis of neutrino mixings in 1957 [15] after reading about the discovery of K-meson mixings [16]. Pontecorvo wondered if such a transition existed between an electron neutrino and an electron anti-neutrino [17]; only electron neutrinos were

known at the time. With the discovery of muon neutrinos in 1962 [18], Pontecorvo strongly believed that neutrinos of one flavor could oscillate into the other flavor [19]. Based on his theory, the probability that a neutrino oscillates depends on the propagation length and the energy of the neutrino [19]. He suggested that if the oscillation length was longer than 10 km, phenomena due to oscillations of neutrinos could be seen from the detections of solar neutrinos. In particular, Pontecorvo stated that "[t]he only effect at the surface of the earth would consist in the fact that the flux of observable solar neutrinos would be half as large as the total flux of solar neutrinos." [19]

Soon after the Homestake experiment became operational in 1967, Davis *et al.* noticed a deficiency in the measured solar neutrino flux compared to the prediction by Bahcall. In 1968, after Pontecorvo's prediction of a reduced solar neutrino flux [19], Davis *et al.* published their first results with an upper limit of solar neutrino flux set to be 0.5×10^7 cm^{-2} s^{-1} [20], roughly one third of the predicted value by Bahcall [12]. This deficit is known as the solar neutrino problem. In the following 25 years, with more data, improved techniques in the measurements, and more refined Standard Solar Model (SSM), the one-third deficit remained.

The reduction in event rates was also observed from the next few solar neutrino flux experiments targeted at different energy ranges. For example, via the use of gallium, both the SAGE [21] and GALLEX [22] experiments detected solar neutrinos with energies above 233 keV, probing the energy window of neutrinos produced by the proton-proton (*pp*) interactions inside the Sun. Using data between 2002 and 2007, the joint results from both experiments observed a solar neutrino flux from *pp* interactions of $\sim 6 \times 10^{10}$ cm^{-2} s^{-1}, which was 50% below the expected *pp* solar neutrino flux on the surface of the Sun [23]. Another solar neutrino experiment, the Kamiokande II experiment[1], made use of Cherenkov radiation from secondary

[1]The first Kamiokande detector was built to detect proton decay. Later upgrades were designed

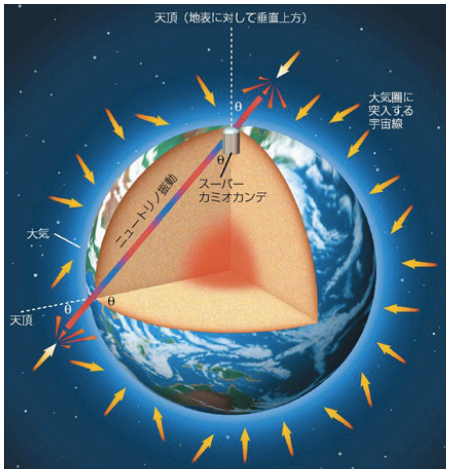

Figure 1.1: Detection of atmospheric neutrinos by the Super-Kamiokande experiment in Japan. The initial Super-Kamiokande detector was sensitive to atmospheric neutrinos beyond 1.33 GeV [27]. Atmospheric neutrinos are isotropic. Depending on the zenith angles between the projectiles of atmospheric neutrinos and the detector, the detected neutrinos traveled through different propagation distances. This figure is adapted from the Super-Kamiokande official webpage from University of Tokyo [28].

leptons produced by neutrino interactions with water molecules. With its effective volume, the Kamiokande II detector was sensitive to neutrinos with energies between 9.3 and 14 MeV and observed a $\sim$ 54% deficit in the rate of solar neutrinos [24]. This solar neutrino rate reduction was further confirmed by the Solar Neutrino Observatory (SNO) and the Super-Kamiokande (SK) experiment. In particular, by detecting both neutral (NC) and charged (CC) current interactions, SNO confirmed in 2001 that, while the CC event rate was $\sim$ 0.35 of the SSM prediction, the total flux was consistent with the SSM [25]. Not only did multiple experiments observe deficiencies in event rates, these reductions also seemed to be energy dependent [26], agreeing with the theory of neutrino oscillations proposed by Pontecorvo [15].

While the solar neutrino problem was observed by multiple independent exper-

to also enhance detections of solar neutrinos.

iments, the initial SK experiment was also designed to study atmospheric neutrinos with energies between 100 MeV and 1.33 GeV [27]. Atmospheric neutrinos are decay products of the secondary particles produced when the cosmic rays interact with the Earth's atmosphere. As shown in Figure 1.1 [28], since atmospheric neutrinos are roughly isotropic, the SK detector, located in Japan, is sensitive to neutrinos above the energy threshold from all around the globe. For a neutrino detected at the SK detector, its propagation length is given by the zenith angle between its direction of travel and the detector; that is, the propagation distances range between the height of the atmosphere (above the detector) and the diameter of the Earth (below the detector). By comparing the observed and expected numbers of atmospheric ν_μ and ν_e events in different zenith and energy ranges, the SK experiment in 1998 provided the first definitive evidence of 6σ to exclude the null hypothesis that there are no oscillations. With the assumption of neutrino oscillations, SK also presented one of the early measurements of atmospheric neutrino oscillation parameters. Both the SNO and SK collaborations were awarded with the Nobel Prize in Physics 2015 [29] for their discoveries of neutrino oscillations [25, 27].

Located at the geographical South Pole, the IceCube Neutrino Observatory with DeepCore is the newest and largest neutrino detector that allows studies of high energy atmospheric neutrinos with high statistics. More than 5,000 optical sensors were deployed deep inside the South Pole ice, covering an instrumented volume of one cubic-kilometer. Similar to the SK detector, IceCube-DeepCore detects neutrinos indirectly via Cherenkov radiations induced by fast-going leptons. However, with an effective volume 300 times larger than SK, IceCube-DeepCore can detect more atmospheric neutrinos with higher energies than SK can. According to the world averaged best fit values of neutrino oscillation parameters [1], atmospheric neutrino oscillations are at maximal for neutrinos with energies of ~ 25 GeV traveling through the core of the Earth. Sensitive to a neutrino energy as low as 10 GeV, IceCube-

DeepCore can observe the atmospheric neutrino oscillation pattern at its maximal amplitude.

Measuring atmospheric neutrino oscillation parameters from the disappearance of muon neutrinos is the goal of this dissertation. When cosmic rays interact with the Earth's atmosphere, two types of atmospheric neutrinos are produced: muon neutrinos ν_μ and electron neutrinos ν_e. Based on the current world averaged best fit values of oscillation parameters [1] and an oscillation length in the order of the Earth's diameter, the oscillation pattern of atmospheric muon neutrinos is more dramatic than that of atmospheric electron neutrinos. Due to neutrino oscillations, some of the atmospheric ν_μ oscillate into other neutrino flavors, reducing the number of ν_μ events detected by the IceCube-DeepCore detector. Therefore, ν_μ seems to "disappear" at the detection site compared to the predicted ν_μ rate with no neutrino oscillations. Hence, atmospheric neutrino oscillation parameters can be measured by comparing the number of ν_μ events observed and the predicted count. A more detailed summary of how the measurement is done is presented in the following with a brief highlight for each chapter of this thesis.

As shown in Figure 1.2, the first three chapters of this thesis present the theory of neutrino oscillations, the production and detection of atmospheric neutrinos, and a description of the IceCube-DeepCore detector. In Chapter 2, the mathematical expression of the oscillation probability is discussed. It is important to note that the oscillation probability of a given neutrino flavor is a function of L/E, where L and E are the propagation length and energy of a neutrino respectively. While a two-flavor neutrino approximation in vacuum is shown in Figure 1.2, this analysis assumes three-flavor neutrino oscillations with matter effects. Chapter 3 then discusses how atmospheric neutrino fluxes are predicted and how neutrinos are detected in the South Pole ice. The production mechanism of atmospheric neutrinos is reasonably well understood with decent agreements between predictions

A summary of this dissertation

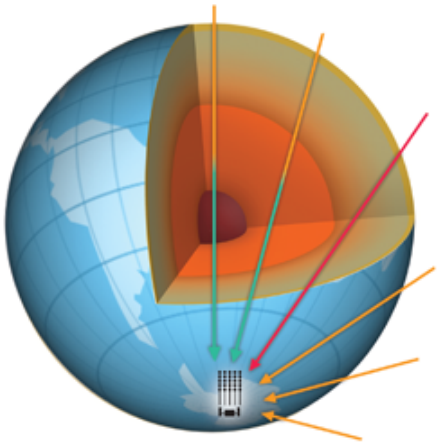

Chapter 2 - Neutrino Oscillations

$$P^{2\nu}_{\text{vac}}(\nu_e \to \nu_\mu) = \sin^2 2\theta_{21} \sin^2\left(1.27\Delta m^2_{21}[\text{eV}^2]\frac{L[\text{km}]}{E[\text{GeV}]}\right)$$

- three-flavor neutrino oscillations
- matter effect

Chapter 3 - Neutrino Production and Detection

- prediction of atmospheric neutrino fluxes
- detection of neutrinos in the South Pole ice
  - neutrino interactions
  - propagations of secondary particles

Chapter 4 - The IceCube-DeepCore Detector

Figure 1.2: A summary of this analysis - Part I. The first three chapters cover the theory of neutrino oscillations, the prediction of neutrinos produced in the Earth's atmosphere and detected at the detection site, and the description of the IceCube-DeepCore neutrino detector located at the South Pole. The figure of the Earth is adapted from [30].

and observations. Although the discussion of a one-dimensional flux calculation can be complex, a final note is presented in Section 3.1.6 to summarize the important neutrino flux ratios for this analysis. The second half of Chapter 3 discusses the physics of neutrino detections, including neutrino interactions with the South Pole ice, propagations and energy losses of secondary leptons, and the optical properties of the South Pole ice. When an incoming muon neutrino interacts with the ice, the final lepton is either a muon neutrino from a neutral current (NC) interaction or a charged muon from a charge current interaction (CC). While ν_μ NC events cannot be distinguished from NC interactions by other neutrino flavors, ν_μ CC events have the characteristic Cherenkov light induced when out-going muons propagate in the ice. These photons are then detected by the optical modules, which make up the

IceCube-DeepCore detector presented in Chapter 4. A thorough understanding on the physics behind neutrino production, propagation, and detection is crucial for the measurement of atmospheric neutrino oscillation parameters.

The next two chapters focus on the event rate predictions and event selection process for this analysis. Chapter 5 presents the technical details on the simulation tools and the prediction of how often a simulated event occurs in reality. In this analysis, ν_μ CC events are considered as signal, and other event types are backgrounds, which include other neutrino flavors, neutrino NC events, atmospheric muons, and events that are purely triggered by detector noise. For each event type, simulation sets are produced by different simulation tools; for each simulated event, a *weight* is assigned to determine its contribution to the total event rate for this event type. Due to neutrino oscillations, a simulated (or detected) neutrino of one flavor interacting with the ice may not have the same flavor as it was produced in the atmosphere; this is taken into account in the weighting scheme. In addition, this analysis is the first in IceCube to measure atmospheric neutrino oscillation parameters using simulated background muons and noise triggered events, allowing looser selection cuts and higher statistics. Chapter 6 discusses the event selection procedure using multiple levels of event requirements. While keeping as many neutrino events as possible, the event selection procedure rejects atmospheric muons, noise-triggered events, and events that lead to poor agreements between data and MC simulations. After the event selection process, over 60,000 events are predicted given three years of detector lifetime, providing a final sample with the highest statistics currently available.

The last three chapters are the most important parts of this thesis - the techniques and results of the atmospheric neutrino oscillation parameter measurement (see Figure 1.3). Because neutrino oscillations depend on the energy, propagation length, and the flavor of a neutrino, the three observables for this analysis are recon-

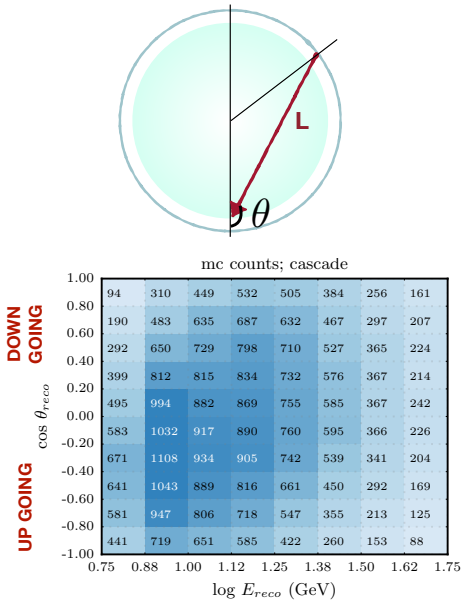

A summary of this dissertation

Chapter 7 - Systematics

- sixteen systematics are taken into account
- thirteen systematics have priors applied

Chapter 8 - Analysis Method

- three dimensional template
  - propagation length (zenith angle): $-1 \leq \cos\,\theta \leq 1$
  - energy: $5.6 \leq$ energy $[\mathrm{GeV}] \leq 56$
  - particle identification by reconstructed track length
- modified χ^2
- expected sensitivity

Chapter 9 - Results

Figure 1.3: A summary of this analysis - Part II. The last three chapters cover the techniques and results of the measurements of atmospheric neutrino oscillation parameters. Sixteen nuisance parameters are included. Two two-dimensional templates are used, one for cascade-like and one for track-like events. Each of the two templates includes events with energies between 5.6 and 56 GeV from all sky. A binned analysis is performed by minimizing a modified χ^2. The measured values of atmospheric neutrino oscillation parameters are presented along with their uncertainties.

structed energy, cosine zenith angle, and event particle identification. First, Chapter 7 discusses the potential sources of systematic uncertainties, each of which is represented by a nuisance parameter. To determine if a nuisance parameter affects the measurements of atmospheric neutrino oscillation parameters, it is important to understand the impacts from the nuisance parameter on the energy and zenith distributions of a given event type. For this analysis, sixteen nuisance parameters are included, thirteen of which have priors applied with their 1σ penalties determined from other independent studies. Chapter 8, presents the binned analysis used for this thesis. Given that oscillation probability depends on the three observables, a

three-dimensional MC template is built. Because IceCube-DeepCore can only identify cascade- and track-like events, reconstructed track length is used for particle identification. Events with track lengths shorter than 50 meters are cascade-like, while events with track lengths between 50 and 1000 meters are track-like. For each cascade or track channel, events are binned by their energies and zenith angles, as shown on the left of Figure 1.3. For this analysis, the zenith angle ranges from vertically up going to vertically down going (i.e. all sky), and the energy window is between 5.6 GeV and 56 GeV (i.e. 0.75 to 1.75 in the log10 [GeV] in energy space). For each bin, a modified χ^2 is determined to quantify the statistical difference between the MC count and the data count, while letting nuisance parameters float. This method is repeated for a range of oscillation parameters to determine the best fit values and their 90% confidence levels. Results of this analysis and the related discussions are presented in Chapter 9. Finally, Chapter 10 concludes this thesis with a few comments on future atmospheric neutrino oscillation studies with IceCube-DeepCore.

Chapter 2: Neutrino Oscillations

This chapter focuses on the theoretical and experimental aspects of neutrino flavor mixing. According to the theory of neutrino oscillations discussed in Section 2.1, the oscillation probability of a given neutrino flavor is a function of L/E, where L and E are the propagation distance and energy of the neutrino respectively. Though multiple literatures have argued the true physics behind neutrino oscillations using assumptions of plane waves versus wave packets, all approaches conclude with the same behavior of neutrino oscillation patterns. Interesting phenomena on neutrino oscillations in matter are also discussed. Since oscillation probability depends on L/E, experiments are designed for some targeted L/E ranges. As discussed in Section 2.2, solar and atmospheric neutrino oscillation studies make use of neutrinos produced by the Sun and by interactions between cosmic rays and the Earth's atmosphere respectively. Detectors are also built near reactors to study the output neutrinos, and accelerators with neutrino beams are also built to study the smallest mixing angle and improve current measurements.

2.1 Theory of Neutrino Oscillations

The theory of neutrino flavor mixing dated back to 1957 when Pontecorvo proposed a transition between an electron neutrino and an electron anti-neutrino [15] after K meson mixing was observed [16]. With the discoveries of muon and tau neutrinos, a full formalism with three-flavor neutrino oscillations was established.

As shown in Section 2.1.1, neutrino oscillations are purely because of the beauty of quantum mechanics. Moreover, with the presence of matter, neutrino mixing leads to both resonated oscillation effect and adiabatic flavor conversion as explained in Section 2.1.2. To better understand the effects due to neutrino oscillations, a two-flavor neutrino mixing is discussed in Section 2.1.3 for both vacuum and matter.

2.1.1 Three Neutrino Flavor Mixing in Vacuum

Neutrino oscillations originate from the fact that neutrino flavor eigenstates are different from their mass eigenstates; that is, three neutrino types cannot all have zero masses. Hence, a neutrino with a definite flavor of α is described by a linear superposition of the mass eigenstates;

$$|\nu_\alpha\rangle = \sum_{i=1}^{3} U_{\alpha i}^{*} \, |\nu_i\rangle \, , \tag{2.1}$$

where $\alpha = e, \mu, \tau$, and $i = 1, 2, 3$.

In Equation 2.1, U is the Pontecorvo-Maki-Nakagawa-Sakata (PMNS) mixing matrix. With three flavor and three mass eigenstates, U is a 3×3 square matrix given by

$$U = \begin{pmatrix} U_{e1} & U_{e2} & U_{e3} \\ U_{\mu 1} & U_{\mu 2} & U_{\mu 3} \\ U_{\tau 1} & U_{\tau 2} & U_{\tau 3} \end{pmatrix} , \tag{2.2}$$

where $|U_{\alpha i}|^2$ corresponds to the fraction of flavor α in a given mass eigenstate ν_i. Though the violation of the unitarity of the PMNS mixing matrix interests particle theorists [31–33] and experimentalists [34,35], no such evidence is found. Thus, this analysis assumes a unitary mixing matrix such that

$$\begin{aligned} \sum_{k=1,2,3} U_{\alpha k} U_{\beta k}^{*} &= \delta_{\alpha\beta}, \\ \sum_{\alpha=e,\mu,\tau} U_{\alpha k}^{*} U_{\alpha j} &= \delta_{kj}. \end{aligned} \tag{2.3}$$

The assumed unitarity guarantees that, while a neutrino of flavor α from a source can either survive as α or oscillate into some other flavors, the total neutrino flux from the source remains unchanged.

Over the past decades, literature has shown mathematical proofs, via different approaches, of the $\nu_\alpha \to \nu_\beta$ transition probability in vacuum, from which a neutrino of flavor α oscillates into a neutrino of flavor β. These derivations come from simple hand-waving arguments [36], plane-wave approximations [37–39], wave-packet treatments [40–44], and the use of Quantum Field theory [45, 46]. Despite some controversial subtleties among different approaches, the mathematical expression of the oscillation probability is robust. This section follows the derivation by Giunti *et al.* [41, 42], in which the neutrino propagation in space-time is treated as a plane-wave, but neutrino production and detection are treated as localized processes described by wave-packets.

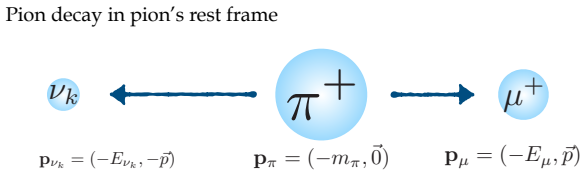

Figure 2.1: Pion two-body decay at pion rest frame. At pion rest frame, the kinematic properties of the decay daughters are determined. Due to momentum conservation, the momenta of outgoing neutrino and muon are equal but opposite in pion rest frame.

Let us first study the kinematics of a neutrino ν_α at the production site. In the language of quantum mechanics, this neutrino is described by its wavefunction

$$\left|\psi_\alpha^P\right\rangle = \left|\nu_\alpha\right\rangle \left|p_k\right\rangle = \sum_{k=1}^{3} U_{\alpha k}^* \left|\nu_k\right\rangle \left|p_k\right\rangle , \tag{2.4}$$

where $|p_k\rangle$ is the momentum state of the corresponding neutrino with a mass m_k. Note that $\left|\psi_\alpha^P\right\rangle$ is a superposition of mass eigenstates $|\nu_k\rangle$, each of which has its

kinematical property determined by the conservation of four-momentum at the production site. A typical neutrino production channel is through a pion decay

$$\pi^+ \rightarrow \mu^+ + \nu_\mu. \tag{2.5}$$

As shown in Figure 2.1, the kinematics of the outgoing neutrinos are well determined at the pion rest frame. Recalled from the relativistic dispersion relation, the energy E_k and the momentum $\vec{p}_k$ of the k^{th} mass eigenstate are related;

$$E_k^2 = p_k^2 + m_k^2. \tag{2.6}$$

From the conservation of four-momentum where $\mathbf{p}_\pi = \mathbf{p}_\mu + \mathbf{p}_{\nu_\mu}$ and the definition of pion rest frame, in which the two momenta of the out-going daughter particles are equal but opposite, the neutrino energy at pion rest frame is determined by the masses of the particles involved in the decay process;

$$E_k = \frac{m_\pi^2 - m_\mu^2 + m_k^2}{2m_\pi}. \tag{2.7}$$

With some algebra, E_k^2 can be expressed as

$$E_k^2 = \frac{m_\pi^2}{4}\left(1 - \frac{m_\mu^2}{m_\pi^2}\right)^2 + \frac{m_k^2}{2}\left(1 - \frac{m_\mu^2}{m_\pi^2}\right) + \frac{m_k^4}{4m_\pi^2}. \tag{2.8}$$

Therefore, based on the energy-momentum dispersion in Equation 2.6, the momentum squared p_k^2 of the k^{th} mass eigenstate is given by

$$p_k^2 = \frac{m_\pi^2}{4}\left(1 - \frac{m_\mu^2}{m_\pi^2}\right)^2 - \frac{m_k^2}{2}\left(1 + \frac{m_\mu^2}{m_\pi^2}\right) + \frac{m_k^4}{4m_\pi^2}. \tag{2.9}$$

Since m_k^2 is much smaller[1] than m_μ^2 and m_π^2, the first terms in Equations 2.9 and 2.8 are considered as the zeroth order contributions.

$$p_0^2 = E_0^2 = \frac{m_\pi^2}{4}\left(1 - \frac{m_\mu^2}{m_\pi^2}\right)^2 \approx 30 \text{ MeV}.$$

[1]Based on cosmological data, the sum of all neutrino mass eigenstates is found to be less than 1 eV [38]. Hence, the mass of the k^{th} mass eigenstate is much smaller than the muon and pion masses which are $\sim$ 105 and 140 MeV respectively.

Note that, both p_0^2 and E_0^2 are independent of m_k, implying that all neutrino mass eigenstates of a neutrino produced by a two body pion decay have the same zeroth order energy and momentum of $\sim$ 30 MeV at the pion rest frame. Due to a non-zero mass of the k^{th} mass eigenstate, the first order correction of p_0^2 is obtained by including the second term in Equation 2.9; that is,

$$\begin{aligned} p_k^2 &\simeq E_0^2 - \frac{m_k^2}{2}\left(1 + \frac{m_\mu^2}{m_\pi^2}\right) \\ &\simeq E_0^2\left[1 - \frac{m_k^2}{2E_0^2}\left(1 + \frac{m_\mu^2}{m_\pi^2}\right)\right]. \end{aligned} \tag{2.10}$$

Therefore, by taking the square root and the limit $m_k^2 \ll E_0^2$, the momentum p_k becomes

$$p_k \simeq E_0 - \xi\frac{m_k^2}{2E_0}, \tag{2.11}$$

where $\xi = (1+m_\mu^2/m_\pi^2)/2$. Applying the same logic, the energy E_k to the first order correction is

$$E_k \simeq E_0 - (1-\xi)\frac{m_k^2}{2E_0}. \tag{2.12}$$

As a result, each of the three mass eigenstates from the neutrino ν_α has different kinematics due to the differences in their masses squared.

Produced at a point in space $\vec{x}_P$ at time t_P, this neutrino ν_α now propagates to the detection site at $\vec{x}_D$ at t_D. Assuming that ν_α is a free particle described by a plane wave traveling in one dimension, the space-time evolution of $\left|\psi_\alpha^P(x,t)\right\rangle$ is obtained by solving the Schrödinger equation via a Hamiltonian operator $\mathcal{H}$;

$$\begin{aligned} i\frac{\partial}{\partial t}\left|\psi_\alpha^P(x_D,t_D)\right\rangle &= \mathcal{H}\left|\psi_\alpha^P(x_D,t_D)\right\rangle \\ \left|\psi_\alpha^P(x_D,t_D)\right\rangle &= \sum_{k=1}^{3} U_{\alpha k}^*\, e^{i(p_k L - E_k T)}\left|\nu_k\right\rangle. \end{aligned} \tag{2.13}$$

Here, $L = x_D - x_P$ is the propagation length; $T = t_D - t_P$ is the time traveled by the neutrino; and E_k and p_k are approximated by Equations 2.12 and 2.11. As each mass eigenstate $|\nu_k\rangle$ propagates from the production site, it becomes a superposition

of flavor eigenstates. Thus, the wavefunction at the detection site is given by

$$\left|\psi_\alpha^P(x_D,t_D)\right\rangle = \sum_{\beta=e,\mu,\tau}\sum_{k=1,2,3} U_{\alpha k}^*\, e^{i(p_kL-E_kT)}\, U_{\beta k}\left|\nu_\beta\right\rangle . \tag{2.14}$$

The amplitude of observing a neutrino of flavor β at the detection site is therefore obtained by its projection on the flavor state $|\nu_\beta\rangle$;

$$\begin{aligned}\mathcal{A}(\nu_\alpha\to\nu_\beta) &= \left\langle\nu_\beta\middle|\psi_\alpha^P(x_D,t_D)\right\rangle \\ &= \sum_{k=1,2,3} U_{\alpha k}^*\, e^{i(p_kL-E_kT)}\, U_{\beta k}. \end{aligned}\tag{2.15}$$

Hence, the oscillation probability of $\nu_\alpha\to\nu_\beta$ is given by

$$\begin{aligned}\mathcal{P}_{(\nu_\alpha\to\nu_\beta)} =& \text{Re}\ |\mathcal{A}(\nu_\alpha\to\nu_\beta)|^2 \\ =& \sum_{k=1,2,3}|U_{\alpha k}|^2|U_{\beta k}|^2 \\ &+ 2\text{Re}\ \sum_{k>j} U_{\alpha k}^*U_{\beta k}U_{\alpha j}U_{\beta j}^*\ \exp\left[i(p_k-p_j)L - i(E_k-E_j)T\right] \\ =& \sum_{k=1,2,3}|U_{\alpha k}|^2|U_{\beta k}|^2 \\ &+ 2\text{Re}\ \sum_{k>j} U_{\alpha k}^*U_{\beta k}U_{\alpha j}U_{\beta j}^*\ \exp\left[-i\xi\frac{\Delta m_{kj}^2}{2E}L - i(1-\xi)\frac{\Delta m_{kj}^2}{2E}T\right]. \end{aligned}\tag{2.16}$$

where the last step comes from Equations 2.11 and 2.12, and $\Delta m_{kj}^2 \equiv m_k^2 - m_j^2$ is defined as the mass squared differences.

However, the dependence of oscillation probability in Equation 2.16 on the neutrino traveling time T is unrealistic; no real experiment measures the neutrino propagation time. Therefore, many neutrino physicists [40–46] argue that the use of wave packets is necessary to understand the connection between propagation time T and length L. As shown in Figure 2.2, a neutrino ν_α produced at a production site is a superposition of three wave packets, each of which represents a mass eigenstate traveling at its group velocity v_k given by Equations 2.11 and 2.12;

$$v_k = \frac{p_k}{E_k} = \frac{1-\xi m_k^2/(2E^2)}{1+(1-\xi)m_k^2/(2E^2)} \approx 1 - \frac{m_k^2}{2E^2}. \tag{2.17}$$

Hence, the propagation time for a neutrino ν_k to travel a distance L can be expressed as

$$T_k = \frac{L}{v_k} \approx L\left(1 + \frac{m_k^2}{2E^2}\right). \tag{2.18}$$

Because the oscillation probability depends on $\Delta m^2_{kj} T/2E$, the leading order term in Equation 2.16 can be obtained without the second term in Equation 2.18. That is, by substituting $T \approx L$, the $\nu_\alpha \to \nu_\beta$ oscillation probability in vacuum is

$$\begin{aligned}\mathcal{P}_{(\nu_\alpha \to \nu_\beta)} = &\sum_{k=1,2,3} |U_{\alpha k}|^2 |U_{\beta k}|^2 \\ &+ 2\mathrm{Re} \sum_{k>j} U^*_{\alpha k} U_{\beta k} U_{\alpha j} U^*_{\beta j} \exp\left[-i\frac{\Delta m^2_{kj}}{2E} L\right].\end{aligned} \tag{2.19}$$

Given that $e^{-i\phi} = \cos\phi - i\sin\phi = 1 - 2\sin^2(\phi/2) + i\sin\phi$, the oscillation probability can be expressed in terms of sinusoidal functions:

$$\begin{aligned}\mathcal{P}_{(\nu_\alpha \to \nu_\beta)} = &\sum_{k=1,2,3} |U_{\alpha k}|^2 |U_{\beta k}|^2 + \sum_{k>j} |U_{\alpha k}|^2 |U_{\beta k}|^2 \\ &- 4\sum_{k>j} \mathrm{Re}(U^*_{\alpha k} U_{\beta k} U_{\alpha j} U^*_{\beta j}) \sin^2\left(\frac{\Delta m^2_{kj} L}{4E}\right) \\ &- 2i\sum_{k>j} \mathrm{Im}(U^*_{\alpha k} U_{\beta k} U_{\alpha j} U^*_{\beta j}) \sin\left(\frac{\Delta m^2_{kj} L}{2E}\right) \\ = &\delta_{\alpha\beta} - 4\sum_{k>j} \mathrm{Re}(U^*_{\alpha k} U_{\beta k} U_{\alpha j} U^*_{\beta j}) \sin^2\left(\frac{\Delta m^2_{kj} L}{4E}\right) \\ &- 2i\sum_{k>j} \mathrm{Im}(U^*_{\alpha k} U_{\beta k} U_{\alpha j} U^*_{\beta j}) \sin\left(\frac{\Delta m^2_{kj} L}{2E}\right),\end{aligned} \tag{2.20}$$

where the last step comes from the assumption of a unitary mixing matrix in Equation 2.3.

Four points are raised from Equation 2.20. First, the oscillation probability comes from the interference terms. While one of the three neutrino masses may be zero, the fact that neutrino oscillations are observed indicates non-zero interference terms and, hence, non-zero mass squared differences Δm^2_{kj}. This implies that at least two neutrino masses are non-zero. Second, the independence of ξ in the oscillation

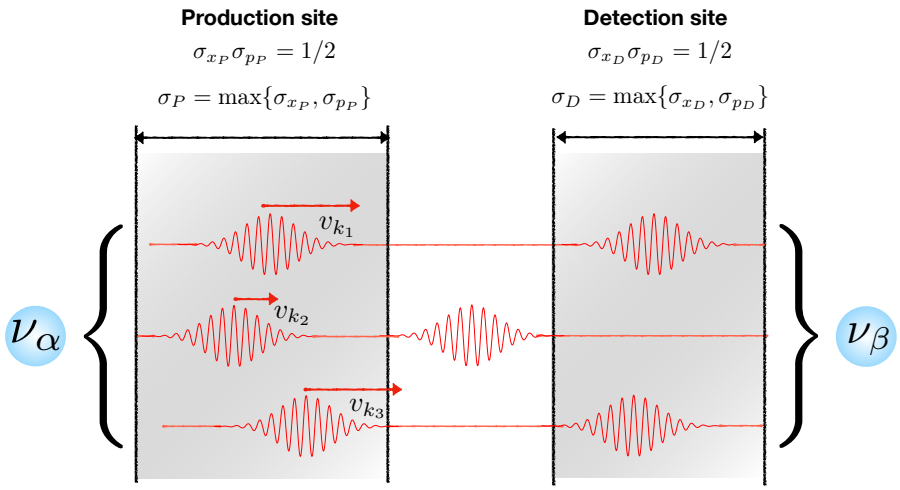

Figure 2.2: Neutrinos as wave packets at production and detection sites. At the production site, a neutrino with a definitive flavor α is a superposition of three mass eigenstates, each of which is a wave packet created at slightly different space-time but within the spatial and temporal uncertainties of neutrino production. These wave packets propagate at different group velocities. At some distance and time later, ν_2 is separated from the others at a distance larger than the coherence length. The other two wave packets arrive at the detection site within the spatial and time uncertainties of the detector. The interference of the two wave packets leads to a detection of neutrino of flavor β.

probability expression implies that neutrino oscillations are the same even if the neutrino is produced through decays of heavier mesons. Oscillation probability is independent of the types of particles involved during the production of a neutrino. Third, the oscillation probability is Lorentz-invariant. Although the kinematics at the neutrino production site are discussed in the pion rest frame, the evolution of the neutrino's wavefunction includes both time-energy and space-momentum. As long as the observables are measured at the same frame of inertia, observers from different frames should obtain the same oscillation probability. Fourth, the argument in the sine functions of Equation 2.20 is in natural units. In (semi-)S.I. units,

$$\frac{\Delta \mathrm{m}^2_{kj} L}{4E} = \frac{\Delta \mathrm{m}^2_{kj}[\mathrm{kg}] \times L[\mathrm{m}] \times c^3}{4 \times E[\mathrm{J}] \times \hbar} = 1.27 \Delta \mathrm{m}^2_{kj}[\mathrm{eV}^2] \frac{L[\mathrm{km}]}{E[\mathrm{GeV}]}. \tag{2.21}$$

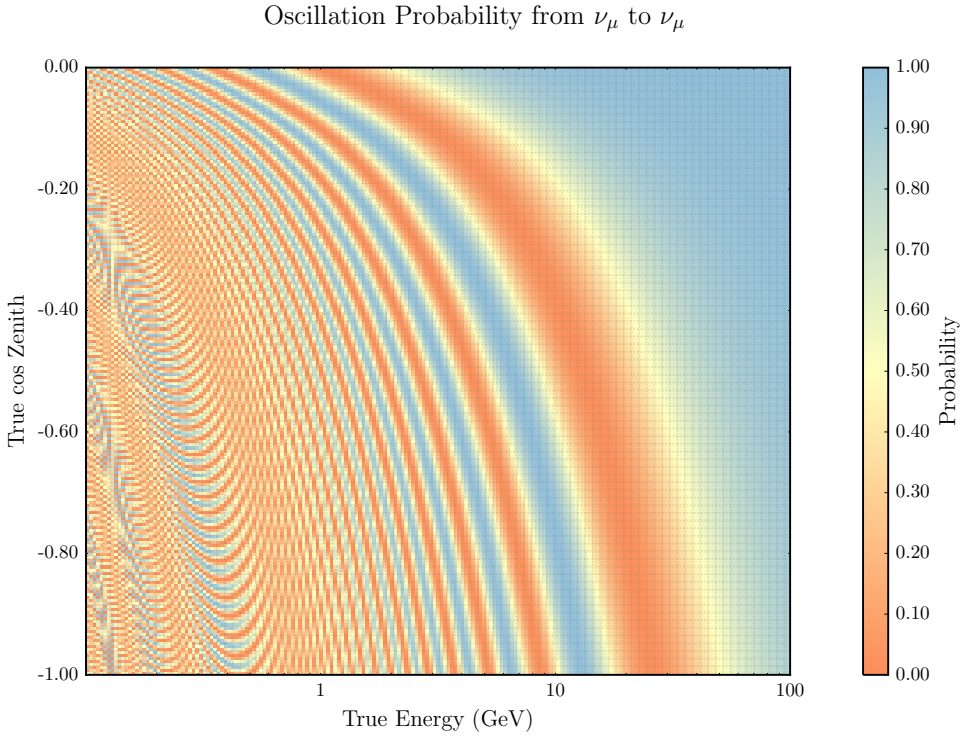

Figure 2.3: Atmospheric ν_μ survival probability in vacuum based on world averaged best fit oscillation parameters from [1]. Color bar represents the $\nu_\mu \to \nu_\mu$ survival probability. A neutrino coming from the horizon without passing through Earth matter has a cos zenith of 0; and cos zenith of -1 corresponds to a direction from which a neutrino passes through the Earth's core with its propagation distance the same as the Earth's diameter. A vacuum condition is assumed in which no matter presence during neutrino propagations. Oscillation pattern for neutrinos with energies below 1 GeV is due to the assumption of three-flavor neutrino mixing.

Note that an oscillation length L_{kj}^{osc} between two mass eigenstates is roughly given by $\Delta \text{m}_{kj}^2 L_{kj}^{\text{osc}}/4E \sim 1$; that is,

$$L_{kj}^{\text{osc}}[\text{km}] \sim \frac{E[\text{GeV}]}{1.27 \times \Delta \text{m}_{kj}^2[\text{eV}^2]}. \tag{2.22}$$

Since atmospheric neutrino flux is roughly isotropic, a detector at a fixed location on Earth is sensitive to a range of L/E based on the neutrino's zenith angle and energy. For a neutrino coming vertically from the other side of the Earth with a cos

θ of -1.0, its propagation length is the diameter of the Earth, whereas a neutrino coming from the horizon has a cos θ of 0.0. Given the world averaged best fit atmospheric oscillation parameters from [1], the survival probability of atmospheric ν_μ is shown in Figure 2.3 in the absence of Earth matter. Note that, according to the current knowledge on the values of neutrino oscillation parameters, ν_μ disappearance is expected to be maximal at $\sim$ 25 GeV for vertically up going neutrinos with cos θ of -1.0.

Although treating neutrino mass eigenstates as plane-waves eases the mathematical proof of oscillation probability expression, the reason why we *see* neutrino oscillations may be understood via a hand-waving argument [40–44] using wave packets[2]. As shown in Figure 2.2, when a neutrino of flavor α is produced at a space-time point (x_P, t_P), three wave packets with definitive sizes are also produced. However, these three mass eigenstates with different momenta may not be produced at exactly the same space-time but at some slightly different points (x_P^k, t_P^k). The three wave packets overlap with each other if the difference between any two space-time points is smaller than the uncertainty given by the Heisenberg uncertainty principle given by $\sigma_{x_P}\sigma_{p_P} \sim 1/2$;

$$|x_P^k - x_P| \leq \sigma_{x_P} \qquad \text{and} \qquad |p_P^k - p_P| \leq \sigma_{p_P}. \tag{2.23}$$

The overlaps of three mass eigenstates within the spatial and temporal uncertainties of the production process leads to an interference of the three states. As the three wave packets travel in space-time, their momenta and velocities are different due to their differences in mass squared (see Equations 2.17 and 2.11). Depending on the neutrino energy and the propagation distance between the production and detection sites, the three mass eigenstates may not arrive at the detector at the same time.

[2] A full mathematical proof of Equation 2.20 assuming a two dimensional gaussian wave packet is presented in Giunti *et al.* [47], which leads to the same oscillation probability expression.

Similar to the uncertainties at the production process, the detection process also has spatial and temporal uncertainties due to the Heisenberg uncertainty principle. If all three wave packets arrive at similar time within $\sigma_{x_D}\sigma_{p_D} \sim 1/2$, the coherent superposition from all three mass eigenstates causes an observation of a neutrino with flavor α. However, if the lagging (or out-pacing) distance from one of the mass eigenstates is larger than the spatial and temporal uncertainties at the detection process, then the corresponding eigenstate (ν_2 in Figure 2.2) cannot interfere at the detection site, hence its oscillation effect is suppressed. Therefore, for a given detection process and a given pair of mass eigenstates, a coherence length[3] can be defined by setting a limit on Equation 2.17 due to the uncertainty principle;

$$|\Delta x_{kj}| = |v_k - v_j|T \sim \frac{|\Delta \mathrm{m}^2_{kj}|}{2E^2}L$$
$$L^{\mathrm{coh}}_{kj} \sim \frac{2E^2}{|\Delta \mathrm{m}^2_{kj}|}\sigma_{x_D}.$$

The dependence of coherence length on the spatial uncertainty of the detector implies that, if one designs an experiment to accurately measure the momentum of a given mass eigenstate, σ_{x_D} grows, and so does the coherence length. Eventually, L^{coh}_{kj} is greater than the corresponding oscillation length L^{osc}_{kj}. This means that, if one attempts to measure the mass of a neutrino from, say, a β decay, one would not see any oscillation effects [47]. Therefore, neutrino oscillations are *solely* caused by the nature of quantum mechanics including both superpositions of mass eigenstates, each of which travels at different speeds, and the Heisenberg uncertainty principle.

Because the effects from three-flavor neutrino oscillations are given by every two mass eigenstates, the unitary mixing matrix in Equation 2.2 is often broken down into three terms [38][4], each of which corresponds to the oscillations of neutrinos

[3]The coherence length was first introduced by Nussinov [44].

[4]The fourth term related to the Majorana phases is excluded here since those parameters $\alpha_{1,2}$ are not accessible by oscillation experiments [39].

between two mass eigenstates;

$$U = \underbrace{\begin{bmatrix} 1 & 0 & 0 \\ 0 & c_{23} & s_{23} \\ 0 & -s_{23} & c_{23} \end{bmatrix}}_{\text{Atmospheric}} \times \underbrace{\begin{bmatrix} c_{13} & 0 & s_{13}e^{-i\delta} \\ 0 & 1 & 0 \\ -s_{13}e^{i\delta} & 0 & c_{13} \end{bmatrix}}_{\text{Cross-Mixing}} \times \underbrace{\begin{bmatrix} c_{12} & s_{12} & 0 \\ -s_{12} & c_{12} & 0 \\ 0 & 0 & 1 \end{bmatrix}}_{\text{Solar}}, \tag{2.24}$$

where δ is the CP-violating phase, $c_{kj} \equiv \cos\,\theta_{kj}$, and $s_{kj} \equiv \sin\,\theta_{kj}$; θ_{kj} are the mixing angles. Each of these three matrices dominates at a specific range of L/E and can be treated as two-flavor neutrino oscillations (see Section 2.1.3). Because the oscillation pattern of each matrix depends on L/E, experiments are designed accordingly to study neutrino oscillations of a given matrix. To understand the atmospheric term in Equation 2.24, large water detectors, such as Super-Kamiokande in Japan [48] and KM3NeT in the Mediterranean Sea [49], are built to study neutrinos produced when cosmic rays interact with the Earth's atmosphere. From observations, atmospheric neutrinos have an energy range from sub GeV to $\sim$ 100 GeV. Given the Earth's diameter of $\sim 10^4$ km as the oscillation length in Equation 2.22, atmospheric neutrino oscillation studies are sensitive to a $\Delta m^2_{32} > 10^{-5}\text{eV}^2$. The second matrix in Equation 2.24 corresponds to the mixing between ν_1 and ν_3. The corresponding mixing angle θ_{13} is measured via the survival probability of electron anti-neutrinos in the MeV range over an oscillation distance of a few km [50]. The last term in Equation 2.24 is related to solar neutrino oscillations between ν_1 and ν_2, which is well studied by the Sudbury Neutrino Observatory (SNO). Born as electron neutrinos from nuclear reactions inside the Sun, these solar neutrinos have energies ranging from above 200 keV to below 20 MeV [51]. Given a propagation distance of 10^8 km between the Sun and the Earth, an experiment on Earth is sensitive to Δm^2_{21} above 10^{-10} eV^2. However, as explained in Section 2.1.2, it turns out that both solar and atmospheric neutrinos behave slightly differently in matter than in vacuum, especially in a dense environment such as the cores of the Sun and the Earth.

2.1.2 Neutrino Oscillations in Matter

When a neutrino travels through matter, it undergoes coherent forward scatterings with the nearby electrons, protons, or neutrons. Modifications on neutrino oscillation probability due to neutrinos traveling in matter were first formulated in 1978 by Wolfenstein [52]. A few years later, Mikheyev and Smirnov predicted that neutrino mixing in matter with a slow changing density enhances neutrino oscillations [53, 54] and may even cause non-oscillatory adiabatic flavor conversion [55–57]. This matter effect on neutrino mixing is known as the Mikheyev-Smirnov-Wolfenstein (MSW) effect.

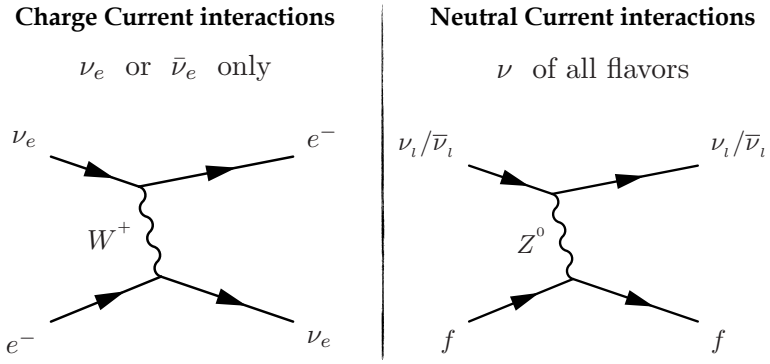

Figure 2.4: Coherent forward scattering with matter during propagations of neutrinos at small momentum transfers: (left) charge current and (right) neutral current interactions. A coherent forward scattering by an electron (anti-)neutrino can occur via an exchange of a $W^{\pm}$ or Z^0 gauge boson, while a coherent forward scattering by a neutrino of other flavors can only undergo an exchange of Z^0.

Figure 2.4 shows the two types of coherent forward scattering. The first type is a neutral current interaction. According to the Standard Model (SM), the Hamiltonian governing the $\nu_l + f \rightarrow \nu_l + f$ scattering at a limit of small momentum transfer returns an interaction potential energy V_Z given by [38]

$$V_Z = -\frac{\sqrt{2}}{2} G_F N_n, \tag{2.25}$$

where G_F is the Fermi coupling constant, and N_n is the number density of neutrons in the medium. Although the Earth and the Sun mostly consist of electrons, protons, and neutrons, V_Z only depend on the number density of neutrons because the Z^0 coupling of a neutrino to an electron is the same, but with opposite sign, as that to a proton. In addition, a neutrino of any flavor can undergo a Z^0 boson exchange equally; this common growth in energy among different neutrino flavors does not alter neutrino oscillation probability. The second type of coherent forward scattering involves an exchange of $W^{\pm}$ boson. Because of flavor conservation in weak interactions, only electron (anti-)neutrinos can undergo this charge current interaction. Similar to V_Z, the interaction potential energy from $\nu_e + e^- \to \nu_e + e^-$ is given by the SM;

$$V_W = +\sqrt{2} G_F N_e, \tag{2.26}$$

where N_e is the electron number density in the medium.

Due to the extra potential energy from charge current ν_e coherent forward scattering, neutrino oscillation probability in vacuum is modified. Recall that the energy dependence in Equation 2.20 comes from solving the Schrödinger equation with an assumption of a free neutrino. In the presence of V_W, an extra phase term, $\Delta\phi_{\text{matter}} = V_W t$, is added to the argument of the exponential function in the wavefunction in Equation 2.13. The extra interaction term leads to a resonance of neutrino oscillation probability [52–55, 58, 59]; Section 2.1.3.2 presents a simplified calculation for a two-flavor neutrino mixing with matter effect. According to Mikheyev and Smirnov [53], the interaction potential energy V_W can be interpreted as an index of refraction n. For a given medium, a *refractive length* is defined by [55]

$$L_n \equiv \frac{\sqrt{2}\pi}{G_F N_e}. \tag{2.27}$$

As shown in Section 2.1.3.2, a resonance occurs when

$$L_{kj}^{\text{osc}} \sim 4E/\Delta \text{m}_{kj}^2 \sim L_n \cos\, 2\theta_{kj}, \tag{2.28}$$

where θ_{kj} is the mixing angle between a given pair of mass eigenstates.

Two phenomena are predicted when a neutrino propagates in matter. First, the oscillation probability is enhanced when the oscillation length is roughly the same as the refractive length. For a small mixing angle, the oscillations between the corresponding mass eigenstates are maximal due to the presence of matter, mimicking the behavior of a large mixing angle. This phenomenon is known as a resonance of oscillation probability [53,54]. The second phenomenon known as flavor conversion [55–57] arises if the electron number density N_e changes adiabatically, such as the density from the solar core to the surface of the Sun. As discussed in Section 2.1.3.2, the effective mixing parameters due to the presence of matter depend on the electron number density. If the number density changes slowly, the effective mixing parameters would change as well. Because mixing parameters determine the flavor content of a given mass eigenstate, a changing density means a changing flavor content as a neutrino propagates without any interference effects discussed in Section 2.1.1. In particular, if the mixing angle in vacuum is maximal, the effective mixing angle in a dense environment is very small (see Equation 2.42). This implies that a neutrino produced as flavor α is dominated by one mass eigenstate instead of a mixture of mass eigenstates if it were in vacuum. As this one mass eigenstate propagates in matter with a slowly changing density, its flavor content changes. Therefore, without any interference of multiple mass eigenstates, a flavor conversion due to the presence of matter occurs. In the case where the mixing angle is not maximal but still large, a combination of neutrino oscillations and flavor conversions can be observed, such as the case of solar neutrino mixing discussed in Section 2.2.1.

2.1.3 Two Neutrino Mixing Approximation

In a two-flavor mixing approximation, the flavor and mass eigenstates are related by a rotational matrix. Therefore, as shown in Section 2.1.3.1, the oscillation probability in vacuum in Equation 2.20 between two flavor eigenstates depends, not only on the mass squared differences, but also on the mixing angles. In addition, when neutrinos pass through matter, their oscillation probabilities are modified due to the coherent forward scattering of electron (anti-)neutrinos. As discussed in Section 2.1.3.2, the MSW effect not only enhances the oscillation probability but also changes the mixing parameters.

2.1.3.1 Two Neutrino Mixing in Vacuum

In a two-flavor approximation, ν_1 and ν_2 are the mass eigenstates, and ν_e and ν_μ are the flavor eigenstates. These two sets of eigenstates are related by a 2×2 rotational mixing matrix with a mixing angle θ_{21},

$$U = \begin{pmatrix} \cos\,\theta_{21} & \sin\,\theta_{21} \\ -\sin\,\theta_{21} & \cos\,\theta_{21} \end{pmatrix}. \tag{2.29}$$

Hence, the two flavor eigenstates are given by

$$\begin{aligned} |\nu_e\rangle &= \cos\,\theta_{21}\,|\nu_2\rangle + \sin\,\theta_{21}\,|\nu_3\rangle \\ |\nu_\mu\rangle &= -\sin\,\theta_{21}\,|\nu_2\rangle + \cos\,\theta_{21}\,|\nu_3\rangle\,. \end{aligned} \tag{2.30}$$

Given a two-neutrino system, the vacuum Hamiltonian is also a 2×2 matrix:

$$\mathcal{H}_{\text{vac}} = \begin{pmatrix} \mathcal{H}_{ee} & \mathcal{H}_{e\mu} \\ \mathcal{H}_{\mu e} & \mathcal{H}_{\mu\mu} \end{pmatrix}. \tag{2.31}$$

Assuming a free neutrino has an energy given by the energy-momentum dispersion relation in Equation 2.6, each element in Equation 2.31 is given by

$$\begin{aligned}\langle\nu_\alpha|\,\mathcal{H}_{\text{vac}}\,|\nu_\beta\rangle &= \sum_{k=1,2}\langle\nu_i|\,U_{\alpha k}\mathcal{H}_{\text{vac}}\sum_{j=1,2}U_{\beta j}\,|\nu_2\rangle \\ &= \sum_{k=1,2}U_{\alpha k}U^*_{\beta k}E_k \\ &\approx \sum_{k=1,2}U_{\alpha k}U^*_{\beta k}\left(p+\frac{m_k^2}{2p}\right).\end{aligned} \tag{2.32}$$

The vacuum Hamiltonian then becomes

$$\mathcal{H}_{\text{vac}} = \frac{\Delta\text{m}^2_{21}}{4E}\begin{pmatrix}-\cos\,2\theta_{21} & \sin\,2\theta_{21}\\ \sin\,2\theta_{21} & \cos\,2\theta_{21}\end{pmatrix}, \tag{2.33}$$

where the constant multiplication of an identity matrix, $\big[p+(\text{m}_1^2+\text{m}_2^2)/4p\big]\mathcal{I}$, is dropped. Either by the energy-momentum relation of a free particle or by diagonalizing Equation 2.43, the energy eigenvalues are

$$E_1 = -\frac{\Delta\text{m}^2_{21}}{4E} \qquad \text{and} \qquad E_2 = +\frac{\Delta\text{m}^2_{21}}{4E}. \tag{2.34}$$

If a neutrino starts as a flavor eigenstate $|\nu_e(0)\rangle$, its time evolution is described by the Schrödinger equation.

$$\begin{aligned}i\frac{\partial}{\partial t}\,|\nu_e(t)\rangle &= \mathcal{H}^{\text{diag}}_{\text{vac}}\;U\,|\nu_e(0)\rangle \\ &= \frac{\Delta\text{m}^2_{21}}{4E}\begin{pmatrix}1 & 0\\ 0 & -1\end{pmatrix}\begin{pmatrix}\cos\,\theta_{21} & \sin\,\theta_{21}\\ -\sin\,\theta_{21} & \cos\,\theta_{21}\end{pmatrix}\begin{pmatrix}1\\0\end{pmatrix} \\ |\nu_e(t)\rangle &= \cos\,\theta_{21}\;e^{+i\Delta\text{m}^2_{21}/4E}\,|\nu_1\rangle + \sin\,\theta_{21}\;e^{-i\Delta\text{m}^2_{21}/4E}\,|\nu_2\rangle\,.\end{aligned} \tag{2.35}$$

Therefore, the $\nu_e \to \nu_\mu$ oscillation probability is given by

$$\begin{aligned}P_{\text{vac}}(\nu_e\to\nu_\mu) &= \big|\,\langle\nu_\mu|\nu_e(t)\rangle\,\big|^2 \\ &= \sin^2\,2\theta_{21}\,\sin^2\!\left(\Delta\text{m}^2_{21}\frac{L}{4E}\right),\end{aligned} \tag{2.36}$$

which is the same as the expression in Equation 2.20. Note that the oscillation probability has a sinusoidal behavior with an amplitude driven by the mixing angle and a frequency proportional to the mass squared difference.

2.1.3.2 Two Neutrino Mixing in Matter

If a neutrino travels through matter and is surrounded by electrons, an interaction potential is introduced from coherent forward scatterings by electron (anti-) neutrinos. This potential V_W in Equation 2.26 is therefore only added to $\mathcal{H}_{ee}$ element in the vacuum Hamiltonian matrix (Equation 2.31).

$$\mathcal{H}_{\mathrm{M}} = \frac{\Delta \mathrm{m}^2_{21}}{4E} \begin{pmatrix} -\cos 2\theta_{21} & \sin 2\theta_{21} \\ \sin 2\theta_{21} & \cos 2\theta_{21} \end{pmatrix} + V_W \begin{pmatrix} 1 & 0 \\ 0 & 0 \end{pmatrix}. \tag{2.37}$$

Since $\mathcal{H}_M$ needs to be diagonalized, it is convenient to re-express the second term diagonally without changing the physics.

$$\begin{aligned} \mathcal{H}_{\mathrm{M}} &= \frac{\Delta \mathrm{m}^2_{21}}{4E} \begin{pmatrix} -\cos 2\theta_{21} & \sin 2\theta_{21} \\ \sin 2\theta_{21} & \cos 2\theta_{21} \end{pmatrix} + \frac{V_W}{2} \begin{pmatrix} 1 & 0 \\ 0 & -1 \end{pmatrix} + \frac{V_W}{2} \begin{pmatrix} 1 & 0 \\ 0 & 1 \end{pmatrix} \\ &= \frac{\Delta \mathrm{m}^2_{21}}{4E} \begin{pmatrix} -\cos 2\theta_{21} & \sin 2\theta_{21} \\ \sin 2\theta_{21} & \cos 2\theta_{21} \end{pmatrix} + \frac{V_W}{2} \begin{pmatrix} 1 & 0 \\ 0 & -1 \end{pmatrix}. \end{aligned} \tag{2.38}$$

The last term is dropped because it is a constant identity matrix. Hence, $\mathcal{H}_M$ can be expressed as

$$\mathcal{H}_{\mathrm{M}} = \frac{\Delta \mathrm{m}^2_{21}}{4E} \begin{pmatrix} -(\cos 2\theta_{21} - x) & \sin 2\theta_{21} \\ \sin 2\theta_{21} & (\cos 2\theta_{21} - x) \end{pmatrix}, \tag{2.39}$$

where, from Equation 2.26,

$$x \equiv \frac{2\sqrt{2} G_F N_e E}{\Delta \mathrm{m}^2_{21}}. \tag{2.40}$$

By defining the *effective* mixing parameters in matter,

$$\Delta \mathrm{m}^2_{21_M} \equiv \Delta \mathrm{m}^2_{21} \sqrt{\sin^2 2\theta_{21} + (\cos 2\theta_{21} - x)^2} \tag{2.41}$$

$$\sin^2 2\theta_{21_M} \equiv \frac{\sin^2 2\theta_{21}}{\sin^2 2\theta_{21} + (\cos 2\theta_{21} - x)^2}, \tag{2.42}$$

the Hamiltonian in matter $\mathcal{H}_M$ can then be expressed in the same form as $\mathcal{H}_{\mathrm{vac}}$ in Equation 2.43.

$$\mathcal{H}_M = \frac{\Delta \mathrm{m}^2_{21_M}}{4E} \begin{pmatrix} -\cos 2\theta_{21_M} & \sin 2\theta_{21_M} \\ \sin 2\theta_{21_M} & \cos 2\theta_{21_M} \end{pmatrix}. \tag{2.43}$$

Thus, the $\nu_e \to \nu_\mu$ oscillation probability in matter is given by

$$P_M(\nu_e \to \nu_\mu) = \sin^2 2\theta_{21_M} \sin^2\left(\Delta m^2_{21_M} \frac{L}{4E}\right). \tag{2.44}$$

As discussed in Section 2.1.2, two behaviors are predicted due to the presence of matter. First, because of the extra interaction potential from nearby electrons, the oscillation parameters are modified by the energy dependent x, which essentially measures the importance of matter effect on neutrino oscillations. Given a very dense environment, the mass squared difference in matter is scaled by $\sim x$, implying a higher frequency of oscillation probability. On the other hand, the mixing angle in matter decreases given a large x, suppressing the oscillation probability. When $x \sim \cos 2\theta$, the effective mixing angle is ~ 1, regardless of the size of the mixing angle in vacuum. If the mixing angle in vacuum is small, the oscillation is still at maximal in the presence of matter, leading to a resonance in the oscillation probability [55]. The second behavior is related to a slowly changing density in matter through which a neutrino propagates. In a given dense environment, the effective mixing angle is small. Since the mixing angle determine the flavor content of a given eigenstate, a small mixing angle implies that one of the mass eigenstates dominate. If the density decreases slowly, the mixing angle slowly increases, changing the flavor content of a given mass eigenstate. Thus, if a neutrino is produced at a dense environment and propagates through an adiabatic gradient of density, an observer at a less dense location observes a flavor conversion [53–55]. This is particularly important in the observations of solar neutrinos as discussed in Section 2.2.1.

Depending on the size of the mixing parameters, an experiment with a targeted L/E range may observe non-negligible MSW effects. Given a high electron number density in the Sun and a neutrino energy range between a few and below 20 MeV [53, 56, 61], solar neutrino experiments, such as the Kamioka Observatory and the Solar Neutrino Observatory (SNO), are sensitive to matter effect due to the Solar core.

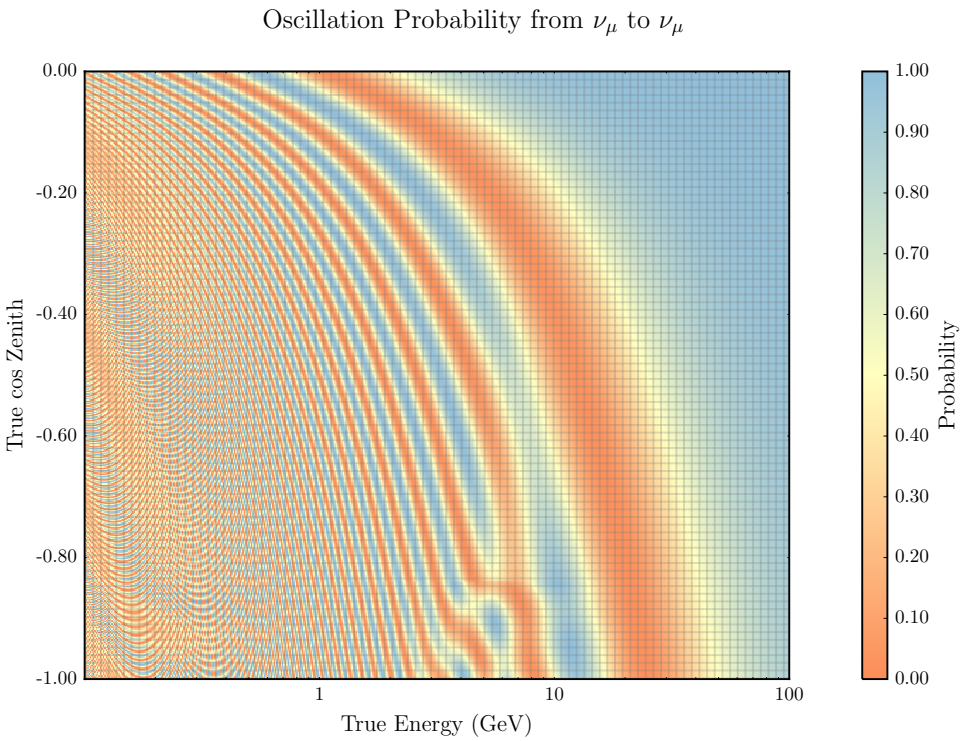

Figure 2.5: Atmospheric ν_μ survival probability in matter based on world averaged best fit oscillation parameters from [1]. Color bar represents the $\nu_\mu \to \nu_\mu$ survival probability. A neutrino coming from the horizon without passing through Earth's core has a cos zenith of 0; and cos zenith of -1 corresponds to a direction from which a neutrino passes through the Earth's core with its propagation distance equal to the Earth's diameter. A matter condition is assumed based on an Earth model from [60]. The distorted oscillation pattern in the region where cos zenith is between -0.8 and -1.0 is due to high electron number densities in the Earth's core.

For atmospheric neutrinos, matter effect cannot be ignored for neutrinos passing through the Earth's core and mantle. Figure 2.5 presents the $\nu_\mu \to \nu_\mu$ survival probabilities assuming neutrinos propagating through Earth's matter. Compared to Figure 2.3 without Earth matter, the survival probability is distorted significantly when neutrinos pass through the Earth's core, where cos zenith is between -0.8 and -1.0.

2.2 Neutrino Oscillation Experiments

From Equation 2.24 in Section 2.1.1, the unitary mixing matrix U can be decoupled into three 2×2 matrices: atmospheric, cross-mixing, and solar terms. To look for signatures of neutrino oscillations from one of the three terms, an oscillation experiment is designed to detect neutrinos from a specific L/E window. In 1957, when no neutrino oscillation pattern was observed in laboratory scales, Pontecorvo proposed oscillation studies using neutrinos produced in the Sun [19]. Because solar neutrino oscillations are significantly enhanced due to the dense environment inside the solar core, solar neutrino experiments are built to study neutrino mixing between ν_1 and ν_2, as discussed in Section 2.2.1. The cross-mixing term in Equation 2.24 is observed via accelerator and reactor neutrino experiments (see Section 2.2.2). The mixing angle θ_{31} related to the cross-mixing term was expected to be very close to 0°; however, recent studies have found a significantly large θ_{31} compared to 0°. Section 2.2.3 discusses atmospheric neutrino oscillation studies. In particular, the first definitive evidence from the Super-Kamiokande experiment in 1998 is presented. A summary on the current knowledge of neutrino oscillation parameters is presented in Section 2.2.4, followed by unanswered, but exciting, questions in Section 2.2.5.

2.2.1 Solar Neutrino Experiments

Solar neutrino experiments study neutrinos produced by various nuclear reaction chains inside the Sun. The right plot [62] in Figure 2.6 presents the energy spectra of solar neutrinos produced by different processes according to the Standard Solar Model (SSM). While most of the solar neutrinos are produced via proton-proton interactions, these neutrinos have energies below 0.5 MeV, which are difficult to detect. On the other hand, the rare boron-8 (^8B) and hep reaction processes are

expected to produce neutrinos up to $\sim$ 15 and 18 MeV. These two nuclear reaction occur at different part of the Sun, as shown on the left plot in Figure 2.6 [61]. The hep process (dashed yellow line), which has not been observed so far, produce neutrinos at a distance away from the solar core, while neutrino flux from ^8B (solid blue) is expected to peak at the extremely dense solar core, which is within the first 10% of the solar radius.

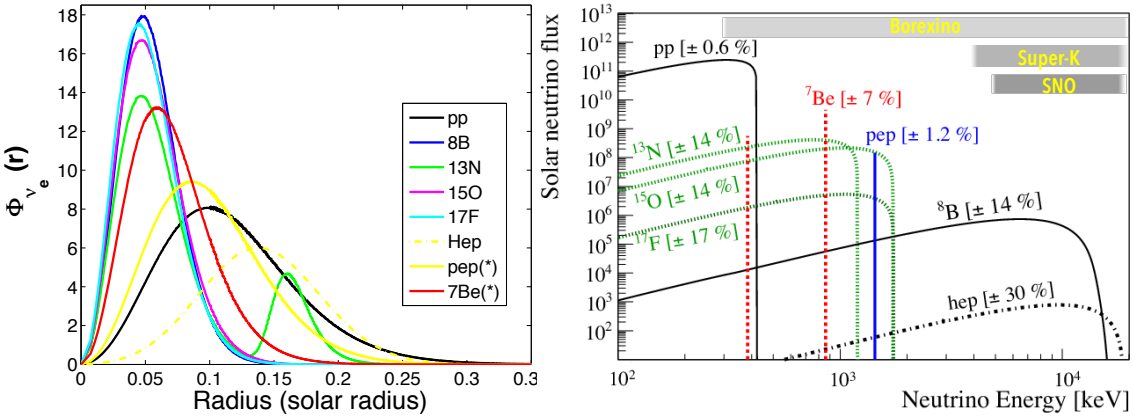

Figure 2.6: Predictions of electron solar neutrino productions according to the Standard Solar Model: (left) electron neutrino fluxes as a function of solar radius and (right) solar electron neutrino energy spectra. Different colors represents different nuclear reactions. These reactions produce electron neutrinos at different radii of the Sun. In particular, the boron-8 (^8B), iron-17, oxygen-15, and nitrogen-13 reactions produce electron neutrinos at the very core of the Sun (within 10% of the solar radius). The plot on the right shows the solar neutrino energy spectra for the different reactions. Proton-proton (pp) reaction produces most of the solar neutrinos with energies below 0.5 MeV, which are hard to detect. The most energetic neutrinos from the Sun are produced by ^8B (up to $\sim$ 15 MeV) and the *Hep* (up to $\sim$ 18 MeV), both of which are rare processes compared to pp chain. Left and right plots are adapted from [61] and [62] respectively.

Given a mean neutrino energy from ^8B reaction process of $\sim$ 8 MeV, if the oscillation length in Equation 2.22 *were* the distance between the Sun and the Earth, a naive approach using the two flavor approximation in vacuum would imply a

mass squared difference Δm^2_{21} to be $\sim 10^{-10}$ eV^2, which is drastically different from the current world averaged best fit value of $7.50^{+0.19}_{-0.17} \times 10^{-5}$ eV^2 [1]. The caveat comes from the MSW matter effects due to a dense environment in the solar core plus the slowly changing density gradient as the neutrinos propagate from the core to the surface of the Sun. With a fairly large world averaged best fit mixing angle θ_{21} of $33.48^{+0.78}_{-0.75}$ degrees [1], both the enhancement of neutrino oscillations and the adiabatic flavor conversion discussed in Sections 2.1.2 and 2.1.3.2 have to be taken into account when measuring the numerical values of solar neutrino oscillation parameters.

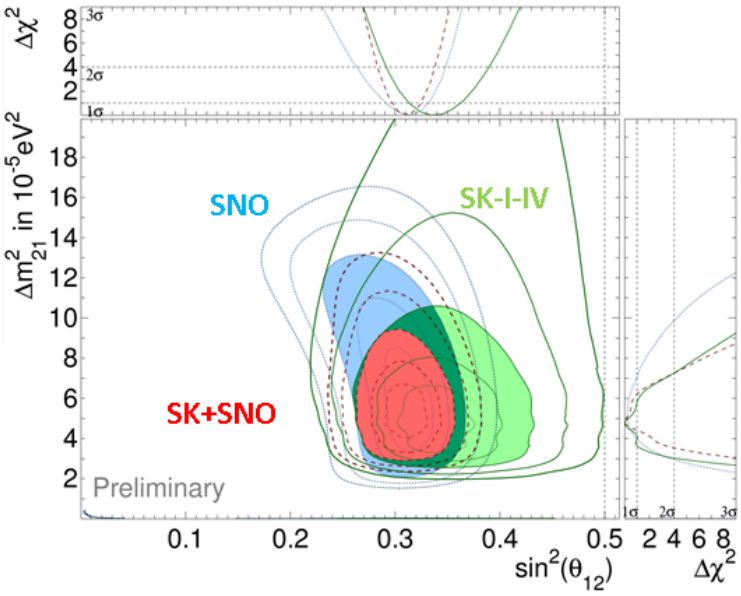

Figure 2.7: Measurements of solar neutrino oscillation parameters from combined analyses by SK and SNO: (top) $\Delta\chi^2$ in the space of $\sin^2\theta_{12}$, (right) $\Delta\chi^2$ in the space of Δm^2_{21}, and (bottom left) two dimensional $\Delta\chi^2$ in the space of both solar mixing parameters. The solid green lines represents the contours from SK alone, with the 3σ confidence level shown as the green shaded area. The blue lines and shaded area are the same for SNO [63]. The red dashed lines and shaded area are the results from combined SK and SNO results. The contours are adapted from [64].

The world averaged best fit mixing parameters measured from solar neutrino oscillation experiments involve hard works from many collaborations. Two of the earlier experiments studying solar neutrinos are the Super-Kamiokande (SK) and the Sudbury Neutrino Observatory (SNO), both of which are sensitive to solar neutrinos above 3 MeV produced by ^8B and hep reaction processes [62]. Located 1 km underneath the peak of Mount Ikenoyama in Kamioka Town, Japan, SK is a large cylindrical water Cherenkov detector with 50 megatons of ultra pure water. Also sensitive to atmospheric neutrino oscillations as discussed in Section 2.2.3, the SK experiment was designed to determine with high statistics if there is indeed a deficit in the observed counts of electron neutrinos from the Sun. With upgraded electronics, improved water system dynamics, and better calibrations, the latest SK-IV can detect low energy neutrinos down to 3.49 MeV [64]. On the other hand, the SNO experiment is located 2 km underground in Vale Inco's Creighton Mine in Sudbury, Ontario, Canada. Featuring the use of heavy water D_2O, the SNO experiment can identify different neutrino interactions and, therefore, count the total neutrino flux [51]. Not only are both detectors located underground to reduce atmospheric muon backgrounds, both SK and SNO experiments measure the same solar neutrino source from ^8B in a similar energy range but in slightly different ways with different systematic effects. Therefore, one of the latest published results in 2017 from SK presented in Figure 2.7 [64] combines constraints on solar neutrino oscillation parameters from both experiments. Both SK and SNO show strong evidence for the MSW matter effects when compared to the vacuum assumption.

2.2.2 Accelerator and Reactor Neutrino Experiments

Accurate measurements of θ_{13} and δ_{CP} require good understanding on the neutrino sources, and hence, multiple accelerators with neutrino beams are built.

These neutrino accelerators includes the MiniBooNE [65], the MINOS [66], the NOνA [67], and the MINERνA [68] at Fermilab, as well as the Tokai-to-Kamioka (T2K) experiment in Japan [69]. Several reactors that produce intense neutrino beams also made remarkable contributions to θ_{13} measurement such as the Daya Bay Reactor Neutrino Experiment [50].

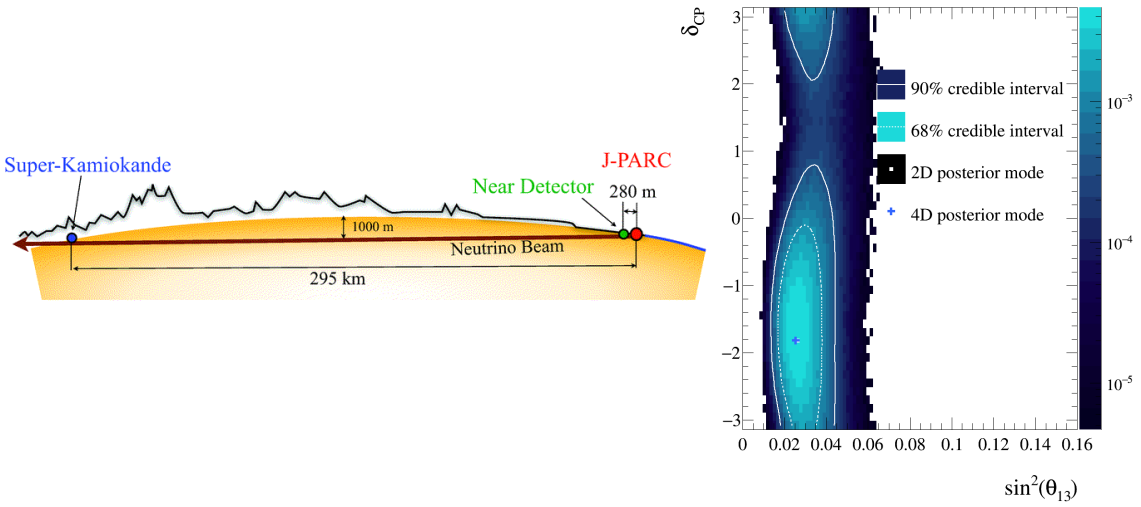

Figure 2.8: The Tokai-to-Kamioka Experiment: (left) a schematic picture of the detector set up and (right) the latest measurement of θ_{13} and δ_{CP}. The left and right plots are adapted from [69] and [70] respectively.

As a long-baseline neutrino oscillation experiment, the Tokai-to-Kamioka (T2K) experiment aims at measuring δ_{CP}, θ_{13}, θ_{23}, and Δm^2_{32}. As shown on the left of Figure 2.8, the T2K experiment consists of two parts: the production site and the detection site [69]. The J-PARC accelerator located at the production site produces muon neutrinos via pion decays. The direction of the neutrino beam with a peak energy at $\sim$ 600 MeV are monitored by the near detector [69]. After traveling a distance of 295 km, the neutrino beam arrives at the far detector, the Super-Kamiokande detector. Given the energy of the beam, the distance between the two detectors, and the world averaged best fit mixing parameters, the first maximal ap-

pearance of electron neutrinos is expected. The right plot in Figure 2.8 shows that the T2K experiments is also capable of measuring θ_{13} and the CP violating phase with high precision [70]; their measurements will be improved in the near future after the upgrades. On the other hand, sharing the same neutrino beam at a peak energy of $\sim$ 3 GeV, neutrino accelerator experiments at Fermilab, including the MINOS [66], the NOνA [67], and the MINERνA [68] detectors, have similar setups as the T2K detector, in which a neutrino beam is monitored by a near detector and arrives at a far detector where oscillation effects are observed. Their measurements of atmospheric oscillation parameters are summarized in Section 2.2.4.

One of the more recent discoveries related to neutrino oscillations is the non-zero θ_{13} by the Daya Bay Reactor Neutrino Experiment [50] located at the south of China. As shown on the left of Figure 2.9 [71], the Daya Bay Reactor Neutrino Experiment has a near-far arrangement of detectors, labeled as **EH**, observing oscillations of electron anti-neutrinos of a few MeV from the nearby reactors, labeled as the black dots. The plot on the right shows the ratio of data counts and expected counts from no oscillation as a function of propagation distance, and a clear deficit is observed. The χ^2 landscape in the $\sin^2\ \theta_{13}$ space is also presented, rejecting the non-zero $\theta 13$ case by more than 5σ [71].

2.2.3 Atmospheric Neutrino Experiments

Atmospheric neutrinos are produced when high energy cosmic rays interact with the air particle in the Earth's atmosphere. The existence of cosmic rays was discovered in 1912, when Hess launched seven balloon flights to perform ionization measurements at high altitudes. Although the radiation intensity first decreases as the altitude goes up, Hess found a strong increase in ionization above 1400 meters [73]. Because experiments were performed during a solar eclipse, at day, and at

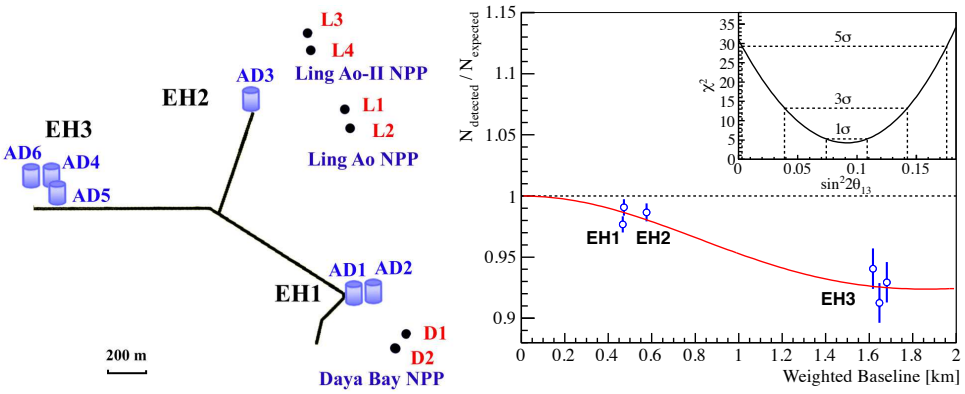

Figure 2.9: The Daya Bay Experiment: (left) the configuration of detectors and reactors and (right) the evidence of non-zero θ_{13}. On the left, black dots with red labels are the locations of reactors, and the cylindrical tanks labeled as **EH** are the neutrino detection cites. The right plot shows the ratio of counts between data and predictions from null hypothesis as a function of propagation length. The discreteness of data points is caused by the distances between reactors and detectors. The χ^2 scan in θ_{13} space is also shown on the top right corner, rejecting a non-zero θ_{13} by 5.2σ. These plots are adapted from [71].

night [74], Hess believed that these cosmic radiation with a very high penetrating power cannot be coming from the Sun [73, 74]. Nowadays, many telescopes are built to study the composition, energy, and the origin of cosmic rays. As shown in Figure 2.10 [72], cosmic ray primaries consist mostly of protons with other particles, such as electrons, positrons, and heavier elements. The energy spectra of these particles are well measured, and the current best model to describe the cosmic ray energy spectrum is provided by *GaisserH4a* [75], shown as the black solid line in Figure 2.10. As explained in Section 3.1, the interactions between these cosmic ray particles and the air molecules in the Earth's atmosphere produce secondary mesons, which decays into leptons, including neutrinos. Depending on the energies of the primary particles, neutrinos produced are observed to have energies ranging between $\sim$ MeV and PeV. Atmospheric neutrino oscillation studies in general are

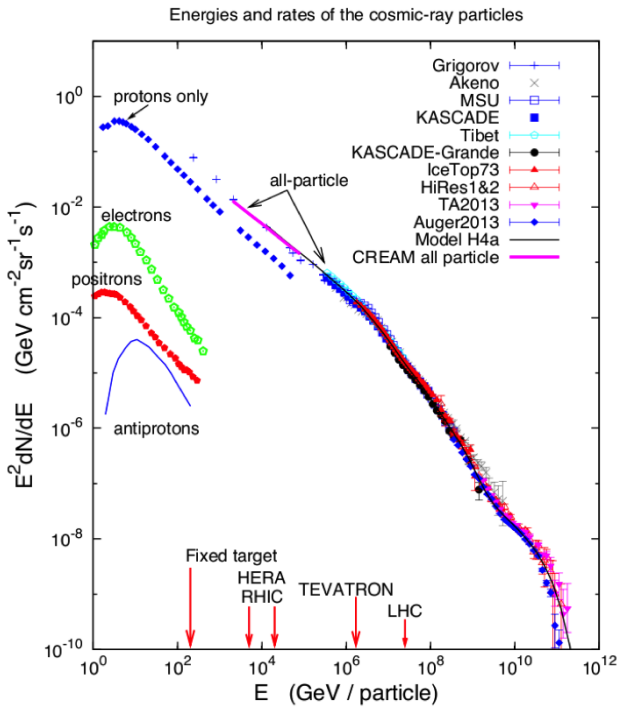

Figure 2.10: Energies and rates of the cosmic-ray particles. Data points are measured energy spectra of different cosmic ray primaries from different experiments, while black and magenta solid lines are predictions from theoretical models. This plot is adapted from [72].

interested in atmospheric neutrinos ranging from a few GeV up to 100 GeV.

One of the most well-known atmospheric neutrino oscillation experiments is the Super-Kamiokande (SK) experiment, which provided the first definitive evidence of atmospheric neutrino oscillations in 1998. As shown in Figure 2.11, the SK experiment is a cylindrical water Cherenkov detector of 36.2 meters in height and 16.9 meters in radius. With over 11,000 photomultiplier tubes (PMTs) mounted along the wall, the cylindrical tank can hold 50 megatons of purified water [48]. When a neutrino interacts with a water molecule in the tank, a charged lepton may be produced, giving out Cherenkov light as it propagates through water. The photons are then detected by surrounding PMTs. Given the effective volume, SK can detect neutrinos with energies between $\sim$ MeV to tens of GeV, allowing both

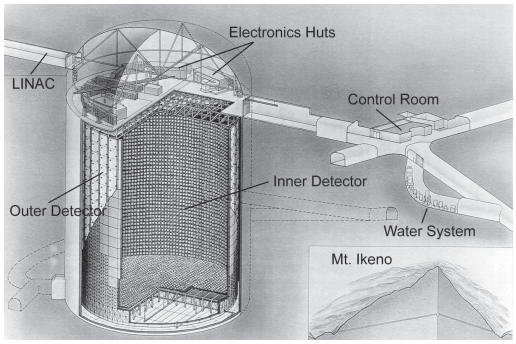

Figure 2.11: A schematic diagram of the Super-Kamiokande water Cherenkov detector. Holding 50 megatons of purified water, the SK detector is a cylindrical tank with a height of 36.2 meters and a radius of 16.9 meters. It consists of 11,146 photomultiplier tubes lined along the inner detectors. This diagram is adapted from [48].

solar and atmospheric neutrino oscillation studies. From 1996 until now, the SK experiments have gone through multiple upgrades and collected valuable data [48]. The SK collaboration also works closely with other neutrino experiments such as the SNO, K2K, and T2K experiments.

Sensitive to an energy range between an MeV and tens of GeV, the SK experiment studies atmospheric neutrino oscillations using both fully contained events, in which all energy of an event is deposited within the inner detector, and partially contained events, in which part of the event energy is detected at the outer detector. Neutrino events detected are divided into two energy ranges: the sub-GeV and the multi-GeV. For events in each of the energy range, the ratio R of $\nu_\mu counts to \nu_e$ counts are expected to be 1.0 assuming no neutrino oscillations. In 1998, the SK collaboration published two separate papers reporting the values of R to be 0.61 and 0.66 for events in sub- [76] and multi- [77] GeV ranges respectively. These values are significantly lower than expectation from null hypothesis. Soon after, the SK collaboration published a more thorough study with a total of 535 days of data [27]. As shown in the bottom row plots in Figure 2.12, all muon-like zenith histograms

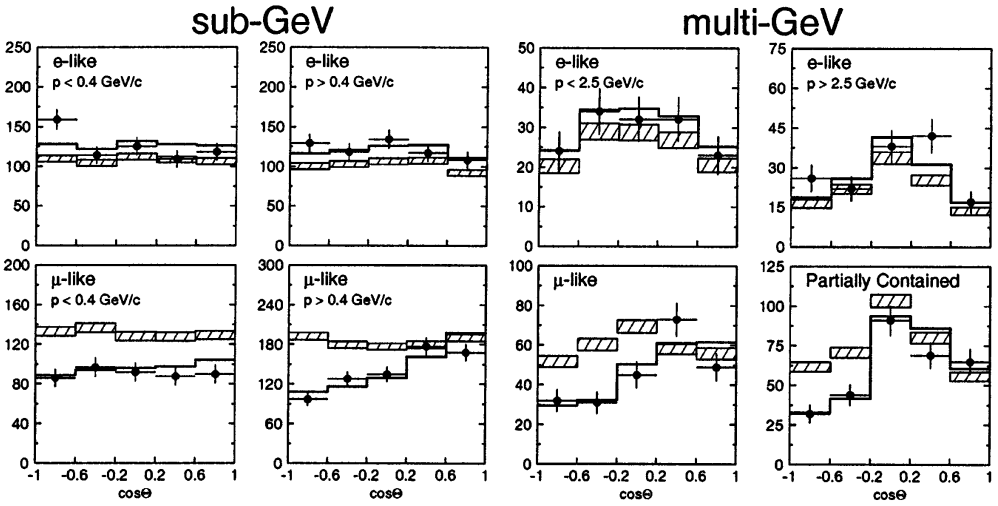

Figure 2.12: Histograms from the Super-Kamiokande experiment in 1998: (left four) events in the sub-GeV energy range and (right four) events in the multi-GeV range. For the four left plots, the top two plots are the electron-like events, while the bottom two are the muon-like events. Sub-GeV events of each flavor type are then divided based on their observed momenta: events with momenta below 0.4 GeV are on the left, while events with momenta above 0.4 GeV are on the right. Events that fall into each neutrino flavor and momentum bin are then further binned by the zenith angle. For each sub plots, black dots represent data histogram, and the hatched region shows the MC expected histograms with no oscillation hypothesis. The best fit expectations from $\nu_\mu \rightarrow \nu_\tau$ hypothesis are also shown as the black solid lines. The same plotting scheme is applied to the multi-GeV events on the four right plots. For the multi-GeV range, electron-like events are divided based on their observed momenta, but the muon-like events are separated into fully or partially contained. For all muon-like histogram, a significant deficit in the up going region ($\cos\theta$ ¡ 0) compared to predictions from the null hypothesis is observed. The SK experiment rejected no neutrino oscillation hypotheses by more than 6σ. These plots are adapted from [27].

showed significant deficits in event counts in the up going region, where neutrinos passing through the Earth have longer propagation distances. Since the theory of neutrino oscillations predicts that neutrinos oscillate as a function of L/E, the same published paper also provided the ratio of L/E between data and MC from no os-

cillation hypothesis, as shown on the right of Figure 2.13 [27]. While no obvious deviations in number of ν_e events between data and null hypothesis, the number of ν_μ events observed is 6σ [27] less than the expectation from no oscillations. With an assumption that neutrinos oscillate, the SK collaboration presented, on the left of Figure 2.13 [27], their measurement of atmospheric neutrino oscillation parameters, including the mass squared difference Δm^2_{32} and the mixing angle $\sin^2 2\theta_{23}$. The measured mixing angle agrees with the previous result from Kamiokande experiment, suggesting a very large θ_{23}, while the measured Δm^2_{32} from SK has a slightly lower value than that from previous measurement.

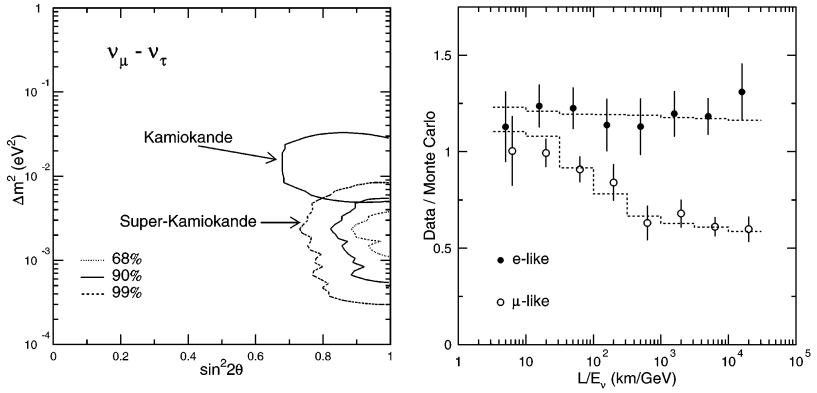

Figure 2.13: The first definitive evidence of atmospheric neutrino oscillation from the Super-Kamiokande (SK) experiment: (left) contour of atmospheric neutrino oscillation parameters and (right) ratio of L/E histogram between data and prediction from null hypothesis. The plot on the left show the 68, 90, and 99% confidence levels of the measured values of atmospheric neutrino oscillation parameters; previous contour from Kamiokande experiment is also shown for comparison. The right plot shows a clear deficit in ν_μ events as a function of L/E, as predicted by the theory of neutrino oscillations, while no clear ν_e disappearance is seen. These plots are adapted from [27].

One of the goals of the IceCube Neutrino Observatory with DeepCore is to improve atmospheric neutrino oscillation parameters using atmospheric neutrinos. While the SK detectors have gone through multiple upgrades to improve the ac-

curacy and precision of oscillation measurements, it does not have a large enough volume to study neutrinos with energies beyond multi-GeV. As discussed in Section 2.1, based on current knowledge of atmospheric neutrino oscillation parameters, the oscillations $\nu_\mu \to \nu_\tau$ are expected to be maximal at 25 GeV. Given an effective volume ~ 300 times larger than SK, IceCube-DeepCore can investigate atmospheric neutrino oscillations at this energy scale for the first time with much higher statistics than SK. While the latest published measurements of atmospheric oscillation parameters is shown in Section 2.2.4, the goal of this dissertation is to improve measurements of these parameters using IceCube-DeepCore.

2.2.4 Summary of Oscillation Parameter Measurements

Since the discovery of neutrino oscillations, many neutrino oscillation experiments have been built to measure the neutrino mixing parameters. As shown in Figure 2.14 [78], uncertainties of neutrino oscillation parameters have shrunk by orders of magnitudes over the past decades. Today, we have a decent knowledge on the numerical values of the mixing parameters in the unitary mixing matrix. Recall from Equation 2.24, the PMNS mixing matrix U is given by

$$
\begin{aligned}
U &= \underbrace{\begin{bmatrix} 1 & 0 & 0 \\ 0 & c_{23} & s_{23} \\ 0 & -s_{23} & c_{23} \end{bmatrix}}_{\text{Atmospheric}} \times \underbrace{\begin{bmatrix} c_{13} & 0 & s_{13}e^{-i\delta} \\ 0 & 1 & 0 \\ -s_{13}e^{i\delta} & 0 & c_{13} \end{bmatrix}}_{\text{Cross-Mixing}} \times \underbrace{\begin{bmatrix} c_{12} & s_{12} & 0 \\ -s_{12} & c_{12} & 0 \\ 0 & 0 & 1 \end{bmatrix}}_{\text{Solar}} \\
&= \begin{bmatrix} c_{12}c_{13} & c_{13}s_{12} & s_{13}e^{-i\delta} \\ -c_{23}s_{12} - c_{12}s_{13}s_{23}e^{i\delta} & c_{12}c_{23} - s_{12}s_{13}s_{23}e^{i\delta} & c_{13}s_{23} \\ c_{23}s_{12}s_{23} - c_{12}c_{23}s_{13}e^{i\delta} & -c_{12}s_{23} - c_{23}s_{12}s_{13}e^{i\delta} & c_{13}c_{23} \end{bmatrix} \\
&= \begin{bmatrix} U_{e1} & U_{e2} & U_{e3} \\ U_{\mu 1} & U_{\mu 2} & U_{\mu 3} \\ U_{\tau 1} & U_{\tau 2} & U_{\tau 3} \end{bmatrix},
\end{aligned}
\tag{2.45}
$$

where δ is the CP-violating phase, $c_{kj} \equiv \cos\theta_{kj}$, and $s_{kj} \equiv \sin\theta_{kj}$; θ_{kj} are the mixing angles. Each of the PMNS matrix elements determines the flavor content of the given

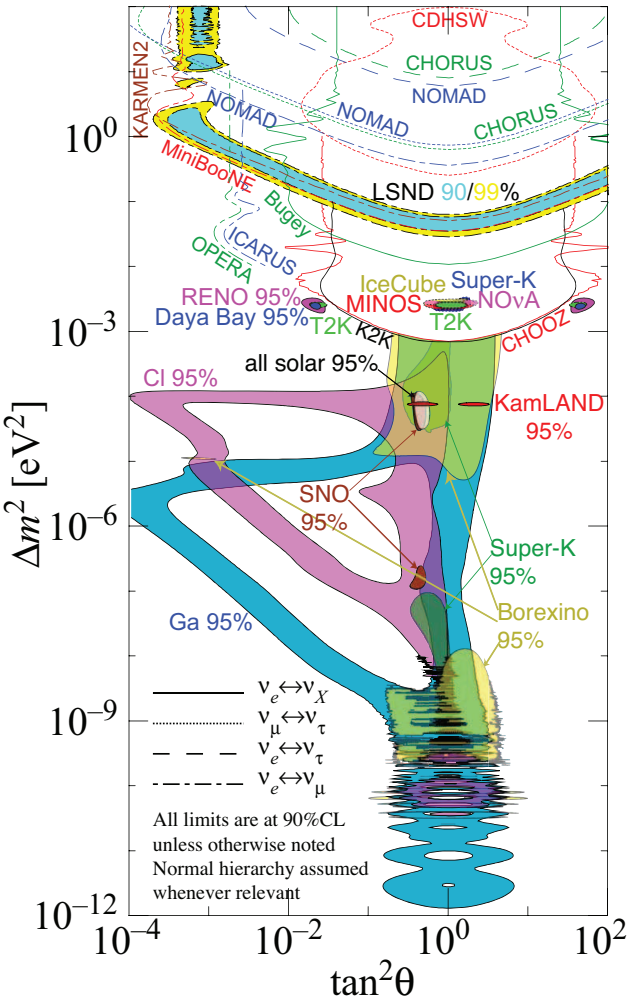

Figure 2.14: The evolution of neutrino oscillation parameter measurements. Both solar (solid lines) and atmospheric (dotted lines) oscillation parameters have shrunk by orders of magnitudes. Note that 90% contours in Figure 2.16 are located at $\Delta m^2 \sim 10^{-3}$ eV^2 and $\tan^2\,\theta \sim 1$. This plot is adapted from [78].

mass eigenstate ν_k. For example, the ν_e fraction of ν_1 is given by amplitude of $|U_{e1}|^2$, which is $\cos^2\theta_{12}\cos^2\theta_{13}$. Besides mixing angles, neutrino oscillations also depend on the mass squared splittings: Δm^2_{21} and Δm^2_{23}. Figure 2.15 [38] presents a summary of neutrino oscillation parameters assuming normal mass hierarchy where ν_3 is the heaviest. For each mass eigenstate, its flavor contents, shown as colored patches, are

obtained from the measured values of mixing angles. The world averaged best fit values of mixing angles and mass squared differences are summarized in Table 2.1 obtained from νFit 2016 [209]. Although the world averaged best fit prefers normal mass ordering, inverted mass hierarchy in which ν_3 is the lightest has not been ruled out. Based on the world averaged best fit values, the 3σ ranges of PMNS mixing matrix elements are given by [209]

$$U = \begin{bmatrix} U_{e1} & U_{e2} & U_{e3} \\ U_{\mu 1} & U_{\mu 2} & U_{\mu 3} \\ U_{\tau 1} & U_{\tau 2} & U_{\tau 3} \end{bmatrix} = \begin{bmatrix} (0.798, 0.843) & (0.517, 0.584) & (0.139, 0.155) \\ (0.234, 0.518) & (0.449, 0.696) & (0.617, 0.787) \\ (0.251, 0.528) & (0.463, 0.706) & (0.600, 0.774) \end{bmatrix}.$$

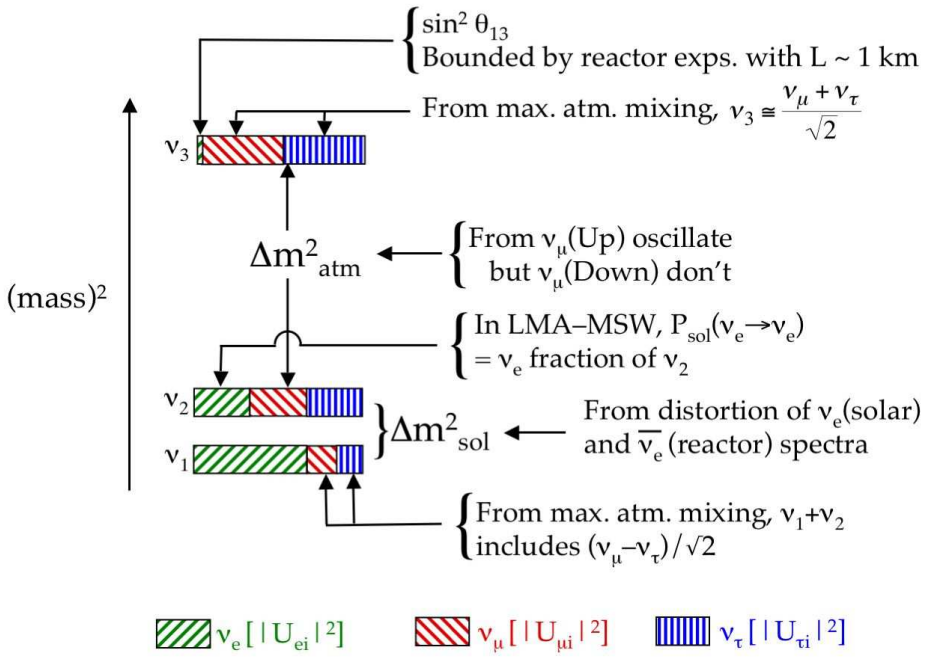

Figure 2.15: A summary of current knowledge on neutrino oscillations. In a given mass eigenstate, there are three flavors, the fraction of which are represented as colored patches. The flavor content is obtained from the measured values of mixing angles. Although the actual neutrino masses are still unknown, the mass squared differences can be measured by observing the oscillation patterns of neutrinos and are shown here as the splitting differences of different mass eigenstates. This plot is adapted from [38].

Table 2.1: World averaged best fit values of neutrino mixing parameters from νFit 2016 [209]. The world averaged best fit prefers a normal mass ordering (NO); the best fit points assuming inverted mass ordering (IO) has a $\Delta\chi^2 = 0.56$ compared to the best fit points assuming NO. Below shows the world averaged best fit values for each mixing parameter in the PMNS matrix. Depending on the mass ordering, Δm^2_{3l} is Δm^2_{31} for NO, whereas Δm^2_{3l} is Δm^2_{32} for IO.

Parameters	Normal Ordering (best fit)	Inverted Ordering ($\Delta\chi^2 = 0.56$)
$\sin^2\theta_{12}$	$0.308^{+0.013}_{-0.012}$	$0.308^{+0.013}_{-0.012}$
$\sin^2\theta_{23}$	$0.440^{+0.023}_{-0.019}$	$0.584^{+0.018}_{-0.022}$
$\sin^2\theta_{13}$	$0.02163^{+0.00074}_{-0.00074}$	$0.02175^{+0.00075}_{-0.00074}$
$\Delta m^2_{21} \times 10^{-5}$ eV^2	$7.49^{+0.19}_{-0.17}$	$7.49^{+0.19}_{-0.17}$
$\Delta m^2_{3l} \times 10^{-3}$ eV^2	$2.526^{+0.039}_{-0.037}$	$-2.518^{+0.038}_{-0.037}$
δ_{CP} ($^\circ$)	289^{+38}_{-51}	269^{+39}_{-45}

The goal of this analysis is to measure Δm^2_{23} and $\sin^2\theta_{23}$ using atmospheric neutrinos. Figure 2.16 [79] shows the latest published results of the atmospheric neutrino oscillation parameter measurements from different experiments. The 90% contours are from both atmospheric oscillation experiments, including SK [80] and IceCube [79], and long baseline accelerator experiments from T2K [70], MINOS [81], NOνA [82]. While most experiments agree to a certain extent, NoνA result excludes maximal mixing. This exclusion was found to be because of an inaccurate energy proxy and is recently corrected during one of the Joint Experimental Theoretical Physics Seminar at Fermilab [83]. The latest NOνA, along with the results from this analysis, can be found in Section 9.2.

2.2.5 Open Questions on Neutrino Oscillations

After the measurement of non-zero θ_{13}, the next open question in neutrino oscillations is the size of the CP violating phase. By comparing neutrino oscillation

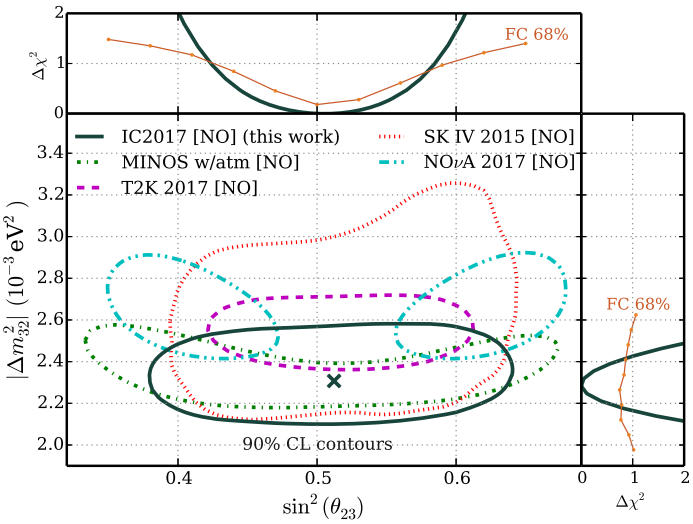

Figure 2.16: A summary on the current status of atmospheric neutrino oscillation parameter measurements: (top) a scan of $\Delta\chi^2$ in $\sin^2\theta_{23}$ from the IceCube publication [79], (right) a scan of $\Delta\chi^2$ in Δm^2_{23} from IceCube publication [79], and (bottom left) the 90% contours from different atmospheric neutrino oscillation experiments. IC2017 (this work) in the legend refers to the latest publication [79] from the IceCube collaboration and does not correspond to the work presented in this dissertation. The experiments included in the contour plot are SK [80] and IceCube [79] and long baseline accelerator neutrino experiments by T2K [70], MINOS [81], NOνA [82]. This plot is adapted from [79] published on 13th Feb 2018.

patterns between a neutrino and an anti-neutrino beams, long baseline experiments are now sensitive to $\delta_{\rm CP}$, as shown in Section 2.2.2. While the latest result from T2K has rejected $\delta_{\rm CP} = 0$ by 1σ (see Figure 2.8 [70]), more data and reduced systematic uncertainties are needed to exclude zero $\delta_{\rm CP}$. If $\delta_{\rm CP}$ is indeed non-zero, the unitary mixing matrix U would be complex. Since

$$|\bar{\nu}_\alpha\rangle = \sum_{i=1}^{3} U_{\alpha i}\,|\bar{\nu}_i\rangle\,,$$

a non-zero CP-violating phase implies that oscillation patterns of neutrinos are different from that of anti-neutrinos. Hence, CP invariance would be violated in the leptonic sector in the Standard Model [38]. This violation in the leptonic sector

may also explain the observed matter-antimatter asymmetry.

As mentioned earlier, the ordering of neutrino mass eigenstates is also not clear. The mass hierarchy in Figure 2.15 assumes that ν_3 is the heaviest; this assumed ordering is called *normal* ordering. However, this ordering can also be *inverted*, in which ν_3 is the lightest. Knowing the neutrino mass ordering is important for neutrinoless double beta decay experiments and for discriminating unification and neutrino mass models [84]. To measure mass hierarchy in vacuum, a precise knowledge on the two mass squared splittings is required so that an experiment can measure a very small difference between Δm^2_{32} and Δm^2_{31}. Neutrino mass hierarchy can also be measured via difference in oscillations in matter of ν_e versus that of $\bar{\nu}_e$. Many up-coming accelerator and atmospheric neutrino experiments are expected to provide hints on the limits of neutrino masses in the next few years and may be able to have a definitive answer by 2035 [84].

One of the ultimate quantities to be measured is the neutrino masses. While a limit on the total neutrino mass from all neutrino flavors is set from observations to be less than 1 eV [38], measurements of absolute neutrino masses cannot be carried out by experiments that observe neutrino oscillations for reasons discussed in Section 2.1.1. A direct way to measure the absolute neutrino masses is based on kinematic determination of β decays. Current projects including the Karlsruhe Tritium Neutrino (KATRIN) and Project-8 experiments are able to reach a sensitivity of 200 meV [85].

Chapter 3: Neutrino Production and Detection

While the previous chapter focuses on the physics of neutrino oscillations during their propagations, this chapter discusses the neutrino production and detection for atmospheric neutrino oscillation studies using IceCube-DeepCore. For this analysis, neutrino sources originate from the decays of mesons produced in the Earth's atmosphere; this production mechanism is fairly well understood. Although many advanced simulation tools are available to predict atmospheric neutrino fluxes, a one dimensional calculation is helpful to better understand the physics behind the production of atmospheric neutrinos. Therefore, a simple, naive analytical approach is presented in Section 3.1, concluded with a final note in Section 3.1.6 on the four atmospheric neutrino flux ratios that play a role in this thesis.

The second half of this chapter, Section 3.2, explains the detection of neutrino interactions at IceCube-DeepCore. After its interaction with the ice, a neutrino with energies above 10 GeV can be detected indirectly through Cherenkov radiation produced when the secondary leptons travels through the ice. Based on the optical properties of the ice, these photons may be scattered, absorbed, or detected by the optical modules deployed in the South Pole ice.

3.1 Atmospheric Neutrino Production

Although neutrino oscillation probabilities do not depend on the production details of neutrinos, measurements of neutrino oscillation parameters require a pre-

cise and accurate prediction on the number of neutrinos at the detection site as a function of neutrino energy. This analysis studies atmospheric neutrinos which are produced through decays of mesons produced when cosmic rays interact with air particles in the Earth's atmosphere. Over the past century, numerous experiments using different techniques were built to study energy spectra of cosmic ray primaries and atmospheric neutrinos. Current knowledge on atmospheric neutrino fluxes is well established [86–95], and predictions from atmospheric neutrino flux models describe data well with small uncertainties [75, 87, 96, 97].

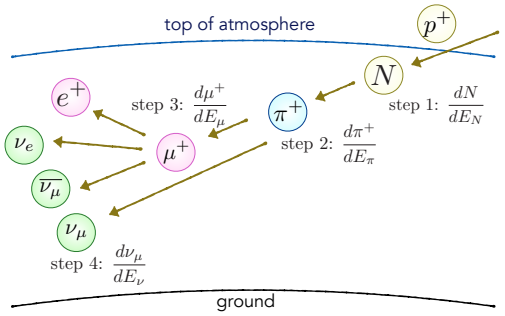

Figure 3.1: A schematic picture of a simplified atmospheric ν_μ flux calculation. Four steps are required to estimate muon neutrino flux. First is to determine the nucleon spectra from their interaction probabilities. Some of those interactions produce mesons such as pions and kaons, leading to the meson spectra. These mesons decay, giving out muons and muon neutrinos. Since muon decays also give out to muon neutrinos, the spectrum of atmospheric muons are also determined. Finally, muon neutrino flux is obtained from both meson and muon spectra. This picture is not drawn in scale.

Although this thesis uses the latest atmospheric neutrino flux tables from Honda *et al.* [86] (see Section 5.1.4), a simplified one dimensional calculation of atmospheric neutrino fluxes is presented in this section. Following Gaisser *et al.* [98], this calculation is performed in four steps as summarized in Figure 3.1. First, discussed in Section 3.1.2, the nucleon fluxes are determined based on some assumed hadronic interaction properties. Second, these nucleons may interact and gives out

mesons, which can either decay or interact with other nucleons; these probabilities determine meson spectra explained in Section 3.1.3. A pion or a kaon can decay into a muon and a muon neutrino. The daughter muon then decays, giving out another muon neutrino and an electron neutrino. Therefore, in Section 3.1.4, the third step is to obtain a muon spectrum from the meson decays. Finally, neutrino fluxes can be determined from both meson and muon contributions as shown in Section 3.1.5. While the calculation may sound a bit complex, the development of each particle can generally be described by the cascade equations (see Chapter 5 in Gaisser *et al.* [98]), which is explained in Section 3.1.1. Once the cascade equations is understood, the spectra of the above particles can be estimated individually with their corresponding assumptions and boundary conditions. At the end, a final note related to the four most important neutrino flux ratios is discussed in Section 3.1.6.

3.1.1 General Cascade Equation

To describe a development of a cascade from an interaction of particles in the atmosphere, a few important variables are typically used in cosmic rays physics, as shown in Figure 3.2. As a particle travels through air, it may interact or decay at a point along its propagation. This point can be identified via three variables. First is the production height h vertically above ground. This height is used to estimate the atmospheric density at the point of interactions and decays. Second is the direction of propagation θ from an observer. Since the Earth is roughly a sphere, this θ may be different from the actual zenith angle θ^* of propagation by the particle. The third variable is the distance l of the interaction or decay point away from the observer. By simple geometry, h can be approximated by $l \cos\theta$ for small $\theta < 60°$; otherwise, a full expression is required and complicates the calculations [98,99]. The last variable is the slant depth X in a unit of [g cm^{-2}] measured from the top of the atmosphere

along the direction of particle's propagation. Given a density of the atmosphere at the production height $\rho(h)$, X is defined as

$$X \equiv \int_{l}^{\infty} dl \rho_{(h)}. \tag{3.1}$$

X is important to estimate the decay probability of particles, and its vertical projection X_v is also shown in Figure 3.2.

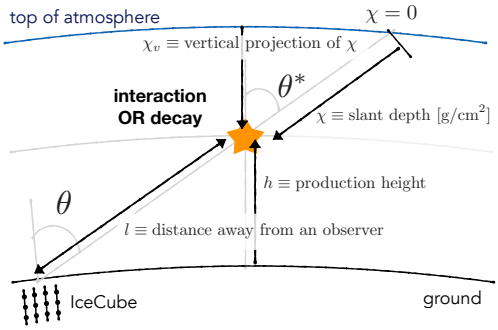

Figure 3.2: A schematic picture of the set-up for cascade equations. The star presents the location at which an interaction or a decay occurs. Four variables are used to define this point. First is the production height h measured vertically from the ground. Second is the direction θ^* from the observer; because of the Earth's curvature, θ^* at the point of interaction/decay is not the same as θ at the point of observation. Third is the distance l of the interaction or decay point away from the observer. Forth is the slant depth X in a unit of [g/cm^2] measured from the top of the atmosphere down along the direction of the propagation of the particle. Its vertical projection X_v is also a convenient variable. X depends on the density and is related to interaction and decay lengths of the particle of interest. This picture is not drawn in scale.

For a particle of type i with an energy E_i, the question of interest is how the number of this particle type at slant depth X, i.e. $N_i(E_i, X)$, changes given an infinitesimal variation in slant depth δX; hence, at a given X, the flux of this particle type with an energy between E and $E + dE$ is given by $N_i(E, X)\ dE$. In general, $N_i(E_i, X)$ decreases through its decays and interactions with other particles[1]. The

[1]Particles can also be stopped by energy loss during propagations. But this term is insignificant

probabilities of decays and interactions are typically described by the decay d_i and interaction λ_i depths, both of which have units of [g cm^{-2}]. In particular, the number of particle lost due to decays $\delta N_i^{\rm d}$ and that due to interactions $\delta N_i^{\rm int}$ over a small slant depth are

$$\delta N_i^{\rm d} = -N_i(E_i, X) \times \frac{\delta X}{d_i} \qquad \text{and} \qquad \delta N_i^{\rm int} = -N_i(E_i, X) \times \frac{\delta X}{\lambda_i},$$

where $\delta X/d_i$ and $\delta X/\lambda_i$ are the probabilities of decays and interactions by particles of type i respectively, and the negative sign indicates a loss of $N_i(E_i, X)$. While particles of type i can be lost via those two processes, the number $N_i(E_i, X)$ also increases because of decays and interactions by other particles of type j. Since we are interested in $N_i(E_i, X)$ with a specific energy E_i, the probability in which a decay or interaction by a particle j would produce a particle i with E_i is included. That is, in addition to the probability in which decays and/or interactions by a particle j giving out particles i, the kinematics of these decays and interactions have to be taken into account.

$$\begin{aligned}
\delta N_j^{j\to i_{(E_i)}+\cdots} &= N_j(E_j, X) \times \frac{\delta X}{d_j} \times \frac{dn_i(E_i, E_j)}{dE_i} \\
\delta N_j^{j+air\to i_{(E_i)}+\cdots} &= N_j(E_j, X) \times \frac{\delta X}{\lambda_j} \times \frac{dn_i(E_i, E_j)}{dE_i},
\end{aligned}$$

where $dn_i(E_i, E_j)/dE_i$ is the normalized energy distribution of the corresponding decay or interaction process. Given the above ways to gain and lose particles of type i with an energy E_i over a small variation of slant depth, the change in $N_i(E_i, X)$ is given by

$$\begin{aligned}
\frac{dN_i(E_i, X)}{dX} = &- \frac{N_i(E_i, X)}{d_i} - \frac{N_i(E_i, X)}{\lambda_i} \\
&+ \sum_j \int_{E_i}^{E_{\rm max}} dE_j \; \frac{N_j(E_j, X)}{d_j} \times \frac{dn_i(E_i, E_j)}{dE_i} \\
&+ \sum_j \int_{E_i}^{E_{\rm max}} dE_j \; \frac{N_j(E_j, X)}{\lambda_j} \times \frac{dn_i(E_i, E_j)}{dE_i}. \qquad (3.2)
\end{aligned}$$

assuming high energy particles

This equation is known as the cascade equation [98]. Note that the integrals start from E_i, which is the minimum energy needed to produce a particle i with an energy of E_i, up to $E_{\max} \to \infty$.

Let us first take a closer look at the decay depth d_i [g cm^{-2}]. By definition, assuming the particle travels close to the speed of light c [98],

$$d_i \equiv \text{decay length [cm]} \times \text{density [g / cm}^3\text{]} = \gamma c \tau_i \rho_{(h)}, \tag{3.3}$$

where $\tau_i \gamma$ is the dilated lifetime, and $\rho(h)$ is the atmospheric density at the production height. Because ρ is a differential gradient of the vertical slant depth X_v over production height, or $\rho = -dX_v/dh$, it is useful to express ρ in terms of X and θ. For a column of atmosphere above and below the point of decay, the pressure P at X_v is given by $P = gX_v$, where g is the gravitational constant. With $\theta < 60°$, some approximations of composition of the atmosphere, and Equation 3.1, the air density is roughly given by [98],

$$\rho \approx \frac{X \cos\theta}{h_0}$$

where h_0 is a scale height at which the vertical slant depth X_v decreases by $1/e$. Obviously, this scale height, hence the decay depth, depends on the altitude at which a decay occurs; in the lower stratosphere, a typical altitude value of $h_0 \sim 6.4$ km is assumed. Thus, with $\gamma = E/mc^2$, the decay probability $1/d_i$ in Equation 3.3 can be expressed as

$$\frac{1}{d_i} = \frac{m_i c^2 h_0}{Ec\ \tau_i X \cos\theta} \equiv \frac{\epsilon_i}{E\ X\ cos\ \theta}, \tag{3.4}$$

where ϵ_i is an important characteristic energy of particles of type i. From Equation 3.2, whether a particle decays or interacts depends on the relative sizes of $1/d_i$ and $1/\lambda_i$ of the particle. Assuming that an interaction depth is as long as the slant depth $\lambda_i \sim X$, the decay rate and the interaction rate is roughly the same when $\epsilon_i/\cos\theta \sim E$. Therefore, ϵ_i is the critical energy at which interactions start to dominate over decays for a vertically down going particle. Given a fixed E, as

the zenith angle θ increases, the interaction probability for particles from a more horizontal direction increases due to longer flight paths. In the lower stratosphere, typical values of ϵ_i are 115 and 850 GeV for charged pions and charged kaons [91].

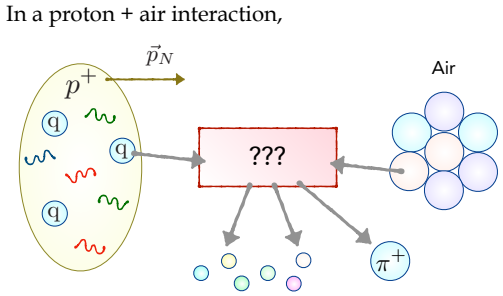

Figure 3.3: A schematic picture of a proton and air interaction. One of the quarks in a high energy proton interacts with the nucleus of an air molecule and gives out a pion. In cosmic rays physics, a dimensionless particle yield $F_{p^+,air}$ is defined to summarize the contributions from both integrated cross section over nucleon momentum and the energy distribution of the out-going pion.

On the other hand, describing interactions between particles i and j (the last term in Equation 3.2) is slightly more complicated. For example, Figure 3.3 illustrates the proton-air interaction, which gives out pions plus other particles. Since we are interested in the probabilities from which the interaction gives out a particle of type i with a specific energy E_i, cosmic rays physicists define a dimensionless particle yield $F_{ji}(E_i, E_j)$ [91] for every interaction process [98].

$$F_{ji}(E_i, E_j) \equiv E_i \frac{1}{\sigma_j^{\text{air}}} \frac{d\sigma_{j+\text{air}\to i}}{dE_i} = E_i \frac{dn_i(E_i, E_j)}{dE_i}, \tag{3.5}$$

where σ_j^{air} is the total cross section of an interaction between a particle j and air, and $\sigma_{j+\text{air}\to i}$ relates to the probability that the interaction gives out a particle of i. The last equality in Equation 3.5 assumes a multiplicity condition of $d\sigma_{j+\text{air}\to i} = \sigma_j^{\text{air}}\, dn_i$. Although the energy distribution in Equation 3.5 cannot be calculated, a reasonably good approximation for a high energy interaction is given by the Feynman scaling

$x_F \sim E_i/E_j$ [98], from which a variation in E_j, for a fixed E_i, is given by

$$dE_j = \frac{-E_i}{x_F^2} dx_F.$$

Thus, the last term in the cascade equation can be rewritten as

$$\begin{aligned}\int_{E_i}^{E_{\max}} dE_j \; \frac{N_j(E_j, X)}{\lambda_j} \frac{F_{ji}(E_i, E_j)}{E_i} &= \int_1^0 \; dx_F \frac{-E_i}{x_F^2} \; \frac{N_j(E_j, X)}{\lambda_j} \frac{F_{ji}(E_i, E_j)}{E_i} \\ &= \int_1^0 \; dx_F \frac{-F_{ji}(x_F)}{x_F^2} \; \frac{N_j(E_j, X)}{\lambda_j}. \end{aligned} \tag{3.6}$$

In summary, $N_i(E_i, X)$ can either lose or gain particles of type i as they propagate through a slant depth in the atmosphere. This development is described by the cascade equation:

$$\begin{aligned}\frac{dN_i(E_i, X)}{dX} = &- \frac{\epsilon_i N_i(E_i, X)}{E_i \; X \; \cos\,\theta} - \frac{N_i(E_i, X)}{\lambda_i} \\ &+ \sum_j \int_{E_i}^{E_\infty} dE_j \; \frac{\epsilon_j N_j(E_j, X)}{E_j \; X \; cos\; \theta} \times \frac{dn_i(E_i, E_j)}{dE_i} \\ &+ \sum_j \int_0^1 \; dx_F \frac{F_{ji}(x_F)}{x_F^2} \; \frac{N_j(E_j, X)}{\lambda_j}. \end{aligned} \tag{3.7}$$

In general, to obtain an energy spectrum of a given type of particles, approximations are made to drop insignificant terms in Equation 3.7. The corresponding differential spectrum can then be obtained by integrating the leftover terms over a range of slant depths and applying appropriate boundary conditions.

3.1.2 Nucleon Fluxes

The first step in the neutrino flux calculation is to determine the total nucleon spectrum from both proton and neutron. Since their interaction rates are much higher than their decay rates, all decay terms in Equation 3.7 are dropped. Therefore, the variation in the number of nucleons $N_N(E_N, X)$ is governed by

$$\frac{dN_N(E_N, X)}{dX} = -\frac{N_N(E_N, X)}{\lambda_N} + \int_0^1 \; dx_F \frac{F_{jN}(x_F)}{x_F^2} \; \frac{N_j(E_j, X)}{\lambda_N},$$

where F_{jN} is the dimensionless particle yield of nucleons due to nucleon-nucleon interactions[2].

To solve for $N_N(E_N, X)$, a typical *ansatz* is considered by assuming separate functions for E_N and X. Based on data from cosmic rays experiments, the primary cosmic rays follow a power-law spectrum; thus, a convenient energy dependent function is $E_N^{-(\gamma+1)}$. By substituting

$$N_N(E_N, X) = g(X) E_N^{-(\gamma+1)}, \tag{3.8}$$

into the cascade equation in Equation 3.8 and $E_j = E_N/x_F$, one gets

$$\begin{aligned} E_N^{-(\gamma+1)} \frac{dg(X)}{dX} &= -\frac{g(X)}{\lambda_N} E_N^{-(\gamma+1)} + \frac{g(X)}{\lambda_N} \int_0^1 dx_F \frac{F_{jN}(x_F)}{x_F^2} \left(\frac{E_N}{x_F}\right)^{-(\gamma+1)} \\ &= -\frac{g(X)}{\lambda_N} E_N^{-(\gamma+1)} + \frac{g(X)}{\lambda_N} E_N^{-(\gamma+1)} \int_0^1 dx_F \; x_F^{\gamma-1} F_{jN}(x_F) \\ &= -\frac{g(X)}{\lambda_N} E_N^{-(\gamma+1)} + \frac{g(X)}{\lambda_N} E_N^{-(\gamma+1)} Z_{NN}^{(\gamma)}, \end{aligned} \tag{3.9}$$

where $Z_{NN}^{(\gamma)}$ is the *spectrum-weighted moment* (discussed in the next few paragraphs) for nucleon productions in nucleon-air interactions. By canceling common terms in Equation 3.9, one gets

$$\frac{1}{g}\, dg = \frac{-(1 - Z_{NN}^{(\gamma)})}{\lambda_N} dX \equiv \frac{-1}{\Lambda_N} dX, \tag{3.10}$$

where Λ_N, known as the nucleon attenuation depth, is essentially the effective interaction depth weighted by the Z-moment. By integrating both sides independently, the total nucleon spectrum from both protons and neutrons is therefore

$$N_N(E_N, X) = g_0 e^{-X/\Lambda_N} E^{-(\gamma+1)}, \tag{3.11}$$

Note that, the attenuation depth Λ_N acts as a scaling depth at which nucleon flux decreases by $1/e$, while preserving the X-independent energy spectrum from the observed spectral power law.

[2]Here, j also happens to be a nucleon, but it should be separated from the subscript N to avoid confusion.

After repeating the above procedure but for the difference, instead of the sum, between proton and neutron fluxes, $\Delta_N \equiv p(E,X) - n(E,X)$, separate solutions for proton and neutron fluxes can be obtained by $(N_N \pm \Delta_N)/2$ respectively. With isospin symmetries $Z_{pp} = Z_{nn}$ and $Z_{pn} = Z_{np}$, the proton and neutron fluxes are given by [100]

$$p(E,X) = \frac{1}{2}\left(g_0\ e^{-X/\Lambda_{+_N}} + f_0\ e^{-X/\Lambda_{-_N}}\right)E^{-(\gamma+1)}$$
$$n(E,X) = \frac{1}{2}\left(g_0\ e^{-X/\Lambda_{+_N}} - f_0\ e^{-X/\Lambda_{-_N}}\right)E^{-(\gamma+1)},$$

where g_0 and f_0 are the X-only dependent function in N_N and Δ_N, respectively, evaluated $X = 0$; and $\Lambda_{+_N} \equiv \lambda_N/[1-(Z_{pp}+Z_{pn})]$ and $\Lambda_{-_N} \equiv \lambda_N/[1-(Z_{pp}-Z_{pn})]$. Note that the relative excess of proton over neutron at the top of the atmosphere δ_0 is defined as [98]

$$\delta_0 \equiv \frac{p_0 - n_0}{p_0 + n_0}, \tag{3.12}$$

where p_0 and n_0 are $p(E,0)$ and $n(E,0)$ at the top of the atmosphere. This value is roughly 0.76 at 10 GeV/nucleon when primary cosmic rays mostly consist of protons [101][3], implying a neutron-to-proton ratio of ~ 0.11 at the top of the atmosphere. This ratio increases towards 1 over a very large slant depth during which the excess protons may interact. Because $f_0 = \delta_0 g_0$, the proton and neutron fluxes can be rewritten as

$$p(E,X) = \frac{g_0}{2}\left(e^{-X/\Lambda_{+_N}} + \delta_0\ e^{-X/\Lambda_{-_N}}\right)E^{-(\gamma+1)} \equiv p_X E^{-(\gamma+1)}$$
$$n(E,X) = \frac{g_0}{2}\left(e^{-X/\Lambda_{+_N}} - \delta_0\ e^{-X/\Lambda_{-_N}}\right)E^{-(\gamma+1)} \equiv n_X E^{-(\gamma+1)}, \tag{3.13}$$

where p_X and n_X are the X-only dependent functions of the proton and neutron fluxes. Since these nucleons produce mesons, hence neutrinos, an excess in pro-

[3]The proton excess ratio δ_0 depends on nucleon energy. As the nucleon energy increases, δ_0 decreases to less than 0.62 at 100 TeV/nucleon [101].

ton over neutron eventually leads to an excess of muon neutrinos over muon anti-neutrinos.

A few comments are made on the spectrum-weighted moment Z_{ji} defined;

$$Z_{ji}^{(\gamma)} \equiv \int_0^1 dx_F \; x_F^{\gamma-1} F_{ji}(x_F). \tag{3.14}$$

In general, a Z_{ji}-moment characterizes the physics of the production of i from a $j+$air interaction [98]. If $\gamma = 1$, the Z_{ji} is simply an integral over the dimensionless particle yield in Equation 3.5, which returns the expectation value of the fraction of energy that goes into particle i during the $j+$ air interaction. In reality, γ is observed to be greater than 1. With a positive exponent in x_F, the integral from 0 to 1 in Equation 3.14 has much larger contributions from the forward region where $x_F \to 1$ than that from $x_F \to 0$. This implies that proton and neutron fluxes depend dominantly on the particle projectiles, especially contributions from those traveling the same direction as the primary proton. A steep ($\gamma > 1$) primary spectrum also means that Z-moments for positive charged particles is larger than the ones for negative charged particles due to the excess protons at the top of the atmosphere [100]. As shown in Section 3.1.3, while Z-moments for π^+ and π^- can still be approximated to be the same, the Z-moment for K^+ is significantly larger than that for K^-. Last, the above definition of Z-moment is energy independent due to the assumed Feynman scaling[4]. Active searches have been conducted to study the energy and spectral index γ dependence in spectrum-weighted moments. Tables of Z-moments for different processes can be found in [90, 91, 98, 105]. Over the past decades, particle theorists have gone from numerically calculating Z's for different hadronic interactions [90, 91, 106] to building simulation models, such as SIBYLL [107], DPMJET [108], JAM [109], GEANT4 [110], and FLUKA [111], for different

[4]Such assumption is found to be broken at $\sim$ TeV [102–104]; however, this assumption is still valid here due to the insignificant contribution to Z-moments from non forward region $x_F \to 0$.

energy ranges. Not only do these hadronic models help understand any deviations between predicted and measured cross sections in particle collider experiments, they are also incorporated into air shower simulations to predict lepton fluxes for cosmic rays and atmospheric neutrino detectors.

3.1.3 Meson Fluxes

From the above expressions for proton and nucleon fluxes, the next step is to determine meson fluxes. For simplicity, charged pion fluxes is derived without taking into account couplings among pions, kaons, and other particles. While numbers of pions decreases via decays and interactions, pions can also be produced by pion-air and nucleon-air interactions. Therefore, the cascade equation for pions ($\pi^+ + \pi^-$) is given by

$$\frac{d\Pi(E_\pi, X)}{dX} = -\frac{\epsilon_\pi \Pi(E_\pi, X)}{E_\pi\ X\ \cos\theta} - \frac{\Pi(E_\pi, X)}{\lambda_\pi} + \int_0^1 dx_F \frac{F_{\pi\pi}(x_F)}{x_F^2}\ \frac{\Pi(E_{\pi_j}, X)}{\lambda_\pi} + \int_0^1 dx_F \frac{F_{N\pi}(x_F)}{x_F^2}\ \frac{N(E_{N_j}, X)}{\lambda_N}. \tag{3.15}$$

Based on $N_N(E_N, X)$ in Section 3.1.2, an *ansatz*

$$\Pi(E_\pi, X) = b(X) e^{-X/\Lambda_\pi} X^{-\epsilon_\pi / E_\pi \cos\theta} \frac{Z_{N\pi}}{\lambda_N} N_N(E_\pi, 0), \tag{3.16}$$

where $\Lambda_i \equiv \lambda_i/(1 - Z_{ii})$, is considered. Using the same strategy for solving the nucleon flux, substituting this *ansatz* into Equation 3.15 returns an expression for $\Pi(E_\pi, X)$;

$$\Pi(E_\pi, X) = \frac{Z_{N\pi}}{\lambda_N} N_N(E_\pi, 0) e^{-X/\Lambda_\pi} \int_0^X dX' \left[e^{-X'\left(\frac{1}{\Lambda_N} - \frac{1}{\Lambda_\pi}\right)} \left(\frac{X'}{X}\right)^{\epsilon_\pi / E_\pi \cos\theta} \right]. \tag{3.17}$$

Although this integration cannot be solved analytically, $\Pi(E_{\pi,X})$ can still be understood by taking high and low energy limits.

In the high energy limit $E_\pi \cos\theta \gg \epsilon_\pi$, where $\epsilon_\pi \sim 115$ GeV [91] as discussed in Section 3.1.1, pion decays can be ignored, and the total pion flux becomes

$$\Pi_{HE}(E_\pi, X) = N_N(E_\pi, 0) \frac{Z_{N\pi}}{1 - Z_{NN}} \frac{\Lambda_\pi}{\Lambda_N - \Lambda_\pi} \left(e^{-X/\Lambda_\pi} - e^{-X/\Lambda_N} \right). \tag{3.18}$$

Two characteristics of pion flux arise from this high energy limit. First, the energy dependence in the pion flux is the same as the one in the nucleon flux in Equation 3.11; that is, $\Pi_{HE}(E_\pi, X) \propto E_\pi^{-(\gamma+1)}$. The second characteristic is the slant depth dependence. At the top of the atmosphere, there are no pions. As X increases, pion flux rises until X reaches a critical value of ~ 140 g/cm^2 [98]. Then, pion flux declines exponentially, reaching an asymptote given by the effective interaction depth Λ_π. Similar to the case in nucleon fluxes, separate solutions for Π^+ and Π^- fluxes can be obtained by repeating the same calculation for $\Delta_\pi \equiv \Pi^+(E_\pi, X) - \Pi^-(E_\pi, X)$ with the isospin relations $Z_{\pi^+\pi^+} = Z_{\pi^-\pi^-}$, $Z_{\pi^+\pi^-} = Z_{\pi^-\pi^+}$, and $Z_{p\pi^+} \approx Z_{n\pi^-}$. According to Lipari [105], the high energy limit of Π and Δ_π are

$$\Pi^+ \pm \Pi^-(E_\pi, X)\Big|_{HE} = \Big[p(E_\pi, 0) \pm n(E_\pi, 0) \Big] A^\pm(X), \tag{3.19}$$

where

$$A^\pm(X) \equiv \frac{Z_{p\pi^+} \pm Z_{p\pi^-}}{1 - Z_{NN}} \frac{\Lambda_{\pm_\pi} \Lambda_{\pm_N}}{\Lambda_{\pm_\pi} - \Lambda_{\pm_N}} \left(e^{-X/\Lambda_{\pm_\pi}} - e^{-X/\Lambda_{\pm_N}} \right), \tag{3.20}$$

and $\Lambda_{\pm_\pi} \equiv \lambda_\pi / [1 - (Z_{\pi^+\pi^+} \pm Z_{\pi^+\pi^-})]$. Hence, the positively and negatively charged pion fluxes are differed by δ_0 defined in Equation 3.12.

$$\Pi^\pm_{HE} = \frac{1}{2}(\Pi + \Delta_\pi) = A^+(X) \pm \delta_0 A^-(X). \tag{3.21}$$

This implies that the developments of the two fluxes are slightly different because of the proton-neutron asymmetry at the top of the atmosphere. In particular, Π^+ reaches a maximum at a higher slant depth in the upper atmosphere than Π^- [105].

On the other hand, in the low energy limit $E_\pi \cos\theta \ll \epsilon_\pi$, pion decays dominate over interactions, and the pion flux becomes

$$\Pi_{LE}(E_\pi, X) = \frac{Z_{N\pi}}{\lambda_N} N_N(E_\pi, 0) e^{-X/\Lambda_N} \frac{X E_\pi \cos\theta}{\epsilon_\pi}. \tag{3.22}$$

With the same procedure in the nucleon case, the individual charged pion fluxes are given by [105]

$$\Pi^{\pm}_{LE}(E_\pi, X) = \left(\frac{Z_{p\pi^\pm}}{\lambda_p} p(E_\pi, X) + \frac{Z_{n\pi^\pm}}{\lambda_n} n(E_\pi, X) \right) \frac{X E_\pi \cos\theta}{\epsilon_\pi}, \tag{3.23}$$

where proton and neutron fluxes are given by Equation 3.13. Note that, because of the linear energy dependence from the decay term, pion energy spectrum at low energy is flatter than the cosmic ray spectrum by one power of energy.

Although the above calculations give us an intuition of how pion fluxes develop in the atmosphere, the meson fluxes in reality are more complicated.

- Given that $\epsilon_\pi \sim 115$ GeV [91], this analysis studying neutrinos with energies between 5 and 56 GeV requires a combination of pion fluxes from both low and high energy limits. This can be estimated by $\Pi^\pm = \Pi^\pm_{LE}/(1 + \Pi^\pm_{LE}/\Pi^\pm_{HE})$, which provides the correct behaviors at the two limits.

- Pion contribution from kaon fluxes cannot be ignored. Similar to pions, kaons are produced from nucleon-nucleon interaction. Since kaons can decay into charged pions, extra terms due to kaon decays are needed in the pion cascade equation in Equation 3.15. Such calculation is presented in [105, 112].

- Although the cascade equation for kaon fluxes is similar to that for pions, kaon fluxes are complicated. Because kaons with energies above $\epsilon_K \sim 850$ GeV [91] interacts with air and regenerate $K^\pm$ and K_L, extra interaction terms due to K_L are needed [105, 112]. In addition, all these kaons can experience three-body decays, in which the kinematics are more complex than a two-body pion decays as discussed in Section 3.1.4.

- The inclusive cross sections of charged kaon productions are different from that of pions. In particular, one cannot assume $Z_{pK^+} \approx Z_{nK^-}$ because of an

extra non-negligible K^+ production channel $p^+ + \text{air} \rightarrow \Lambda^0 + K^+ + \text{others}$ [98]. Given that cosmic rays are mostly protons and that there is no analogous K^- production from neutrons, the inclusive cross section of K^+ production is larger than that of K^-. Most importantly, the particle yield in Equation 3.5 due to the extra K^+ production channel contributes at high Feynman scaling x_F. As discussed in Section 3.1.2, Z-moments depend largely on the contributions from large x_F; this implies $Z_{pK^+} \gg Z_{nK^-}$. Such an asymmetry leads to a large K^+/K^- ratio, which affects muon charge ratio as well as ratio between neutrino and anti-neutrino fluxes at high energy when contribution from kaons dominates.

- Often, a π-to-K ratio is used for analyses studying atmospheric muon and neutrino fluxes within an energy range where contributions from both pions and kaons are important. This ratio is defined as

$$R_{\pi/K} = \frac{Z_{p\pi^+} + Z_{p\pi^-}}{Z_{pK^+} + Z_{pK^-}}. \tag{3.24}$$

  Among the four Z-moments in Equation 3.24, Z_{pK^+} has the largest uncertainty. Because a pion or kaon decays into a muon and a muon neutrino, $R_{\pi/K}$ affect both $\nu_\mu/\bar{\nu}_\mu$ and $\mu^+/\mu-$ ratios. And, because atmospheric electron (anti-)neutrinos are produced from muon decays, $\mu^+/\mu-$ ratio is important for $\nu_e/\bar{\nu}_e$ flux ratio. A simplified calculation of μ^+/μ^- from only charged pions is presented in Section 3.1.4, and a full prediction from both pion and kaon contributions is performed by Gaisser [101].

3.1.4 Atmospheric Muon Fluxes

Similar to the case in nucleon and pion fluxes, we start with the cascade equation for atmospheric muons produced mostly by the decays of charged pions

and kaons via

$$\begin{aligned} \pi^{\pm} &\to \mu^{\pm} + \nu_{\mu}(\bar{\nu}_{\mu}) \qquad \text{branching ratio} = 100\% \\ K^{\pm} &\to \mu^{\pm} + \nu_{\mu}(\bar{\nu}_{\mu}) \qquad \text{branching ratio} = 63.5\%. \end{aligned} \tag{3.25}$$

Because the kinematics in pion and kaon decays are well studied, the cascade equation for atmospheric muons $\mathcal{M}(E_{\mu}, X)$ from both $\mu^{+} + \mu^{-}$ can be written directly in terms of the muon energy distribution from meson decay; that is,

$$\frac{d\mathcal{M}(E_{\mu}, X)}{dX} = \sum_{j=\pi,K} \int_{E_{min}}^{E_{max}} dE_j \left[BR \times \frac{N_j(E_j, X)}{d_j} \times \frac{dn_{\mu}(E_{\mu}, E_j)}{dE_{\mu}} \right]. \tag{3.26}$$

Here, BR is the branching ratio of the corresponding decay; N_j and d_j are the meson flux and the corresponding decay depth. Each energy integral covers the allowed energy range based on the kinematics of the corresponding decay.

Let us first consider the muon production term only from pion decays. The kinematics at pion rest frame are discussed in Section 2.1.1. The energies and momenta of the parent pion and daughter muon at rest frame are then Lorentz-transformed to an observer frame. Since the angular distribution of pion decays in the rest frame is isotropic, the normalized energy distribution of the daughter particles is constant in the observer frame [98]

$$\frac{dn_{\nu}}{dE_{\nu}} = \frac{dn_{\mu}}{dE_{\mu}} = \frac{1}{(1 - r_{\pi})E_{\pi}}, \tag{3.27}$$

where all energies are measured at the observer frame, and $r \equiv m_{\mu}^2/m_{\pi}^2 \sim 0.56$ given the pion and muon masses of $\sim$ 140 and 105 MeV respectively. In addition, due to energy conservation, a muon from a pion decay can have an energy between $r_{\pi}E_{\pi}$ and E_{π}. Thus, to produce a specific muon energy E_{μ}, the parent pion is required to have an energy between E_{μ} and E_{μ}/r_{π}. Therefore, the muon production term in

Equation 3.26 due to pion decay alone is given by

$$\begin{aligned}\mathcal{M}_{\pi}(E_{\mu},X) &= \int_{E_{min}}^{E_{max}} dE_{\pi}\frac{\Pi(E_{\pi},X)}{d_{\pi}}\frac{dn_{\mu}(E_{\mu},E_{\pi})}{dE_{\mu}} \\ &= \int_{E_{\mu}}^{E_{\mu}/r_{\pi}} dE_{\pi}\frac{\Pi(E_{\pi},X)}{d_{\pi}}\frac{1}{(1-r_{\pi})E_{\pi}} \\ &= \frac{\epsilon_{\pi}}{(1-r_{\pi})X\cos\theta}\int_{E_{\mu}}^{E_{\mu}/r_{\pi}} dE_{\pi}\frac{\Pi(E_{\pi},X)}{E_{\pi}^{2}}, \end{aligned} \tag{3.28}$$

where the $X\ \cos\theta$ comes from the pion decay depth d_{π} defined in Equation 3.4.

Since the pion fluxes are broken down into two energy limits, two muon fluxes are determined for the two energy limits. First, in the low energy limit, Π_{LE} in Equation 3.22 is used, together with nucleon flux from Equation 3.11. The muon spectrum at low energy limit is therefore

$$\begin{aligned}\mathcal{M}_{\pi_{LE}}(E_{\mu},X) &= \frac{1}{1-r_{\pi}}\frac{Z_{N\pi}}{\lambda_{N}} \times g_{0}e^{-X/\Lambda_{N}} \times \int_{E_{\mu}}^{E_{\mu}/r_{\pi}} dE_{\pi}\frac{E_{\pi}^{-(\gamma+1)}}{E_{\pi}} \\ &= \frac{1}{1-r_{\pi}}\frac{Z_{N\pi}}{\lambda_{N}} \times g_{0}e^{-X/\Lambda_{N}} \times \frac{1-r_{\pi}^{\gamma+1}}{\gamma+1}E_{\mu}^{-(\gamma+1)} \\ &= \frac{Z_{N\pi}}{\lambda_{N}}\frac{1-r_{\pi}^{\gamma+1}}{(1-r_{\pi})(\gamma+1)}\ N_{N}(E_{\mu},0)\ e^{-X/\Lambda_{N}}. \end{aligned} \tag{3.29}$$

Unlike the total pion flux at low energy limit, atmospheric muon spectrum has the same spectral index as the nucleon spectrum because the terms related to pion decay cancel out; a pion loss from its decay contributes to a muon. Atmospheric muon contribution due to charged kaon decays is the same as Equation 3.29 but with a branching ratio of 0.635 instead of 1.

Similar procedure is performed to obtain the high energy limit of atmospheric muon spectrum, which is given by [98]

$$\begin{aligned}\mathcal{M}_{\pi_{HE}}(E_{\mu},X) =& \frac{Z_{N\pi}}{1-Z_{NN}}\frac{\Lambda_{\pi}}{\Lambda_{\pi}-\Lambda_{N}}\frac{1-r_{\pi}^{\gamma+2}}{(1-r_{\pi})(\gamma+2)} \\ &\times \frac{\epsilon_{\pi}}{X\cos\ \theta}\left(e^{-X/\Lambda_{\pi}}-e^{-X/\Lambda_{N}}\right)\frac{N_{N}(E_{\mu},0)}{E_{\mu}}. \end{aligned} \tag{3.30}$$

When $E_{\pi}\cos\theta \gg \epsilon_{\pi}$, pion interactions dominate over decays, and less muons are produced. Hence, the total muon spectrum at high energy is steeper than that at

lower energy. Moreover, the high energy muon spectrum is inversely proportional to $X\cos\,\theta$. This implies that, for the same energy, atmospheric muon contribution from pion decays increases from vertical direction to the horizon; a high energy muon from the horizon has a longer flight path and a higher chance to decay than a muon with the same energy from a vertical direction.

As mentioned in Section 3.1.3, an approximate expression that covers both low and high muon energy limits is given by $\mathcal{M} = \mathcal{M}_{LE}/(1 + \mathcal{M}_{LE}/\mathcal{M}_{HE})$. After taking into account both muon decay via

$$\mu^{\pm} \rightarrow e^{\pm} + \nu_{\mu}(\bar{\nu}_{\mu}) + \bar{\nu}_{e}(\nu_{e}) \tag{3.31}$$

and muon energy loss during propagation, the differential atmospheric muon spectrum observed on the ground is given by integrating $d\mathcal{M}(E_{\mu}, X)/dX$ from the top of the atmosphere $X = 0$ to the detection site. From Gaisser *et al.* [98], the total muon contribution from both charged pion and kaon decays is given by

$$\frac{d\mathcal{M}}{dE_{\mu}} \sim S_{\mu}(E_{\mu})\frac{N_N(E_{\mu}, 0)}{1 - Z_{NN}}\left[\frac{\mathcal{A}_{\pi\mu}}{1 + \mathcal{B}_{\pi\mu}\cos\,\theta E_{\mu}/\epsilon_{\pi}} + \frac{0.635\mathcal{A}_{\mathcal{K}\mu}}{1 + \mathcal{B}_{K\mu}\cos\,\theta E_{\mu}/\epsilon_{K}}\right]. \tag{3.32}$$

Here, $S_{\mu}(E_{\mu})$ is a suppression factor due to muon energy loss and decay, which becomes significant when $E_{\mu} < 100$ GeV. Note that, for a given meson M,

$$\begin{aligned}\mathcal{A}_{M\mu} &= \frac{Z_{N\pi}(1 - r_M^{\gamma+1})}{(1 - r_M)(\gamma + 1)} \\ \mathcal{B}_{M\mu} &= \frac{\gamma + 2}{\gamma + 1}\frac{1 - r_M^{\gamma+1}}{1 - r_M^{\gamma+2}}\frac{\Lambda_{\pi} - \Lambda_N}{\Lambda_{\pi}\ln(\Lambda_{\pi}/\Lambda_N)},\end{aligned} \tag{3.33}$$

where $\mathcal{A}_{\mathcal{M}\mu}$ and $\mathcal{B}_{\mathcal{M}\mu}$ are related to the coefficients from low and high energy limit respectively. The dependence of differential muon spectrum on $E_{\mu}\,\cos\,\theta$ comes from the interaction dominated $\mathcal{M}_{HE}$ at high energy.

Since one meson typically decays into one muon, the muon charge ratio μ^{+}/μ^{-} reflects any asymmetry in the productions of charged mesons. Same as before, the individual positively and negatively muon fluxes can be obtained from both

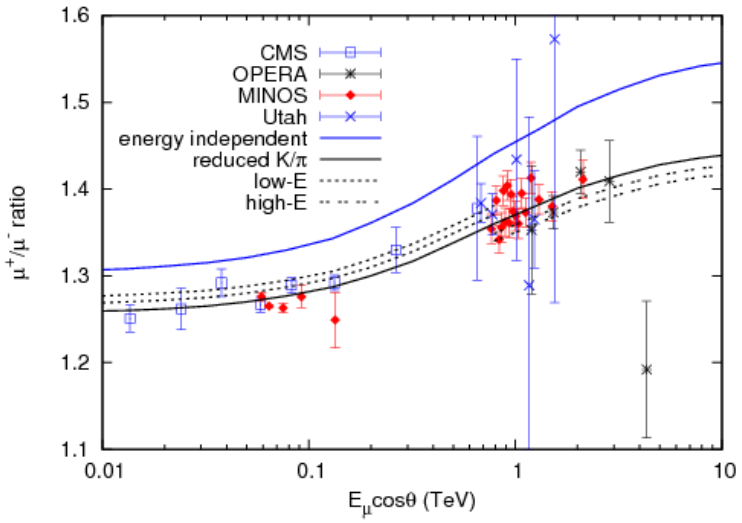

Figure 3.4: Comparison between measured and predicted charged muon ratio as a function of $E_\mu \cos\theta$. Data points represent data from accelerator experiments, and lines represent three model predictions. Solid blue line assumes an energy independent composition parameter $\delta_0 = 0.76$ and a nominal value of $Z_{pK^+} = 0.0090$. Due to the energy dependence on δ_0, multiple fixed values of δ_0 are considered for the two low and high energy ranges. The two dotted black lines in the low energy region represent predictions with δ_0 fixed at 0.71 and 0.69, and those dotted lines in the high energy region are calculated using δ_0 of 0.64 and 0.62. The continuous solid black line assumes a δ_0 of 0.665. All black lines have a Z_{pK^+} value of 0.0079, which agree with data better than the solid blue line. This plot is taken from [101].

total muon flux $\mathcal{M} = \mathcal{M}^+ + \mathcal{M}^-$ and their difference $\Delta_\mu = \mathcal{M}^+ - \mathcal{M}^-$. After charged kaon decays are considered, the predicted muon charge ratio is presented in [101]. This analytical solution is compared to data in Figure 3.4 [101]. At the low energy region where $E_\mu \cos\theta \ll \epsilon_\pi \sim 115$ GeV, muon charge ratio is relatively flat at ~ 1.26, which is above 1.0 due to proton excess from the primary cosmic rays. As $E_\mu \cos\theta$ increases to above ϵ_K, kaon decay dominates. The importance of kaon contribution is also enhanced by the falling contribution from pion decay since $E_\mu \cos\theta$ above ϵ_π. Due to the large asymmetry between the Z-moments for

K^+ and K^- (discussed in Section 3.1.3), the muon charge ratio increases drastically in a $E_\mu \cos$ range between ϵ_π and ϵ_K. From [101], Gaisser [101] concluded that a nominal value of $Z_{pK^+} = 0.0090$ assumed in the solid blue curve of Figure 3.4 does not agree with data from accelerator experiments. The agreement between data and prediction improves with a lower $Z_{pK^+} = 0.0079$, suggesting a higher π-to-K ratio than previously expected. As discussed in Section 3.1.5, not only does the π-to$K$ ratio affect μ^+/μ^- and, thus, $\nu_e/\bar{\nu}_e$, it also affects $\nu_\mu/\bar{\nu}_\mu$ flux ratio. Therefore, a precise value of Z_{pK^+} measured from accelerator experiments is important.

3.1.5 Atmospheric Neutrino Fluxes

The derivation of atmospheric muon neutrino fluxes is very similar to the muon fluxes presented in Section 3.1.4 but differs by the allowed neutrino energy range due to the kinematics from meson decays. For a pion with an energy E_π, the allowed energy of the daughter neutrino ranges from 0 to $(1-r)E_\pi$, where $r \equiv m_\mu^2/m_\pi^2$. Therefore, a neutrino with an energy E_ν can be a decay product from a pion with an energy ranging between $E_\nu/(1-r)$ and infinity. The pion-contributed neutrino spectrum $\mathcal{N}_\pi(E_\nu, X)$ is therefore the same as the muon spectrum in Equation 3.28 but with a different energy range for the integral. Therefore, the differential energy spectrum for atmospheric muon neutrino, $\nu_\mu + \bar{\nu}_\mu$, is given by integrating over slant depth;

$$\frac{d\mathcal{N}_\pi}{dE_\nu} = \frac{\epsilon_\pi}{(1-r_\pi)\cos\theta} \int_0^\infty dX \frac{1}{X} \int_{E_\nu/(1-r)}^\infty dE_\pi \frac{\Pi(E_\pi, X)}{E_\pi^2}. \tag{3.34}$$

To solve Equation 3.34 over both low and high neutrino energies, a procedure similar to the calculation of muon and meson fluxes is performed. By integrating pion flux at low energy limit (Equation 3.22) over both meson energy and slant depth, the atmospheric ν_μ energy spectrum at low energy limit is given by

$$\frac{d\mathcal{N}_\pi}{dE_\nu} = \frac{Z_{N\pi}}{1-Z_{NN}} \frac{(1-r_\pi)^\gamma}{\gamma+1} N_N(E_\nu, 0). \tag{3.35}$$

Similar to the differential muon energy spectrum in Equation 3.29, this low energy limit follows the primary energy spectral index. However, the dependence on the r_π in the case of neutrinos is slightly different compared to that of muons due to the different energy distributions during the decay process. Similarly, from Equation 3.18, the high energy limit of the differential atmospheric muon neutrino spectrum is

$$\begin{aligned}\frac{d\mathcal{N}_\pi}{dE_\nu} =& \frac{Z_{N\pi}}{1-Z_{NN}}\frac{\Lambda_\pi}{\Lambda_\pi-\Lambda_N}\ln\frac{\Lambda_\pi}{\Lambda_N} \\ &\times \frac{(1-r_\pi)^{\gamma+1}}{\gamma+2}\frac{\epsilon_\pi}{X\cos\theta}\frac{N_N(E_\nu,0)}{E_\nu},\end{aligned} \tag{3.36}$$

where the natural log comes from integrating the exponential terms in Equation 3.18 over slant depth. Together with the neutrino contribution from charged kaon decays, the overall differential energy spectrum for atmospheric muon neutrino is, therefore, [98]

$$\frac{d\mathcal{N}}{dE_\nu} \sim \frac{N_N(E_\nu,0)}{1-Z_{NN}}\left[\frac{\mathcal{A}_{\pi\nu}}{1+\mathcal{B}_{\pi\nu}\cos\theta E_\nu/\epsilon_\pi}+\frac{0.635\mathcal{A}_{K\nu}}{1+\mathcal{B}_{K\mu}\cos\theta E_\nu/\epsilon_K}\right], \tag{3.37}$$

where, for a given meson M,

$$\begin{aligned}\mathcal{A}_{M\nu} &= \frac{Z_{N\pi}(1-r_M)^{\gamma+1}}{(1-r_M)(\gamma+1)} \\ \mathcal{B}_{M\nu} &= \frac{\gamma+2}{\gamma+1}\frac{1}{(1-r_M)^{\gamma+2}}\frac{\Lambda_\pi-\Lambda_N}{\Lambda_\pi\ln(\Lambda_\pi/\Lambda_N)}.\end{aligned} \tag{3.38}$$

Compared to the differential energy spectrum for atmospheric muons in Equation 3.32, atmospheric muon neutrino energy spectrum is differed by the suppression factor[5] and the dependence on r_M, which is related to the energy distribution during the decay process (see Equation 3.27). This implies that the difference between muon and muon neutrino contributions from the same parent is due to the differences in how the parent meson distributes its energy to its daughter particles.

[5]The suppression factor S_μ in the case of muons does not apply to neutrinos. Neutrinos do not decay, and its energy loss through propagation is negligible.

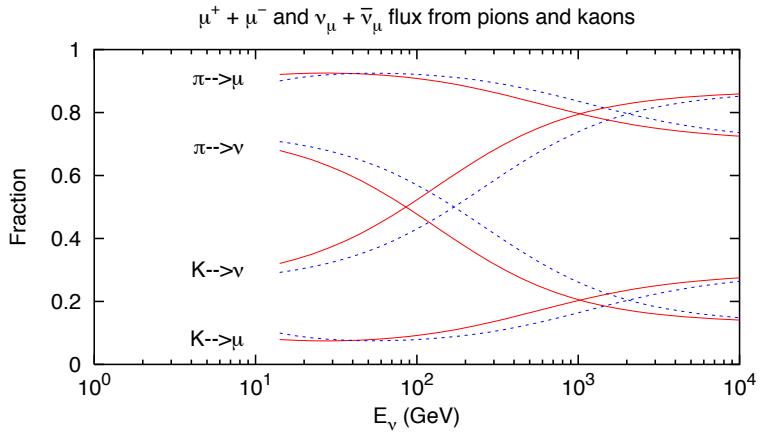

Figure 3.5: Fractional contribution to atmospheric muons and muon neutrinos from pions and kaons. Solid lines represent the fraction from particles traveling vertically with $\cos\theta = 1$; dashed lines are from $\theta = 60°$. Differences between contributions from pion and kaon at a given direction originate from the differences in the kinematics of the meson decays. This plot is adapted from [89].

Figure 3.5 [89] summarizes the fractional contributions to atmospheric muons and muon neutrinos from pion and kaon decays given $\theta = 0°$ and $60°$. As neutrino energy increases from $\sim$ 10 GeV to $\epsilon_\pi \approx 115$ GeV, the importance of pion decay decreases, reducing both muon and muon neutrino fractions. Since muon mass is ~ 0.75 of pion mass, a daughter muon from a pion decay carries most of the pion energy, causing a steeper fall in the neutrino fraction from pion compared to that in muon fraction from pion. Because of this falling contribution from pions, neutrino contribution from kaon decay becomes relatively more important until the neutrino energy reaches $\epsilon_K/\cos\theta \sim \epsilon_K \approx 850$ GeV. In a kaon decay, a kaon with a mass of $\sim$ 500 MeV distributes, on average, half of its energy to the daughter muon, leading a steeper growth of neutrino contribution from kaon decay compared to that of muon from the same parent [98]. Beyond $\sim$ 1 TeV, the contributions flatten out because kaon interaction takes over kaon decay.

The individual ν_μ and $\bar{\nu}_\mu$ energy spectra can be obtained via the total muon

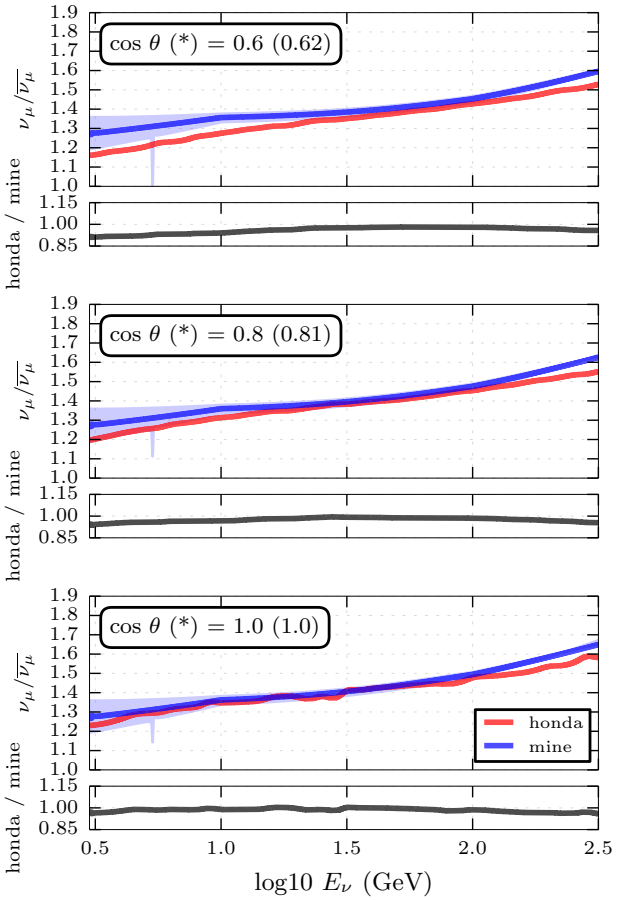

Figure 3.6: Comparison between 1D analytical and 3D simulated $\nu_\mu/\bar{\nu}_\mu$ flux ratio: (top) cos $\theta = 0.6$, (middle) cos $\theta = 0.8$, and (bottom) cos $\theta = 1.0$. Red solid lines represent the $\nu_\mu/\bar{\nu}_\mu$ flux ratios from a three dimensional simulation by Honda *et al.* [86]. Blue lines are the one dimensional analytical results discussed in this section; the blue band represents the uncertainties on the flux ratios due to uncertainties of Z-moments from [93]. The spikes at log10 $E_\nu \sim 0.75$ are because of the natural log of effective interaction length ratios in Equation 3.38.

neutrino fluxes $\mathcal{N}$ and their difference Δ_ν. The resulting flux ratio, $\nu_\mu/\bar{\nu}_\mu$, due to both pion and kaon decays is very similar to the muon charge ratio given by [101] and is presented as the blue solid lines in Figure 3.6 at three different values of cos θ. With the uncertainties on the relevant Z-moments given by [93], the uncertainties on the $\nu_\mu/\bar{\nu}_\mu$ flux ratios are shown as the blue shaded areas. Overall,

$\nu_\mu/\bar{\nu}_\mu$ flux ratios increase with neutrino energy. As discussed in Section 3.1.3, due to proton excess at the top of the atmosphere, more K^+ are produced than K^-. With the extra K^+ production channel, Z_{pK^+} is much larger thanZ_{pK^-}, leading to an asymmetry in the production of ν_μ and $\bar{\nu}_\mu$. This asymmetry becomes more dramatic as neutrino energy increases due to the growing importance of kaon decays relative to the falling contributions from pion decay. These predictions from the one dimensional analytical approach are compared to the solid red lines predicted by Honda *et al.* [86] via a three dimensional simulation[6]. For vertically down going neutrinos, the two predictions agree fairly well. A slight deviation at high energy comes from neutrino contributions from particles other than pions and kaons. The agreement between two methods gets worse as $\cos\theta$ decreases because of the ignored neutrino contribution from muon decay.

For atmospheric electron neutrino fluxes, because one muon decays into one electron neutrino (Equation 3.31), $\nu_e/\bar{\nu}_e$ flux ratio could be approximated by μ^+/μ^-. However, the analytical solutions for atmospheric electron neutrino fluxes are more complicated when one includes the contribution from the three-body decay by long kaon. Figure 3.7 shows the comparison between the analytical results (with charged pion and charged kaon) and simulated predictions by Honda *et al.* [86]. While the overall orders of magnitude agree between calculations and simulations, the simulated flux ratios seem to be higher at low energy and lower at high energy than the analytical results, which is potentially due to the ignorance of long kaon decay. Moreover, the analytical approach gives smoother flux ratios compared to the simulations by Honda *et al.* These differences between the two predictions are likely caused by naive assumptions made during the one dimensional approach.

[6]By taking into account Earth's magnetic field, better atmospheric density profile, and better hadronic interaction models, Honda *et al.* [86] provides tables of atmospheric neutrino flux predictions at the South Pole (see Section 5.1.4).

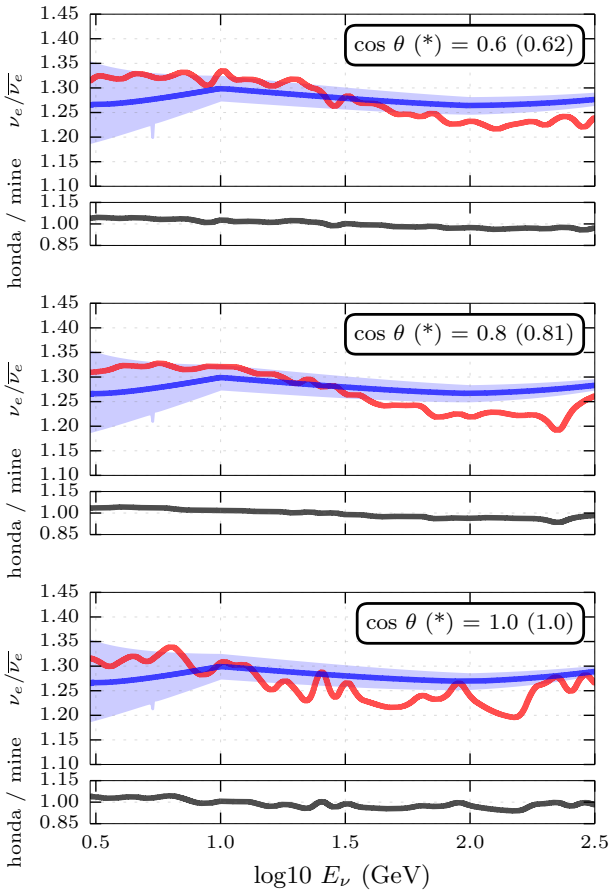

Figure 3.7: Comparison between 1D analytical and 3D simulated $\nu_e/\bar{\nu}_e$ flux ratio: (top) cos $\theta = 0.6$, (middle) cos $\theta = 0.8$, and (bottom) cos $\theta = 1.0$. Red solid lines represent the $\nu_e/\bar{\nu}_e$ flux ratios from a three dimensional simulation by Honda *et al.* [86]. Blue lines are the one dimensional analytical results discussed in this section; the blue band represents the uncertainties on the flux ratios due to uncertainties of Z-moments from [93]. The spikes at log10 $E_\nu \sim 0.75$ are because of the natural log of effective interaction length ratios in Equation 3.38.

3.1.6 Final Notes on Atmospheric Neutrino Fluxes

In general, analyses using atmospheric neutrinos as neutrino sources care about four neutrino flux ratios: $\nu_\mu/\bar{\nu}_\mu$, $\nu_e/\bar{\nu}_e$, $(\nu_\mu+\bar{\nu}_\mu)/(\nu_e+\bar{\nu}_e)$, and vertical / horizontal. As discussed in the previous subsection, the former two flux ratios directly depend on the π to K ratio, which depends on the Z_{pK^+}. In particular, flux ratios with

neutrino energies between $\epsilon_\pi/\cos\theta$ and $\epsilon_K/\cos\theta$ are the most sensitive to π to K ratio due to the growing importance of kaon decay and steep falling spectrum from pion.

The calculations for the latter two flux ratios are discussed by Barr *et al.* [92], in which multiple analytical approaches are performed to predict neutrino fluxes assuming that the detector site is located at Kamioka in Japan. In the following plots from [92], a 1D approach corresponds to the calculations discussed in the previous subsection; a 3D approach takes into account bending of particles due to Earth's magnetic field; a NM approach is the same as the 3D approach but without bending of particles; and a pseudo 1D approach uses the 3D code but assumes 1D conditions for verification purposes.

The ratio between $\nu_\mu + \bar{\nu}_\mu$ and $\nu_e + \bar{\nu}_e$ fluxes is well known. Because a pion or kaon decays into a muon neutrino and a muon, which then decays and produces another muon neutrino and an electron neutrino, the ν_μ to ν_e flux ratio is roughly 2 [86,87,92,98]. This is a fairly good estimate for atmospheric neutrinos with energies below 2 GeV [98]. As neutrino energy increases, high energy muons produced reach the ground before they get a change to decay and produce ν_e. As shown in the solid lines on the left plot of Figure 3.8 [92], the ν_e energy spectrum falls faster than the ν_μ spectrum. Thus, the ν_μ to ν_e flux ratio increases with neutrino energy as shown on the right of Figure 3.8 [92].

While most of the discussions above are zenith-integrated, the last interesting ratio is the ratio of vertical to horizontal total ν_μ fluxes. Given that fluxes are usually expressed as $E\cos\theta$ (see Equation 3.37), it is useful to investigate a vertical to horizontal flux ratio for a given energy range. The left of Figure 3.9 [92] presents the predicted angular distributions of ν_μ fluxes for three different energy ranges. Note that $\cos\theta = 0$ corresponds to horizontal flux. As neutrino energy increases, the peak at the horizon becomes more apparent. Because flux equations depend on

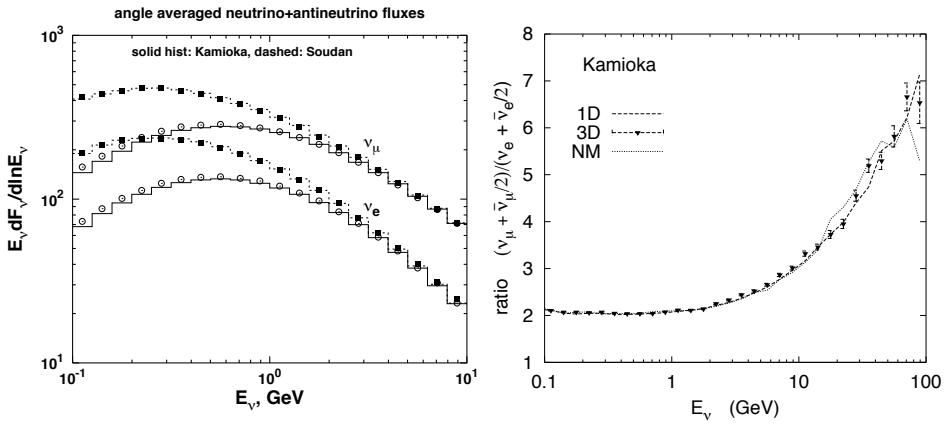

Figure 3.8: Comparison between 1D and 3D analytic ν_μ and ν_e fluxes.: (left) differential energy spectra and (right) ratio of total ν_μ to ν_e fluxes. The left plot shows the differential energy spectra for both total ν_μ and ν_e fluxes. The circle data points and solid lines represent the predicted fluxes from the three- and one- dimensional approach at Kamioka, while the square data points and dashed lines are predicted for a detector located at Soudan. The right plot presents the $(\nu_\mu + \bar{\nu}_\mu)/(\nu_e + \bar{\nu}_e)$ flux ratios at Kamioka from three different analytical approaches. These plots are adapted from [92].

$1/E_\nu \cos\theta$, a larger zenith angle and smaller cos θ generally increases the neutrino fluxes. This effect is enhanced for muons of a higher energy from large zenith angle, which have higher chance to decay before hitting the ground compared to those of same energy but from vertically down going. The ratio of vertical to horizontal ν_μ fluxes is shown on the right of Figure 3.9 [92]. The three different approaches deviate significantly for neutrino energies below 1 GeV. In the 1D approach, all secondary particles are assumed to follow the same direction as the primary cosmic ray, which is a valid assumption for down going particles with an averaged projectile the same as the incident primary. This assumption, however, underestimate fluxes from the horizon, because secondaries from slightly below the horizon can be scattered above the horizon. Since low energy particles are more easily scattered compared to high energy, the deviation between 1D and 3D approaches for low energy neutrinos.

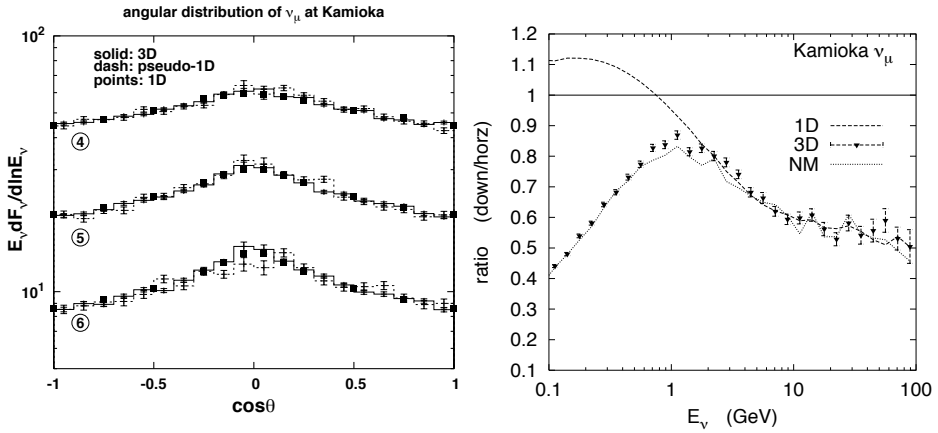

Figure 3.9: Comparison between 1D and 3D analytic ν_μ fluxes.: (left) angular distributions from three different energy ranges and (right) ratio of vertical to horizontal ν_μ fluxes. The left plot shows the predicted angular distributions at Kamioka given three different energy ranges: 2.5 - 4.0 GeV for (4), 4.0 - 6.3 GeV for (5), and 6.3 - 10 GeV for (6). For each energy range, three predictions are presented: data points for 1D, solid lines for 3D, and dashed lines for pseudo 1D. The right plot shows the vertical to horizontal flux ratio as a function of neutrino energy. Results from three approaches are shown: data points for 3D, a dashed line for 1D, and a dotted line for NM. These plots are adapted from [92].

Above $\sim$ 5 GeV, the three approaches lead to similar vertical / horizontal flux ratio.

3.2 Neutrino Detection

IceCube-DeepCore detects neutrinos indirectly via Cherenkov radiation. Section 3.2.1 explains the three possible neutrino interactions with the ice given an energy range between a few GeV and up to 100 GeV. In particular, a charge current interaction produces a charged lepton, whose propagation through ice (see Section 3.2.2) emits Cherenkov light while experiencing energy loss due to ionization. Photons from Cherenkov radiation then travel through the ice and may be scattered

and/or absorbed based on the ice properties described in Section 3.2.3. Eventually, photons that do not get absorbed or scattered out of the instrumented volume then arrive at the optical sensors and are detected as explained in Chapter 4.

3.2.1 Neutrino Interactions

According to the Standard Model (SM), neutrinos can only weakly interact with matter through $W^{\pm}$ and Z^0 force carriers. Thus, a neutrino interaction can either be charge current (CC) or neutral current (NC). As shown in Figure 3.10, a CC interaction involves an exchange of a $W^{\pm}$ gauge boson. An incoming neutrino emits a W^{+} and interacts with the down quark of a neutron in a nucleus. This interaction produces a charged lepton of the same flavor and converts the neutron into a proton. On the other hand, a NC interaction, defined as an interaction via a neutral Z^0 boson, does not give out charged leptons but transfers energy and momentum between a neutrino and the target. Over the past decades, observations [**?**,113,114] have found that weak couplings between gauge bosons and neutrinos are flavor independent. Therefore, such lepton universality is assumed in this analysis; CC and NC interactions with neutrinos of the same energy but different flavors all have the same cross sections. Since IceCube-DeepCore can only identify cascade- and track- like events, lepton universality implies that all NC interactions have the same event topology and, thus, their flavors cannot be identified.

Nevertheless, cross sections between neutrinos of any flavor and the targets do depend on the neutrino energy. Figure 3.11 shows the cross sections of ν_μ CC interactions over a range of neutrino energies [115]. For energy below ~ 1 GeV, quasi elastic scattering (QE) is the dominant interaction (see Section 3.2.1.1) whereas deep inelastic scattering (DIS) discussed in Section 3.2.1.3 dominates when the neutrino energy is above 100 GeV. Further complication comes into play when a neutrino has

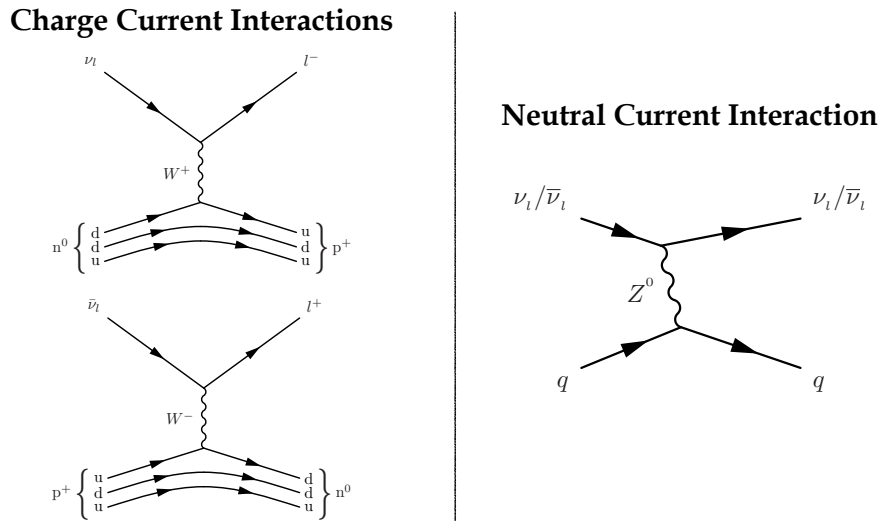

Figure 3.10: Feynman Diagrams of Charge and Neutral Neutrino Interactions: (left) Charge Current (CC) and (right) Neutrino Current (NC) Interactions. A CC neutrino interaction involves an exchange of a $W^{\pm}$ vector gauge boson, whereas a NC interaction involves an exchange of a Z^0.

an energy between $\sim$ 1 and 100 GeV due to resonance production (RES) explained in Section 3.2.1.2. Thus, this analysis requires understandings of all three non negligible interaction processes. For more detailed information, a summary in both theories and experiments of neutrino cross section over an energy range from eV to EeV is given by [116].

3.2.1.1 Quasi Elastic Scattering

Being the most important interaction of neutrinos with energies below 1 GeV, quasi elastic (QE) scattering between neutrinos and nucleons has long been an active research topic for many long baseline neutrino experiments. In general, an elastic scattering is defined as a scattering in which the four-momentum of an incident particle is the same as that of the outgoing particle; that is, the point-like target

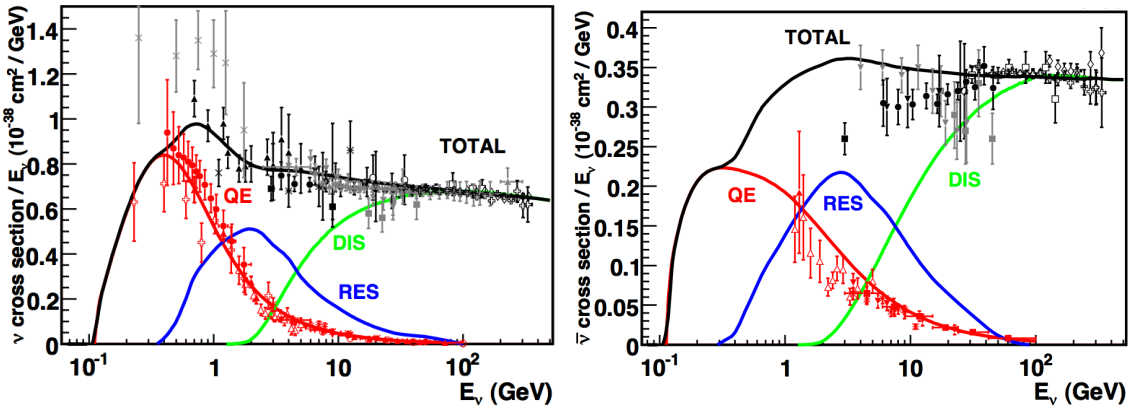

Figure 3.11: Current Understanding of ν_μ CC Cross Section As a Function of Energy: (left) ν_μ CC and (right) $\overline{\nu}_\mu$ CC. This figure is adapted from [115]. Since our interested neutrino energy ranges from a few GeV to below 100 GeV, the dominant processes are quasi-elastic scattering, resonance production, and deep inelastic scattering.

does not receive any energy or momentum transfer (Q^2). In a neutrino-nucleon scattering, however, up and down quarks are bounded within a nucleon; plus, the coupling between a complex nucleon and a gauge boson is not provided by the SM. These leads to a non-zero Q^2 between a neutrino and a nucleon, adding complications to the cross section calculation. Fortunately, given a neutrino with an energy below 1 GeV, the target nucleon remains as a single nucleon after scattering. Moreover, the Q^2 of the scattering process is small enough such that its cross section can be calculated using the formalism of an elastic scattering with nucleon corrections and a perturbation around small Q^2. This approximation is, therefore, called quasi elastic scattering.

While many theoretical models have been proposed to provide a mathematical expression for the differential cross section of QE neutrino-nucleon scattering [117], one of the earliest mathematical expressions for the differential cross section of QE neutrino-nucleon scattering was presented by C.H. Llewellyn Smith in 1972 [118].

Because a nucleon is assumed to be point-like with four correction terms called form factors (FFs) [119], Sir Llewellyn Smith expressed the differential cross section as [118]

$$\frac{d\sigma}{dQ^2} = \frac{G_f^2 M^2 \cos^2\theta_c}{8\pi E_\nu^2}\left[A_{(Q^2)} \mp \frac{s-u}{M^2}B_{(Q^2)} + \frac{(s-u)^2}{M^4}C_{(Q^2)}\right]. \tag{3.39}$$

Here, G_f is the well measured Fermi coupling constant; M is the mass of the targeted nucleon; θ_c is the Cabibbo mixing angle in the quark sector; s and u are the Lorentz invariant Mandelstam variables. Most importantly, the three coefficients $A_{(Q^2)}$, $B_{(Q^2)}$, and $C_{(Q^2)}$, depend on the nucleon form factors F_1, F_2, F_p, and F_A, which cannot be determined theoretically and have to be measured from accelerator experiments. To today's knowledge, the Dirac and Pauli electromagnetic isovector form factors, F_1 and F_2, are well measured independently from experiments that study electron elastic scattering. The pseudoscalar form factor F_P is proportional to the ratio squared between the mass of the incident neutrino and that of the nucleon $(m_\nu/M)^2$, which is a small contribution to the differential cross section. However, the numerical values of the axial form factor F_A is not as well known compared to the other three form factors. Throughout many years of observations by various reactor and accelerator experiments [120–122], data seems to suggest that F_A has a dipole form given by

$$F_{A_{(Q^2)}} = \frac{g_A}{(1+Q^2/M_A^2)^2}, \tag{3.40}$$

where g_A is the axial coupling constant that is well measured by neutron β decay [123–126], and M_A is an axial mass for the QE neutrino-nucleon scattering, whose numerical value is not well understood.

A review of M_A measurements is given by [116], which includes results from traditional bubble chambers with light targets such as hydrogen and deuterium as well as measurements from modern experiments using heavier targets. While early data suggests a world averaged value for M_A of ~ 1 GeV, recently measured

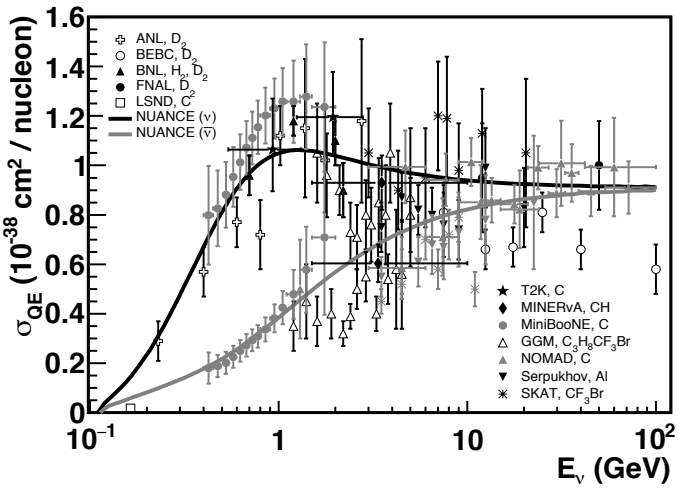

Figure 3.12: ν_μ and $\overline{\nu}_\mu$ QE scattering differential cross sections from various experiments. Plot is adapted from [127]. Black and gray curves represent the predicted QE differential cross section with an assumed $M_A = 1.0$ GeV for ν_μ and $\overline{\nu}_\mu$ respectively. Data points are obtained from experiments using light and heavy targets.

cross sections with modern experiments challenge the previous understanding of axial mass M_A for QE neutrino-nucleon scattering at neutrino energy $\sim$ 1 GeV [128–130]. As shown in Figure 3.12 [127], the MiniBooNE experiment using carbon as the scattered target measures a slightly larger cross section [131, 132] at neutrino energy of $\sim$ 1 GeV. While similar observations in the cross section of QE electron-nucleon scattering is believed to be related to correlations among target nucleons in a nucleus [133], such an enhancement in QE neutrino-nucleon scattering leads to a large uncertainty of its differential cross section.

3.2.1.2 Resonance Production

When an incident neutrino has an energy between $\sim$0.5 and 10 GeV, it can lead to an inelastic scattering with the targeted nucleon. In this case, the energy and momentum transfer between the neutrino and the targeted nucleon is large

enough to produce a nucleon at its excited state such as a Δ. The resonance then immediately decays into a nucleon, often giving out a single pion. Figure 3.13 shows a Feynman diagram of a possible resonance production, in which a Δ^+ is produced and quickly decays back to a neutron while giving out a charged pion. Although the cross section of one Feynman diagram is not impossible to compute, complication comes when there are at least six final states for each neutrino flavor by a CC interaction. Moreover, the final states can also include multiple pions, kaons, and heavier mesons, which can re interact with the nearby nucleons. All these possibilities add complexities to accurately determine the total cross section of resonance production (RES) theoretically and experimentally.

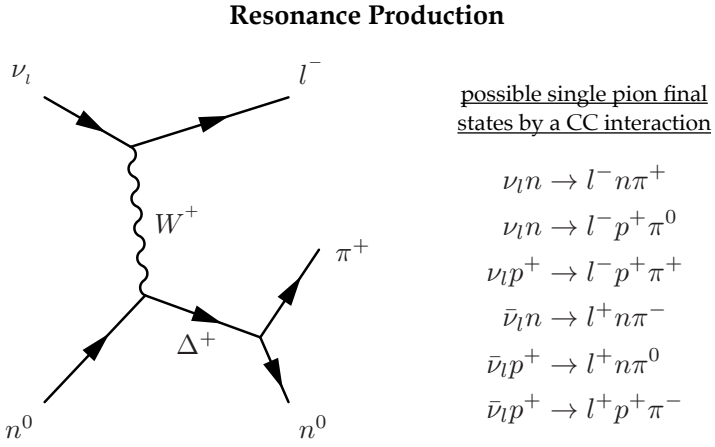

Figure 3.13: Single Pion Resonance Production; (left) a Feynman diagram of one possible interaction and (right) all possible single pion resonance production interactions.

The most common theoretical model on RES is given by Rein and Sehgal (RS) [134]. Using the relativistic quark model of Feynman, Kislinger, and Ravndal [135], the RS model provides the first order approximation to cross section calculations for single pion resonance productions below 2 GeV. Later, Rein modified his model by taking into account contributions to the amplitude from helicity and interference

[136]. In the past decades, further improvements to the model have been made to include the effect from the mass of the outgoing lepton [137], contributions from heavier resonances [138], and other non resonant pion productions [139]. Most importantly, the forms of form factors have been deduced using both Δ excitation predictions and data [140]. Similar to the axial mass in the QE neutrino-nucleon scattering, the axial form factor for RES with a dipole form agrees with available data the best. Adapted to many neutrino simulation tools, this dipole assumption is similar to Equation 3.40, which depends on a well measured axial coupling constant for RES and its less known axial mass.

Most of the on-going experiments nowadays study single pion RES independent of specific models. A detailed summary of these measurements by three major neutrino long base line experiments is presented in [141]. While using different simulation software, targeted materials, and analysis techniques, results from K2K [142], MiniBooNE [143], and SciBooNE [144] are consistent at $\sim$ 1 GeV. Cross section Measurements at higher neutrino energy of a few GeV are also performed recently by MINERνA [145, 146]. Despite successful agreements on RES cross section measurements in the long baseline neutrino community, more data is still needed to fully understand resonance production, including not only single pion production but also contributions from multi-meson productions and re-interactions of final states, as well as the effects of heavier targets such as carbon.

3.2.1.3 Deep Inelastic Scattering

Well described by the quark parton model in the theory of quantum chromodynamics (QCD), a deep inelastic scattering (DIS) involves a neutrino above a few GeV, which has a small enough wavelength to prob deep inside the targeted nucleon. At such a high energy and momentum transfer Q^2, a constituent quark

inside the nucleon is knocked out. Since quarks cannot be observed individually due to color confinement, they reform themselves into baryons and/or mesons during the hadronization process, which absorbs part of the kinetic energy from the incoming neutrino. Hence, such a high energy scattering between a neutrino and a nucleon is deep and inelastic.

Unlike QE and RES where the targeted nucleon can be treated as a point-like scatter whose coupling with the weak force carriers is modified by some form factors, DIS requires an understanding of the internal structure of the nucleon. This internal structure is measured by two structure functions $W_{1,2(Q^2,E_\nu-E_l)}$ [147], which depend, not only on Q^2, but also on the energy of the incoming and outgoing leptons due to the inelastic nature in DIS. The actual dependence of $W_{1,2}$'s on Q^2 and the lepton energies was unclear until Bjorken suggested in 1969 the existence of point-like constituents inside the nucleon [148]. If the neutrino targets at a point like parton inside the nucleon, the structure functions should depend only on a dimensionless Bjorken x_B variable, which is proportional to the ratio of Q^2 to the kinetic energy loss by the incident neutrino. By definition [149],

$$y = \frac{E_\nu - E_l}{E_\nu} \quad ; \text{and} \qquad x_B = \frac{Q^2}{2M_N(E_\nu - E_l)}, \tag{3.41}$$

where M_N is the nucleon mass, whereas $E_\nu - E_l$ is the energy difference between the incident neutrino and outgoing lepton. Nowadays, with a slightly better understanding on the internal structure of nucleons, corrections and improvements have been made to better predict cross sections of DIS between neutrinos and nucleons [150–156].

Within the past decade, long baseline experiments using neutrinos above 30 GeV have measured the structure functions as a function of modified Bjorken x variable and Q^2 [158]. Within a neutrino energy range between 30 and 380 GeV, Figure 3.14 [158] shows that data from various long baseline experiments indicates

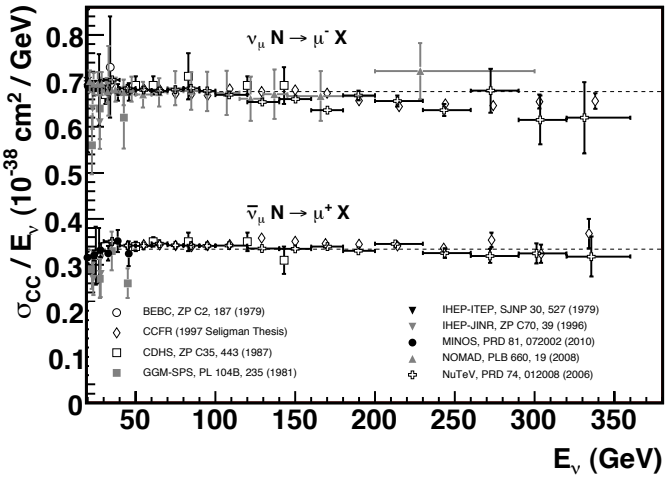

Figure 3.14: DIS cross section measurements. Data points taken from various long baseline neutrino experiments, which study ν_μ and $\overline{\nu}_\mu$ CC interactions with targeted nucleon from 30 to 380 GeV. Dotted lines represent the world averaged cross sections from [157]. Horizontal lines suggest that the cross sections for DIS CC interactions between ν_μ/ $\overline{\nu}_\mu$ and nucleons are linearly proportional to the neutrino energy. This plot is taken from [158].

a linear relation between neutrino energy and the cross sections for DIS CC interactions between $\nu_\mu/\overline{\nu}_\mu$ and nucleons[7]. Furthermore, with the use of heavier targets such as lead and iron, recent experiments study the effect on neutrino-nucleon DIS cross sections due to heavier quarks in the nucleon [159–161].

3.2.2 Propagation of Leptons

After a CC interaction between a neutrino and a nucleon, a secondary lepton is produced and propagates through the ice. During its propagation, it encounters the hydrogen and oxygen atoms along its path, from which radiation may be emitted.

[7]This linear dependence breaks down as neutrino energy goes up $\sim$ 10 TeV due to the heavy mass of the W boson. As the neutrino energy further reaches the W resonance, the neutrino DIS cross section is expected to increase drastically. However, for the purpose of this analysis, a linear proportionality is sufficient.

The secondary lepton loses energy and may eventually be stopped by the ice. How a lepton interacts with the ice depends on its energy and flavor. In general, the mean stopping power of a given material can be described by

$$\left\langle -\frac{dE}{dx} \right\rangle = a(E) + b(E) \times E, \tag{3.42}$$

where E is the energy of the lepton, and dx is the amount of material traversed in [g/cm^2]. $a(E)$ and $b(E)$ are the electronic stopping power due to ionization and the energy loss parameter due to radiative processes respectively. The radiative processes include Bremsstrahlung, pair production, and photo nuclear interactions. For this analysis, interested in an energy range between 5 GeV and 56 GeV, Bremsstrahlung is the dominate source of energy loss for relativistic electrons. In contrast, for secondary muons which are much heavier than electrons, the energy loss by a secondary muon is dominated by ionization, as shown in Figure 3.15. Because the signal event type for this analysis is ν_μ CC, which gives out a secondary muon after the neutrino interaction, the mechanism of how a muon loses energy via ionization is discussed in Section 3.2.2.1. Most importantly, for any charged particle traveling above a critical speed, Cherenkov radiation is emitted as discussed in Section 3.2.2.2. While the lepton's energy loss via Cherenkov radiation is less than 1% of that by ionization, the ultraviolet photons emitted by Cherenkov radiation are the particles actually detected by the IceCube optical sensors.

3.2.2.1 Muon Energy Loss by Ionization

A classical derivation of energy transfer from a moving charged particle can be estimated using the first-order Born approximation. Figure 3.16 presents the statement of problem. Consider a particle of mass M and of charge Ze[8] moving at a velocity $\vec{v}$ along a cylindrical barrel with an impact parameter b and a height of

[8] Z is in unit of electron charge, whereas e is the electron charge.

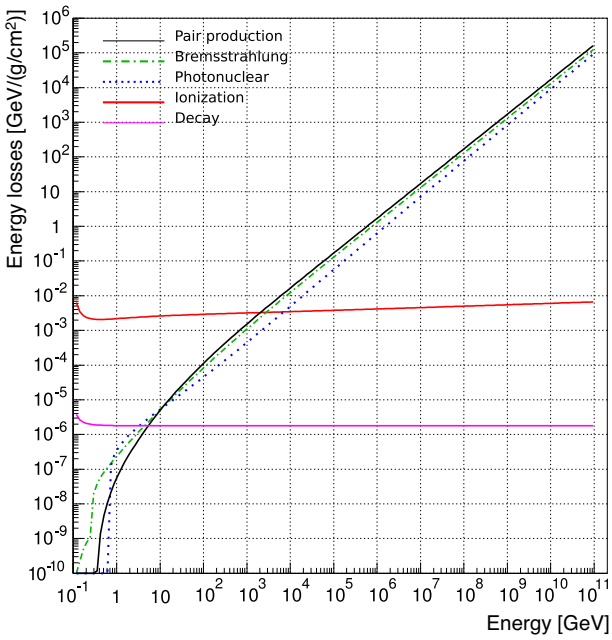

Figure 3.15: Energy losses for ice due to different mechanisms. Below 1 TeV, stopping power for ice due to radiative processes, including Bremsstrahlung (dash-dotted green), pair production (solid black), and photo nuclear interactions (dotted blue), are negligible compared to ionization (solid red). This plot is taken from [162].

dx, a momentum $\vec{p}$ is asserted on an electron on the surface of the barrel. Since the parallel component of $\vec{p}$ will cancel out when the charged particle travels to the other side after some time, only the perpendicular component $p_\perp$ matters. This $\Delta p_\perp$ is caused by a force asserting on the electron during dt, which is related to the speed of the moving charged particle; that is,

$$\Delta p_\perp = \int dt\ F_\perp = \int dx \frac{dt}{dx}\ F_\perp = \int \frac{dx}{v}\ F_\perp \tag{3.43}$$

Because $F_\perp$ on the electron is due to the electric field $\mathcal{E}_\perp$ of the moving particle,

$$\Delta p_\perp = \frac{e}{v} \int dx\ \mathcal{E}_\perp = \frac{e}{v} \times \frac{Ze}{2\pi\epsilon_0 b}, \tag{3.44}$$

where the second part of the equation comes from Gauss's Law, which states that the integral of an electric field over an enclosed surface is equal to $1/\epsilon_0$ times the

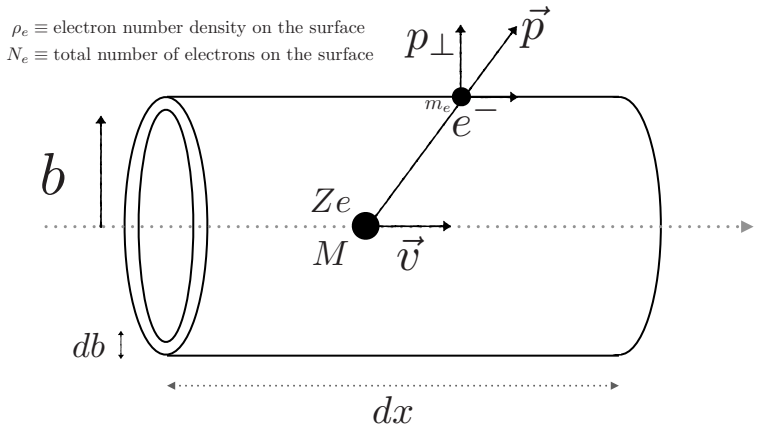

Figure 3.16: A Schematic Diagram for the Energy Loss Due to Ionization. A particle with a charge of Ze and a mass of M travels across a cylindrical barrel of a radius b and a height of dx at a velocity of $\vec{v}$. It asserts a force on an electron, with a mass of m_e on the surface with a perpendicular momentum $p_\perp$. N_e electrons are equally distributed, with a number density of ρ_e, on the surface of the barrel with a thickness of db. A statement of the problem is to derive a classical expression for the energy loss $-dE/dx$ of the moving particle as it propagates through the medium.

total charge inside the enclosed surface. Therefore, the energy transferred to the electron is

$$\Delta E = \frac{\Delta p_\perp^2}{2m_e} = \frac{1}{2m_e}\left(\frac{2Zm_e r_e c}{\beta b}\right)^2 = \frac{2Z^2 m_e r_e^2 c^2}{\beta^2 b^2}, \tag{3.45}$$

where $\beta = v/c$, and r_e is the classical electron radius given by $e^2/4\pi\epsilon_0 m_e c^2$. However, ΔE is the energy transferred to only one electron on the cylinder; to get the energy transfer to all electrons, ΔE is multiplied by the total number of electrons:

$$\Delta E = \frac{2Z^2 m_e r_e^2 c^2}{\beta^2 b^2} \times \rho_e \; 2\pi b \; db \; dx = \frac{4\pi Z^2 m_e r_e^2 c^2 \rho_e}{\beta^2} \; \frac{db}{b} \; dx, \tag{3.46}$$

where ρ_e is the electron number density. Last but not least, the total energy loss from cylinders of all sizes is given by integrating ΔE over all b; that is,

$$-\frac{dE}{dx} = \frac{4\pi Z^2 m_e r_e^2 c^2 \rho_e}{\beta^2} \; \ln\frac{b_{\max}}{b_{\min}}, \tag{3.47}$$

where the boundaries, $b_{\min}$ and $b_{\max}$, are determined by two considerations. First, the minimum b happens when the moving charged particle collides with the electron head on, in which all momentum gained by an electron transfer to its kinetic energy; that is,

$$\begin{aligned} \Delta E(b_{\min}) = \frac{2Z^2 m_e r_e^2 c^2}{\beta^2 b_{\min}^2} &= \frac{\gamma^2 m_e (2v)^2}{2} \\ b_{\min} &= \frac{Z r_e}{\beta^2 \gamma}, \end{aligned} \tag{3.48}$$

where $\gamma = \sqrt{1-\beta^2}$. On the other hand, at the upper bound of b, no excitation occurs during the collision time, and the electron remains at its energy level with an orbiting frequency of ω. Thus, $b_{\max}$ should be approximately the wavelength of the electron:

$$b_{\max} \approx \frac{\gamma v}{\omega}. \tag{3.49}$$

By plugging the minimum and maximum b , the energy loss by the moving charged particle can be expressed in terms of its velocity $\beta\gamma$,

$$-\frac{dE}{dx} \propto \frac{1}{\beta^2} \ln\left(\alpha\beta^2\gamma^2\right). \tag{3.50}$$

The classical approach is of course inadequate. Bethe took into account the relativistic effect and formulated the Bethe-Bloch equation [164, 165], which describes the energy loss of a charged particle moving through a medium. While many corrections have been made, including effects from atomic physics by Bloch and charged particles with different spins [166], the ln $(\beta^2\gamma^2)$ dependence in energy loss remains. Figure 3.17 shows the modified energy loss by Bethe-Bloch equation as a function of $\beta\gamma$ [163]. The energy loss by a muon propagating through water due to ionization is at minimum at $\beta\gamma \sim 4$ GeV. Through simulations, the energy loss by a muon through ice due to ionization is presented as the solid red line in Figure 3.15. Within a muon energy range from 1 to 10 GeV, the energy loss due to ionization is between

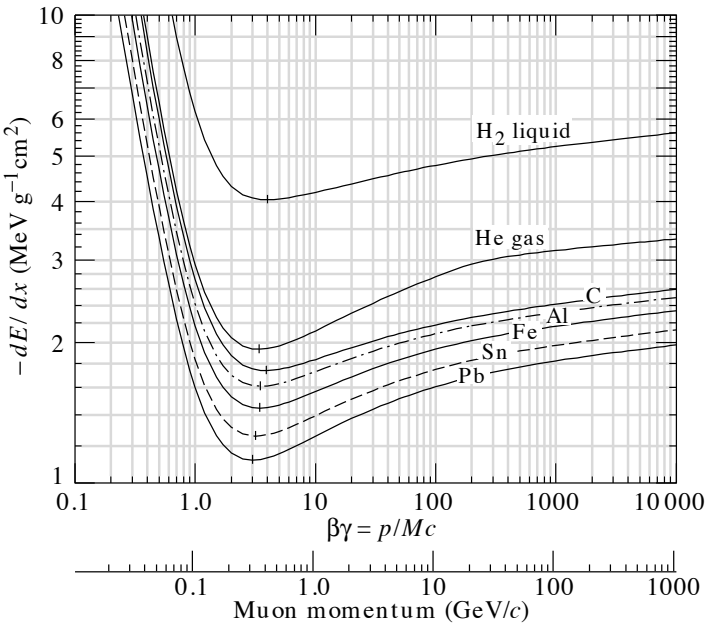

Figure 3.17: Energy Loss as a Function of $\beta^2\gamma^2$ and Muon Momentum. As a muon with $\beta\gamma \sim 3$ travels through water, its energy loss due to ionization is at a minimum value of $\sim$ 4MeV/(g cm^{-2}), which is equivalent to an energy loss of 0.4 GeV per meter in water. This plot is adapted from [163].

0.002 and 0.003 GeV/(g cm^{-2}). Given that water density is 1 g / cm^3, a minimum ionizing muon on average loses $\sim$ 1 GeV every 5 meters.

3.2.2.2 Cherenkov Radiation

First detected by Pavel Cherenkov in 1937 [167], Cherenkov radiation is a characteristic bluish light emitted when an energetic charged particle passes through a dielectric medium at a speed greater than the speed of light in that medium. When a charged particle passes by an atom, the particle disturbs the electromagnetic field of the atom, which is then raised to some excited states. As the excited atom returns to its ground state, some photons are emitted. As illustrated in Figure 3.18, this perturbation to the medium usually dies out as the particle travels through. How-

ever, if the particle travels fast enough, the perturbations from all excitations add up coherently, giving out a cone-shaped electromagnetic shock wave at a Cherenkov angle with respect to the propagation direction of the incoming particle.

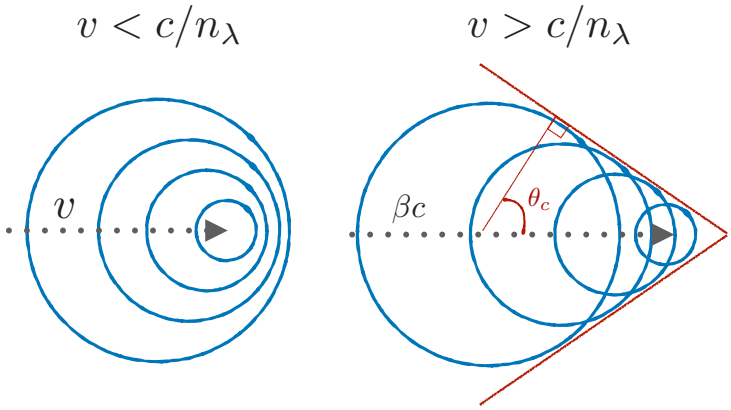

Figure 3.18: Cherenkov Radiation. When an incoming particle travels through a medium, it excites the nearby atoms. As they return to their ground states, radiation is induced. If the incoming particle has a fast enough speed, disturbances from all excitations add up coherently at an angle θ_c with respect to the particle direction. This Cherenkov radiation produces a shock wave in a cone shape.

The number of photons of a certain wavelength λ emitted depends on the Cherenkov angle θ_c of the same λ, which depends on the index of refraction of that wavelength n_λ in a given medium. Given the speed of light of λ as $v_\lambda = c/n_\lambda$, and the fast moving particle with a speed of βc, where $\beta = v/c$, the Cherenkov angle is

$$\cos\theta_c = \frac{v_\lambda}{\beta c} = \frac{1}{n_\lambda \beta}. \tag{3.51}$$

In particular, the Cherenkov angle in ice for an ultraviolet photon with a wavelength of ~ 400 nm is $\simeq 41°$. From the above equation, Frank-Tamm derives an expression for the photon yield due to Cherenkov radiation [168], which is

$$\frac{d^2N}{dxd\lambda} = \frac{4\pi^2(Ze)^2}{hc\lambda^2}\sin^2\theta_c, \tag{3.52}$$

where Ze is the electric charge of the fast moving particle. These photons, therefore, continue to travel through the ice and may be detected by the IceCube detectors.

3.2.3 Optical Properties of South Pole Ice

Since most IceCube analyses are based on Cherenkov radiation detected by the optical modules, the detector's properties of photon propagation has to be understood. Similar to the secondary leptons produced by a CC neutrino interaction, once photons are produced, they interact with the nearby particles as they travel. At this stage, however, tracing individual interaction process becomes difficult. Thus, interactions between photons and ice molecules are generally described by the optical properties of the ice. As discussed in Section 3.2.3.2, two general optical properties, absorption and scattering, are studied by comparing simulation and flasher data. Another ice property, explained in Section 3.2.3.1, is found to affect photon propagation locally at deployment sites.

3.2.3.1 Local Properties

Since the deployment of AMANDA, a predecessor of IceCube, we have known of the existence of air bubbles in the South Pole ice. Earlier analyses studying ice properties at depths between 800 and 1000 m found that, while scattering lengths are wavelength independent for photons at wavelengths between 410 and 610 nm, the absorption lengths for light at the same wavelength range are strongly wavelength dependent and significantly too long compared to the test results from laboratories [169, 170]. This suggests a high concentration of air bubbles within the studied depth range. Later studies found that, as pressure increases with depth, air bubbles become air hydrate crystal, which has a very similar refractive index as normal ice [169, 171]. At depths below $\sim$ 1500 m, all air bubbles are transformed into the

hydrate crystal state, and optical properties within the visible frequencies depend solely on the concentration of dust in the ice [171–173].

However, new air bubbles are created as hot water refreezes whenever a string is deployed. In December 2010, a pair of optical cameras was included in String 80 to observe the refreezing process. Figure 3.19 shows a schematic diagram of the set up and an image captured by one of the camera systems. The two camera systems are five meters apart, each of which has a camera and an LED. The two cameras face each other, while the LEDs face away. When one camera emits light, the other camera takes a picture to capture any scattered photons. The image on the right of Figure 3.19 was taken 10 months after the deployment [174]. Given a little to no dust condition at the bottom of IceCube, photons emitted away from the camera should not be scattered back. However, the white area of the image suggests that there is more scattering than expected due to air bubbles introduced during deployment. In addition, the distinct border line between black and white areas hints that these air bubbles may form a column at the central core of the original hole with a radius of ~ 50 cm. This is most likely because the pressure from water refreezing starts from the wall of the hole towards the center, pushing air particles towards the central core.

Using simulation, the effect of air bubble columns is found to be decoupled from the global ice properties discussed in Section 3.2.3.2. Given a light source near the bubble column of a given string, there are two possible effects on the DOMs along the string. First, with the presence of air bubbles, less photons reach the DOMs on the side facing the source compared to the absence of air bubbles, whereas more photons arrive at the DOMs away from the source. Second, if the light source is inside the bubble column, more photons are received by the DOMs on the same string. Both effects are much smaller on the DOMs of a neighboring string. Hence, one can treat the effects due to ice properties and that due to bubble

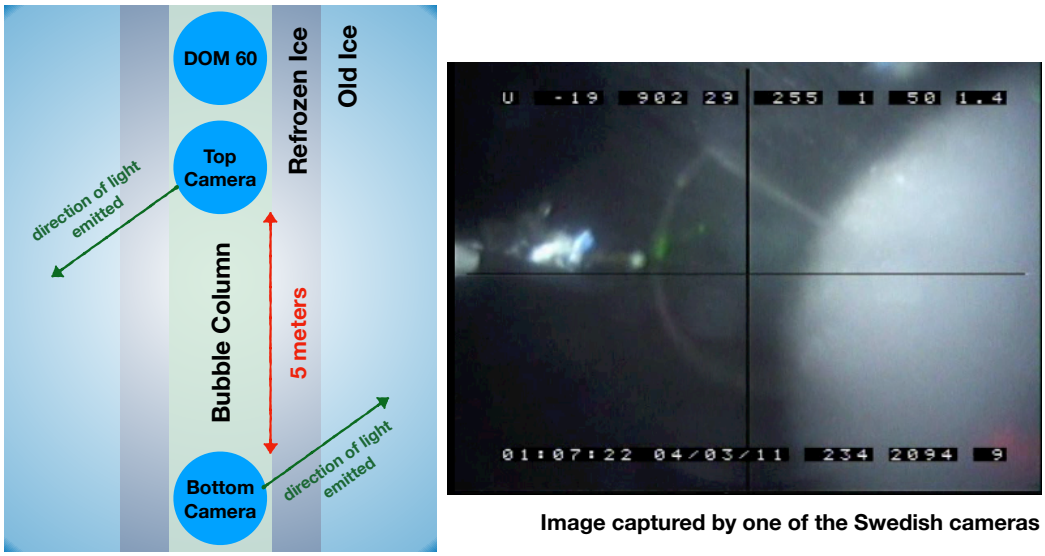

Figure 3.19: Evidence of Air Bubbles in Ice: (left) a schematic diagram showing how bubble columns can be formed and (right) an image captured by one of the deployed cameras. A pair of cameras is deployed at the bottom of String 80 in December 2010. The white area of the image comes from scatted photons within the bubble column, while the black area is believed to have less air bubbles. Image is taken from [174].

column independently.

With the above scattering characteristics due to bubble columns, angular acceptance curves are introduced to simulation software based on which photons arriving at a DOM are distributed. Given N photons arriving at a DOM from cos η defined on the left plot of Figure 3.20, the angular acceptance at cos η is defined to be the ratio of the number of photons actually accepted by the DOM from that direction to N. The right plot in Figure 3.20 shows the angular acceptance curve assuming a bubble column with a radius of 50 cm [174]. However, the 50 cm bubble column model does not fit to the data well. A new unfolding approach is then developed to fit a polynomial function for the angular acceptance curves over many iterations to best match data [175]. Figure 3.21 shows the latest bubble column

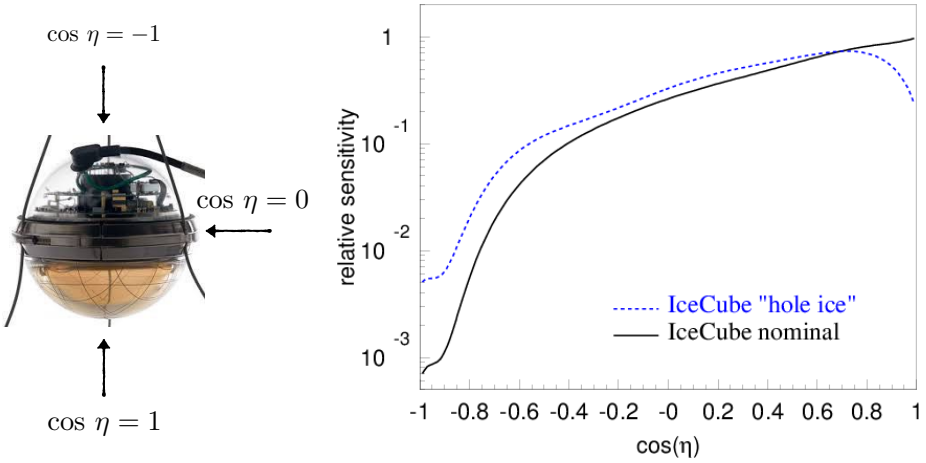

Figure 3.20: Angular Acceptance Curve assuming a bubble column with a radius of 50 cm: (left) orientation of coordinates and (right) angular acceptance assuming a bubble column with a radius of 50 cm. cos η is defined to be the angle between a DOM and an incoming photon. Black and blue curves are the acceptance curves when the air bubble columns have radii of 0 and 50 cm respectively. The plot is taken from [174]. Due to the presence of air bubble, some photons from head on direction are scattered away; hence, less head on photons are accepted compared to no air bubbles.

model. Along with the coefficients of the fitted polynomial, two parameters are actually physics related. They are the hole ice parameter p, which can adjust the overall shape of the acceptance curve (solid lines in Figure 3.21), and the forward parameter $p2$, which controls the acceptance of normally incident photons (dashed lines in Figure 3.21).

3.2.3.2 General Properties

Over the past 20 years, numerous studies have been performed to study the absorption and scattering parameters of the South Pole glacial ice [169–173,176–181]. In particular, [180] explains in detail how absorption and scattering coefficients are

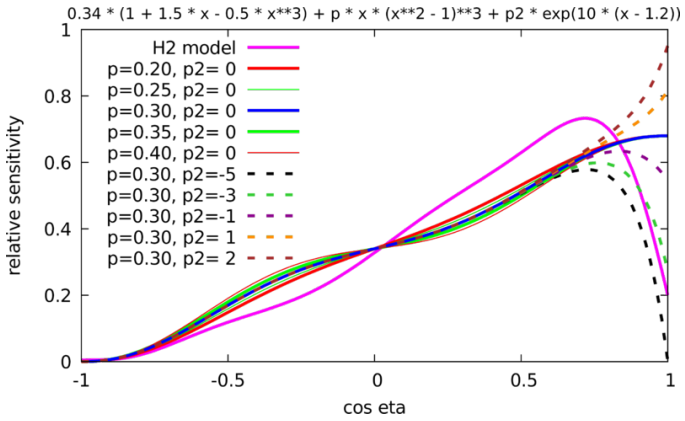

Figure 3.21: Angular Acceptance of Different Coefficients. When fitting to data, two coefficients are allowed to vary: the hole ice parameter, p, and the forward parameters, $p2$. Solid magenta line represents the change in acceptance with different values of p, while dashed lines represent the acceptance curves by varying $p2$.

measured, based on which [178] provides currently the best ice models for IceCube analyses.

First described mathematically by Mie in 1908 [176], a scattering in ice of a photon at a certain frequency from Cherenkov radiation is not isotropic. After n scatterings, averaged scattering angle $\langle \cos\theta \rangle_n$ is non-zero. According to Kirk [182], this $\langle \cos\theta \rangle_n$ is equivalent to the averaged scattering angle for one single scatter multiplied n times; that is, $\langle \cos\theta \rangle_n = \langle \cos\theta \rangle^n$. Due to the anisotropy, the effective scattering length λ_e is not the same as the scattering mean free path λ_s. At the i^{th} successive step of length λ_s, its effective length is weighted by $\langle \cos\theta \rangle^i$. Therefore, after n scattering, the total effective scattering length becomes

$$\lambda_e = \lambda_s \sum_{i=0}^{n} \langle \cos\theta \rangle^i, \tag{3.53}$$

which converges to

$$\lambda_e = \frac{\lambda_s}{1 - \langle \cos\theta \rangle} \tag{3.54}$$

for a very large n. Thus, the scattering coefficient b_e for a specific photon wavelength is defined as

$$b_e = \frac{1}{\lambda_e}. \tag{3.55}$$

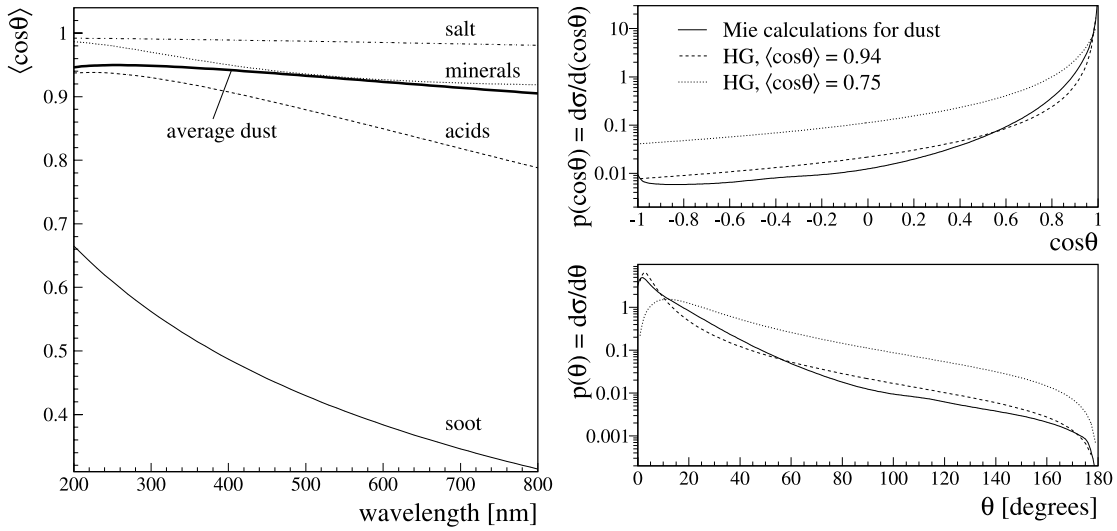

Figure 3.22: Predictions of scattering properties in the ice: (left) averaged scattering angle as a function of wavelength and (right) predictions of scattering probability density function. On the left, calculations based on Mie theory [183] predicts an averaged $\langle \cos\theta \rangle$ of 0.94. Right plots show the predicted scattering probability density function from Mie theory, which can be approximated by the Henyey-Greenstein (HG) function with just one parameter. Both plots are taken from [180].

To obtain more realistic predictions on the wavelength dependent effective scattering coefficient and the averaged scattering angle $\langle \cos\theta \rangle$, [180] performs numerical calculations based on Mie theory in [183]. As shown on the left plot of Figure 3.22, assuming four different dust components in the ice, the effective scattering coefficients for light between 300 and 600 nm can be described by a power law with an exponent α; $b_e(\lambda) \propto \lambda^{-\alpha}$, where λ is now the photon wavelength. Therefore,

$b_e(\lambda)$ can be expressed as

$$b_e(\lambda) = b_e(400) \left(\frac{\lambda}{400}\right)^{-\alpha}, \tag{3.56}$$

where one would only need to figure out b_e at 400 nm. Since $b_e(\lambda)$ only weakly depends on wavelength, an averaged $\langle \cos\theta \rangle$ of 0.94 is used for generating a scattering probability density function (PDF) as shown on the right of Figure 3.22. While Mie theory [183] provides a prediction for the scattering PDF, Mie calculation is approximated in [180] using the Henyey-Greensten (HG) function [184], which conveniently describes all possible scatterings via one single variable $\langle \cos\theta \rangle$.

On the other hand, wavelength dependent absorption coefficients $a(\lambda)$ are described by the absorption lengths λ_a's. A λ_a is defined to be the distance at which the survival probability of photons of a particular wavelength drops to $1/e$. In [180], Mie calculation [183] shows that absorption coefficients due to dust depend on photon wavelengths via a power law, similar to the case in scattering coefficients. In addition to dust, absorption also have an exponential contribution from the pure ice [170], which depends mildly on the ice temperature and, thus, depth [171]. Therefore, the total absorption coefficient can be written as [180]

$$a(\lambda) = a_{\text{dust}}(400) \left(\frac{\lambda}{400}\right)^{-\kappa} + Ae^{-B/\lambda}, \tag{3.57}$$

where the second term is the absorption due to the intrinsic ice, and the first term is the absorption due to dust with κ being the exponent of the power law dependence, similar to the α in the case of scattering.

With the above set up, an early ice study was performed using data from AMANDA [170]. A fit is performed for an individual pair of emitter and receiver by letting all coefficients and the exponents float. The resultant ice model is described by two tables of parameters, $b_e(400)$ and $a_{\text{dust}}(400)$, as a function of photon wavelength and depth. The absorption and scattering maps are shown in Figure 3.23.

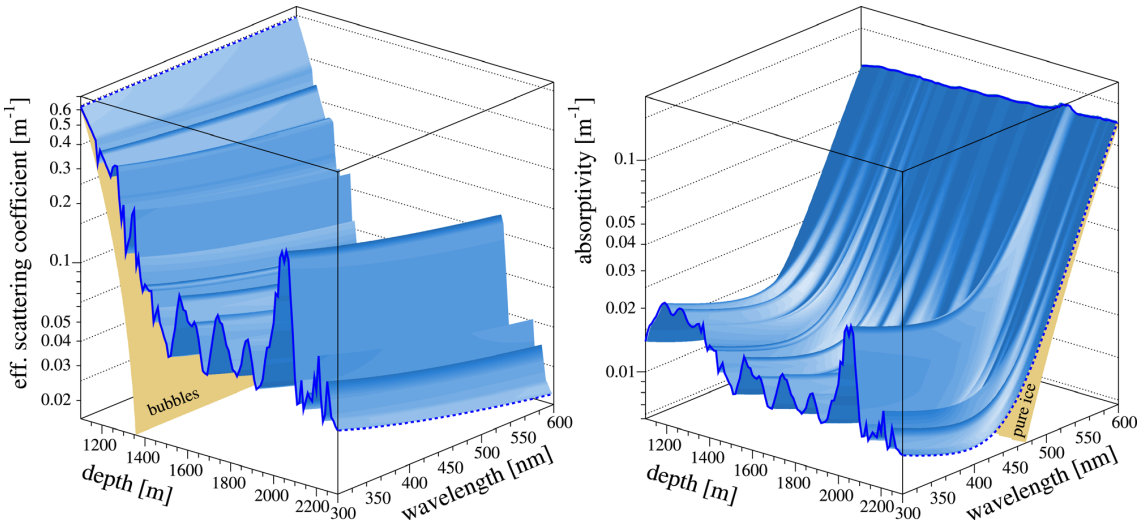

Figure 3.23: An ice model from AMANDA data: (left) effective scattering coefficients as a function of ice depth and photon wavelength and (right) absorption coefficients as a function of ice depth and photon wavelength. The blue dashed lines at depth of 2300 m show the power law wavelength dependence for scattering coefficient and a sum of power law and exponential wavelength dependence for absorption coefficient. The four peaks between 1500 and 2200 m correspond to stadials in the last glacial period 65,000 years ago.This plot is taken from [180].

In the scattering plot, the blue dashed line at a depth of 2300 m shows the power law wavelength dependence. Similarly, the blue dashed line at the same depth in the absorption coefficient plot shows a combination of power law and exponential wavelength dependence due to dust and intrinsic ice. While the large scattering coefficients above 1300 m are likely due to air bubbles, the four peaks between 1500 and 2200 m in both maps are caused by the last glacial period about 65,000 years ago. These two maps are stored into two coefficient tables.

An updated ice study [178] with flasher data from one of the IceCube string is performed. Each of the 60 DOMs has a flasher board, which consists of six

horizontal and six tilted LEDs; each LED can emit pulses of photons at 405 nm. During flasher runs, each DOM on String 63 flashes in a sequence; in each sequence, all six horizontal LEDs are turned on simultaneously at the same settings. Photons emitted by the LEDs then propagate through the ice and are detected after some time by neighboring DOM receivers, which record the charges collected and photon arrival times.

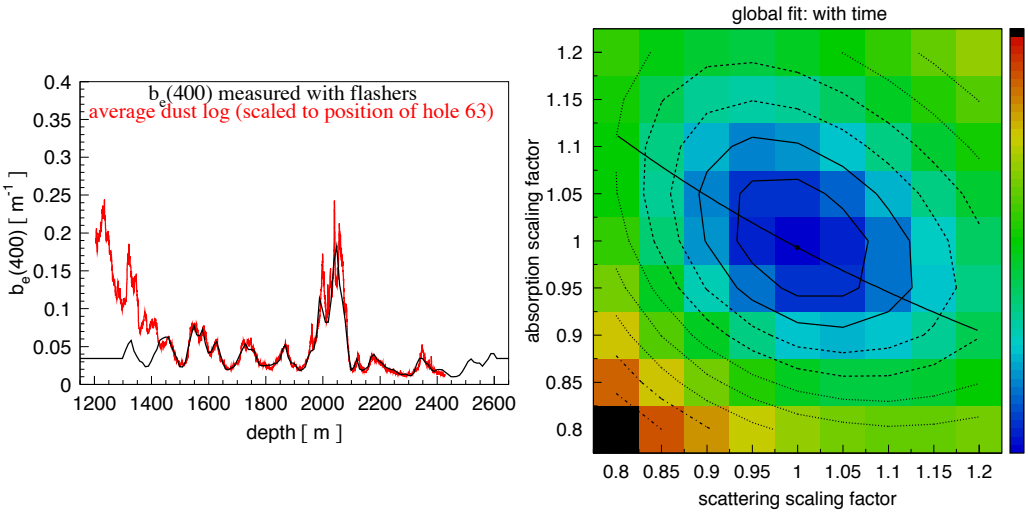

Figure 3.24: Updated ice mode: (left) agreement between results and data from dust logger and (right) likelihood scan in the space of absorption and scattering factor. Both plots are copied from [178]. Left plot shows that the black curve from the updated ice model agrees with the red curve obtained from dust logger. The right plot is the χ^2 scan with respect to the absorption and scattering scaling coefficient factors. Color axis represents log likelihood when fitting to flasher data and ranges from 1.05×10^5 to 4.01×10^5. The smallest contour around the dark blue region is the 1σ C.L.

With IceCube flasher data, the recent ice study [178] presents a direct fit approach to obtain a scattering and an absorption coefficients for every 10 m depth interval. Improvements are added to the updated ice study: modifications are added

to better approximate the PDF of $\langle \cos\theta \rangle$; a depth and temperature dependent correction term according to [181] is applied to the pure ice contribution in the absorption modeling (the second term in Equation 3.57); local properties due to air bubble columns discussed in Section 3.2.3.1 are taken into account. For every depth interval, a global fit is performed in two steps. First, a rough best fit values are found for $b_e(400)$ and $a_{\text{dust}}(400)$. To save computational time, coefficient tables from previous study [180] are used, and both $b_e(400)$ and $a_{\text{dust}}(400)$ are scaled by the same relative amount during the first minimization. With the rough best fit values, the second step involves another minimizer to fit five parameters to the flasher data. These parameters include photon yield from a flasher board, overall offset time from flasher start time, a shape parameter related to the scattering PDF, and two scaling factors α_{sca} and α_{abs} with respect to the coefficient tables from [180]. Therefore, the best fit absorption and scattering coefficients for a certain depth interval are given in terms of the absorption and scattering coefficients tables.

Figure 3.24 shows the results of the updated ice study. Good agreement between best fit scattering coefficients and data from dust logger [185] between 1500 and 2400 m supports the validity of this updated ice model. Air bubbles above 1400 m are not taken into account because IceCube DOMs are deployed below 1450 m. The χ^2 scan in the space of absorption and scattering scaling factors is presented on the right of Figure 3.24. The resultant best fit absorption and scattering scaling factors are stored in two separate tables and are used for both simulation and reconstruction for the majority of IceCube analyses.

Chapter 4: The IceCube Neutrino Observatory with DeepCore

The IceCube Neutrino Observatory is a cubic kilometer neutrino detector, which consists of an array of optical sensor, called Digital Optical Modules (DOMs), deep under the glacial ice at the Amundsen-Scott South Pole Station. DeepCore, a subset of IceCube with a denser configuration of DOMs with higher efficiency, is embedded at the very bottom near bedrock, where ice is expected to be exceptionally clear. After seven consecutive austral summers, the construction of IceCube-DeepCore was completed in December 2010 after the deployment of DeepCore strings. During the deployment of each string, a 2450 m-deep and 60 cm-wide borehole was drilled using a hot water drill [186–188][1]. A string with 60 DOMs was gradually and carefully lowered down before water refroze.

Figure 4.1 shows the vertical scale of IceCube. Between 1450 and 2450 m below the ice surface, a total of 5160 DOMs on 86 vertical strings, each of which has 60 DOMs, is deployed in a hexagonal array. With an inter string distance of 125 m, 79 out of 86 strings are the IceCube strings, on which DOMs are 17 m apart. Such sparse spacings between DOMs and strings allows detection of neutrinos between $\mathcal{O}$(TeV) and $\mathcal{O}$(PeV), such as the event observed in 2015 (see the left of Figure 4.2 [190]).

As a subset of in-ice DOMs, the remaining eight strings constitute the Deep-

[1]I cannot express my appreciation to the drillers through words. The extreme weather makes everything more difficult and time consuming. The fact that IceCube-DeepCore is successfully and safely built within 7 years involves hard work by smart physicists, engineers, and helpers.

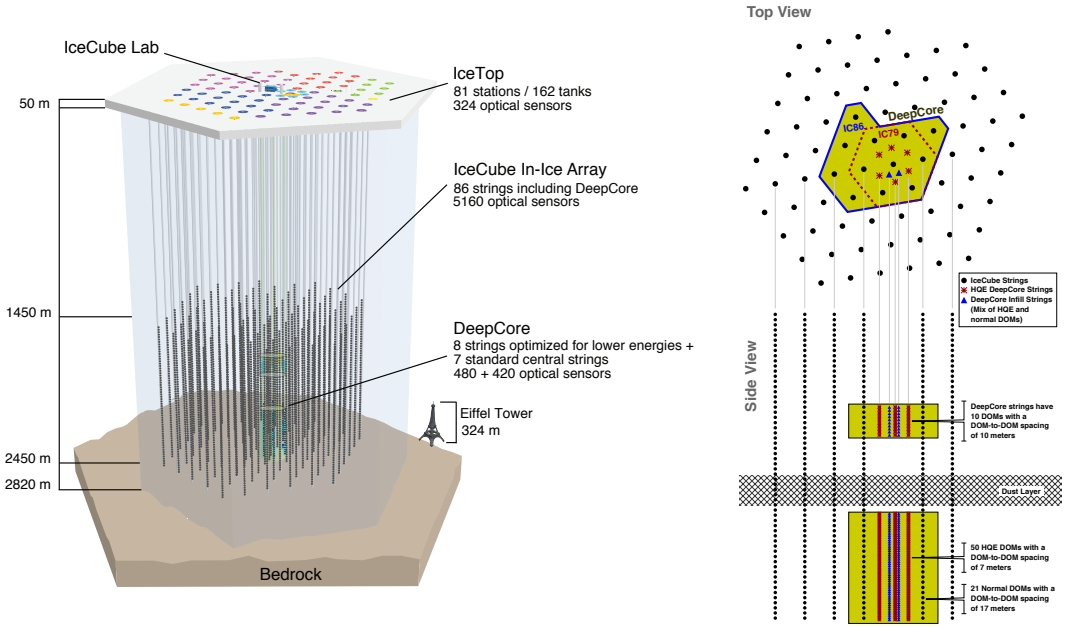

Figure 4.1: The IceCube Neutrino Observatory: (left) vertical scale of IceCube and (right) schematic layout of DeepCore with IceCube. Left and right figures are taken from [188] and [189] respectively.

Core detector. Shown as the shaded areas on the right side of Figure 4.1, the DeepCore volume is divided into two sections. The top part above the dust layer between 2000 and 2100 m consists of 10 DOMs, each of which is 10 m apart, per DeepCore string. The bottom part below the dust layer consists of 50 high quantum efficiency (HQE) DOMs per string with a DOM-to-DOM distance of 7 m. Such a dense spacing among DOMs, together with the nearby IceCube strings, pushes the energy threshold down to $\sim$ 10 GeV, allowing detection of dark matter, searches beyond the Standard Model, and studies of atmospheric neutrino oscillations. At $\sim$ 25 GeV, where the amplitude of atmospheric neutrino oscillations is expected to be maximal, the event display is presented on the right of Figure 4.2. Compared to the glorious PeV event on the left, not only do low energy events look less interesting, but their reconstructions can also be more challenging with information from fewer

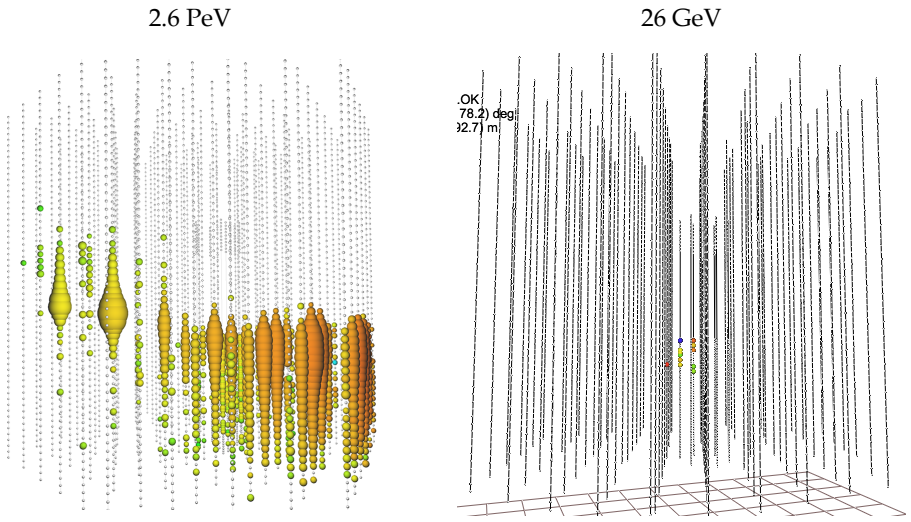

Figure 4.2: A PeV high energy and a GeV low energy events detected by IceCube: (left) a 2.6 PeV event observed in 2015 [190] and (right) a 26 GeV event observed in 2012.

DOMs.

Besides its configuration, DeepCore is also at an ideal location for low energy studies. First, ice below 2100 m is exceptionally clear. Below the dust layer, the average effective scattering length and absorption length are estimated to be ~ 50 and ~ 190 m respectively at a photon wavelength ~ 400 nm, which means DeepCore ice is $\sim 45\%$ clearer than the ice between 1500 and 2000 m [189]. Moreover, embedded inside IceCube, DeepCore is thickly shielded by the rest of the IceCube volume, which acts as a highly efficient veto for better identifying down going atmospheric background events. Lastly, with 30 megatons of ice inside the main DeepCore volume, IceCube-DeepCore can collect data with high statistics compared to other atmospheric neutrino oscillation experiments given the same detector exposure.

As mentioned above, the IceCube-DeepCore detector consists of strings of DOMs, each of which detects Cherenkov photons deep in the ice induced by relativistic charged particles. The structure of an individual DOM and its signal digitization

are discussed in Section 4.1. In general, every two neighboring DOMs on a string are connected by twisted copper wire pairs, which supply power and communication to the DOM. All twisted pairs then form a wire bundle that runs to the IceCube Laboratory (ICL) at the surface in the center of the IceCube array, where power supplies, communications, and data are centralized. Section 4.2 then discusses the calibration tasks performed regularly. In particular, since each DOM independently processes signals detected locally, a standard time base for all DOMs is critical for accurate reconstructions. The timing calibration calibrates all DOM 20 MHz clocks to a reference IceCube Time (ICT) defined by the GPS-disciplined rubidium clock in the ICL. To provide accurate reconstructions of events, a time resolution within an order of nanosecond is required. Finally, global data acquisition and quick processing and filtering, explained in Section 4.3, are performed to immediately identify potentially interesting events.

4.1 Digital Optical Modules

Being the fundamental unit of IceCube-DeepCore, a digital optical module (DOM) is an optical sensor with a mounted photomultiplier tube to detect photons. Section 4.1.1 discusses the different components of an individual DOM. While some parts of a DOM are dedicated to calibration tasks, the main purpose of a DOM is to analyze the PMT waveform, from which the number of photons detected and their arrival time are obtained. This procedure is discussed in Section 4.1.2.

4.1.1 Structure of a Digital Optical Module

Designed to deal with high pressure environment due to water-refreezing, a 33 cm-wide glass sphere protects the DOM from a continuous pressure of 25 MPa and from a short term pressure up to 68 MPa. The structure inside the glass sphere is

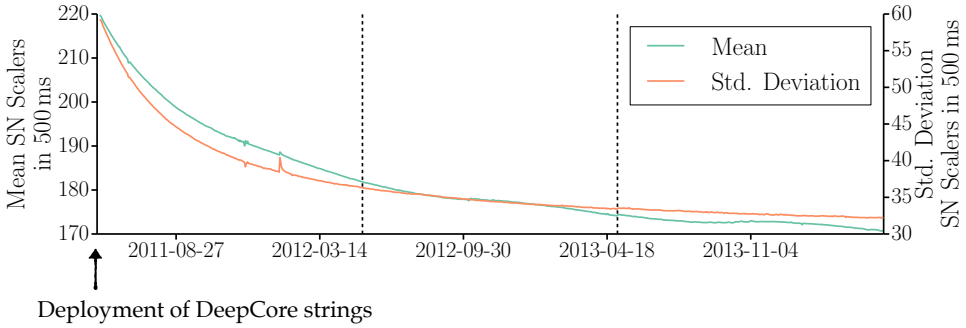

Figure 4.3: Noise rate from strings deployed in the last deployment season. Left axis represents the mean noise scaler rate, which is the summed dark noise rate from the selected strings; right axis shows the standard deviations of the rates. An obvious exponential decay in noise rate suggests that the newly deployed DOMs are quite noisy. Plot is taken from [188].

illustrated on the left of Figure 4.4. The top hemisphere of a DOM consists of electronic boards that performs data acquisition, control, calibration, communication, and low-voltage power conversion. Mounted below the electronic boards, the half spherical PMT is responsible to detect photons arriving at the bottom hemisphere of the DOM.

The outer glass sphere is made of glass with very little radioactive trace elements to reduce dark noise to $\sim$ 300 Hz at a temperature range between -40°C and -20°C [191]. However, a contribution from detector dark noise is still found from the HQE DOMs in DeepCore strings deployed during the last deployment season in 2011. As shown in Figure 4.3 [188], the mean noise rate, which is the summed dark noise rate from the selected strings, experiences an exponential decay since their deployment. Thermal emission from PMTs and radioactive decays from limited radioactive material in the glass are found to be the sources of dark noise. As the system reaches equilibrium, the dark noise rate reduces by $\sim$ 25% over the course of three years [188]. To avoid disagreements between data and MC due to dark

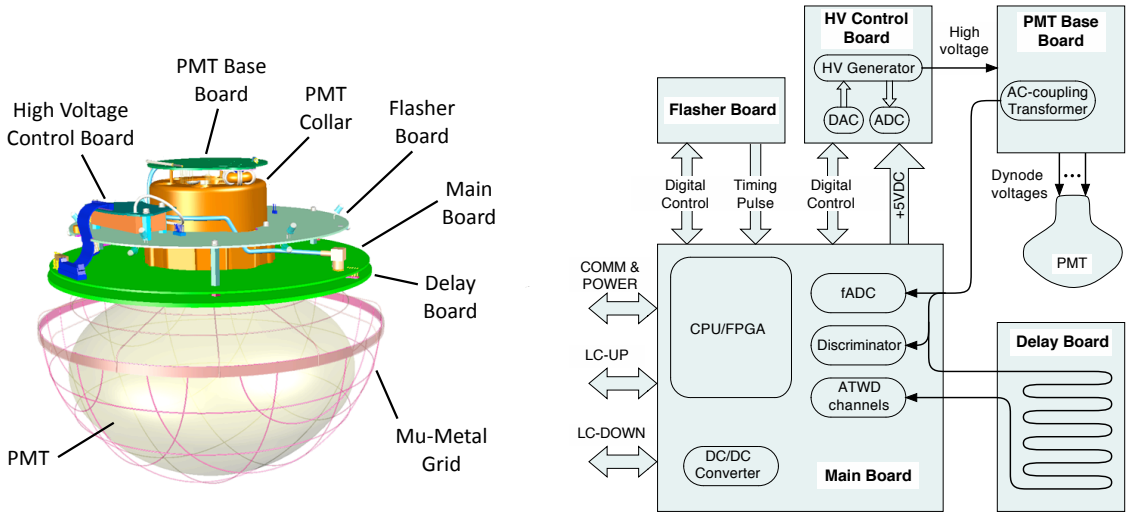

Figure 4.4: A Digital Optical Module: (left) the mechanical structure and components of a DOM and (right) a schematic diagram of the circuit board. Figures are taken from [188].

noise, this analysis excludes IC86-I data taken during the first year after the last deployment. Since noise hits do not show space-time correlations, noise triggered events are usually rejected at final level in most analyses. The event selection process in this analysis, discussed in Chapter 6, shows that, while the contribution from noise-triggered events is non negligible at lower selection levels, noise contamination in the final sample is less than 0.2%.

To capture photons from relativistic charged particles, the PMT is one of the most important ingredients in a DOM. Two types of PMTs are instrumented; every DOM on all IceCube strings contains a standard 25.4 cm-wide Hamamatsu R7081-02 PMT, whereas PMTs in DeepCore DOMs are the high quantum efficiency (HQE) Hamamatsu R7081-02MOD [191]. Both PMT versions are sensitive to photons with wavelengths ranging from 300 to 650 nm but at different optical efficiency. At a photon wavelength of 405 nm and a temperature of -45°, a HQE and a standard PMTs have quantum efficiencies of 29% and 21% respectively [189], implying a

better performance from DeepCore DOMs than IceCube DOMs by 1.39. For both DeepCore and IceCube DOMs, the half spherical PMT, with its bulb faces downwards (see Figure 4.4), is surrounded by a mu-metal cage to reduce the effect from the geomagnetic field at the South Pole. Each PMT is also safely secured onto the bottom glass hemisphere using a high-strength optically matched silicone gel, which is tested to have minimum light reflection and long time reliability at -45°C [188].

Power is supplied to the PMT via the PMT high voltage subsystem, which consists of a high voltage (HV) Control Board (top middle of the right plot in Figure 4.4) and a PMT Base Board. The Control Board consists of a HV generator, an analog-to-digital converter (ADC), and a digital-to-analog converter (DAC). DAC and ADC sets and reads out the PMT high voltage respectively, whereas the HV generator provides a maximum high voltage supply of $\sim$ 2000 V and a power supply of less than 300 mW [191]. The PMT Base Board divides input voltages to ten dynodes. With the PMT cathode set at ground potential, a special toroidal transformer is used to AC couple the front-end amplifier and the high voltage anode due to cascades of accelerated electrons [191]. A voltage of $\sim$ 1300 V between the photocathode and the last anode leads to a nominal gain of 10^7 and, thus, a single photon pulse at $\sim$ 8 mV [188]. The PMT Base Board then transmits the signal to the Main Board.

The Main Board is the brain of the DOM. Not only does it control all devices inside the DOM, it also checks if the PMT signal reaches 0.25 times the typical single photoelectron (SPE) peak amplitude; if so, the Main Board digitizes the PMT waveforms. As discussed in Section 4.1.2, the Main Board also includes a delay board, which allows time for the Main Board to make a decision whether a signal is digitized and stored for transmission to the data acquisition (DAQ) system in ICL. The Main Board also exchanges local coincident (LC) information with nearby DOM. When asked by central system on the surface, the Main Board also

performs calibration tasks for the internal DOM clock and PMT gain and timing. Section 4.2 focuses on calibration in IceCube.

Finally, every DOM has a Flasher Board, most of which have six evenly spaced pairs of LEDs. One LED from each pair can emit light at 405 nm horizontally into the ice, while the other can emit photons of the same wavelength at 48° above the horizon [188]. In addition to standard LEDs, eight DOMs on String 79 and eight DOMs on String 14 have LEDs with multiple wavelengths. For ice studies and calibration purposes, flasher runs are performed, and LEDs from a DOM are turned on. LEDs from one DOM can generate 10^6 to 10^{11} photons, which is equivalent to a deposited energy range from 7 GeV to 1 PeV [188]. These LEDs are crucial to study absorption and scattering properties of the ice.

4.1.2 Waveform Digitization

Controlled by a Field Programmable Gate Array (FPGA) on the Main Board, waveform digitization refers to extracting charge and time information from the amplified PMT waveforms and storing the data. In general, a PMT waveform, if passing the 0.25 PE threshold, is digitized by two different systems. First, a Fast Analog-to-Digital converter (FADC) continuously samples the waveform at 10-bit 40 Msps for 6.4 μs [188] with a 25 ns sampling period [192]. Such low time resolution but long exposure sampling captures longer signals with lower amplitudes and longer photon traveling time. The second system, called an Analog Transient Waveform Digitizer (ATWD), provides a more detailed time sampling. An ATWD has four gain channels, each of which has a 128 sampling capacitors [188] with a typical 3.3 ns sampling period [192]. Prior to arriving at an ATWD chip, the PMT waveform is amplified at three different gains: $\times 16$, $\times 2$, $\times 0.25$. The ATWD chip then first attempts to digitize the waveform amplified by $\times 16$ and stores information in one

of the channels; if it gets saturated ($\sim$ 7.5 mV), the ATWD chip then works on the waveform amplified by $\times$2; if the second channel is saturated, the ATWD digitizes the $\times$0.25 waveform. The last channel of each ATWD chip is used for calibration. The total recording time for an ATWD chip is 427 ns. Because an ATWD chip cannot record any signals during waveform digitization, two ATWD chips are used in a ping-pong configuration to minimize DOM dead-time.

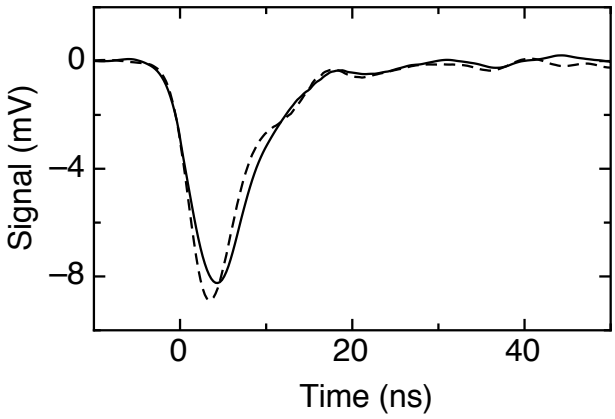

Figure 4.5: An average of 10,000 SPE waveform from the PMT waveform. The solid and dashed lines are measurements in laboratory from PMTs with new and old transformer designs; the new design was the one deployed. Tests performed in laboratory shows that DOMs behave pretty much the same, thus one template can be generalized for all DOMs [191]. Figure is taken from [191].

The two most important pieces of information to be extracted from a PMT waveform are the number of photons arrived and their arrival times, based on which the energy and direction of an event are reconstructed. To get these two pieces of information, tests are performed on a sample of DOMs in laboratories to understand DOM responses due to a single photoelectron (SPE). The charge and arrival time distributions are then used as templates for extracting number of photons and their arrival times in waveform digitization during data taking.

Studies in laboratories have found that all sampled PMTs return a pretty

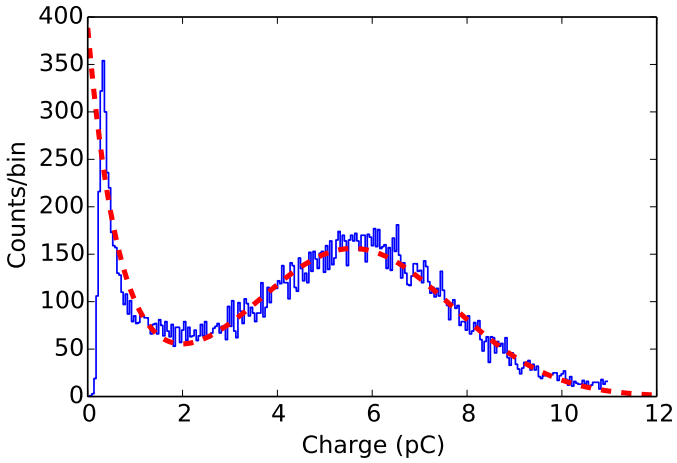

Figure 4.6: A charge distribution due to one single photoelectron. Charge measurements due to one photoelectron are performed on a sample of DOMs. The charge distribution is fitted to a combined exponential and Gaussian function to estimate its shape (red dashed line). The normalized PDF is then used as a SPE template for reconstructions and calibrations in cases of multiple photons. Figure is taken from [188].

consistent Gaussian shape in single photoelectron (SPE) waveform with width of 3.2 ns [191]. The solid line in Figure 4.5 [191] is an averaged waveform from 10,000 PMTs. The measured charge distribution from a sample of test DOMs is shown in Figure 4.6. In general, the peak of the Gaussian component determines the amplification of the PMT with an averaged charge resolution of $\sim$ 30% [188, 191]. The first narrow peak is due to the backscattering of primary photoelectrons at the PMT's first dynode [193], resulting in low charge pulses from fewer secondaries. For data collected before 2015, the shape of the charge distribution is fitted to a combination of an exponential and a Gaussian functions [194]; after 2015, an extra exponential decay term is added to the fitted function [195]. The normalized fitted function is, therefore, the charge probability density function (PDF) which is used as a SPE template [191,194]. Similarly, the arrival time distribution shown in Figure 4.7 [196]. The width of the first peak is $\sim$ 2 ns, followed by some delayed hits. These

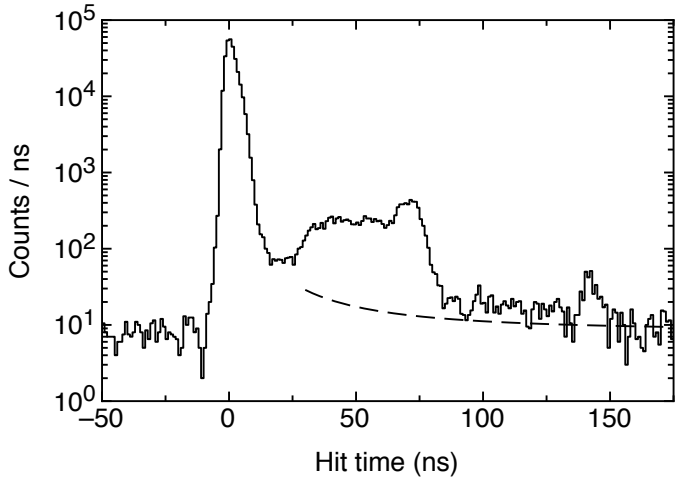

Figure 4.7: A arrival time distribution due to one single photoelectron. Time measurements due to one photoelectron are performed on a sample of DOMs; the width of a time bin is 1 ns. The arrival time distribution has a peak $\sim$ 2 ns after the laser turns on, followed by some after pulses. The dashed line following the falling of the first peak corresponds to contributions from random backgrounds. Later pulses, excess above the dashed line, is due to scattering of secondary electrons back to the photocathode, initiating another pulse. The normalized PDF is then used as a template for reconstructions and calibrations in cases of multiple photons. Figure is taken from [196].

later pulses potentially come from scattering of few electrons from the first dynode back to the photocathode, which may initiate another pulse [193, 196].

Although the PMT response from a single PE is well studied, many photons can arrive at a PMT at the same time, triggering many cascades of accelerated electrons. Therefore, waveform digitization on IceCube raw data uses the above time and charge templates to analytically fit the number of photons arrived and their arrival times. The Main Board first assumes that the PMT waveform is caused by one photoelectron, fits one time and charge template to the digitized waveform, and calculates the χ^2. Next, two photoelectrons are assumed and their time and charge templates are added accordingly, and the analytical fit is repeated. This

process is re-iterated until the χ^2 no longer improves for the last few iterations.

As a summary, once a PMT waveform is sent to the Main Board, it is split into two paths. One is passed to a discriminator to check if the PMT signal exceeds 0.25 PE, and the other is passed to the delay board, which delays the signal for 75 ns [196] while waiting for the decision from the discriminator. If the signal does pass the threshold, the PMT waveform is passed to the FPGA, while the Main Board asks if its nearby DOMs receive any triggered signals. If one of the four neighboring DOMs on the same string records a triggered signal within 1 μs, a condition known as a hard local coincidence (HLC), then ATWD digitizes the PMT waveform, and the outputs from all triggered DOMs are sent to the centralized computers at ICL. If HLC is not met, digitized waveforms from FADC are sent to the surface instead. Each of these digitized waveforms, with DOM locations, charge, and time information, is then called a DOM hit; a series of these pulses within a certain time window is called a pulse series.

4.2 Calibration

Pulse series with their charges and their arrival times from hit DOMs are the basis of all IceCube analyses. To ensure recorded data are accurate and precise, calibrations have to be performed regularly. Other than the few calibration tasks briefly summarized in this section, calibrations on the optical properties in ice have long been a major concern, and a summary of studies is presented in Section 3.2.3.

First, waveform digitization, providing the most crucial information for every energy reconstruction algorithm, is calibrated DOM-by-DOM once every year. Every DOM Main Board has a variable-voltage electronic pulser controlled by a software called DOMCal. The Main Board first finds the smallest voltage that barely triggers the discriminator. This voltage is then used to map from the input volt-

age to the output voltage for each of the four 128 sampling capacitors on a ATWD chip [188]. The gain of each ATWD channel can also be measured precisely to determine any biases from the corresponding $\times 16$, $\times 2$, or $\times 0.25$ nominal amplification. Lastly, with a known photon arrival time from the internal light pulser, the sampling offset time due to the PMT transit time is also corrected.

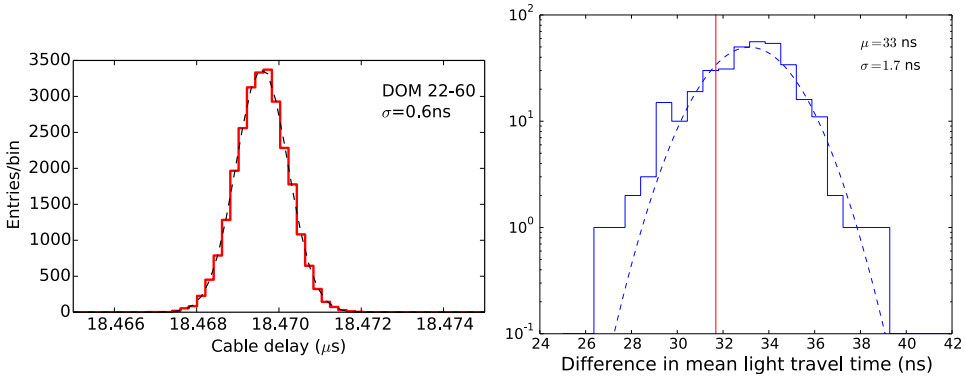

Figure 4.8: RAPCal measurements and performance: (left) a distribution of delay time from one DOM and (right) a distribution of the difference between measured and expected photon arrival time. On the left, multiple RAPCal measurements are done on one of the deployed DOMs with eight hours of data. Red line represents the distribution of delay time, and black dashed line represents the Gaussian fit with a time resolution of 0.6 ns. On the right is a distribution, from flasher data, of the difference between expected and recorded arrival time of the first photon at a DeepCore DOM above a flashing DeepCore DOM. Given a 7 meter vertical spacing, the expected arrival time is the red vertical line, which is slightly different from the mean value of the distribution by 1 ns due to optical properties of the ice. Both figures are taken from [188].

Second, because every DOM is a data acquisition unit, timestamps recorded by all 5160 DOMs must have a standard time base within $\mathcal{O}$(ns) accuracy. This timing calibration is done through the continuously-running Reciprocal Active Pulsing calibration (RAPcal) procedure [197]. When there is no data transmission between a DOM and the ICL, a bipolar 5 ns pulse is transmitted from the ICL to the DOM. When the DOM receives the bipolar pulse, it measures the digitized waveform using

its local clock and, after a fixed time delay δ, transmits back to the ICL both the measured waveform and a reciprocated pulse. This process is repeated once every second [188]. For each round trip, four timestamps are recorded. $T_{\text{tx}}^{\text{ICT}}$ is the time at the ICL when a bipolar pulse is transmitted; $T_{\text{rx}}^{\text{DOM}}$ is the time at the DOM when the pulse is received; $T_{\text{tx}}^{\text{DOM}}$ is the time at the DOM when the reciprocated pulse and measured waveform are sent to the ICL; and $T_{\text{rx}}^{\text{ICT}}$ is the time at the ICL when the data from the DOM is received. The midpoint of T^{ICT} is given by $(T_{\text{tx}}^{\text{ICT}} + T_{\text{rx}}^{\text{ICT}} - \delta)/2$, and a similar midpoint is defined to T^{DOM}. Then, using the midpoints of time information from every two consecutive pulses, a linear relationship is built between the master clock at the ICL and the local clock at the DOM;

$$T = \frac{1}{2}\Big[(T_{\text{rx}}^{\text{ICT}} - T_{\text{tx}}^{\text{ICT}}) - (1+\epsilon)(T_{\text{tx}}^{\text{DOM}} - T_{\text{rx}}^{\text{DOM}})\Big],$$

where ϵ is a small offset of the DOM clock [188]. Given an eight hour data-taking run, multiple RAPCal measurements are done on one of the deployed DOMs, and the delay time distribution is shown on the left of Figure 4.8 with a time resolution of 0.6 ns. This time measurement runs continuously for all DOMs. The mean values of the distributions are stored at the ICL and are applied to the data during processing and filtering (see Section 4.3.2) at the ICL. During commissioning for each string, the RAPCal procedure is verified using flasher data, in which all LEDs on each DOM along the string flash simultaneously at maximum brightness. For each of the flashing DOM, the arrival time of the first photon at the DOM above the flashing DOM is recorded. Given the bottom of a DeepCore string, where DOMs are 7 meters apart, the expected photon arrival time is 32 ns. A distribution of the difference between expected and recorded arrival time is shown on the right of Figure 4.8. With a Gaussian fit, the distribution has a mean value of 33 ns and a width of 1.7 ns. While the 1 ns difference between expected and recorded arrival

times is due to the optical properties of the ice, the nanosecond accuracy among all DOMs is achieved.

Overall optical efficiency of DOMs is also calibrated based on studies done in laboratory and *in situ*. An earlier laboratory measurement uses a pulsed 337 nm laser to shine photon beams to thirteen IceCube DOMs, one at a time, at different angles [188, 196] and measured efficiency at the center of the PMT to be $\sim 25\%$. A later study, also performed in a laboratory, improves the measurements by testing more DOMs, applying new technologies to monitor the light beam, using multiple wavelengths, and putting the test DOMs into a water tank [198]. However, these tests taken in laboratory do not truly replicate the environment deep in the ice, such as tilted DOMs, bubble columns, and thick wire bundles around DOMs which blocks light from certain angles. Therefore, an *in situ* measurement using down going minimum ionizing muons of ~ 82 GeV is performed [188, 199]. By comparing the averaged charges between data and simulations over a range of DOM efficiency, an uncertainty of 3% is derived. After taking into account other uncertainties, such as the single photoelectron (SPE) templates used to determine photon acceptance and propagation of the simulated photons, the central value of DOM efficiency is 10% higher than the baseline value [199]. This result is adapted to the simulation.

4.3 Data Acquisition

The data flow in the data acquisition system (DAQ) is shown in Figure 4.9. Digitized information from DOMs is continuously sent to the central System, which consists of 19 racks of computing and network hardware at the ICL. The DAQ at the ICL then checks for trigger conditions (see Section 4.3.1) and combines all DOM hits within a time window around the trigger to form an event. As discussed in Section 4.3.2, triggered events are then quickly processed and filtered to keep

all potentially interesting events. Events are then sent to the data warehouse in Madison, Wisconsin, for various analyses.

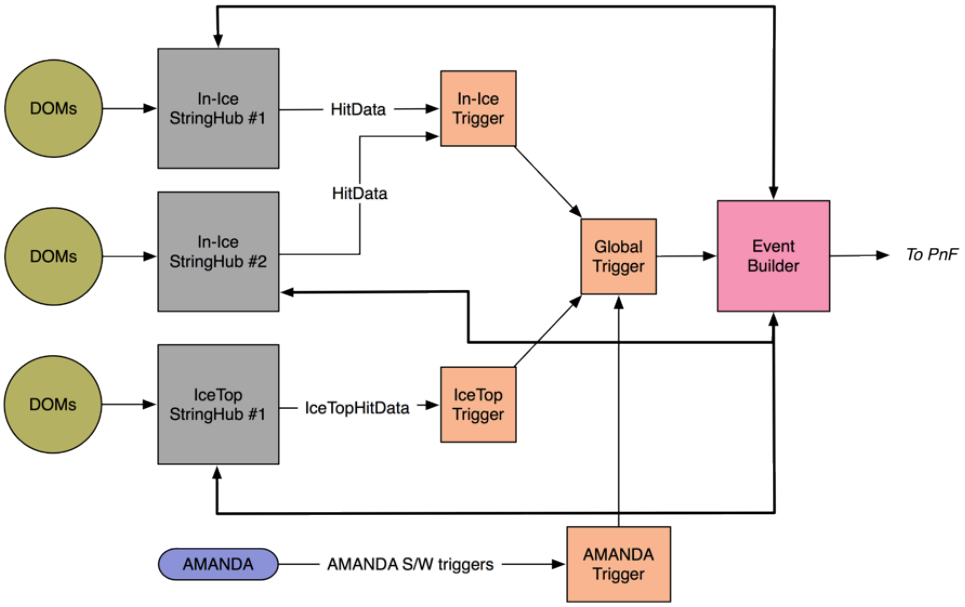

Figure 4.9: Data Acquisition in IceCube. Data from a DOM is transmitted to a DOMHub. Together with StringHubs, timing calibrations are performed. The calibrated data is then transmitted to the trigger system, which forms events if certain criteria are met. Events are then sent to the processing and filtering (PnF) system for quick analyses. This figure is taken from [200].

4.3.1 Trigger

In the ICL, several machines, known as DOMHub, are dedicated to process digitized data from all DOMs. Responsible for controlling DOMs of a single string, each DOMHub has eight DOM readout (DOR) cards to supply high voltage power, manage calibration tasks, and receive data from all 60 DOMs. Data from individual DOMHub are then transmitted to the corresponding StringHub, which is responsible for mapping hits from DOM clock units to the clock domain of the ICL, for applying timing calibration by the RAPcal procedure discussed in Section 4.2 to the DOM

data, and for arranging the DOM hits on the string in chronological order.

An *event* is triggered if DOM data satisfy certain conditions. For this analysis, a trigger condition is defined to be a simple multiplicity trigger (SMT) with at least three HLC hit DOMs in the DeepCore volume within a time window of ± 2.5 μs; this trigger condition is called SMT3. An event then includes hits detected from all IceCube DOMs 4 μs before and 6 μs after the trigger window. If other trigger conditions are met within the event time window, then two events are combined into one. This resultant event is then bundled into a data frame and is passed to the Processing and Filtering (PnF) system.

4.3.2 Processing and Filtering

At this stage, the SMT3 trigger rate is ~ 250 Hz [188], which must be reduced to a level that can be handled by the limited satellite bandwidth allocation. Thus, an online processing and filtering (PnF) system is designed. Not only does it clean the pulse series of an event, the PnF system also performs quick, simple reconstructions to apply calibrations, extract pulses, and remove noise triggered events. Based on those reconstructions, events that are not interesting are rejected.

For analyses interested in the low GeV energy range, hit cleaning is essential to identify hits by low energy neutrinos from random noise hits and hits due to obvious down going atmospheric muon background. The first step is to clean the pulse series; HLC hits are kept, and non HLC hits are removed if it does not satisfy a distance and time correlation consistent with an event. The cleaned hits, with less contributions from dark noise, are then divided into DeepCore hits and IceCube veto hits. The averages of locations and times from all DeepCore hits are calculated; if any of the veto hits satisfy a causality condition with the averaged DeepCore time and location, then this event is most likely a background muon event. This simple

cut drops the data rate to $\sim$ 20 Hz, about ten times less than the SMT3 trigger rate.

All events are grouped together as *runs*, each of which consists of data typically from eight hours of detector lifetime. All events passing the veto criteria are sent to the data centers in the North over satellites. Events passing at least one filter contain detailed information such as compressed waveforms and reconstruction, whereas only basic information is sent for events that do not satisfy any filters. Further offline processing is performed with more complex algorithms, as discussed in Section 6, to further remove noise triggered and atmospheric background events.

4.3.3 Monitoring

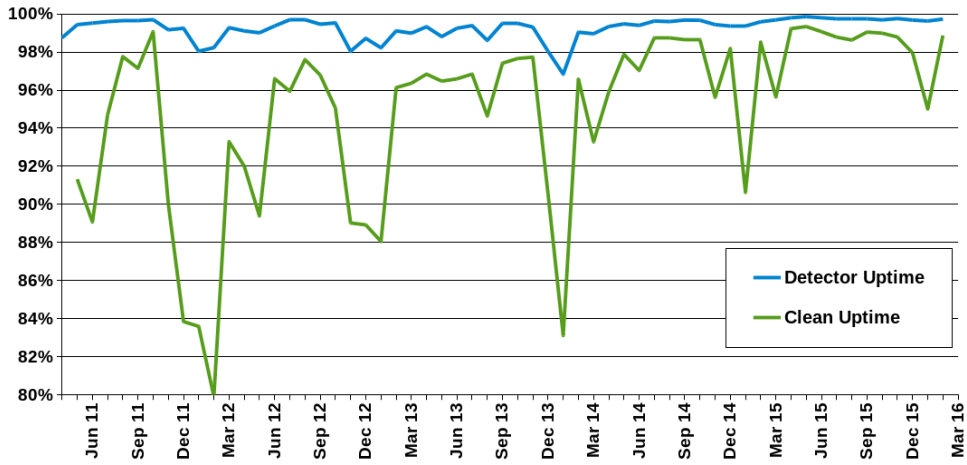

Figure 4.10: Detector Uptime from 2011 to 2016. Shown as the solid blue line, the detector uptime is the fraction of time when the detector is taking data over total time and reaches an averaged of 99% between 2011 and 2016. The clean uptime (green solid line) is the uptime for physics analyses, which often require that the full detector is operating and periods of runs longer than a certain number of hours. This figure is taken from [188].

Being thoroughly and closely monitored, the status of the detector is very

stable with an average detector uptime greater than 99% since the last deployment in 2011 (see Figure 4.10 [188]). IceCube Live is an internal database, which visibly displays detector status live through a web interface, allowing quick responses from experts whenever disruptions in trigger and filter rates are spotted. Information related to runs can also be found in IceCube Live, including run status, duration, event rate, and a launch rate map from all DOMs.

As of 2016, 87 out of 5484 ($\sim$ 1.6%) DOMs are dead due to freeze-in damage, water, cable failures, or loss of communications after power outages [188]. Moreover, 177 operating DOMs have developed issues mostly related to exchanging local coincidence with a neighboring bad DOM. Based on the currently known status, a survival fraction in 2030 is estimated to be $\sim$ 97% [188]. All dead and malfunctioning DOMs are recorded and often removed from event reconstructions in physics analyses.

Besides the down time of each individual DOM, data taking is occasionally interrupted due to various reasons, such as calibration runs, updates of software, power outage, hardware failure, and software crushes. These runs are usually shorter than the normal time period of eight hours. The clean uptime (see the green solid line in Figure 4.10 [188]) is the fraction of time period during which data is taken with full detector operating without interruption. With the upgraded back-up power supplies, which recovers the detector from a power outage to full operation within 15 minutes [188], the clean uptime had been improving since 2011. Every year, a standard list of good runs is provided to all analyzers, who can then select data for their analyses accordingly.

This analysis uses three years of IceCube-DeepCore data from IC86-II (2012) to IC86-VI (2014). DeepCore strings were deployed in December, 2010, and IC86-I (2011) data is excluded from this analysis due to high dark noise rate. A run of data taken between 2012 and 2014 is considered good if it is longer than an hour

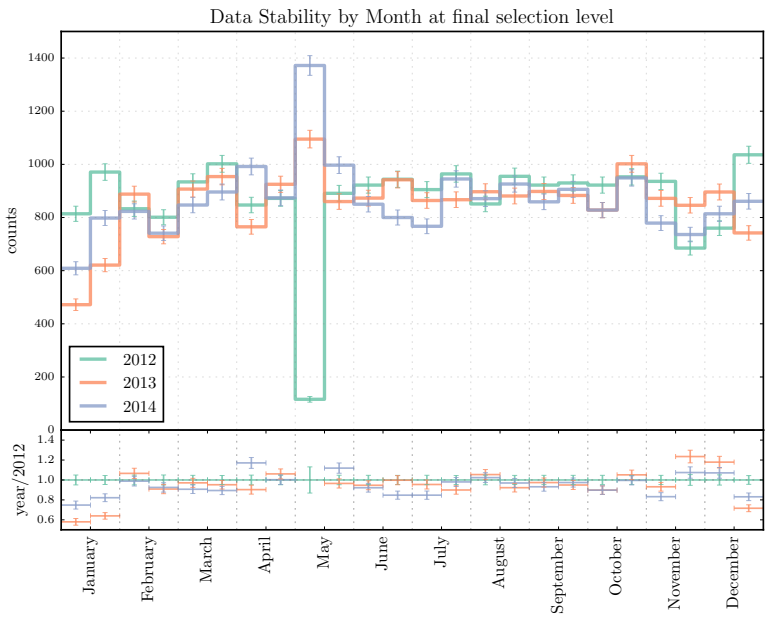

Figure 4.11: Data stability from IC86-II to IC86-VI: (top) bimonthly counts for IC86-II (2012), IC86-III (2013), and IC86-VI (2014) data and (bottom) their ratios compared to data counts from IC86-II (2012). Data taking usually starts in the beginning of May; fluctuations in data event counts in May are due to the variations of which exact day data taking starts. In December and January, upgrades are performed during the summer time at the South Pole, leading to small fluctuations in the data event counts.

with all the good DOMs functioning normally, and dead DOMs are excluded from events reconstructions. Figure 4.11 shows the data stability after the event selection process presented in Chapter 6. The fluctuation in May is because data taking of the year usually starts in the beginning of May. Fluctuations in December and January are potentially due to active upgrades during the summers at the South Pole. Because the change in the fitted function of the SPE template (see Section 4.1.2) does not matching MC, this analysis does not include data taken from 2015 and after.

Chapter 5: Simulations and Expected Rate Predictions

As a counting experiment, measuring atmospheric neutrino oscillation parameters requires accurate and precise predictions of expected number of events for all flavors, including atmospheric backgrounds. Therefore, this chapter discusses calculation of predicted rates in this analysis.

As explained in Section 5.1, neutrino rate prediction consists of neutrino generation at the detector (see Section 5.1.1), oscillation probabilities (see Section 5.1.3), and atmospheric neutrino fluxes (see Section 5.1.4). Prediction of atmospheric muon rates is explained in Section 5.2, and Section 5.3 briefly discusses simulation of noise triggered events. In addition to the absolute rates, their uncertainties are also important to the analysis. While sources of uncertainties depend on the event types, their common uncertainties are related to the detector. Thus, Section 5.4 presents a way to estimate variations in predicted rates due to properties of ice and efficiency of DOMs.

5.1 Neutrino Rates

This section discusses the method to predict neutrino rates at IceCube DeepCore. Recalled from Section 3.1, when cosmic rays interact with air particles in the Earth's atmosphere, pions and kaons are produced. As these mesons decay, muon neutrinos and electron neutrinos are produced. These atmospheric neutrinos travel through the Earth and may transform into other flavors based on their energies and

propagation distances. Neutrinos that arrive at DeepCore may interact depending on their energy and flavor dependent cross sections. For those that interact in the ice, secondary leptons are produced, emitting Cherenkov light. These photons arrive at the photomultiplier tubes of the DOMs, and an neutrino detection is triggered if at least three DOMs inside the DeepCore receive a gain of 0.25 PE within ± 2.5 μs (SMT3).

Based on the above picture, the prediction of neutrino rates consists of three main components. First is the atmospheric neutrino flux; Section 5.1.4 explains the latest atmospheric neutrino flux calculations used in this dissertation. Second is the oscillation probability, which is calculated by the Prob 3 software [201] as discussed in Section 5.1.3. The last component is related to neutrino interactions in the ice and detector responses; these are predicted using simulation and photon propagation software packages (see Section 5.1.1). While it makes sense to think of neutrino rates from production to detector responses, prediction of neutrino rates is performed in the reverse order for practical reasons, and the three components are put together as explained in Section 5.1.5.

5.1.1 Neutrino Generation in Ice

In IceCube DeepCore, neutrinos between 1 GeV and 1 TeV are generated by a software tool called the *GENIE* Neutrino Monte Carlo generator [202]. Targeted at producing neutrinos between MeV and PeV energy range, *GENIE* is a commonly used neutrino generator for the experimental neutrino physics community. This common package is adapted into the standard IceCube simulation software for analyses studying GeV neutrinos.

For each simulated neutrino event, a quantity called *OneWeight* with a unit of [GeV cm^2 sr] is calculated [203]. Without specifying any flux model, *OneWeight*

is associated with various cross sections of possible interactions of a given neutrino event; it is defined as

$$\text{OneWeight} = \frac{1}{N_{\text{gen}}} \times \frac{P_{\text{int}}}{E^{-\gamma}} \times \Omega A \int_{E_{\text{min}}}^{E_{\text{max}}} dE' E'^{-\gamma}. \tag{5.1}$$

Here, Ω and A are the generation solid angle and area, and γ is the energy spectral index of the neutrino energy generation spectrum between E_{min} and E_{max}. N_{gen}, on the other hand, is the total number of neutrinos generated in a given data set[1]. Finally, given by the *GENIE* software, P_{int} is the total interaction probability, which takes into account all possible cross sections for the generated neutrino energy E.

One of the main advantages to use *GENIE* is its extensive archives of neutrino scattering data. For multi-GeV neutrinos, three major interaction processes are non negligible, including quasi elastic scattering (QE), resonance production (RES), and deep inelastic scattering. With a set of comprehensive physics models, *GENIE* can produce neutrino interactions weighted according to various energy dependent cross sections and kinematic constraints. In addition, *GENIE* conveniently provides a re-weighting mechanism that propagates cross section uncertainties due to QE and RES to uncertainties in the total interaction probability of a charged current event. Recall from Chapter 3.2 that these two cross sections depend on their axial masses, whose default values in *GENIE* are 0.99 and 1.12 GeV for QE and RES respectively [202]. In addition to the interaction probability using those default values, *GENIE* also calculates probabilities for the same event when these axial masses are ± 1 and ± 2 standard deviations away. As discussed in Section 7.3, this built-in feature in *GENIE* provides a handle to deal with cross section systematics for this analysis.

Despite the advantages, the current neutrino sets produced by *GENIE* assume that the Earth is made entirely out of ice. This assumption is not expected to af-

[1] N_{gen} takes into account the factor of neutrinos and antineutrinos in the same data set. For example, given a muon neutrino set, 70% of the set are muon neutrinos, while 30% are muon anti neutrinos. Such fractions are included in N_{gen} for the corresponding generated neutrino event.

fect the total interaction probability of events interacting inside IceCube-DeepCore. However, for neutrino interactions happening at the very bottom of the ice, their interaction probability may not reflect the reality due to the existence of bed rock underneath the ice. In addition, the *GENIE* software can only simulate single neutrino events, ignoring possible coincident background muons interacting during the neutrino interaction. Finally, the generating energy from *GENIE* only goes up to 1000 GeV. Contamination from high energy neutrinos sneaking into this analysis is tested using a different neutrino generator called *NuGen* which can generate neutrinos from 100 GeV up to $\sim$ EeV [204]. It is found that *GENIE* itself is sufficient for this oscillation parameter measurement.

5.1.2 Particle Propagations in Ice

Once a neutrino interaction in the ice is generated, many particles are produced and propagated through the ice. At the end, each individual photon is propagated and may reach a simulated DOM. While propagations of particles do not affect *OneWeight*, the number of photons reaching a DOM is affected by variations in, for instance, optical properties of the ice and the efficiency of DOMs. For this reason, this section explains briefly how particles, photons in particular, are propagated in simulations.

Propagations of particles are simulated using various software packages. Muon propagation is done by *PROPOSAL* [162], whereas hadrons and other leptons are propagated by *GEANT4* [110]. As these leptons and hadrons travel through the ice, they lose their energies and emit photons as discussed in Section 3.2.2. A software package called *CLsim* [205] converts the energy losses into number of Cherenkov photons, each of which is then propagated through the ice. Recalled from Section 3.2.3, the current best ice study [179] provides a table of absorption and scattering

coefficients as a function of depth, and this table is spline-interpolated to obtain a continuous function. For each photon, *CLsim* looks up its absorption and scattering lengths from the coefficient tables mentioned in Section 3.2.3.2 based on the depth at which the photon is created. *CLsim* then calculates the distance at which the photon is scattered, moves it to that point, and assigns a new direction to the photon based on the scattering probability density function such as the right plot of Figure 3.22. This random walk algorithm repeats until either the photon reaches a simulated DOM or is absorbed distance.

Once a photon reaches a DOM, a software package called *PMTResponseSimulator* [206] simulates the behavior of the photomultiplier tube (PMT) in the DOM. This simulation package determines whether this photon is accepted and, if so, how many electrons at the PMT anode should be assigned to it. The acceptance of a photon depends on the efficiency of the DOM as well as an angular dependent probability (see Figure 3.21). Because the half spherical PMT faces down, a photon arriving from the top of the DOM is less likely to be accepted than a photon from the bottom. If this photon is accepted, a photoelectron of 1 PE is emitted at the PMT cathode. Then, the second step of the *PMTResponseSimulator* is to determine the number of electrons at the anode of the PMT, or the voltage drop, due to the photoelectron. This number is randomly drawn based on a single photoelectron (SPE) charge distribution (see Figure 4.6) discussed in Section 4.1.2. This charge response probability distribution function is obtained from a separate study [194], in which an exponential and a Gaussian functions are fitted to the observed charges in laboratories. However, recent studies indicate that this fitted SPE charge distribution, especially the first narrow peak, used in simulation cannot accurately describe charges observed in multi-GeV events. Given only a few hit DOMs in an event, this bias is more important for simulations and reconstructions in low energy events than that in high energy events. Because of this observed disagreement, a special

charge-independent reconstruction algorithm discussed in Section 6.5 is adapted to minimize the impact due to low charge pulses during event reconstruction. At the end, for each pulse at the anode, a time is randomly stamped from a Gaussian PDF. A waveform and a SPE pulse are, therefore, simulated.

Finally, two other software packages called *DOMLauncher* [207] and *trigger-sim* [208] are used to simulate the behavior of the DOM main board and to check for trigger conditions. In general, the DOM electronics apply a threshold of 0.25 PE to the SPE pulses. The *DOMLauncher* then digitizes the pulses passing the threshold, discussed in Section 4.1.2, while simulating physics effects, such as electronic noise, clock phase of the fast analog-to-digital converter (FADC), and uncertainty of relative timing among the DOMs. After the *DOMLauncher* checks for and records any local coincidence conditions, the *trigger-sim* package looks for detector trigger conditions. For an event that passes a trigger condition, *trigger-sim* forms a pulse series within a certain trigger window. From that point, simulated events are processed through the standard software used for the online processing and filtering system as described in Section 4.3.2.

5.1.3 Oscillation Probabilities

Assuming three flavor mixing through the Earth, the oscillation probabilities for this analysis are calculated using the *Prob3++* software [201] which is based on the calculation in Barger *et al.* [59]. For this analysis, detector depth and neutrino production height are set to 2 and 20 km respectively. Unless otherwise specified, oscillation probabilities are calculated with normal mass hierarchy ordering and best fit values from 2016 νFit global fits [209]. The assumed Earth model is the Preliminary Reference Earth Model (PREM) with 60 layers [60]. The density as a function of the Earth's radius is shown in Figure 5.1 with clear segments between

the inner core, outer core, mantle, and crust as the radius increases. In addition, due to lepton universality, the flavors of generated neutrinos undergoing NC interaction cannot be identified. Therefore, their oscillation probabilities are not calculated.

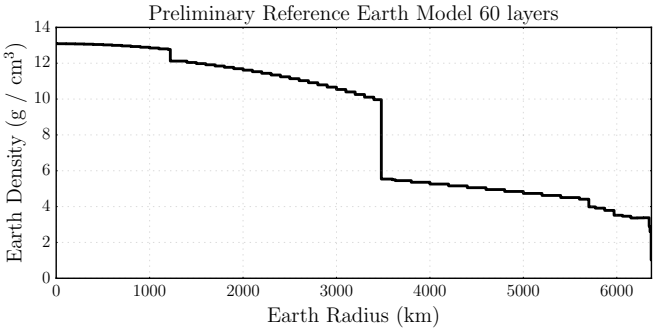

Figure 5.1: Preliminary Reference Earth Model with 60 Layers. Data points are taken from [60]. From left to right, the different segments correspond to the inner core, outer core, mantle, and crust of the Earth.

Since a neutrino event generated by *GENIE* is simulated at a fixed flavor, which is the flavor of an oscillated neutrino after passing through the Earth, this generated neutrino ν_{GENIE} is transformed either from an atmospheric ν_e or from an atmospheric ν_μ. Therefore, two probabilities are calculated for every generated neutrino event; one is $P(\nu_{e_{\text{atm}}} \rightarrow \nu_{GENIE})$, while the other one is $P(\nu_{\mu_{\text{atm}}} \rightarrow \nu_{GENIE})$. The energy and direction of the generated event are used to calculate both probabilities due to energy conservation and the fact that neutrinos are expected to travel in straight lines from the atmosphere to the detector. Because we do not know the original flavor of the neutrinos detected, both $\nu_{e_{\text{atm}}}$ and $\nu_{\mu_{\text{atm}}}$ are considered for every simulated neutrino event.

5.1.4 Atmospheric Neutrino Fluxes

For this analysis, the one dimensional calculation of atmospheric neutrino production described in Section 3.1 is inadequate. Not only does the simplified calculation ignore the Earth's magnetic field, it also assumes that directions of secondary particles produced from air showers are the same as the primary cosmic ray particles. This assumption leads to disagreements between predictions and observations near the horizon. Therefore, a three dimensional calculation is required for this analysis.

Using cosmic ray simulators, the latest three dimensional calculation available is performed by Honda *et al* [86]. Assuming an $E^{-2.66}$ neutrino energy spectrum, several improvements are made in this calculation compared to their earlier work [87]. First, a new interaction model for neutrino production below 32 GeV is adapted because of its better agreements between predictions and data obtained by accelerator experiments in a previous study [88]. Second, a more complete model for the Earth's atmosphere [210] is used; this new model includes data of air density profile at the polar region, which is expected to have large seasonal variation due to the extreme weather. Third, effects due to the geomagnetic field on atmospheric neutrino fluxes at the polar region is studied using a standard mathematical model of the Earth's magnetic field [211]. With the above modifications, atmospheric neutrino fluxes at the polar region are calculated. The neutrino fluxes averaged all directions are shown in Figure 5.2 [86].

In units of [GeV^{-1} cm^{-2} s^{-1} sr^{-1}], the calculated atmospheric neutrino fluxes at the Pole are stored in a form of tables. For each neutrino and anti neutrino flavor, the fluxes are tabulated at discrete values of energies between 0.1 GeV and 10 TeV from all zenith and azimuthal angles. These data points are spline-interpolated, from which the flux is determined for a given neutrino flavor based on its energy,

zenith, and azimuthal angles.

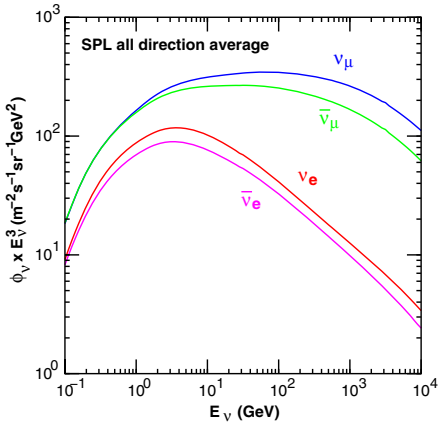

Figure 5.2: Calculated atmospheric neutrino fluxes at the polar region by Honda *et al*; plot taken from [86]. Three dimensional calculations are performed.

Despite the new modifications on the flux calculation, Honda *et al.* mentions that error estimations in earlier work are still valid. In his previous work [87], the uncertainties on $\nu_\mu/\overline{\nu}_\mu$ and $\nu_e/\overline{\nu}_e$ below 100 GeV are $\sim 5\%$, whereas the uncertainty on $(\nu_\mu + \overline{\nu}_\mu)/(\nu_e + \overline{\nu}_e)$ for the same energy range is $\sim 2\%$. Such small percentage uncertainties in flux ratios are due to pion decay being the dominant production channel for atmospheric neutrinos below 100 GeV. Moreover, the zenith dependent uncertainties are calculated with different hadronic models and found to be $\sim 3\%$ because of the growing contribution from kaon production.

5.1.5 Neutrino Rate Prediction

Expected neutrino rates at IceCube DeepCore are calculated by putting together atmospheric fluxes by Honda *et. al.* [86], oscillation probabilities with *prob3++*, and *OneWeight*'s which are related to the total interaction probabilities calculated by the *GENIE* generator. If a neutrino generated comes from an atmospheric ν_e,

then the weight assigned to this event is given by

$$w_{\text{atm } \nu_e} = \nu_e \text{ Flux} \times P(\nu_e \to \nu_{\text{GENIE}}) \times \text{OneWeight}, \tag{5.2}$$

where all values are evaluated at the generated energy, zenith, and azimuthal angles.

As mentioned in Section 5.1.3, every neutrino event generated or detected can either come from atmospheric ν_e or atmospheric ν_μ. Two weights are calculated independently, and the total weight of the i^{th} neutrino event is given by the sum of two weights;

$$w_i = w_{\text{atm } \nu_e} + w_{\text{atm } \nu_\mu}. \tag{5.3}$$

Note that w_i has a unit of $[\text{s}^{-1}]$. Neutrino rate of a given flavor is therefore given by the sum of all weights in the dataset, which is $\sum_i w_i$, with its corresponding MC statistical uncertainty given by $\sqrt{\sum_i w_i^2}$.

5.2 Atmospheric Muon Rates

Similar to neutrino rate prediction, atmospheric muon rate is calculated using simulation weighted by the expected flux. In IceCube, two simulation software packages are available. Discussed in Section 5.2.1, *CORSIKA* provides a more accurate prediction of rate, while *MuonGun* in Section 5.2.2 simulates muons more efficiently. As concluded in Section 5.2.3, both simulation tools are needed to predict atmospheric muon rate for this analysis.

5.2.1 CORSIKA

COsmic RaySImulations for KAscade, or *CORSIKA*, is an open source program for simulating extensive air showers induced by high energy cosmic rays [212]. It allows users to select the types of primaries from protons, the lightest, to iron, the heaviest. These primaries then enter the atmosphere and either interact with

air particles or decay. Several hadronic interaction models are built in to simulate the interaction. Secondary particles are then tracked and either interact or decay. The process repeats until all particles reach the ground. This simulation package is adapted to the IceCube simulation software.

For the purpose of this analysis, five types of primaries are included in the simulated muon sets; they are protons, helium, nitrogen, aluminum, and iron at a ratio of 10:5:3:2:1. These primaries then interact with the air particles according to the SIBYLL 2.1 hadronic interaction model [107]. Their secondaries continue to decay or interact until a stopping requirement is reached. For an energy range between 600 GeV and 100 TeV, more than 500,000 air shower events are generated to, hopefully, provide enough statistics. For those muons that reach the detector, their propagations are simulated using *PROPOSAL* [162], and detector response simulation is the same as described in Section 5.1.2. At the end, *CORSIKA* events are weighted to the GaisserH4a flux model [75].

Simulating muons using *CORSIKA* has its pros and cons. Because it simulates all the details of an air shower, prediction of atmospheric muon rate is accurate and precise. In addition, multiple air showers can be randomly combined to simulate events with multiple muons from different showers, which are also known as muon bundles. However, if the user wants to change an initial input, such as the hadronic interaction model or the atmospheric density profile, the entire simulation chain would have to be repeated from scratch. Moreover, despite more than 500,000 available simulated muon events, *CORSIKA* muon statistics at final level in the event selection is $\sim$ 1 month worth of lifetime, which is clearly not enough for analyzing multiple years of data. Furthermore, only $\sim$ 3% of muons from the generated air showers actually reach the detector; thus, substantial amount of computational resources is used in generating muons that do not interact with the instrumented ice.

5.2.2 MuonGun

Due to the inefficiency in *CORSIKA*, *MuonGun* [213] is designed to separate air shower simulations from the generation of muons interacting with the ice. Based on the concept of [214], *MuonGun* requires an injection surface, which is defined as the black cylinder in Figure 5.3. Aiming at the targeted volume, *MuonGun* then shoots muons from the injection surface, and their propagations through the ice are simulated by *PROPOSAL* [162]. Compared to *CORSIKA* events, muons generated by *MuonGun* have higher chances to interact with the detector; thus, more useful muon events are available at the end.

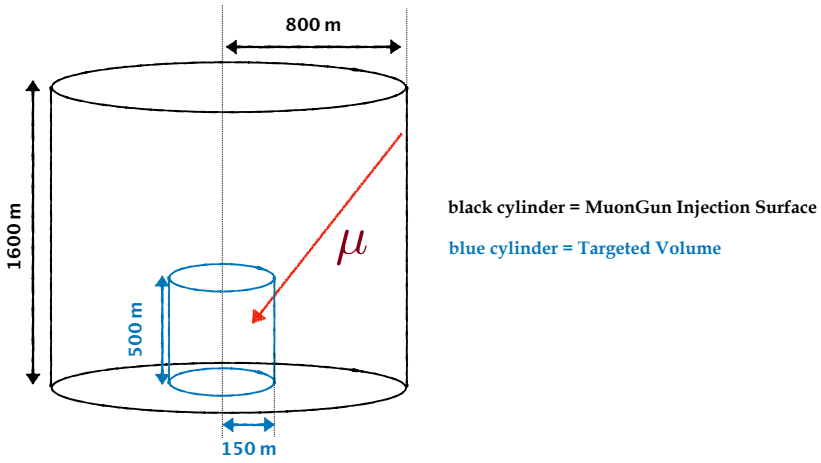

Figure 5.3: *MuonGun* injection surface and targeted volume. *MuonGun* simulates muons from the Injected surface, which is slightly larger than IceCube. The targeted volume is very close to the size of DeepCore. Atmospheric muon flux at the injection surface is parameterized from the flux of *CORSIKA* muons at the injection surface.

Although *MuonGun* can generate muons in a timely manner, it suffers from two issues. First, *MuonGun* itself does not have any information directly related to the physical atmospheric muon flux. Instead, the energy and zenith angle of generated events are randomly picked from a probability distribution function (PDF)

given by a flux model. This PDF cannot be determined by *MuonGun*, and thus it cannot provide proper weights for the generated events by itself. Second, the current version of *MuonGun* used can only generate single muons. Muon bundles have been observed from data before any selection cuts. While work is under way to produce multiple muon events using *MuonGun*, the currently available simulated data set cannot provide a realistic muon rate for this analysis.

5.2.3 Atmospheric Muon Rate Prediction

To predict the atmospheric muon rate for this analysis, both *CORSIKA* and *MuonGun* are used. All muons produced by *CORSIKA* are weighted by the GaisserH4a flux model [75] and are propagated to the injection surface defined in Figure 5.3. This flux at the injection surface is then parameterized and used as a PDF to weight events simulated by *MuonGun* according to their generated energies, zenith and azimuthal angles, and its position on the injection surface.

As shown in Chapter 6, during the event selection, muon background rates at looser cut levels are calculated using *CORSIKA* events since they provide a more realistic modeling with muon bundles and still have enough statistics. However, as more and more atmospheric muon backgrounds are rejected, *CORSIKA* events run out of statistics. Since most remaining muons are single muons, events produced by *MuonGun* are then used at final level instead of *CORSIKA* muons.

5.3 Detector Noise

In addition to neutrinos and background muons, noise triggered events are found to be significant at looser levels of the selection chain. Extensive studies have been performed to investigate the causes of dark noise [188]. Currently, detector noise in IceCube can be explained by Poissonian (time uncorrelated) and non Pois-

sonian (time correlated) behavior [215]. Mentioned in Section 4.1, Poissonian noise is caused by random thermionic emissions at the photocathode inside the PMT, whereas time correlated noise are bursts of hits due to radioactive decays from materials in the DOM glass pressure housing.

For this analysis, a software package called *Vuvuzela* simulates random noise triggered events [215]. Despite their significant contribution before the event selection process, most noise events are rejected by tight cuts with high efficiency. However, due to the radioactive decays, IC86-I data is considered to be noisy (see Figure 4.3). As DeepCore DOMs were deployed during the last deployment season in December, 2010, these radioactive processes are expected to take some time to reach equilibrium, as explained in Chapter 4.

5.4 Variations in Flux Predictions Due to Detector Effect

While variations in predicted rates depend on uncertainties of the corresponding flux models, neutrino and background muon event rates can also be biased due to any uncertainties in the modeling of the detector. As explained in Section 5.1.2, particle propagations are simulated based on the number of photons accepted by a DOM and detector response to the accepted photons. If the actual ice properties or efficiencies of DOMs are different from the base assumptions in the simulation packages, the predicted rates would be affected.

To take this into account, multiple simulation sets are produced by varying parameters related to the ice properties and DOM efficiency. Ranges of these detector parameters are determined from previous calibration studies. As discussed in Section 4.2, studies have shown that uncertainty on optical efficiency of DOMs is less than 20% [196, 198, 199]. Ice studies using flasher data [178, 180] suggest an anti-correlation between photon absorption and scattering in the ice, each of which

has a $\sim$ 10% uncertainty (see the right plot in Figure 3.24). Effects from bubble column are not as well understood; therefore, systematic sets are produced for wider ranges of the two hole ice related parameters.

To simulate sets with a range of DOM efficiencies, previously generated neutrino interactions are reused. For example, to generate seven neutrino simulation sets with DOM efficiency ranging from 0.88 and 1.12, one could first generate a set of neutrino events at a DOM efficiency of 1.75. This leads to N number of photons arriving at the surface of a given DOM in a given event. Since the effect of DOM efficiency is reflected on the number of photons accepted by the DOM, one can scale the number of accepted photons down to the desired DOM efficiency. If a DOM efficiency is set to 1.12, then, for a DOM in an event, the number of accepted photon is now $1.12/1.75 = 64\%$ of N, randomly throwing away 36% of photons that arrive at the DOM. DOM efficiency sets for muon events are generated in a similar way but with only three sets ranging from 0.69 to 0.99 due to limited computational resources.

A similar approach is used for simulating sets for varying parameters associated with bubble columns in the ice. As discussed in Section 3.2.3.1, effects from bubble columns are expected to be local. The presence of bubble columns does not change the overall DOM efficiency, but it does change the directions of the arrived photons. Such angular dependent acceptance is shown in Figure 3.21, in which two parameters are needed to describe its shape variation. The hole ice parameter p changes the overall shapes, while the hole ice forward parameter $p2$ affects the forward region where photons arrive at the PMT head on. For neutrinos, systematic sets are produced for five hole ice parameters p, from 15 to 35, and six hole ice forward parameters $p2$, from -5 to +2. For muons, only three sets are generated for both p, from 0.15 to 0.35, and $p2$, from -2 to 0.

While reusing generated sets is time saving, re-generation of neutrino interac-

tions is unavoidable to produce simulation sets for varying absorption and scattering coefficients. It is because variations in those coefficients change the overall number of photons reaching the simulated DOMs. Figure 3.24 shows that the 1σ uncertainties on the both coefficient scaling factors, α_{abs} and α_{sca}, are $\sim$10%; the two scaling factors are with respect to the coefficient table mentioned in Section 3.2.3.2. Hence, to save computational resources, only two neutrino systematic sets at 1 and 1.1 are produced for each absorption and scattering. In addition, Figure 3.24 also indicates that photon absorption and scattering are not independent of each other. Thus, an additional set, where both α's are 7.1% away from 1, is produced. For muon, three systematic sets at 0.8, 1, and 1.1 are produced for each scaling factor, and two off axis sets at 7.1% and 1.142% are also generated.

Simulated sets at different values for different detector parameters are produced for all three neutrino flavors and background muons. All sets are brought to final event selection level (see Section 6). Their rates are calculated the same way as described in this chapter, and their variations in percentage with respect to the baseline rate, calculated using nominal values for all detector parameters, are shown in Table 5.1. Overall, variations in predicted rates are less than 4% for all neutrino systematic sets related to ice properties; these variations are up to 15% due to optical efficiency of DOMs. Variations in muon rate predictions are more dramatic for all systematic parameters because of limited MC statistics, which is $\sim$ one year worth of detector lifetime even with the use of *MuonGun*. A general idea of uncertainties due to detector systematics can be given by comparing total rates; however, better understandings in their effects on different energy and direction slices, discussed in Section 7.4, are also important.

Table 5.1: Variations in total rate due to detector systematics. For each flavor and for each parameter value, a rate R_s from the systematic set is calculated and compared to the baseline rate R_b. Their variations in percentage, defined as $(R_s - R_b)/R_b$ [%], are presented. Highlighted rows correspond to the baseline sets, where the value of a parameter is equal to the base assumption of the modeling of the detector in simulations.

Variations in	Parameter	Values	ν_e CC	ν_μ CC	ν_τ CC	ν NC	μ
DOM Efficiency	$\mathcal{E}_{\mathrm{DOM}}$	0.693	-	-	-	-	1042
	$\mathcal{E}_{\mathrm{DOM}}$	0.792	-	-	-	-	401
	$\mathcal{E}_{\mathrm{DOM}}$	0.88	-15.0	-10.2	-13.0	-10.5	-
	$\mathcal{E}_{\mathrm{DOM}}$	0.94	-7.47	-5.17	-6.57	-5.38	-
	$\mathcal{E}_{\mathrm{DOM}}$	0.97	-3.11	-2.59	-4.07	-2.73	-
	$\mathcal{E}_{\mathrm{DOM}}$	1.0	0	0	0	0	0
	$\mathcal{E}_{\mathrm{DOM}}$	1.03	2.90	1.73	3.00	2.78	-
	$\mathcal{E}_{\mathrm{DOM}}$	1.06	7.28	4.50	4.80	5.48	-
	$\mathcal{E}_{\mathrm{DOM}}$	1.12	14.8	9.86	10.2	10.2	-
Bulk Ice	α_{abs}	0.8	-	-	-	-	-82.7
	α_{abs}	1	0	0	0	0	0
	α_{abs}	1.1	-3.27	-1.57	-3.78	-1.79	107
	α_{sca}	0.8	-	-	-	-	8.47
	α_{sca}	1	0	0	0	0	0
	α_{sca}	1.1	0.39	-0.59	-1.77	-0.60	-6.22
	α_{abs} and α_{sca}	0.929	1.42	-0.04	2.34	0.10	-39.4
	α_{abs} and α_{sca}	1.142	-	-	-	-	178
Air Bubbles	p	15	0.03	-0.42	-0.29	-0.55	2.61
	p	20	0.24	-0.15	-0.49	0.17	-
	p	25	0	0	0	0	0
	p	30	-0.50	0.07	-1.03	0.55	-5.06
	p	35	-0.36	-0.03	-1.60	-0.50	-
	$p2$	-5	-0.70	-0.65	-2.71	-1.96	-
	$p2$	-4	-	-	-	-	-16.6
	$p2$	-3	-0.20	-0.37	-1.31	-0.67	-
	$p2$	-2	-	-	-	-	-6.14
	$p2$	0	0	0	0	0	0
	$p2$	1	0.55	-0.25	-0.33	0.54	-
	$p2$	2	0.33	-0.39	-0.74	0.67	-

Chapter 6: The GRECO Event Selection

The GeV Reconstructed Events with Containment for Oscillations, *GRECO*, is an event selection procedure searching for signatures of atmospheric neutrino oscillations using IceCube-DeepCore. Developed by Michael Larson [216], the *GRECO* selection is used to look for a statistical excess of ν_τ events oscillated from atmospheric neutrinos. Since ν_μ disappearance is closely coupled to ν_τ appearance, the same selection can be used for identifying neutrinos with energies between 5.6 and 56 GeV and for measuring atmospheric neutrino oscillation parameters. At final level, the purity of ν_μ CC signal events is $\sim 57\%$, while other neutrino flavors contribute $\sim 35\%$ with an $\sim 8\%$ contamination from noise triggered events and atmospheric muon backgrounds. The *GRECO* sample currently has the highest efficiency compared to previous samples with roughly the same percentage of background contamination.

This selection procedure is done via successive levels of cuts; lower level cuts remove obvious backgrounds using quick, simple algorithms, while cuts at higher levels better identify signal events and improve agreements between data and MC. At each level, a rate of each event type is calculated. Neutrino rates assume neutrino oscillations based on the world averaged best fit oscillation parameters [209]. Muon rates for lower levels are calculated from *CORSIKA* events, while muon rates at higher levels are obtained from *MuonGun* events. The total rate from all event types are compared to the data rate at each level. A summary of rates at each level is presented in Table 6.1.

As mentioned in Section 4.3.2, during the standard data processing and filter-

ing procedures, the DeepCore filter is applied to only keep events passing the SMT 3 trigger with a threshold of three hard coincident (HLC) hits in the DeepCore fiducial volume; this simple filtering is called Level 2. With a data rate of $\sim$ 20 Hz at Level 2 filtering, the *GRECO* selection starts with a basic filtering called Level 3, which efficiently vetoes obvious noise triggered and atmospheric muon events (see Section 6.1). To further remove atmospheric muons backgrounds, two boosted decision trees (BDTs) are trained to improve sample purity. As explained in Section 6.2, the first BDT at Level 4 uses variables from simple calculations, whereas the second BDT at Level 5 involves slightly more complicated reconstruction algorithms detailed in Section 6.3. Section 6.4 discusses a set of straight cuts at Level 6 which further reduces the rates of pure noise and atmospheric muon backgrounds. At this point, neutrino events contribute a majority of the sample; therefore, a computational expensive reconstruction algorithm with improved resolutions is run at Level 7 (see Section 6.5). Last but not least, additional cuts explained in Section 6.6 are applied to further remove background muons and to improve agreements between data and MC.

6.1 Level 3 - Basic Filtering

The goal of Level 3 event filtering is to remove obvious background atmospheric muons and noise triggered events with quick, simple veto and reconstruction algorithms. Using basic information such as times, charges, and positions of hit DOMs, Level 3 selection is able to reduce data rate by a factor of $\sim$ 20 (see Table 6.1). Based on the estimations from simulations, more than 90% of background atmospheric muon and noise triggered events are removed, while neutrinos are mostly kept after Level 3.

After passing the SMT3 trigger, an event is handed to an algorithm called

Noise Engine, which determines if this event is triggered by random dark noise from the photomultiplier tubes (PMTs) as explained in Section 4.1. Noise Engine begins by selecting hits that occur within a certain time window and distance from the three HLC core hits. For each of the selected hits, the algorithm pairs it up with all other selected hits. For the two hits in every hit pair, a direction of line segment between the two hits is drawn, from which their angular separation is determined. All hit pairs are then binned in a two dimensional histogram of the angular separations. A simplified Noise Engine in one dimensional schematic diagram is shown in Figure 6.1. Since hits in a noise triggered event are randomly distributed, if one of the bins has more than three hit pairs, then the event is less likely to be noise triggered and, therefore, is kept.

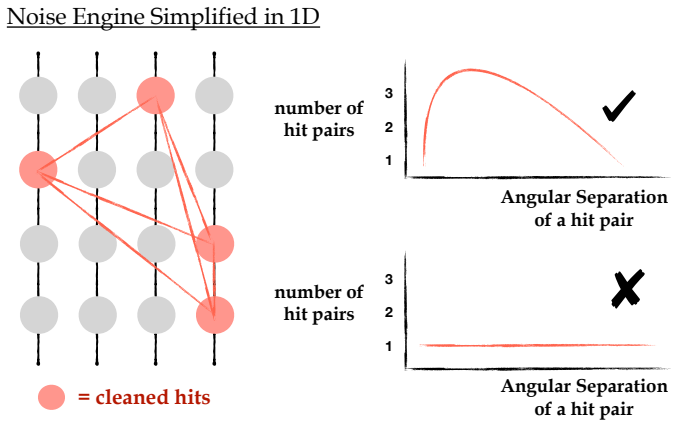

Figure 6.1: NoiseEngine. For each event, every two cleaned hits are paired up. The angular separation of each hit pair is binned. An events is kept if at least one of the angular separation bins has three or more entries. The schematic diagram is not drawn in scale.

Noise events are further reduced by placing minimum requirements on the total charges and number of hits in all DeepCore related DOMs. Shown as the yellow shaded area around the red dotted hexagon in Figure 4.1, the DeepCore fiducial volume is defined to be the bottom 50 DOMs for the eight DeepCore strings

(Strings 79 - 86), as well as the bottom 22 DOMs for the seven IceCube strings within and around DeepCore (Strings 26, 27, 35, 36, 37, 45, 46). Hits within the DeepCore fiducial volume are selected, and their charges and number of hits within a certain time window are accumulated. A minimum of 2 PE and two hits are required for an event to be kept.

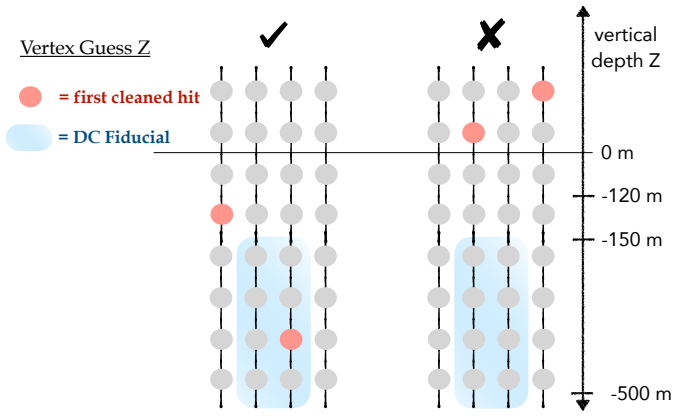

Figure 6.2: Vertex Guess Z. An events is kept if its first cleaned hits has a vertical depth below -120 m. The schematic diagram is not drawn in scale.

Next, assuming a vertex of an event is simply given by the earliest hit of a cleaned pulse series, a quick way to identify DeepCore events is by requiring the first cleaned hit of the event below a depth threshold. As shown in Figure 6.2, this variable is called VertexGuessZ. In the IceCube coordinate, a depth of 0 m is defined at the middle of the detector. Because DeepCore DOMs are located between -500 and -150 m, a loose cut is applied such that only events with vertical positions of their first cleaned hits below -120 m are kept.

In addition, a simple veto algorithm, called NAbove200, is applied to identify down going muon events. This simple approach involves accumulating all charges deposited above the DeepCore region; that is, charges from all cleaned hits located between -150 and +500 m are summed. However, dust layer is located between -210

and -135 m. To be more conservative, the very top part of the DeepCore region is also included in the total charge calculation. As a result, an event is kept if it has a total charge less than or equal to 12 PE from all cleaned hits located above -200 m.

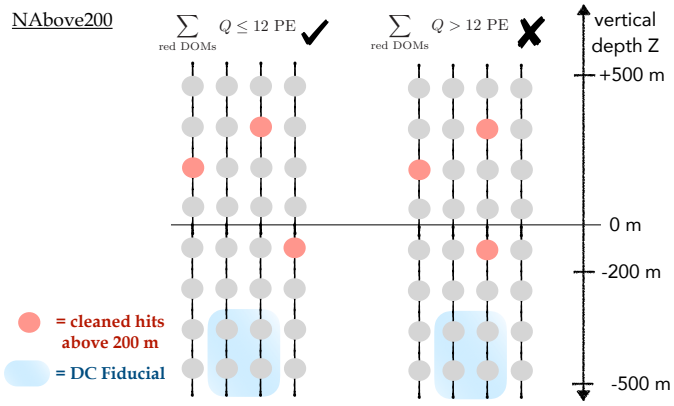

Figure 6.3: NAbove200. An events is kept if the total charge from all cleaned hits are less than or equal to 12 PE. The schematic diagram is not drawn in scale.

Another charge variable used at Level 3 filtering is C2QR6, which is defined as the ratio between charges collected in the first 600 ns and the total accumulated charge. A typical background muon event has a low charge ratio because charges are deposited over a longer timescale. In this calculation, the first two hits, which are likely to be random dark noise, are excluded. An event with this charge ratio greater than 0.4 is kept.

The next quick veto algorithm involves taking the ratio of charges outside the DeepCore fiducial volume to that inside the fiducial volume. Since background atmospheric muon events tend to deposit more charges in the veto region than in DeepCore, an event with a charge ratio less than 1.5 is kept.

To further reject obvious down going atmospheric muon backgrounds, another veto algorithm is applied using time and distance correlation between hits in the DeepCore region and hits in the veto region. As shown in Figure 6.4, hits in an event

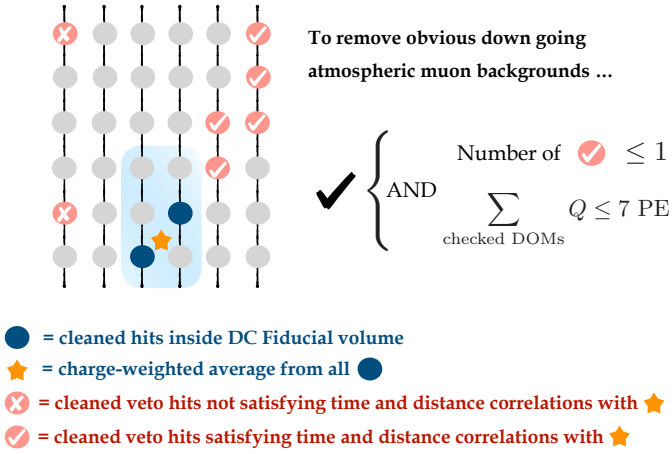

Figure 6.4: Identifying atmospheric muon background via time and distance correlations. An event is kept if number of veto hits (checked red DOMs) that satisfy time and distance correlations with the averaged DeepCore hit (yellow star) is less than 1 and the total charge from those veto hits are less than or equal to 7 PE. The schematic diagram is not drawn in scale.

are classified into two groups; one are hits inside the DeepCore fiducial volume (dark blue DOMs), and the remaining hits are the in IceCube veto regions (red DOMs). Among all hits inside DeepCore, an averaged time is determined, as well as the charge-weighted averaged position (the yellow star). This averaged time and position from DeepCore hits are then used to check for correlation with hits in the veto region. Hits in the veto region are selected (checked red DOMs) if they are consistent with speed of light from the averaged time and position of the DeepCore hits, and the charges of selected veto hits are summed. An atmospheric muon event is expected to have more than one veto hit, and the total charge calculated by this veto algorithm is large. Hence, an event is kept if one or less veto hit is found and if their total charge calculated is less than 7 PE.

To identify obvious down-going atmospheric muon backgrounds, the total charges between DeepCore hits and causally related veto hits are compared. First,

hits in the IceCube veto region occurring 5 μs before the SMT3 trigger are collected. Then, based on their differences in times and distances, causally correlated hits are identified, and their charges are summed. This total veto charge is then compared to the total charge from the cleaned hits inside the DeepCore fiducial volume. Figure 6.5 shows the four conditions from which an event is kept.

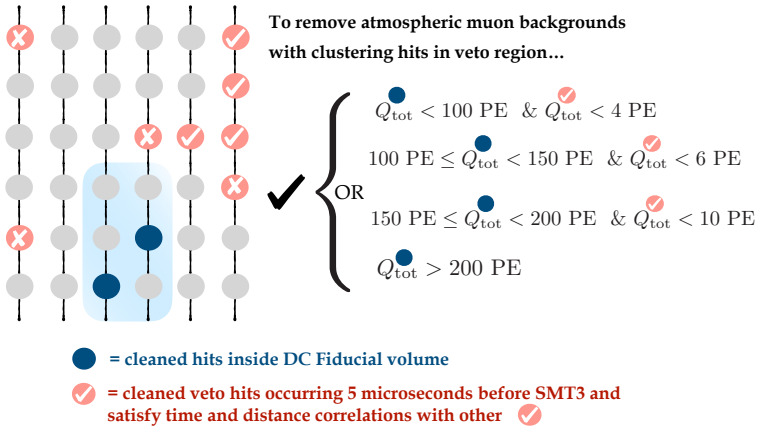

Figure 6.5: Identifying atmospheric muon background via charge comparison between DeepCore hits and causally correlated veto hits. In the IceCube veto regions, hits that occur 5μs before the SMT3 triggers are collected. Among the collected hits, causally related hits are identified. Their charges are summed and compared to the total charge from all cleaned hits in the DeepCore area. An event is kept if any of the four requirements on the right are met. The schematic diagram is not drawn in scale.

After all the above cuts, reduction in rates for all event types from Level 2 DeepCore filter to Level 3 filtering are summarized in Table 6.1. Data rate decreases from $\sim$ 20 Hz at Level 2 to $\sim$ 1 Hz after Level 3. From simulations, more than 70% of each ν_μ, ν_e, and ν_τ are kept. Despite the $\sim$ 25% loss in ν_μ signal events, background atmospheric muon and noise triggered events are significantly reduced by $\sim$ 90% and 96% respectively. As a side note, total MC rate does not agree well with data rate by $\sim$ 13%. This can be resolved by applying more sophisticated selection cuts

at higher levels to remove data events that are not well modeled by simulations. Also note that muon rates at Level 3 filtering are calculated from *CORSIKA* events instead of events from *MuonGun*, which does not simulate all possible channels for the production of atmospheric muons, as discussed in Section 5.2.

6.2 Level 4 - First Boosted Decision Tree

With a straight cut and a boosted decision tree (BDT), the next step in the *GRECO* selection further reduces the contributions from background atmospheric muons and noise triggered events by a factor of ~ 10. Using simple event variables related to charges, vertex locations, and event topologies, the Level 4 BDT is trained to identify neutrino events of all three flavors from background atmospheric muons.

A BDT is a common machine learning algorithm and is well described in [217]. In general, a decision tree consists of layers of nodes. To train a single tree, a set of signal sample, a set of background sample, and a list of training variables are required. During training, the first node of the tree randomly selects a variable out of the given variable list. Then, a signal and a background histograms of that variable are built from the given samples. By scanning through each possible cut value of the chosen variable, an optimized cut is placed at which signal-background separation is maximized. Events passing the cut are handed to one of the nodes in the next layer, while events failing the cut are handed to a different node. Those nodes, again, randomly pick some variables out of the list, and this process repeats until a stopping criterion is reached. For each of the end leaves, a purity is defined based on the ratio of signal rate to total rate of events fallen into this leaf; based on the purity of this end leaf, a score is assigned to this subset of events. Boosting comes into play when many decision trees are considered. After a score is assigned to an event from a decision tree, one can determine whether the tree misidentifies

the event. This error is turned into a boost factor for the tree. When training starts in the next tree, the weights of events which were badly misidentified by the previous tree are now increased by the boost factor. The final BDT score of an event after training all trees is the averaged score of the event from all trees weighted by the boost factor.

For the Level 4 BDT, a ROOT-based software package called the Toolkit for Multivariate Analysis (TMVA) [218] is used for training. 400 trees are used, each of which has a maximum depth of three layers and 10000 total number of nodes. Level 4 BDT is then trained to identify neutrinos of all three flavors from atmospheric muon background. To avoid over training, a different set of simulations is used for training than for testing.

Six variables are used for training the Level 4 BDT, three of which are already discussed at Level 3 filtering: VertexGuessZ, C2QR6, and NAbove200. Similar to C2QR6, one of the remaining three variables is QR6, which is the ratio of charges collected in the first 600 ns to the total accumulated charge. The last two variables are based on slightly more complicated reconstruction algorithms. One of them is the reconstructed speed from the *Improved LineFit* algorithm [219] which performs a modified least-square minimization on the time and space of hits in a cleaned pulse series assuming an infinite muon track. In general, atmospheric muons tend to be more energetic and have speeds closer to the speed of light compared to secondary muons from neutrino interactions.

The last variable considered is based on the topology of an event [220]. From basic mechanics, in a Cartesian coordinate (x, y, z), the elements in the moment of inertia matrix for a rotating rigid body made up of N discrete particles is given by

$$I_{ab} = \sum_{i}^{N} m_i \left(\mathbf{r}_i^2 \delta_{ab} - r_{ia} r_{ib} \right), \tag{6.1}$$

where a and b can be x, y, or z axis; m_i is the mass of the i^{th} particle; $\mathbf{r}_i^2$ is the

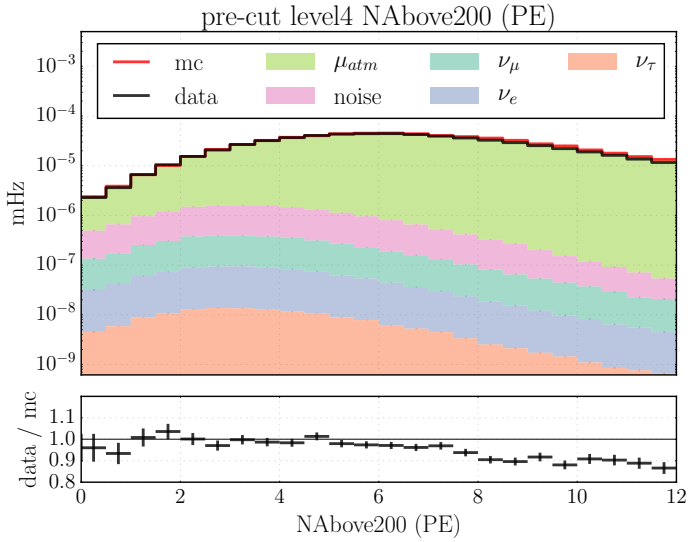

Figure 6.6: Distribution of NAbove200 at GRECO Level 4 (pre-cut). NAbove200 is the total charge from all hit DOMs located above DeepCore volume. Each shaded region represents the distribution of each flavor. The MC histograms are stacked and summed to the red solid line, which is the total MC distribution. The black line represents the data distribution. Concentration of signal and background events in different regions of PEs helps BDT to identify signal events from background.

distance between the origin and i^{th} particle. This concept is adapted to describe the overall shape of an event with N hits each of which has a charge of q_i. Hence, the diagonal elements are

$$\begin{aligned} I_x &= \sum_i^N q_i\big(y_i^2 + z_i^2\big), \\ I_y &= \sum_i^N q_i\big(x_i^2 + z_i^2\big), \\ I_z &= \sum_i^N q_i\big(x_i^2 + y_i^2\big), \end{aligned} \tag{6.2}$$

where x_i, y_i, z_i are the distance of the i^{th} hit from String 36 at Z = 0 m. For a ball-shaped cascade-like event, the numerical values of these three Is are similar, while an elongated track-like event has one of the three Is being very small. Therefore,

three ratios are defined

$$R_a = \frac{I_a}{I_x + I_y + I_z} \tag{6.3}$$

where a can either be x, y, or z. The minimum ratio out of the three is used as a variable to train the Level 4 BDT.

As an example to show how a node in the BDT identifies signal events from backgrounds, Figure 6.6 shows the distribution of NAbove200, which is the total charge from all cleaned hits located above -200 m. Given that a typical down going muon deposits its energy outside the DeepCore region as it passes the detector, muon events are mostly concentrated at high charge region on the right. On the other hand, neutrino events tend to have less charges in the veto region. This difference between signal and background distributions helps the BDT to identify signal from background events.

At Level 4, two cuts are applied. The first one is a BDT score cut to remove a majority of background muon events. The BDT score distribution is shown in Figure 6.7. As expected, signal neutrino events are separated from muon background events, most of which have very low BDT scores. A cut is, therefore, applied to keep events with a score above 0.04. The second cut applied is to further remove noise events. As shown in Figure 6.7, a $\sim$ 40% disagreement between data and MC at high BDT score region where noise triggered events dominate. Thus, an additional cut on total number of hits in the DeepCore fiducial volume is applied; only events with more than three hits inside DeepCore are kept.

After the two straight cuts at Level 4, rates from all event types are summarized in Table 6.1. With respect to rates after Level 3 filtering, more than 50% neutrino events are kept after Level 4 cuts, while $\sim$ 95% muons and noise triggered events are removed. Disagreement between data and MC is also improved.

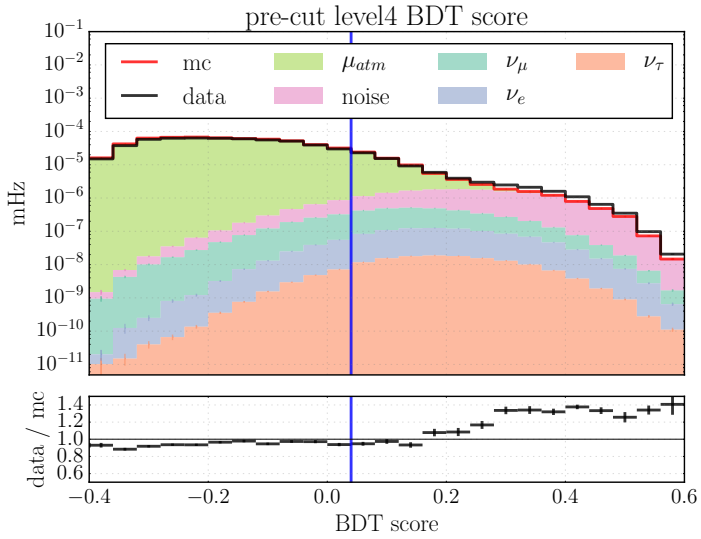

Figure 6.7: Distribution of BDT score at GRECO Level 4 (pre-cut). Each shaded region represents the distribution of each flavor. The MC histograms are stacked and summed to the red solid line, which is the total MC distribution. The black line represents the data distribution. Most atmospheric muon events have low scores, while most neutrinos and noise triggered events have high score. The blue vertical line at BDT score of 0.04 is the cut value applied to Level 4 selection. Events with a score above 0.04 are kept.

6.3 Level 5 - Second Boosted Decision Tree

The second BDT at Level 5 is trained with variables obtained from more complicated, time consuming calculations. This helps reduce the atmospheric muon background rate by an additional factor of ~ 10. The Level 5 BDT uses six variables and has the the same settings and simulations used for training Level 4 BDT.

The first two variables in the list are the simplest. The first variable is the amount of time for an event to accumulate 75% of the total charges. Only hits inside the DeepCore fiducial volume within a certain time window are taken into account. The second variable is the radial position of the earliest HLC hit DOM; the center of IceCube is defined to be String 36, which is the central string of DeepCore

fiducial volume. Both of these variables help identify atmospheric muon events, which usually start away from the DeepCore volume and take longer time to collect charges.

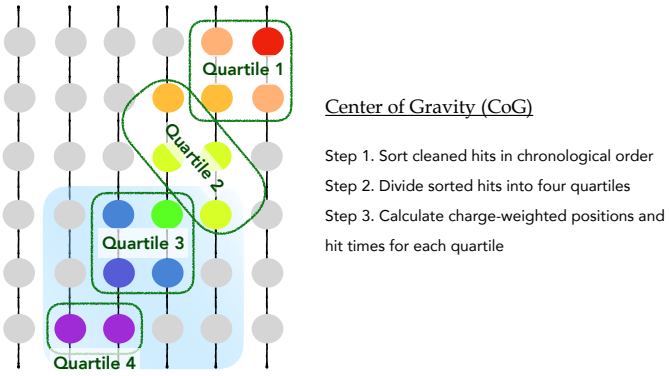

Figure 6.8: Center of Gravity algorithm. Colors (from red to blue) represent hit times (from earliest to latest). All cleaned hits are sorted by hit times and divided into four quartiles. Two variables are used in training the Level 5 BDT. They are the spatial separation between the first and forth quartiles and the vertical distance between the averaged vertical position of hits in the first quartile and the averaged vertical position of all cleaned hits. The schematic diagram is not drawn in scale.

The next two variables are related to distances between clusters of hits calculated by the *Center of Gravity* algorithm [221]. As shown in Figure 6.8, this algorithm first sorts all hits in a cleaned pulse series based on their hit times and then divides them into four quartiles, each of which has a corresponding averaged time and location weighted by charges. A useful variable for BDT training is the spatial separation between the first and the last quartiles because atmospheric muons usually travel long distances across the detector, having a large separation between the early hits and the later hits. For the same reason, the vertical distance between the averaged vertical position of the first quartile and that of all cleaned hits is also included in the BDT training to identify down going background muons.

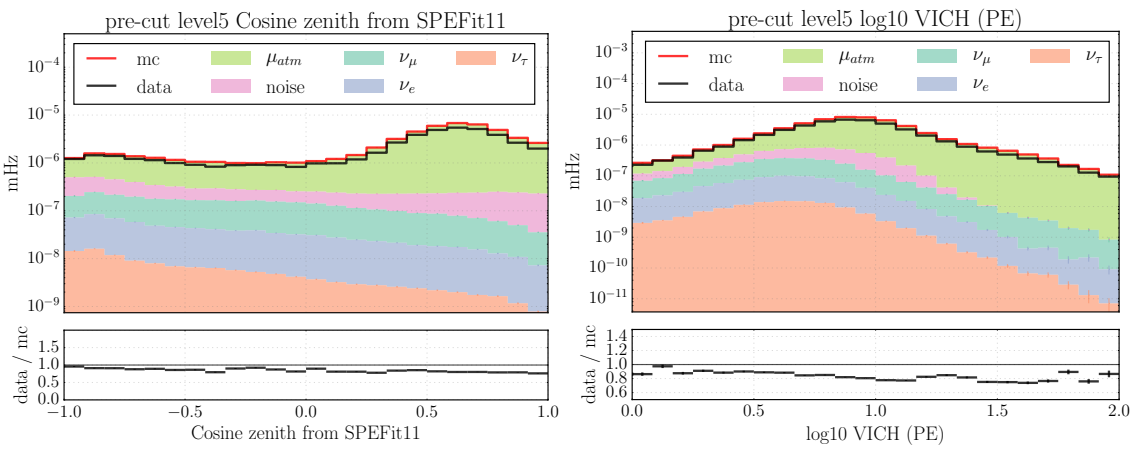

Figure 6.9: Distribution of Two Variables Used in GRECO Level 5 BDT (pre-cut): (left) cosine reconstructed zenith from *SPEFit11* and (right) veto identified causal hits (VICH). Each shaded region represents the distribution of each flavor. The MC histograms are stacked and summed to the red solid line, which is the total MC distribution. The black line represents the data distribution. Most atmospheric muon events are down going and deposits hits in the veto region defined by causality; hence, background muon distributions have different features in the two histograms than the distributions of neutrino events.

Because most background muons are down going, a reconstructed zenith by the *SPEFit11* algorithm is added to the list of variables for training the Level 5 BDT. Similar to *Improved LineFit*, *SPEFit11* assumes a muon traveling across the detector, leaving a long track. However, instead of a least-square fit, *SPEFit11* maximizes the likelihood based on the probability that pulses in a cleaned pulse series are causally related to the incoming muon track [219]. As shown in the left plot in Figure 6.9, background muons contribute a large fraction of down going events, whereas neutrinos have relatively flat distributions across all sky.

The last variable on the list is the accumulated charge from veto hits, which are defined by the veto identified causal hits, or *VICH*, algorithm [222]. For every event, a veto region is defined based on the position of the triggered DOM. For a typical background muon entering the IceCube detector from the top, it may

trigger the SMT3 trigger in DeepCore region and then leaves the detector. The veto region for this event is therefore defined in region where locations of DOMs satisfy causality with the triggered DOM within an averaged 2 μs muon decay time. Any hits that fall inside the veto region are considered as veto hits, and their charges are accumulated. The distribution of the summed veto charge is shown on the right plot in Figure 6.9. As expected, most atmospheric muon backgrounds have large veto charges, while all neutrino flavors have small total charge from veto hits.

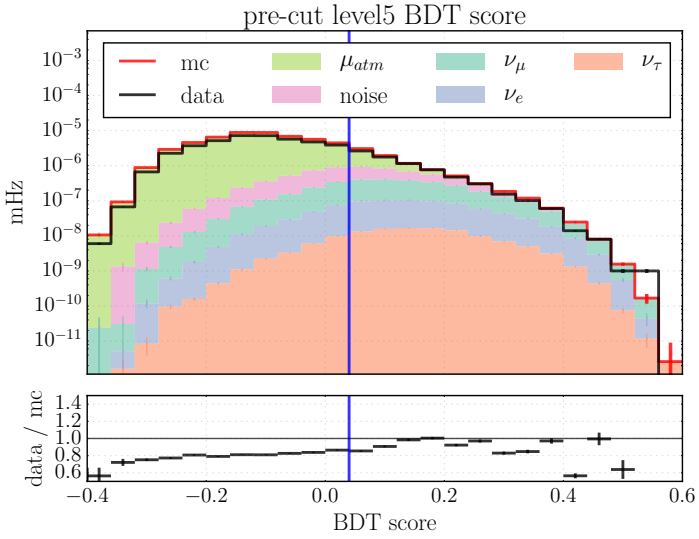

Figure 6.10: Distribution of BDT score at GRECO Level 5 (pre-cut). Each shaded region represents the distribution of each flavor. The MC histograms are stacked and summed to the red solid line, which is the total MC distribution. The black line represents the data distribution. Most atmospheric muon events have low scores, while most neutrinos and noise triggered events have high score. The blue vertical line at BDT score of 0.04 is the cut value applied to Level 5 selection. Events with a score above 0.04 are kept.

Similar to the Level 4 BDT cut, a score cut is applied at 0.04 to remove atmospheric muon events. Figure 6.10 shows the BDT score distribution. Again, background muon events have low scores compared to neutrino events. Table 6.1

summaries the rates for each event type after Level 5 cut is applied relative to Level 4. More than 65% of neutrino events are kept, whereas over 90% background muon events are removed. Noise triggered rates are also significantly reduced by $\sim$ 85%.

6.4 Level 6 - Straight Cuts

Straight cuts are applied at Level 6 to further remove atmospheric muon and noise triggered backgrounds by factors of $\sim$ 13 and 18 respectively. Two cuts are applied to remove persistent noise triggered events, and two more cuts are dedicated to remove sneaky and un-contained atmospheric muon backgrounds.

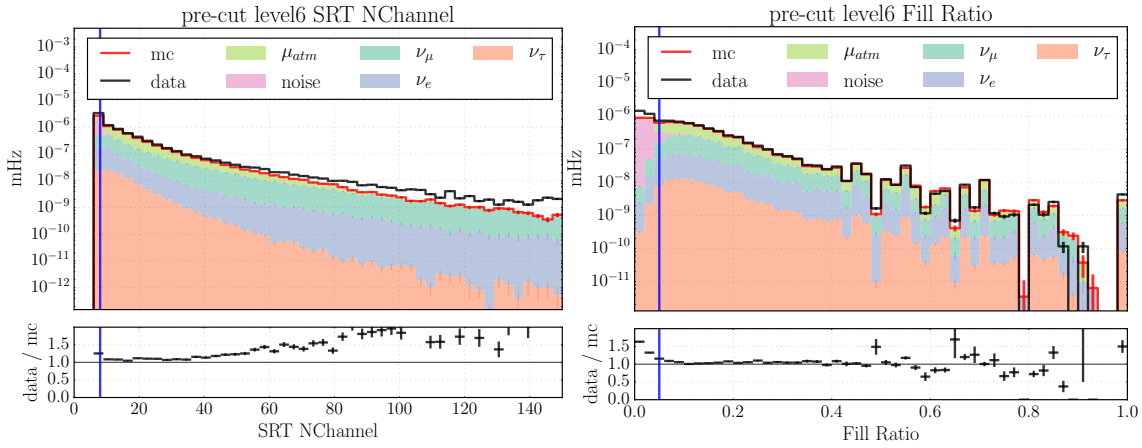

Figure 6.11: Distribution of Two Variables Used in GRECO Level 6 (pre-cut): (left) number of hits from a cleaned pulse series and (right) Fill ratio. Each shaded region represents the distribution of each flavor. The MC histograms are stacked and summed to the red solid line, which is the total MC distribution. The black line represents the data distribution. With less hits compared to other flavors and hits scattering randomly across the detector, noise triggered events often have lower values of number of channels and fill ratio. Thus, as show in the vertical blue lines, two cuts are applied to remove events with less than eight hits and a fill ratio less than 0.05.

The first noise-related cut is to keep events with at least eight cleaned hits inside the DeepCore fiducial volume. Because noise events have fewer hits in gen-

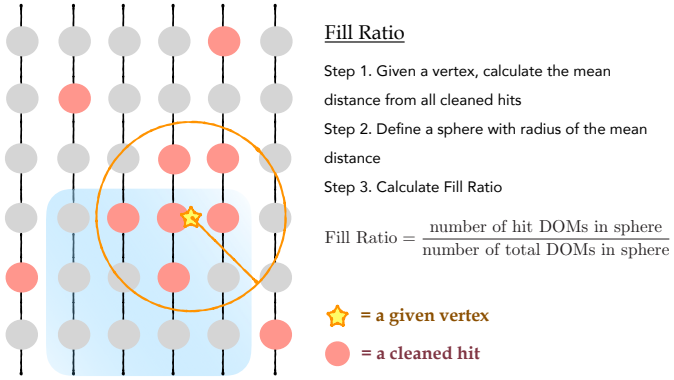

Figure 6.12: Fill Ratio algorithm. Colored DOMs are cleaned hit DOMs, and yellow star represents a given vertex. With the given vertex, the Fill Ratio algorithm determines the mean charge weighted distance between all hit DOMs and the vertex. A sphere is defined using a radius of the mean distance calculated. The fill-ratio is then defined to be the ratio between number of hit DOMs within the sphere and the number of total DOMs outside the sphere. The schematic diagram is not drawn in scale.

eral, previous cuts have already required events to have more than three hits. An additional requirement on number of hits at Level 6 is to prepare for the final reconstruction at Level 7. As discussed in the next section, *PegLeg* reconstruction algorithm fits eight parameters to an event; at least eight degrees of freedom per event are required for a reasonable fit. Therefore, only events with eight or more cleaned hits are kept. As shown on the left plot in Figure 6.11, most noise events have less than eight hits. This cut alone reduces the noise rate by a factor of ~ 17.

In addition to a cut on numbers of hits, a more sophisticated algorithm called *Fill Ratio* can effectively identify noise triggered events. *Fill Ratio* looks for the topology of hits in an event around a given vertex. A sphere is defined around the vertex with a radius proportional to the mean distance from all cleaned hits. The pattern of hits in an event can be estimated by the ratio of number of hit DOMs inside the sphere to the total number of DOMs inside the sphere. The distribution of this ratio is shown on the right of Figure 6.11. Since hits in a pure noise event

are randomly scattered across the detector, most noise triggered events tend to have longer mean distances away from their vertices and less hit DOMs inside the sphere; hence, these events have very low values of fill ratio. A straight cut is therefore applied at 0.05, below which noise triggered events cluster.

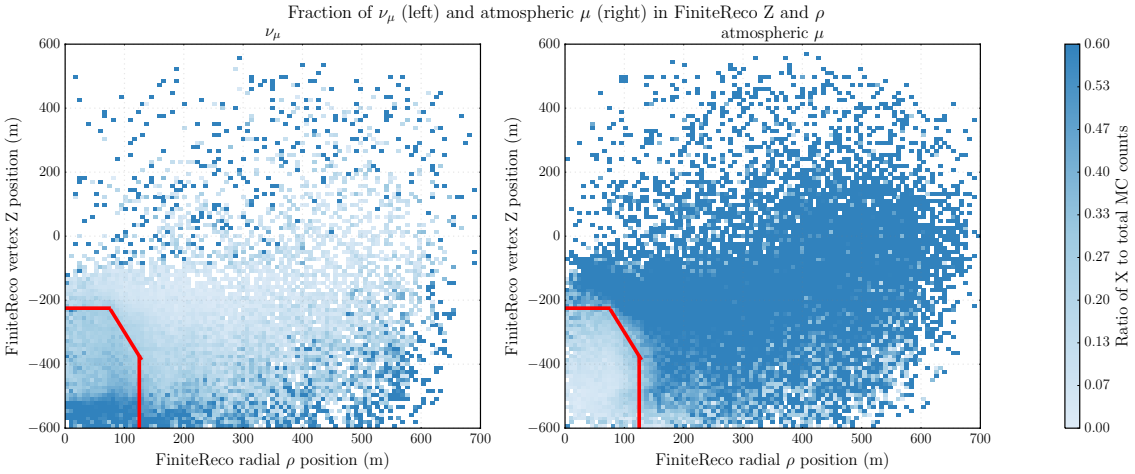

Figure 6.13: Two Dimensional Fraction of radial and vertical positions of FiniteReco vertices in GRECO Level 6 (pre-cut): (left) fraction of ν_μ contribution to total MC (right) fraction of atmospheric μ contribution to total MC. Color bar represents the fraction of contribution from a flavor to total number of events. Most background muon events have reconstructed vertices away from DeepCore fiducial volume; therefore, a hard cut is applied to keep events with vertices inside the box defined by the three red lines.

On the other hand, atmospheric muon events can be further removed by a containment cut using the *FiniteReco* algorithm [222]. This algorithm assumes a muon track passing through the detector. Four different track hypotheses are considered: a starting track, a stopping track, a fully contained track, and an infinite track that does not stop or start in IceCube. For each track hypothesis, probabilities of DOMs seeing a hit or not are calculated. Using a log likelihood algorithm, the best fit hypothesis returns the vertex information of the interaction. From the reconstructed vertex position, the vertical and radial position from String 36 are

calculated. The right plot in Figure 6.13 shows the contribution from atmospheric muon events to total MC as a function of vertical position Z and radial position ρ. Clearly, most of the background muon events have vertices away from DeepCore region which has a radius of 125 m and a vertical position below -150 m. To remove those background muons, a hard cut is applied to keep events with reconstructed vertices inside the red box in Figure 6.13. Therefore, an event is kept if its *FiniteReco* vertex has a vertical position less than -225 m, a radial distance from String 36 less than 125 m, and the vertical position is less than -3 times the radial distance.

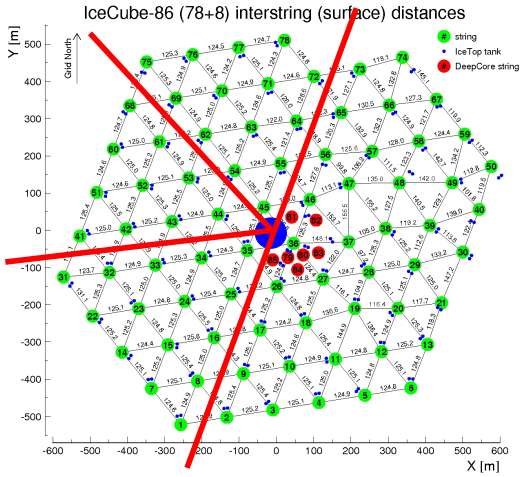

Figure 6.14: Definition of Corridors in GRECO Level 6 (pre-cut). This plot is from [223]. A background muon may travel through IceCube such that it does not hit any IceCube strings; these paths are called corridors. For a vertex near String 36, corridors are shown as red solid lines. Hits in the nearby IceCube strings along all corridors are accumulated. Only events with less than two corridor hits are kept.

The last straight cut at Level 6 is a corridor cut [223]. Despite previous efforts to identify background muons using hits in the veto region, some sneaky muons may not hit enough DOMs in the veto region to be spotted. For example, as shown in Figure 6.14, given a vertex near String 36, the particle interacting can come from a finite number of paths that do not hit any DOMs on any IceCube strings; these

paths are called corridors. Corridors are defined for all DeepCore strings based on IceCube string configuration. For every event, given a reconstructed vertex, the closest DeepCore string to the vertex is found, as well as a set of corridors associated with that DeepCore string. For each corridor, the algorithm looks through the closest IceCube strings along the path and counts the number of hits on these strings that satisfy time and distance correlations with the vertex. An event with two or more corridor hits is removed.

As shown in Table 6.1, four straight cuts at Level 6 reduce background rates by $> 92\%$ relative to Level 5, and ν_μ events are now the most significant contribution of the sample. Total MC rate also agrees with data with a Data / MC ratio ~ 1. Note that atmospheric muon rates from Level 6 onwards are calculated from *MuonGun* events instead of *CORSIKA* shower events, which no longer have enough statistics. With most obvious atmospheric muons rejected at lower levels, the remaining muon backgrounds beyond Level 6 are mostly single muon events, which can be efficiently generated by *MuonGun*.

6.5 Level 7 - PegLeg Reconstruction

With $\sim 78\%$ of the sample are neutrino events, a more accurate but CPU-intensive reconstruction called *PegLeg* is run at Level 7. Developed by Martin Leuermann, *PegLeg* is targeted at reconstructing particles with energies between 5 and 100 GeV [224]. It assumes that an event is caused by a minimum ionizing particle which gives a cascade plus a track event topology. Based on this hypothesis, minimizations are performed to obtain eight best fit parameters, including energy and direction of the incoming particle. Detail on how *PegLeg* works is fully explained in [224]; this section presents a brief description and discusses resolutions of important observables. While no selection cut is made at Level 7, events that

cannot converge during *PegLeg* reconstruction are rejected.

PegLeg is based on a general reconstruction tool in IceCube called *Millipede* [225]. In general, given either a track or a cascade hypothesis, *Millipede* calculates the total poisson log likelihood from all DOMs; each log likelihood compares the observed number of photons at a DOM to its expected number of photons. The total number of photons expected from a given event is related to the Frank-Tamm relation (see Equation 3.52) in Section 3.2.2.2. The expected number of photons received by a given DOM takes into account the relative position between the DOM and the event vertex as well as the propagation time during which photons travel from the source to the DOM. The effects due to optical properties of the ice are also included with the use of absorption and scattering coefficient tables explained in Section 3.2.3.2. These photons arriving at a DOM are then converted into charges recorded by the PMT based on the single photoelectron (SPE) template discussed in Section 4.1.2; from all charges collected by all hit DOMs, the energy of the event can be estimated. In the reconstruction of an event, *Millipede* allows the vertex position (x, y, z), interaction time (t), lepton directions (θ, ϕ), and the energy (E) of the event to float.

For a cascade hypothesis with only one light source, *Millipede* performs a two layer minimization. In the outer layer, the log likelihood is minimized with respect to the vertex positions, lepton directions, and time of interaction. At each iteration of likelihood minimization, the deposit energy is internally minimized using a second minimizer. This two layer method helps save computational resources since reading coefficient tables is memory intensive. On the other hand, with a track hypothesis, *Millipede* divides a muon track into segments and places a light source at every 10 $\sim$ 15 m. Therefore, the expected number of photons at each DOM is a superposition of light produced by multiple cascade-like light sources along the track. Since each light source has a set of parameters contributing to the total log likelihood, minimizing

the log likelihood with a track hypothesis is time consuming and computationally heavy. At the end, *Millipede* returns seven best fit parameters that describe the energy and direction of the in-coming particle as well as the position and time of interaction.

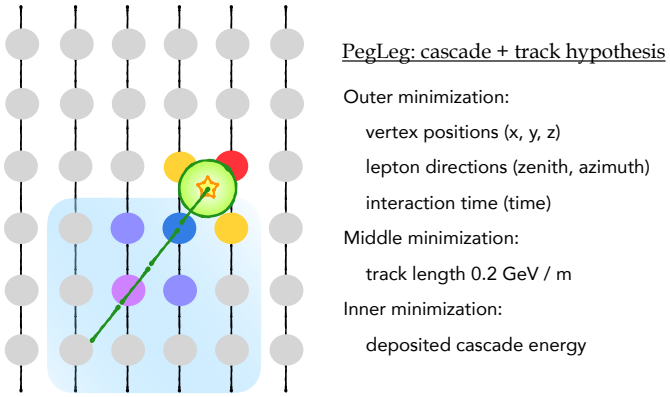

Figure 6.15: PegLeg reconstruction. Colors (from red to purple) represent DOM hit times (from earliest to latest), and the yellow star represents a vertex to be fitted. With a cascade (green circle) and a track (multiple green lines) hypothesis, PegLeg first minimizes the vertex positions, lepton propagation directions, and time of interaction. During each of the iteration, track length is internally minimized assuming the event is caused by a minimum ionizing muon. Within the track length minimization, the cascade energy is again internally minimized. The schematic diagram is not drawn in scale.

While *Millipede* is designed for reconstructing high energy events, *PegLeg* modifies the standard algorithm to work for low energy reconstruction. As its name suggests, *PegLeg* starts with a cascade at a vertex position and increments finite track segments along a specific direction. Since a minimum ionizing particle deposits $\sim$ 0.2 GeV every meter, the segments are set to be 5 m long. Similar to *Millipede*, *PegLeg* reconstructs an event in three layers. First, the same poisson log likelihood function is minimized with respect to six parameters: three for vertex positions, two for lepton directions, and one for interaction time. Here, the *MultiNest* mini-

mizer [226] is used to ensure global minimum is found[1]. The second layer happens within each iteration during the *MultiNest* minimization. At each step with the six parameters fixed, *PegLeg* performs a likelihood scan in the track length space. By adding and/or removing segments of tracks, a new likelihood value is calculated until this value converges. Within this track length scan, the third layer in the reconstruction is to optimize the cascade deposit energy at the vertex while all other parameters are fixed. At the end, the total energy of the event is the sum of cascade energy at the vertex and the track energy, which is linearly proportional to the track length.

In addition to track length minimization, the *PegLeg* algorithm also features a charge-independent reconstruction. As discussed in Section 5.1.2, the SPE template measured in laboratories and used in simulations is recently found to model the charge per DOM slightly incorrectly, introducing biases to the estimated charges in hit DOMs. Because observed charges is the basis of energy reconstruction, this bias in SPE template leads to a disagreement between data and MC in the reconstructed energy distribution; this is particular important for low energy events due to the limited information with fewer hit DOMs per event. To reduce the dependence and bias on observed charge during an event reconstruction, an observed charge by a hit DOM is replaced by a fixed charge of 1 PE for the next 45 ns during the third layer of minimization of optimizing cascade deposit energy. This modification shows minimal impact on angular and energy resolutions but improves agreements in histogram shapes between data and MC.

Angular and energy resolutions of *PegLeg* reconstruction for ν_μ events are shown in Figure 6.16. On the left, *PegLeg* performs reasonably well for events

[1]The *MultiNest* minimizer throws random points in the given parameter space, finds the log likelihood values, and builds a log likelihood space as more new points are thrown in. It is different from other common minimizers which find the local minimum around a seeded point.

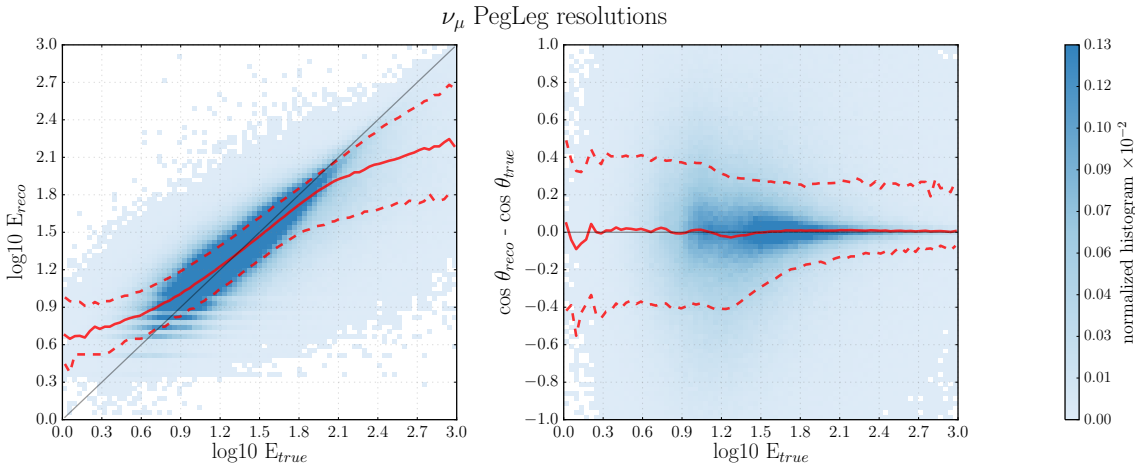

Figure 6.16: PegLeg resolution for ν_μ in GRECO Level 7: (left) normalized histogram of true and reconstructed log10 energies and (right) normalized histogram of cos zenith resolution and reconstructed cos zenith. Color bar represents the normalized rates. Thin red solid lines represent the median values from slices of true values, while the dashed lines are the 1σ deviations. Gray solid line represents the ideal case when reconstructed values are exactly the same as the truth. PegLeg performs well for events between 5 and 100 GeV.

with energies between $\sim$ 5 and 100 GeV with a narrow 1σ deviation. Above 100 GeV, *PegLeg* underestimates the true energy because muons at high energy are no longer minimum ionizing. The right side of Figure 6.16 shows that cos zenith has a relatively poor resolution with a much wider spread. Given that low energy events only hit a handful of DOMs, the directionality of a given event is hard to determine. However, events between 5 and 100 GeV still have reasonably good resolution.

The rate information is shown in Table 6.1. While no explicit cut is applied at Level 7, event rates are slightly dropped compared to Level 6. It is because events, in which *PegLeg* fails to converge, are rejected. In particular, noise triggered event rate is dropped by $> 95\%$ since no physical event is available for *PegLeg* to reconstruct.

6.6 Level 8 - Additional Cuts

After the PegLeg reconstruction, four additional cuts are applied. Two cuts are dedicated to further remove atmospheric muons, while the other two aims at improving agreement between data and MC.

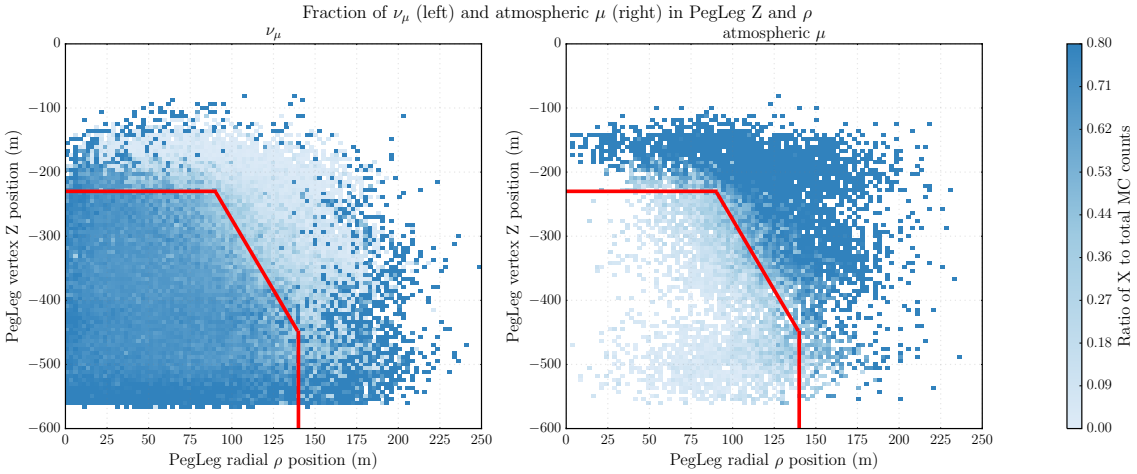

Figure 6.17: Two Dimensional Fraction of radial and vertical positions of PegLeg vertices in GRECO Level 8 (pre-cut): (left) fraction of ν_μ contribution to total MC (right) fraction of atmospheric μ contribution to total MC. Color bar represents the fraction of contribution from a flavor to total number of events. Most background muon events have reconstructed vertices away from DeepCore fiducial volume; therefore, a hard cut is applied to keep events with vertices inside the box defined by the three red lines.

More background muons are rejected using similar techniques as before. The first cut uses the vertical and radial position of the *PegLeg* reconstructed vertex. As shown in Figure 6.17, this containment cut is very similar to the one using *FiniteReco*. Because *PegLeg* is a more sophisticated reconstruction than *FiniteReco*, it is able to more accurately and precisely reconstruct where an interaction occurs. Events confined in the red box in Figure 6.17 are kept. The second cut also looks for correlations between two variables: the RMS of hit times and the averaged

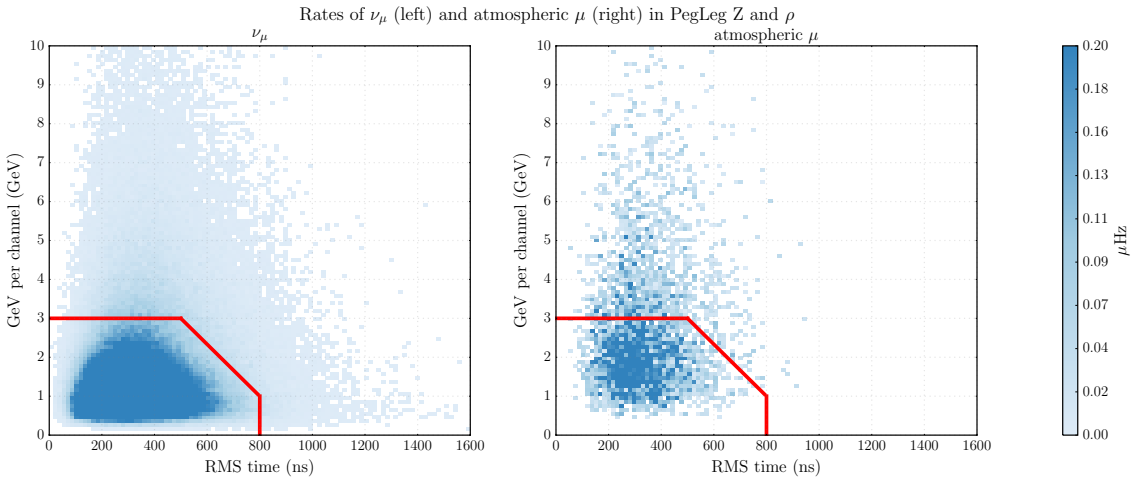

Figure 6.18: Two Dimensional Event Rates from in GRECO Level 8 (pre-cut): (left) rate of ν_μ (right) rate of atmospheric μ. Color bar represents the rate per bin of the corresponding flavor in μHz. The two variables are RMS of hit times in an event and the averaged *PegLeg* energy per hit. Only events with less than fourteen hits are taken into account. Compared to the distribution of μ, most ν_μ events cluster in the region with low averaged energy per hit and smaller RMS of hit time. Therefore, a cut is applied to keep events inside the box defined by the three red lines.

reconstructed energy by *PegLeg* per hit. For events with less than fourteen hits, ν_μ events are found to have a clearer clustering compared to background muons in the two dimensional histograms in Figure 6.18. Therefore, for events with less than fourteen hits, a cut is applied to keep events inside the region defined by the three red lines. Although this cut does not have a great separation power between signal and background events, it helps enhance the sample's purity.

Two final cuts are applied in order to improve agreement between data and MC. First, from the left plot in Figure 6.19, MC clearly disagrees with data at high normalized RMS of total charges, which corresponds to high energy events. While events with normalized RMS of total charges greater than 0.85 are removed from the final sample, this cut does not give much impact since those events rejected

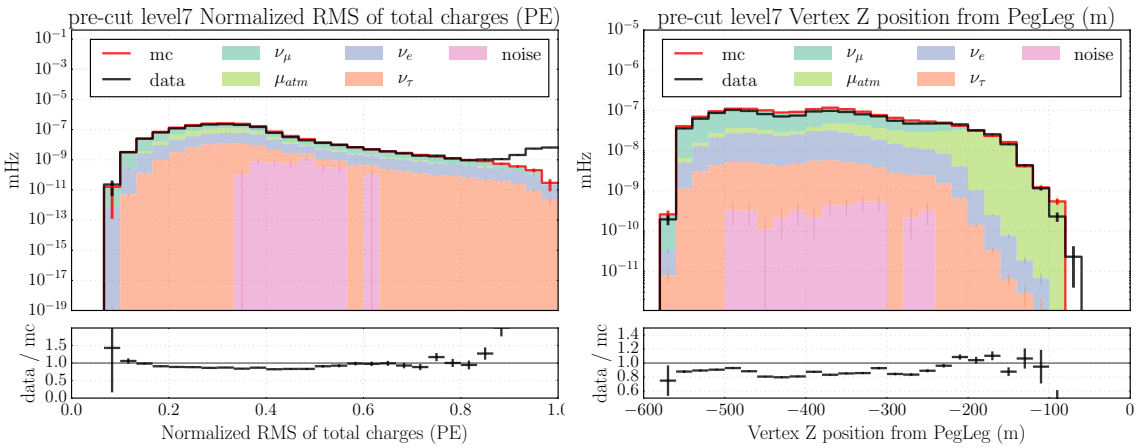

Figure 6.19: One Dimensional Distribution of Two Variables in GRECO Level 8 (pre-cut): (left) distribution of normalized RMS of total charges and (right) distribution of *PegLeg* reconstructed vertical position of vertex. Each shaded region represents the distribution of each flavor. The MC histograms are stacked and summed to the red solid lines, which are the total MC distributions. The black lines represent the data distributions. Based on the left plot, events with normalized RMSs of total charges beyond 0.85 PE are removed from the final sample. On the right plot, despite no apparent disagreement at the bottom of the detector, it was believed that not including bed rock in simulation chains worsens the goodness of fit when oscillation parameter measurement is performed. Therefore, events with reconstructed vertical position below -500 m are rejected.

contribute only a few percent of the total events. The second cut related to the vertex vertical position is less obvious. As discussed in Section 5.1.1, GENIE simulation assumes the entire Earth is made out of ice. This assumption is expected to mainly affect neutrino simulation at the bottom of the detector; however, it is hard to quantify the associated uncertainty without proper simulations. Therefore, despite no obvious disagreement at the bottom of the detector as shown on the right plot in Figure 6.19, events with reconstructed vertex vertical position below -500 m are rejected.

The rates from all flavors at final level are tabulated in Table 6.1. While the

containment cut using the vertex vertical and radial positions from *PegLeg* helps lower the background muon rates by $> 70\%$, the harsh cut on the vertical position unfortunately throws away $\sim 25\%$ of ν_μ signal events.

Table 6.1: Rates at Level 8 in mHz. Neutrino rates are calculated with the assumption that neutrinos oscillate according to the world averaged best fit oscillation parameters [209]. Muon rates calculated before Level 6 cuts are from *CORSIKA* events; after Level 6 cuts, muon rates are obtained from *MuonGun* events because *MuonGun* has more statistics.

Levels	Data	ν_μ	ν_e	ν_τ	μ	Noise	Data / MC
Level 2 (DeepCore Filtered)	19092	6.360	1.721	0.270	9178	8117	1.103
Level 3	1092	4.758	1.262	0.210	970	284	0.867
Level 4	68.592	2.503	0.783	0.134	52.251	11.963	1.014
Level 5	7.422	1.628	0.544	0.103	4.100	1.800	0.908
Level 6	1.841	1.011	0.362	0.073	0.315	0.102	0.988
Level 7	1.370	0.905	0.285	0.063	0.300	0.004	0.880
Level 8	0.871	0.680	0.233	0.051	0.080	0.002	0.834

Chapter 7: Systematic Uncertainties

This chapter focuses on systematic uncertainties that can affect the measurements of atmospheric neutrino oscillation parameters. Systematics discussed include atmospheric neutrino and muon fluxes in Section 7.1, parameters involved in the calculation of oscillation probability in Section 7.2, cross sections when neutrinos interact with the ice in Section 7.3, biases due to ice properties and optical sensors in Section 7.4, and overall normalization terms in Section 7.5. For each systematic, a brief description on the implementation is presented, as well as its effects on the energy and zenith distributions of signal ν_μ CC and/or background atmospheric muons. Some of the systematics are important to the measurements, while others are found to have negligible impacts on the sensitivity. Section 7.6 summarizes the systematic parameters included in this analysis along with their 1σ uncertainties.

7.1 Fluxes

As discussed in Chapter 2, when cosmic rays interact with the Earth's atmosphere, pions and kaons are produced and decay, giving out atmospheric neutrinos and muons. For muons, the GaisserH4a model [97] is used to determine the atmospheric muon flux. A shape uncertainty due to variations in atmospheric muon energy spectral index is implemented and discussed in Section 7.1.6. For every neutrino flavor, an atmospheric neutrino flux table is provided by Honda *et al.* [86]. Recalled from Section 5.1.4, the flux of a given simulated neutrino event is obtained

from the spline-interpolated flux table based on the energy and zenith angle of the given event. While neutrino flux uncertainties due to ν_e to ν_μ ratio (see Section 7.1.3) and atmospheric neutrino energy spectral index (see Section 7.1.4) are easy to implement, these neutrino flux tables do not provide a convenient way to implement neutrino flux uncertainties due to hadron production.

Instead, Barr *et al.* [227] discusses in great details neutrino flux uncertainties caused by variations in hadron production and primary flux. For determining neutrino flux uncertainties due to hadron production, Barr *et al.* considers a two dimensional parameter space given by the incident primary energy and the secondary meson energy. Since sources of variations in hadron production are different for different regions in the energies of primary and secondary particles, Barr *et al.* divides the two dimensional parameter space into regions, each of which corresponds to a dominate source of uncertainty. For a given region, an uncertainty is determined either from available data or by extrapolation of existing data. On the other hand, Barr *et al.* incorporates neutrino flux uncertainties due to primary flux via four parameters in the Gaisser, Stanev, Honda, and Lipari (GSHL) parameterization. Based on existing cosmic ray data, uncertainties are assigned to the four parameters. With the assigned uncertainties on hadron production and primary fluxes due to various sources, Barr *et al.* runs simulations many times; at each time, one of the uncertainty source is increased or decreased by the assigned uncertainty. Then, a total neutrino flux uncertainty is determined by summing up differences in quadrature between the rate obtained from one simulation to that without deviation. Most importantly, Barr *et al.* presents the uncertainties on $\nu_\mu/\bar{\nu}_\mu$, $\nu_e/\bar{\nu}_e$, and ratio of vertical to horizontal fluxes as functions of energy and zenith angle. These plots are adapted for this analysis to implement the $\nu/\bar{\nu}$ and *up / hor* neutrino flux uncertainties as discussed in Sections 7.1.1 and 7.1.2 respectively.

Last but not least, observed in data at final level, coincidence events are consid-

ered as a systematic source. Since the *GENIE* software does not simulate coincident muon events during a neutrino interaction, a coincident fraction nuisance parameter is introduced and discussed in Section 7.1.5.

7.1.1 ν to $\bar{\nu}$ Ratio

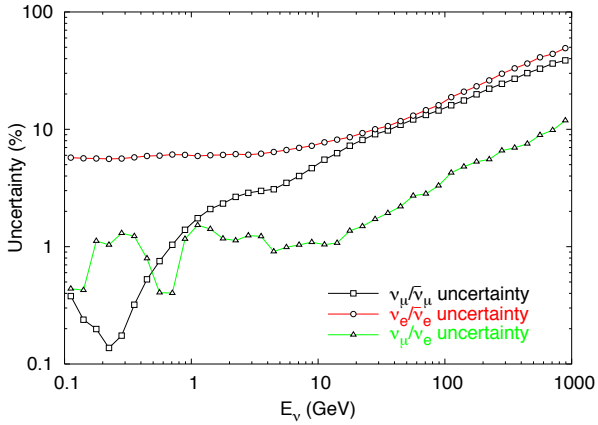

Figure 7.1: Uncertainties of Neutrino Fluxes As A Function of Energy. This plot is copied from [227]. Red line represents the uncertainty on $\nu_e/\bar{\nu}_e$, while the black line represents the uncertainty on $\nu_\mu/\bar{\nu}_\mu$. All uncertainties increase with neutrino energy. Higher energy neutrinos are produced from higher energy mesons, which have a higher chance to interact with air particles than to decay. Moreover, as energy increases, kaon decays become more important, and kaon production has large uncertainties.

According to the study done by Barr *et al.* [227], uncertainties on $\nu_\mu/\bar{\nu}_\mu$ and $\nu_e/\bar{\nu}_e$ flux ratios arise from both muon flight path in the atmosphere and a large uncertainty on kaon production. The black and red lines in Figure 7.1 show the uncertainties on neutrino flux due to $\nu_\mu/\bar{\nu}_\mu$ and $\nu_e/\bar{\nu}_e$ flux ratios as a function of energy. Both uncertainties increase from 3-6% at 5 GeV to above 10% at 60 GeV. In addition to their energy dependence, the two uncertainties also vary with zenith angle, which are shown in Figure 7.2 at two energy slices. For energy above 3

GeV, $\nu/\bar{\nu}$ uncertainties are larger for neutrinos from vertical directions than those from near the horizon; it is because vertical muons with shorter path lengths have a higher chance to hit the ground before they decay. For neutrinos with energies greater than 30 GeV, uncertainties from vertical neutrinos are twice as large as the ones from horizontal neutrinos due to the growing importance of koan production. At this high energy, interactions between pions and air particles start to dominate over pion decays. Thus, neutrinos from koan decays become the main atmospheric neutrino sources. Due to a large uncertainty on pion to kaon ratio, the uncertainties on $\nu/\bar{\nu}$ are larger at the vertical directions than that near the horizon.

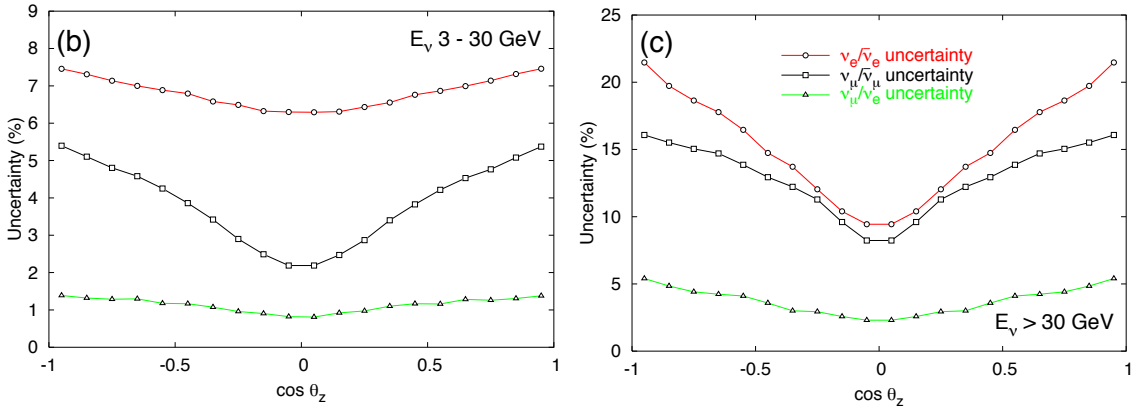

Figure 7.2: Uncertainties on neutrino fluxes due to $\nu/\bar{\nu}$ As A Function of Zenith Angle: (left) for neutrino energy between 3 and 30 GeV and (right) for neutrino energy above 30 GeV. This plot is copied from [227]. In general, neutrinos coming from near horizon have smaller $\nu/\bar{\nu}$ uncertainties than those from vertical directions. This asymmetry grows as neutrino energy increases because, at high energy, kaon decays become more important.

For this analysis, the black and red curves of Figures 7.1 and 7.2 are parameterized. For a given ν_μ or ν_e event, although its weight can be modified to any percentage values due to the uncertainty on $\nu/\bar{\nu}$ flux ratio, the corresponding black or red curve defines the 1σ range of this uncertainty for this event based on its

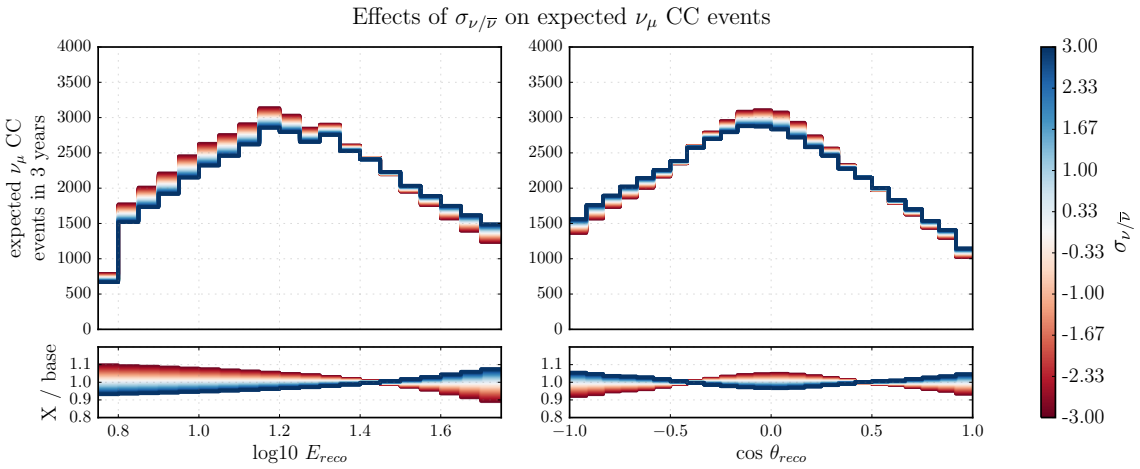

Figure 7.3: Effects of $\sigma_{\nu/\bar{\nu}}$ on ν_μ CC Histogram Shape: (left) ν_μ CC log10 reconstructed energy histogram and (right) ν_μ CC reconstructed cos zenith histogram. Histograms are built for a range of $\sigma_{\nu/\bar{\nu}}$. All histograms are normalized to the same total counts to look for effects on histogram shape. Ratio plots are with respect to the $\sigma_{\nu/\bar{\nu}} = 0$. From from -3$\sigma$ to 3σ, the shape of histogram is changed by within 1% in both energy and zenith distributions.

energy and zenith. Furthermore, to simplify its implementation, the uncertainty on $\nu_\mu/\bar{\nu}_\mu$ is assumed to be correlated to that on $\nu_e/\bar{\nu}_e$. Thus, one nuisance parameter on $\nu/\bar{\nu}$ flux ratio in a unit of σ is implemented for both flavors. Figure 7.3 shows the changes in the shapes of energy and zenith histograms for signal ν_μ CC when $\nu/\bar{\nu}$ [σ] goes from -3 to +3. As $\nu/\bar{\nu}$ [σ] increases, there are relatively more events at higher energy bins than that at lower energy bins. Similarly, the effect of $\nu/\bar{\nu}$ [σ] on the zenith histogram shape follows the shape of Figure 7.2.

7.1.2 Neutrino Vertical to Horizontal Flux Ratio

Similar technique is applied to determine the uncertainty of vertical to horizontal neutrino ratio for atmospheric ν_μ and ν_e fluxes. Figure 7.4 from Barr *et al.* [227] shows the uncertainty of up / down ratio is insignificant for neutrinos above a few

GeV. However, the uncertainty of up / horizontal flux ratio increases with neutrino energy from a few GeV to 1000 GeV for both ν_μ and ν_e shown as the green and blue curves respectively. At higher energy, vertical flux is more uncertain due to shorter path lengths; a denser atmosphere for mesons increases their chances to interact than to decay.

Assuming that the uncertainties on neutrino fluxes due to ν_μ and ν_e up / horizontal flux ratios are correlated, a nuisance parameter *up/hor* in a unit of σ is introduced such that *up/hor* $= 1$ corresponds to the parameterized green and blue curves in Figure 7.4 for ν_μ and ν_e events respectively. Again, the 1σ definition depends on the energy of a given ν_μ or ν_e event. As shown in Figure 7.4, the impacts due to *up/hor* $[\sigma]$ on the shapes of energy and zenith ν_e CC distributions are less than 3% for all bins when *up/hor* $[\sigma]$ goes from -3 to +3. Since the uncertainty of up / horizontal ν_μ flux ratio is smaller than that of ν_e in Figure 7.4, the expected impacts on the shapes of energy and zenith ν_μ CC distributions are even smaller.

7.1.3 ν_e to ν_μ Ratio

Unlike the systematics related to $\nu/\bar{\nu}$ and *up/hor* neutrino flux ratios, the uncertainty related to the ratio of ν_e to ν_μ flux ratio is implemented simply by the ratio of number of atmospheric ν_e to that of ν_μ. A nuisance parameter ν_e/ν_μ is introduced such that $\nu_e/\nu_\mu = 1$ is defined as the ν_e/ν_μ ratio from the Honda15 flux tables [86]. Since ν_e events concentrate in low energy and up going regions, having more ν_e relative to ν_μ increases the number of events in lower energy and up going bins, as shown in Figure 7.6. The shapes of energy and zenith distributions are changed by $\sim$5% given a ν_e/ν_μ range from 0 to 4. However, atmospheric ν_e/ν_μ ratio is fairly well measured. An earlier work by Honda *et al.* found an uncertainty of ν_e/ν_μ ratio less than 2% given an energy range from 0.1 to 100 GeV [87]. Despite its

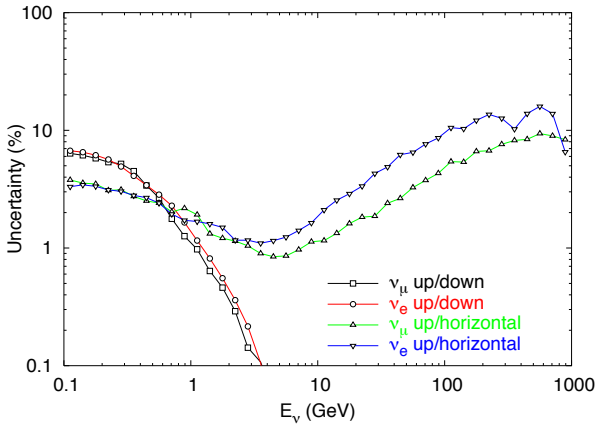

Figure 7.4: Uncertainties on neutrino fluxes due to Vertical to Horizontal Flux As A Function of Energy. This plot is copied from [227]. Uncertainties on the ratio of vertical to horizontal fluxes increase with increasing energy because mesons from vertical directions pass through a denser atmosphere, increasing the chance of meson interaction. Blue and green lines are used to define the 1σ range of *up/hor* $[\sigma]$ for ν_μ and ν_e fluxes.

heavy dependence on atmospheric density profile, the ν_e/ν_μ uncertainty over a year is small. Hence, a strong prior is applied with its 1σ penalty defined as a deviation of 0.05 from ν_e/ν_μ ratio = 1.

7.1.4 Neutrino Energy Spectral Index

The uncertainty due to the shape of the neutrino energy spectrum can be implemented via a shift in the spectral index $\Delta\gamma_\nu$. Mentioned in Section 5.1.4, the flux Honda15 table assumes an $E^{-2.66}$ energy spectrum [86]. As shown in Figure 7.7, shifting the spectral index from -3.16 to 2.16 causes a substantial change in the ν_μ CC energy distribution; some energy bins can change up to 50% when $\Delta\gamma_\nu$ goes from -0.5 to +0.5. However, similar to ν_e/ν_μ flux ratio, the energy spectral index for atmospheric neutrinos is also fairly well studied by other experiments. Therefore, the nuisance parameter $\Delta\gamma_\nu$ with a Gaussian prior centered at 0 has a strong 1σ

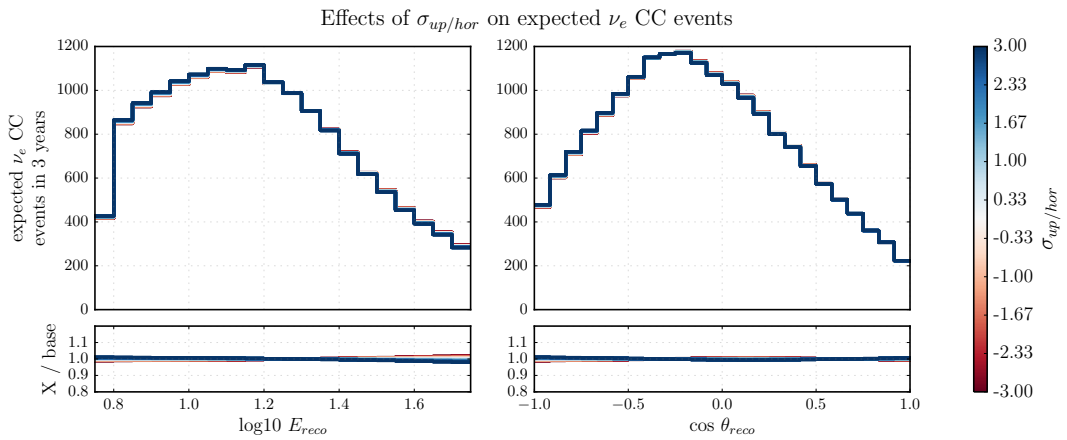

Figure 7.5: Effects of $\sigma_{\text{up/hor}}$ on ν_e CC Histogram Shape: (left) ν_e CC log10 reconstructed energy histogram and (right) ν_e CC reconstructed cos zenith histogram. Histograms are built for a range of $\sigma_{\text{up/hor}}$. All histograms are normalized to the same total counts to look for effects on histogram shape. Ratio plots are with respect to the $\sigma_{\text{up/hor}} = 0$. From from -3$\sigma$ to 3σ, the shape of histogram is barely changed by less than 3% for all bins.

penalty of 0.1.

7.1.5 Coincident Fraction

The last neutrino flux related uncertainty is introduced when coincident events are found in data at the final level of event selection. A coincident neutrino event is an event with one or more background atmospheric muon(s) detected during the time window of a neutrino interaction. However, this kind of events cannot be simulated by the *GENIE* software we currently use. To resolve this problem, a CORSIKA set is merged with a *GENIE* set to produce a coincident *GENIE* set in which all neutrinos are coincident events; this coincident set is then processed to final level.

Figure 7.8 shows the energy and zenith distributions from both 0% and 100% coincident ν_μ CC events. As the coincidence fraction increases from 0% (red curve)

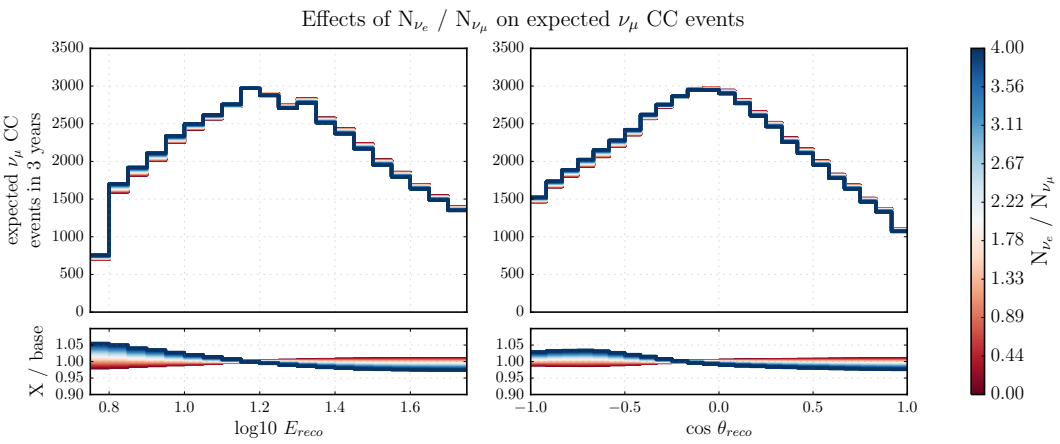

Figure 7.6: Effects of ν_e/ν_μ on ν_μ CC Histogram Shape: (left) ν_μ CC log10 reconstructed energy histogram and (right) ν_μ CC reconstructed cos zenith. Histograms are built for a range of ν_e/ν_μ relative to $\sim$ 1:2 ratio in Honda *et al.* [86]. All histograms are normalized to the same total counts to look for effects on histogram shape. Ratio plots are with respect to the $\nu_e/\nu_\mu = 1$. Varying ν_e/ν_μ changes the shapes of both distributions by less than 5%.

to 100% (blue curve), the energy distribution is slightly tilted towards the high energy side due to the presence of the coincident muon. At the same time, these extra down going muons contaminate down going ν_μ CC events. Since event selection is designed to remove down going events, more down going events are rejected in the case of 100% coincidence than that of 0%.

Given that previous IceCube analyses saw $\sim$10% coincident events in their final levels, this analysis using a much smaller detector volume is expected to see even less coincident events. Hence, a nuisance parameter, named coincident fraction, is introduced with a mean at 0% and its 1σ penalty defined to be 10%. In addition, since coincidence fraction cannot be negative, the prior of coincident fraction is one sided.

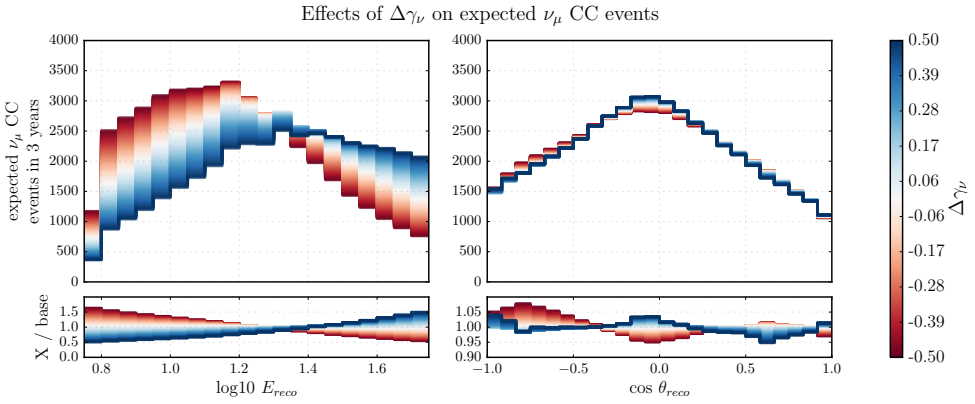

Figure 7.7: Effects of $\Delta\gamma_\nu$ on ν_μ CC Histogram Shape: (left) ν_μ CC log10 reconstructed energy histogram and (right) ν_μ CC reconstructed cos zenith. Histograms are built for a range of $\Delta\gamma_\nu$. All histograms are normalized to the same total counts to look for effects on histogram shape. Ratio plots are with respect to the $\Delta\gamma_\nu = 0$. By varying $\Delta\gamma_\nu$ between -0.5 and +0.5, the shape of energy histogram is changed by $\sim$50%; however, γ_ν is fairly well measured by other experiments. Thus, $\Delta\gamma_\nu$ is not expected to change drastically.

7.1.6 Atmospheric Muon Energy Spectral Index

In this analysis, the only uncertainty related to atmospheric muon flux is its energy spectral index based on [228]. In that study, a simple power law spectrum with a floating overall flux normalization and an energy spectral index is fit to external data from numerous cosmic ray experiments. From the power law fit, a 1σ deviation is derived as a function of primary proton energy. This deviation from primary flux is then propagated to an uncertainty of atmospheric muon flux as a function of muon energy using several *CORSIKA* sets. Because simulated atmospheric muon events by *CORSIKA* contain all the information when an air shower is produced, a 1σ uncertainty on each *CORSIKA* muon event can then by assigned from the primary flux uncertainty based on the muon energy. However, as discussed in Section 5.2.3, the more efficient *MuonGun* generator is preferred rather

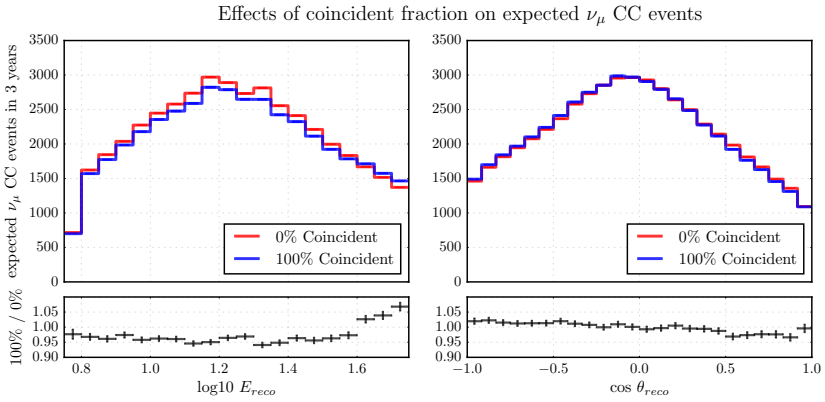

Figure 7.8: Effects of Coincident Fraction on ν_μ CC Histogram Shape: (left) ν_μ CC log10 reconstructed energy histogram and (right) ν_μ CC reconstructed cos zenith. Error bars are plotted in both distributions and ratio plots. Red lines represent the histograms from *GENIE* sets with no coincident events, while blue lines are the histograms from sets where all events are coincident. All histograms are normalized to the same total counts to look for effects on histogram shape. Ratio plots compare the set of 100% coincidence to that of 0%. The set with 100% coincident events slightly changes the shape of distributions towards higher energy and more up going.

than *CORSIKA*. Thus, the muon uncertainties from *CORSIKA* muon events are propagated on to the injection surface of *MuonGun* as discussed in Section 5.2.2. At the end, every *MuonGun* event is assigned a 1σ uncertainty based on its energy, direction, and injected depth.

Based on the above study, a nuisance parameter γ_μ in a unit of σ is introduced. By varying γ_μ [σ] from -5 to +5, a greater impact is observed on the shape of atmospheric muon zenith distribution than that of the energy distribution (see Figure 7.9). Although veto algorithms during event selection are good at recognizing vertically down going muon events, events from above the horizon but not vertically down are less obvious to be identified. According to the zenith distribution in Figure 7.9, while events in the up going bins, where $\cos\theta_{\text{reco}} < 1$, are most likely due to

mis-reconstruction, less than 5% change in event counts per bin is expected from a wide range of γ_μ [σ].

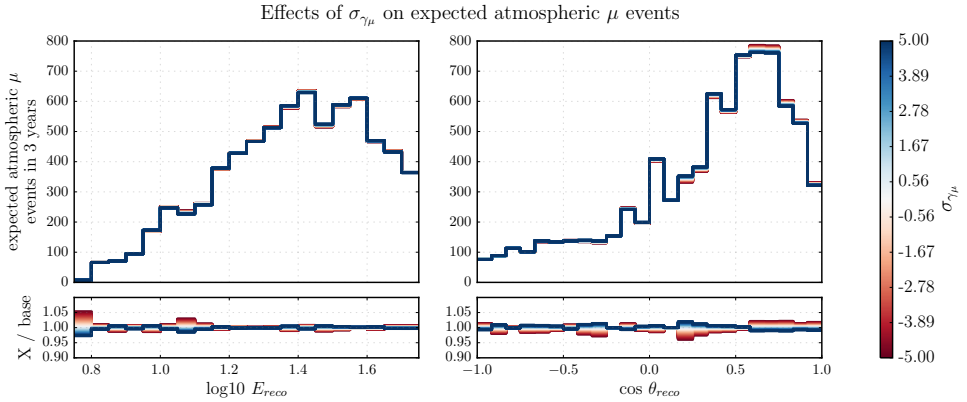

Figure 7.9: Effects of σ_{γ_μ} on μ Histogram Shape: (left) μ log10 reconstructed energy histogram and (right) μ cos reconstructed zenith histogram. Histograms are built for a range of σ_{γ_μ}. All histograms are normalized to the same total counts to look for effects on histogram shape. Ratio plots are with respect to the $\sigma_{\gamma_\mu} = 0$. From -5σ to +5σ, the shape of histogram is changed by at most 5%. Despite its small effects on the μ histograms, σ_{γ_μ} is still included in this analysis to provide the only uncertainty related to atmospheric μ flux.

Three important points are noted regarding to the implementation of this systematic related to atmospheric muon energy spectral index. First, unlike the case of γ_ν, the parameter related to this uncertainty is in a unit of σ based on the spectral power law fit; it is not the spectral index itself. Second, since the power law fit includes the flux normalization term, the γ_μ [σ] parameter in this analysis can only affect the shape of the muon histogram but not the overall normalization in order to avoid degeneracy. Third, although it barely changes the shape of atmospheric muon histograms as shown in Figure 7.9, this parameter is still included because it is the only uncertainty related to atmospheric muon flux.

7.2 Oscillation Probability

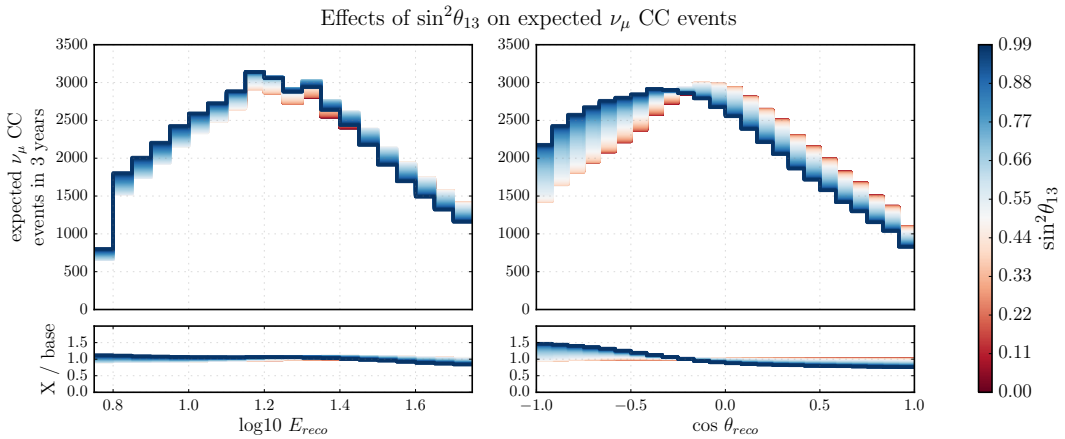

Figure 7.10: Effects of θ_{13} on ν_μ CC Histogram Shape: (left) ν_μ CC log10 reconstructed energy histogram and (right) ν_μ CC reconstructed cos zenith. Histograms are built for a range of $\sin^2\theta_{13}$. All histograms are normalized to the same total counts to look for effects on histogram shape. Ratio plots are with respect to the νfit global fit $\sin^2\theta_{13}$ value of 0.0218 [1]. Despite a drastic difference in histogram shape from $\sin^2\theta_{13}$ = 0 to ∼1, its 1σ range is ± 0.001 [1], which is too small to have any impact on histogram shape.

This analysis assumes three neutrino oscillations, of which the oscillation probabilities calculation includes θ_{12}, θ_{13}, Δm^2_{21}, and δ_{CP}. As discussed in Chapter 2, θ_{12} and Δm^2_{21} are related to $\nu_e \rightarrow \nu_\mu$ oscillations, which dominates at the MeV energy scale. Because of the spacings among optical sensors in IceCube-DeepCore, we are not sensitive to events below a few GeV. On the other hand, the effects of δ_{CP} is observed via comparing oscillation patterns between neutrinos and anti-neutrinos at below MeV energy scale, which cannot be detected by IceCube-DeepCore. Therefore, uncertainties on predicted neutrino rates due to solar neutrino oscillation parameters and CP violating phase are not taken into account.

Due to its small numerical value, the remaining parameter θ_{13} is found to have

no impact on this analysis. Technically, IceCube is sensitive to $\nu_e \rightarrow \nu_\tau$ oscillations. Figure 7.10 shows the change in the shape of ν_μ CC energy and zenith distributions for a range of $\sin^2\theta_{13}$ from 0 to ∼1. However, according to 2014 νfit global fit [1], the global best fit value for $\sin^2\theta_{13}$ is 0.0218 with a small 1σ range of ± 0.001. Therefore, ν_μ CC histogram is barely impacted within the 1σ range. Moreover, its effect on the sensitivities of this analysis is studied and found to have insignificant impact; thus, this parameter is not included for this measurement analysis.

7.3 Cross Sections in the Ice

Recalled from Section 3.2.1, a neutrino interaction can either be charge current (CC) or neutral current (NC). For neutrino NC interactions, a ν NC / ν_μ CC normalization is implemented as a systematic at a prior mean of 1. and a 1σ penalty width of 20%. On the other hand, the dominant neutrino CC interaction processes with the ice are quasi-elastic scattering (QE), resonance production (RES), and deep inelastic scattering (DIS). Uncertainties on neutrino predicted rates due to QE and RES are implemented using information from the *GENIE* software, whereas DIS systematics for both neutrinos and anti-neutrinos are found to have insignificant impact.

As mentioned in Section 5.1.1, when a QE or a RES neutrino event is generated, the *GENIE* software provides a weight for the event assuming a default value of the corresponding axial mass, which are 0.99 and 1.12 GeV for QE and RES interactions respectively [202]. In addition, the neutrino generator conveniently provides four extra weights for this event, each of which corresponds to an axial mass deviated by -2, -1, +1, or +2 σ(s) away. For QE axial mass, -1σ and $+1\sigma$ are defined as -15% and +25% from the default value; for RES axial mass, $\pm 1\sigma$ corresponds to a $\pm 20\%$ change from the default axial mass [202]. These four weights are then

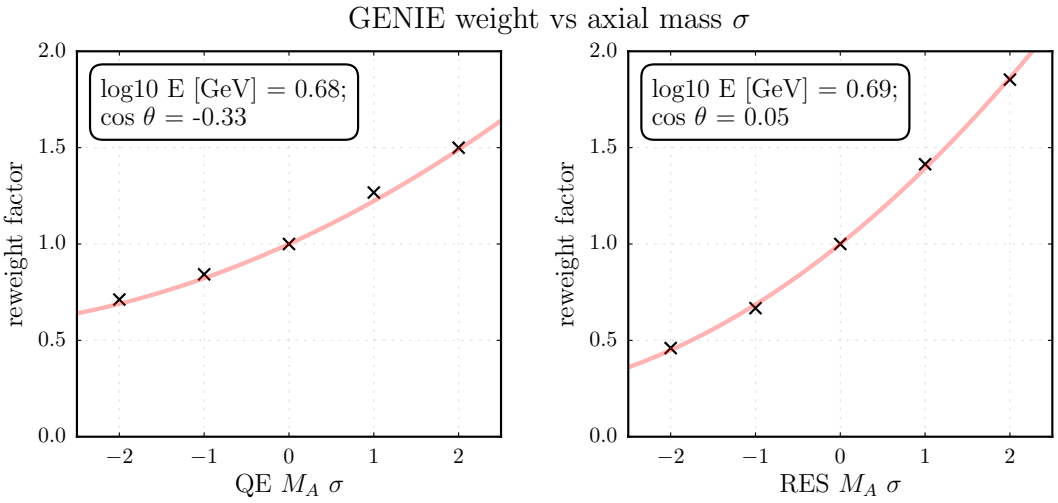

Figure 7.11: Examples of weight parameterizations in terms of axial mass deviations for one QE and one RES events: (left) re-weighting factors as a function of QE axial mass deviation for a QE ν_μ event and (right) re-weighting factors as a function of RES axial mass deviation for a RES ν_μ event. For each QE or RES neutrino simulated event, five weights due to a range of axial mass deviations are provided. They are divided by the weight with no axial mass deviation to obtain five re-weighting factors, which is parameterized as a function of axial mass deviation. The fitted parabola for each event is then used to scale the event weight at a given axial mass σ deviation.

converted into re-weighting factors by taking their ratios with respect to the weight with no axial mass deviation. The re-weighting factors are parameterized using a parabola function. Figure 7.11 shows the parameterizations of re-weighting factors as functions of axial mass σs for one of QE ν_μ events and one of RES events. For a given value of QE or RES axial mass σ, the weight of an event is therefore multiplied by the corresponding re-weighting factor obtained from the fitted parabola.

Two nuisance parameters are therefore introduced: *axm qe* [σ] for QE axial mass and *axm res* [σ] for RES axial mass. Both are in units of σ defined by the *GENIE* generator [202]. Figures 7.12 and 7.13 show the effects on ν_μ CC energy and zenith histograms when QE and RES axial masses are varied from -3σ to +3σ

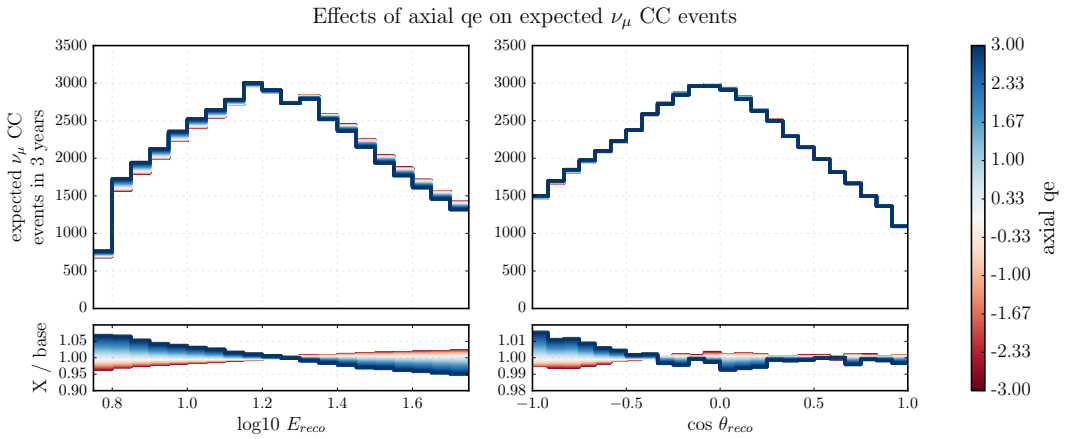

Figure 7.12: Effects of QE Axial Mass on ν_μ CC Histogram Shape: (left) ν_μ CC log10 reconstructed energy histogram and (right) ν_μ CC reconstructed cos zenith. Histograms are built for a range of QE Axial Mass in unit of σ. All histograms are normalized to the same total counts to look for effects on histogram shape. Ratio plots are with respect to the histogram with the default QE axial mass value used in *GENIE* software. Both energy and zenith histogram changes shape as the QE axial masses go from -3σ to 3σ.

respectively. As the axial masses increase, the energy histograms are tilted from more high energy events to more low energy events. Although both axial masses have the similar effects on energy and zenith histograms, their orders of magnitudes are slightly different. Therefore, both QE and RES systematics are included in this analysis.

On the other hand, uncertainties related to ν and $\bar{\nu}$ DIS are implemented based on a study [229] where the shape of differential DIS cross section obtained from *GENIE* is fitted to that from NuTeV[1] data. The published DIS study from NuTeV [231] presents the differential DIS cross sections in terms of inelasticity y, defined in Equation 3.41 in Section 3.2.1.3, for several values of Bjorken scaling variable x. Since the *GENIE* software also provides the Bjorken scaling variable for

[1]As a long baseline neutrino experiment located at Fermilab, NuTeV studies collision between an iron target and ν_μ and/or $\bar{\nu}_\mu$ beams at an energy range between 30 and 500 GeV [230].

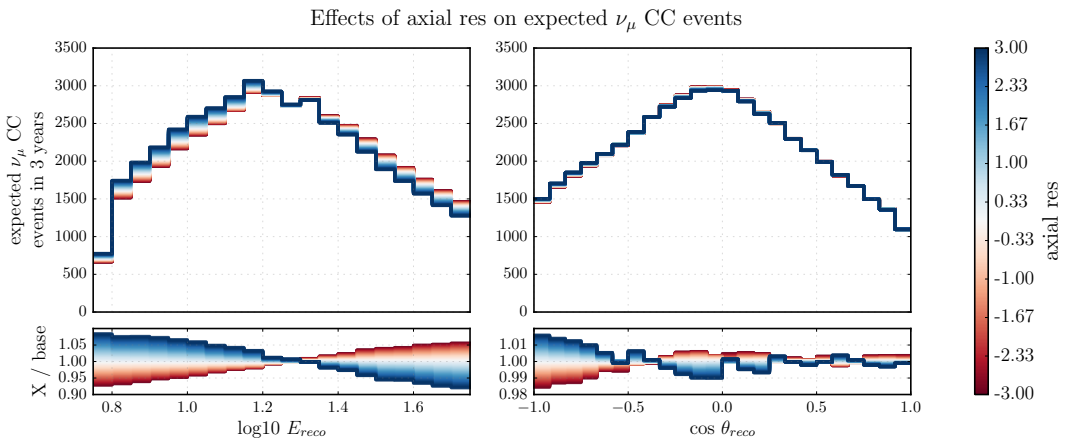

Figure 7.13: Effects of RES Axial Mass on ν_μ CC Histogram Shape: (left) ν_μ CC log10 reconstructed energy histogram and (right) ν_μ CC reconstructed cos zenith. Histograms are built for a range of RES Axial Mass in unit of σ. All histograms are normalized to the same total counts to look for effects on histogram shape. Ratio plots are with respect to the histogram with the default RES axial mass value used in *GENIE* software. Both energy and zenith histogram changes shape as the RES axial masses go from -3σ to 3σ.

every DIS neutrino event generated, a study [229] is then performed to match the shapes of differential DIS cross sections from *GENIE* events and those from NuTeV data [231]. This matching is done separately for neutrinos and anti-neutrinos. Once the shapes match, the 1σ variation on the weight of a given neutrino event due to its DIS cross section is then defined to be the shape difference between the two differential cross sections [229].

From the DIS study by NuTeV [231], the uncertainty on the world averaged differential DIS cross section is ∼2-3% for neutrino energies between 30 to 300 GeV. Hence, their effects on the energy and zenith ν_μ CC distributions are small (see Figure 7.14). Since these two parameters, one for neutrinos and one for anti-neutrinos, give insignificant impact on the sensitivities of this oscillation parameter measurements, differential DIS parameters are not included in this analysis.

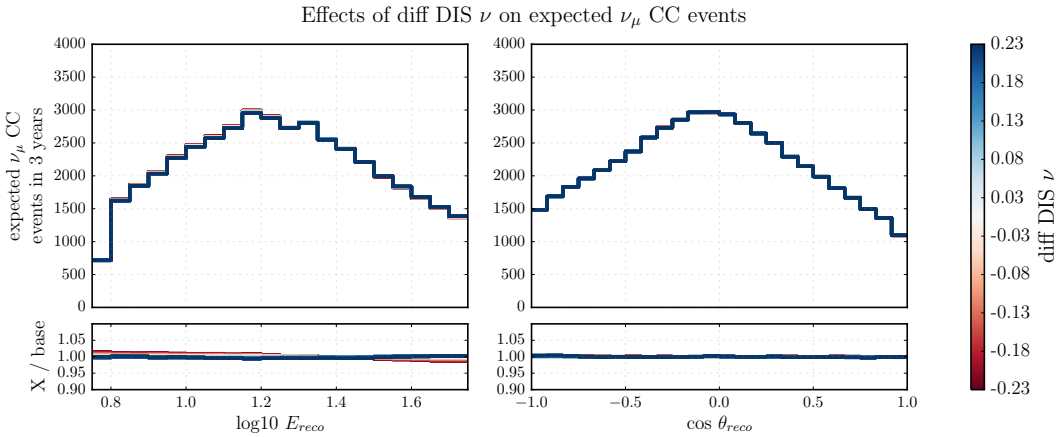

Figure 7.14: Effects of DIS on ν_μ CC Histogram Shape: (left) ν_μ CC log10 reconstructed energy histogram and (right) ν_μ CC reconstructed cos zenith. Histograms are built for a range of DIS parameters. All histograms are normalized to the same total counts to look for effects on histogram shape. Ratio plots are with respect to the histogram with DIS parameter = 0. Neither energy nor zenith histogram changes its shape as the DIS parameter changes. The effect due to DIS on $\bar{\nu}_\mu$ events is similar.

7.4 Detector Related Uncertainties

IceCube-DeepCore is built by deploying optical sensors into a large volume of ice. As discussed in Section 4.2, the optical efficiencies of DOMs are carefully studied both in laboratories and *in situ*. Results from these studies are adapted for the implementation of systematic uncertainty due to DOM optical efficiency (see Section 7.4.1). Moreover, as explained in Section 3.2.3, optical properties of the ice can be classified into global and local properties. Implementations of systematics related to bulk ice properties, including photon absorption and scattering lengths, are discussed in Section 7.4.2. Local optical properties due to air bubbles along deployed strings are also explained in Section 7.4.3.

7.4.1 DOM Optical Efficiency

As discussed in Section 5.4, variations in predicted rates from uncertainties due to DOM efficiency are determined via simulating MC sets for a range of DOM efficiencies. However, variations in event rates also depend on the energies and zenith angles of the events. Therefore, instead of the total rates, event counts given three years of data as a function of DOM efficiency are presented in slices of energy and zenith angle ranges in Figure 7.15. In general, with more efficient DOMs, more photons in an event are detected. Hence, more information is given to various reconstruction algorithms to better identify the event type. Therefore, at final level of the event selection, more signal ν_μ CC events and less background μ events are kept in all energy and zenith slices. Moreover, the top left and bottom left plots in Figure 7.15 shows the changes in ν_μ CC and background muon event counts for different energy slices. For both plots, more signal and background events between 10 and 32 GeV are kept because event selection is trained to keep as much signal events as possible; these signal events concentrate at an energy of $\sim$25 GeV at which the amplitude of atmospheric neutrino oscillations is expected to be maximal. Similarly, the two right plots show that more events coming from the horizon are kept comparing to that from vertically up going and down going. It is because particles traveling across the detector horizontally have more hit DOMs than those traveling vertically.

A nuisance parameter *DOM efficiency* is therefore implemented with a prior mean centered at a measured efficiency from earlier tests using surplus DOMs in laboratories. The latest study in the North measured a quantum efficiency of 25% at the center of PMT using a light source at 390 nm [188]. Later, an *in situ* measurement found that the central value of the DOM efficiency should be 10% higher than the lab result [188]. This new definition of DOM efficiency baseline value is

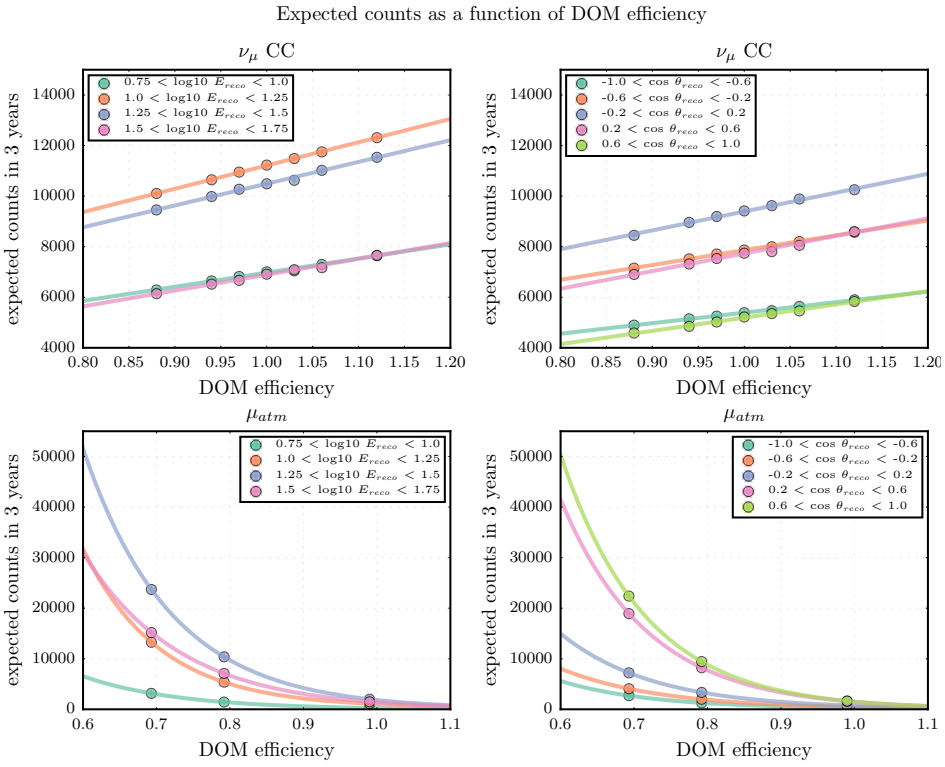

Figure 7.15: Expected Counts As a Function of DOM Efficiency: (top left) expected ν_μ CC counts in log10 energy slices, (top right) expected ν_μ CC counts in cos θ slices, (bottom left) expected atmospheric μ counts in log10 energy slices, and (bottom right) expected atmospheric μ counts in cos θ slices. With more efficient DOMs, more information about an events is known, which helps identify its flavor type. Since event selection is designed to keep signal events and remove background events, expected neutrino rate increases and muon rate decreases at final level as a function of DOM efficiency.

the prior mean for the nuisance parameter *DOM efficiency*. The corresponding 1σ penalty is defined as 10% of the prior mean.

7.4.2 Bulk Ice

As explained in Section 3.2.3.2, the current best ice model is obtained by fitting simulations to flasher data [179]. The resultant best fit scattering and absorption coefficients as a function of depth layers are stored in tables and used for simulating

photon propagations. Similar to the case of *DOM efficiency*, uncertainties in event counts due to absorption and scattering coefficients are estimated by generating multiple simulation sets. Each of these sets assumes a scaling factor multiplied to the coefficient tables.

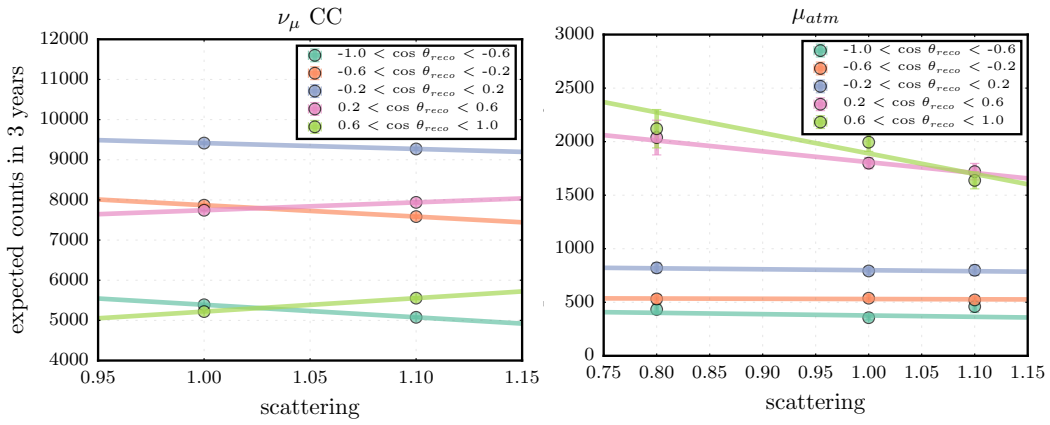

Figure 7.16: Expected Counts As a Function of Scattering in Cos θ Slices: (left) expected ν_μ CC counts and (right) expected atmospheric μ counts. A higher scattering coefficient means more scattering, which reduces the number of up going particles and increases the number of down going particles.

The effects on expected event counts in several zenith ranges due to photon scattering and absorption are shown in Figures 7.16 and 7.17 respectively. With a higher scattering coefficient, more photons are scattered away from their original paths along the propagation of the lepton. More photons from an up going lepton are scattered down, and less light reaches the DOMs because the photomultiplier tubes (PMTs) inside the DOMs face down. This reduces the expected number of up going ν_μ CC events after the event selection. Moreover, with more scattering, down going events have more photons scattered up; hence, the expected down going event counts

increase. Similarly, given a higher absorption coefficient, more photons are absorbed as they propagate from the light sources to the DOMs. Thus, less information is received to identify the event type, causing a decrease and an increase in expected ν_μ CC and atmospheric muon counts respectively at the final level. This effect is relatively more dramatic for down going events because less back-scattered photons can be detected with the PMTs facing down.

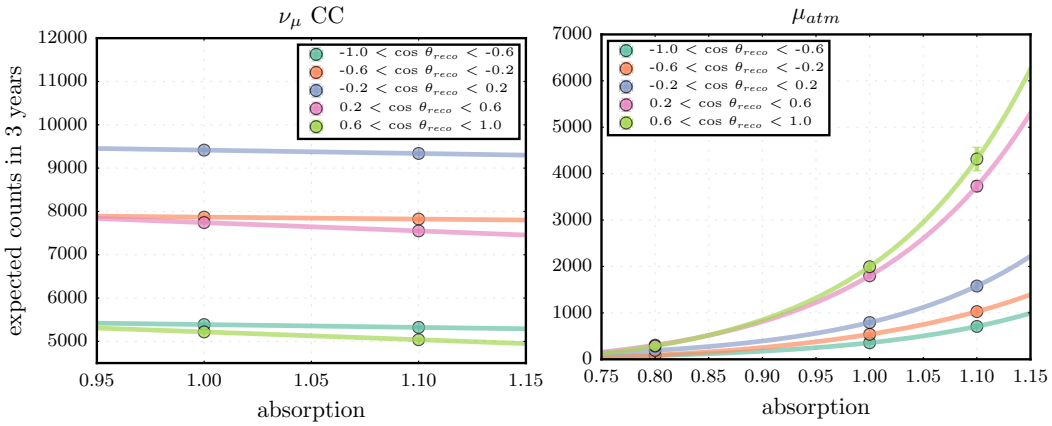

Figure 7.17: Expected Counts As a Function of Absorption in Cos θ Slices: (left) expected ν_μ CC counts and (right) expected atmospheric μ counts. A higher absorption coefficient means more absorption. More photons get absorbed along their propagation, giving less information for event selection and reconstruction. This reduces the number of signal events and increases the number of down going particles.

Two nuisance parameters are needed to describe global optical properties: absorption scaling factor α_{abs} and scattering scaling factor α_{sca}. While these scaling factors are with respect to the corresponding coefficient tables, each scaling factor has a total uncertainty of $\sim 10\%$ [179], which is used as the definition of 1σ penalty for this analysis. In addition, as shown on the right plot in Figure 3.24, photon

absorption and scattering are anti correlated [179]. This special relation is handled by an analysis technique explained in Section 8.1.2.

7.4.3 Hole Ice

As discussed in Section 3.2.3.1, the effect of air bubble columns is decoupled from the general absorption and scattering properties of the ice [179]. Not only does the bubble column of one string has negligible impact on photon propagations around a neighboring strings, air bubbles along a string in general only change the directions of the incoming photons. Hence, the two systematics due to ice properties and bubble columns are treated independently. The current hole ice model [179] describes the local scattering effects through a photon angular acceptance curve by a DOM (see Figure 3.21). Two parameters are used to introduce variations to the angular acceptance curve. The first parameter is the hole ice parameter p which adjusts the overall shape of the acceptance curve, while the second one is the hole ice forward parameter $p2$ which controls the acceptance of normally incident photons.

Similar to other detector related systematics, simulation sets are generated to predict the effects due to air bubbles on expected event counts. As shown in Figure 7.18, the effect of hole ice parameter p on expected event counts is very similar to that of scattering coefficient shown in Figure 7.16 since air bubbles introduce extra scattering effect around a DOM. On the other hand, Figure 7.19 shows how the hole ice forward parameter $p2$ changes the expected event counts. According to the photon acceptance curves in Figure 3.21, a higher value of $p2$ means more photons are distributed directly up facing the PMTs. Thus, up going events are easier to be identified, increasing the expected number of up going events.

Both the hole ice parameter p and the hole ice forward parameter $p2$ are included as nuisance parameters in this analysis. The hole ice model [179] found

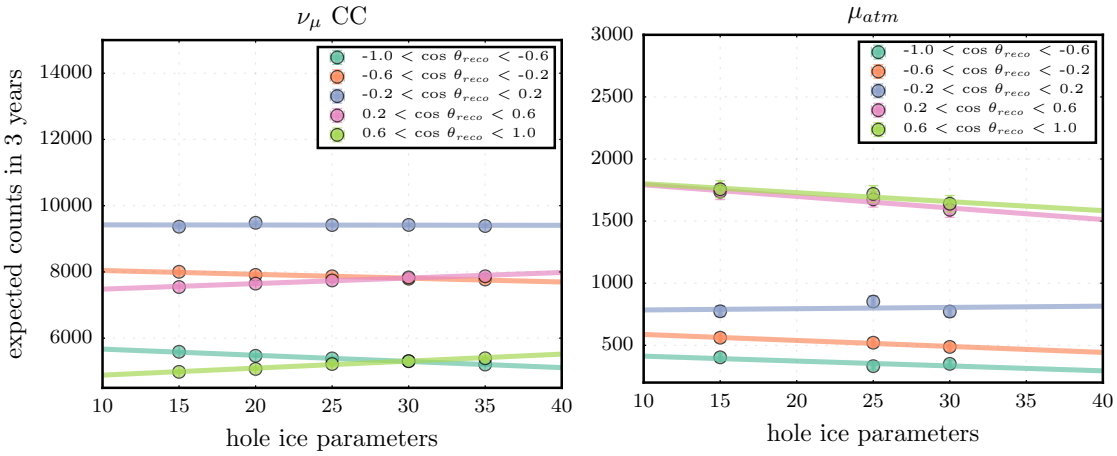

Figure 7.18: Expected Counts As a Function of Hole Ice Parameter in Cos θ Slices: (left) expected ν_μ CC counts and (right) expected atmospheric μ counts. A larger value of hole ice parameter means more scattering, which reduces the number of up going particles and increases the number of down going particles.

that the numerical value of p lies between 15 cm and 35 cm with a best fit of $\sim$ 25 cm. However, the hole ice study [179] fixes the hole ice forward parameter $p2$ at 0. To allow extra freedom for normally incident photons near cos $\eta \sim 1$ (see the left plot in Figure 3.21), this forward parameter $p2$ is allowed to float without any prior applied.

7.5 Normalizations

Finally, two overall normalizations are introduced as nuisance parameters to freely scale total number of ν_μ CC and atmospheric muon events. It is because we do not have an accurate measurement of their absolute fluxes. Moreover, ν_τ CC normalization is fixed to be one because a unitary MNS mixing matrix is assumed

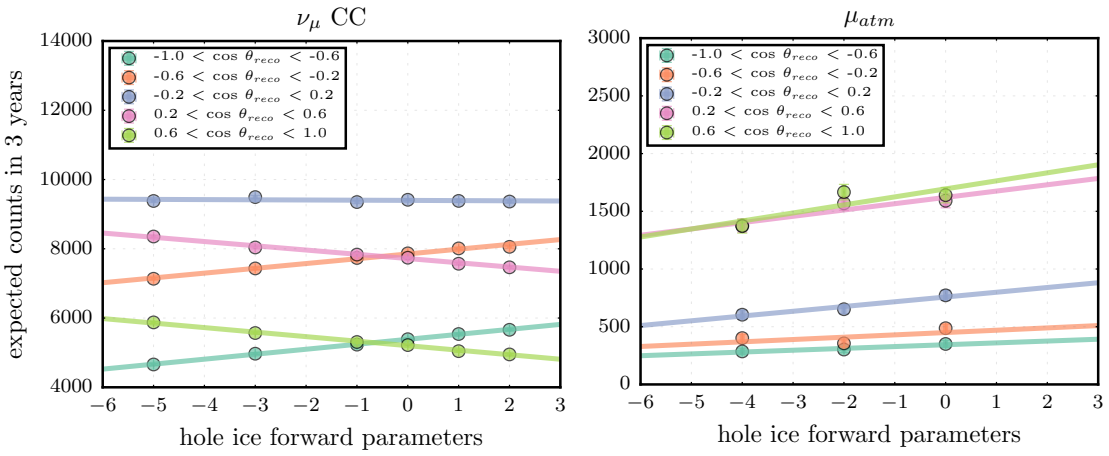

Figure 7.19: Expected Counts As a Function of Forward Parameter in Cos θ Slices: (left) expected ν_μ CC counts and (right) expected atmospheric μ counts.

in this analysis. Lastly, because noise contributes less than 1% to the total expected counts at final level, whether noise normalization is fixed or allowed to float during minimization gives zero impact on the result. Therefore, normalization of noise is also fixed to one.

7.6 Summary

In summary, a total of sixteen nuisance parameters are considered in this analysis. Six parameters are related to atmospheric fluxes; three are related to cross sections of neutrinos interaction with the ice; two are normalization terms; and five are related to the uncertainties due to the detector. Table 7.1 summaries the prior means and their 1σ definitions.

Table 7.1: A summary of systematics included in this analysis.

Parameters	Units	Prior Means	1σ Penalty
Flux Related Systematics			
γ_μ	σ	0.0	± 1.0
γ_ν	Δ from -2.66	0.0	± 0.1
ν_e/ν_μ	σ	1.0	± 0.05
$\nu/\bar{\nu}$	σ	0.0	± 1.0
up / hor	σ	0.0	± 1.0
coincident fraction	%	0.0	$+0.1$
Cross Section Related Systematics			
RES	σ	0.0	± 1.0
QE	σ	0.0	± 1.0
N_{NC}/N_{CC}	-	1.0	± 0.2
Normalization Systematics			
N_{ν_μ} CC	w.r.t expected ν_μ CC counts	-	-
N_μ	w.r.t expected μ_{atm} counts	-	-
Detector Related Systematics			
DOM efficiency	w.r.t $\sim 35\%$	1.0	± 0.1
hole ice parameter	cm	25	± 10
hole ice forward parameter	-	-	-
absorption scaling factor α_{abs}	w.r.t. absorption coefficient table	1.0	± 0.1
scattering scaling factor α_{sca}	w.r.t. scattering coefficient table	1.0	± 0.1

Chapter 8: Analysis Method

The measurement of atmospheric neutrino oscillation parameters performed in this dissertation is done using a binned χ^2 method. Given that the oscillation probability of a neutrino depends on its energy, propagation length, and flavor, events at final level are binned by reconstructed energy, direction, and track length. Section 8.1 discusses in details the construction of the Monte Carlos (MC) histograms. Final templates predicted by MC are then compared to that from data; these templates assume some injected values of oscillation parameters, which are allowed to float when fitting to data. As explained in Section 8.2, a modified χ^2 is used to quantify, bin by bin, the statistical differences between observed and predicted counts. The best fit histogram is then found via minimizing the χ^2 while taking sixteen systematic uncertainties into account (see Section 8.4). The corresponding p-value is then determined from many fluctuated trials, as discussed in Section 8.5.

The above describes the procedure to find the best fit oscillation parameters; yet, the most important aspect of a measurement analysis is the confidence level of those measured parameters, which is discussed in Section 8.6. Final expected sensitivity is presented in Section 8.6.1, and the impacts on sensitivity due to systematics are also studied in Section 8.6.2. Last but not least, further tests on the fitter's robustness are shown in Section 8.6.3.

8.1 Construction of Final Templates

This section covers the construction of final templates. Settings for analysis histogram binning, including observables and bin sizes, are explained in Section 8.1.1. Then, Section 8.1.2 describes a multi-dimensional technique called Hyperplane, which provides a continuous space for all discrete parameters. Final template used for the analysis are presented in Section 8.1.3.

8.1.1 Binning

Because the oscillation probability of a neutrino depends on its energy, propagation length, and event type, data are binned in energy, zenith, and particle identification respectively.

For a vertically down going atmospheric ν_μ, the amplitude of $\nu_\mu \rightarrow \nu_\tau$ oscillations is maximized at 25 GeV. Thus, the energy range for this analysis covers events from 5.6 to 56 GeV in log10 space: $0.75 \leq \text{log10 E} < 1.75$. Based on the energy resolution from PegLeg reconstruction, eight energy bins are considered. The comparison between energy resolutions and bin sizes is shown on the left of Figure 8.1. Overall, the energy bins are roughly the same size as the energy resolutions. The contamination from high energy neutrino events sneaking into the energy range is also found to be negligible.

The second observable is the distance of neutrino propagation, which is related to cosine of the neutrino zenith angle, $\cos\theta$, based on the geometry of the Earth. Figure 8.2 demonstrates the conversion. By the law of cosines, the neutrino propagation length, L, can be expressed in terms of the radius of the Earth (6378.2 km), the height of the atmosphere from ground (20 km), and $\cos\phi$, which is related to the neutrino zenith angle, $\sin\theta$, according to the law of sines. Although most

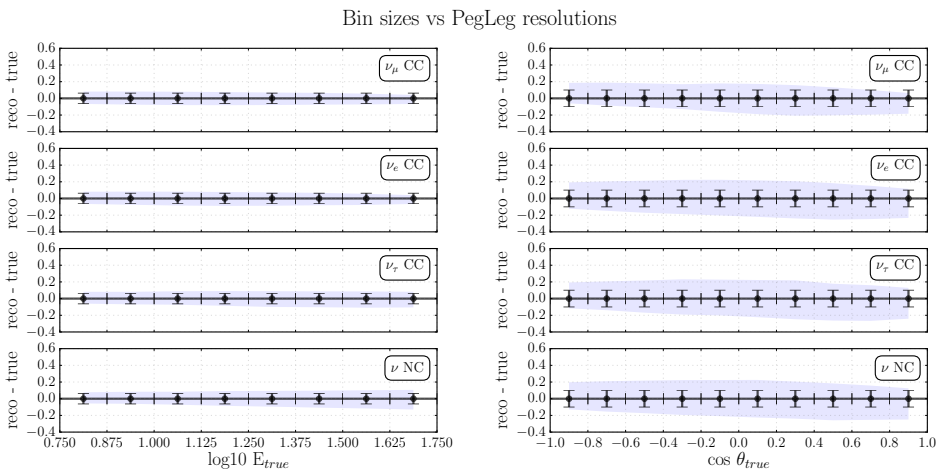

Figure 8.1: Comparison between bin sizes and PegLeg resolutions: (left) log10 energy and (right) cos zenith angle. Each plot corresponds to a neutrino flavor. Black error bars are the bin sizes. Shaded bands represent the 1σ width from the means, which are subtracted off of the differences between reconstructed and true values. Bin sizes for energy are roughly the same size as the resolution, but cos zenith angle bin sizes are slightly smaller than the cos zenith resolution.

of the signal ν_μ events come from the northern sky, including down going events can increase statistics of background atmospheric muons, which helps model the background template. Therefore, the cos θ range for this analysis is between -1 (i.e. vertically up going) and 1 (i.e. vertically down going) to include events from both the southern and the northern hemisphere. A total of 10 cos zenith angle bins are considered. Although the bin sizes are in general slightly smaller than the cos zenith angle resolutions from PegLeg reconstruction (see the right plot of Figure 8.1), no bias would be introduced because PegLeg reconstruction treats data and MC events the same way, and events from all sky are included in the analysis.

The third observable for the measurement of atmospheric neutrino oscillation parameters is event type. Since IceCube can only identify track-like and cascade-like events, a particle identification variable is defined as reconstructed track length

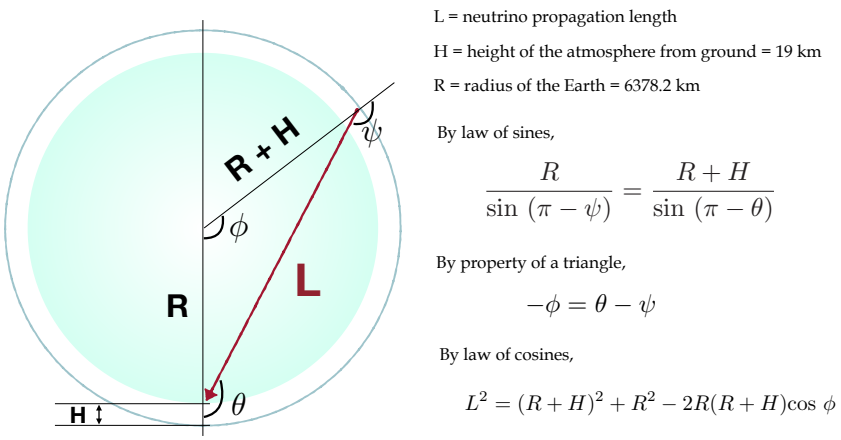

L = neutrino propagation length

H = height of the atmosphere from ground = 19 km

R = radius of the Earth = 6378.2 km

By law of sines,

$$\frac{R}{\sin\,(\pi-\psi)} = \frac{R+H}{\sin\,(\pi-\theta)}$$

By property of a triangle,

$$-\phi = \theta - \psi$$

By law of cosines,

$$L^2 = (R+H)^2 + R^2 - 2R(R+H)\cos\,\phi$$

Figure 8.2: Conversion between propagation length and cos θ based on the Earth's geometry.

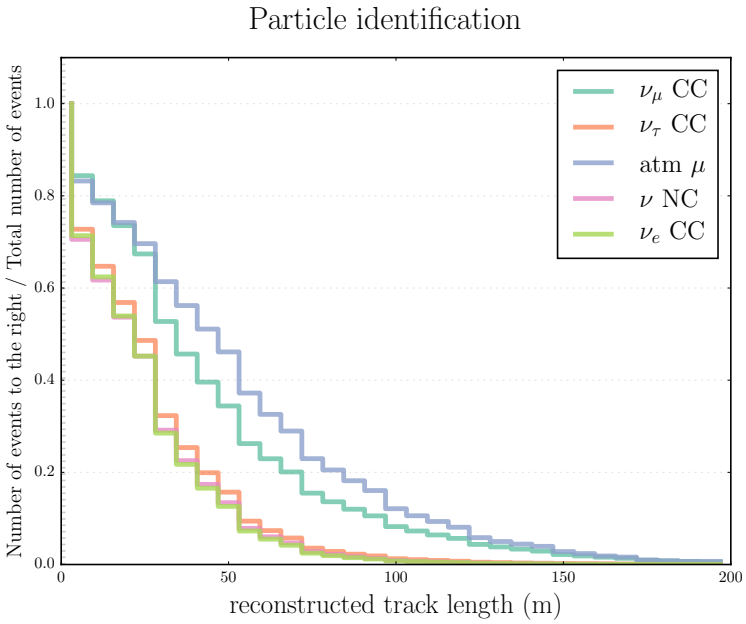

Figure 8.3: Reconstructed track length as particle identification. Each line represents the separation power of track-like events from cascade-like events based on reconstructed track length. An event is considered as cascade-like if its reconstructed track length is shorted than 50 meters, whereas a track-like event has a reconstructed track length between 50 and 1000 meters.

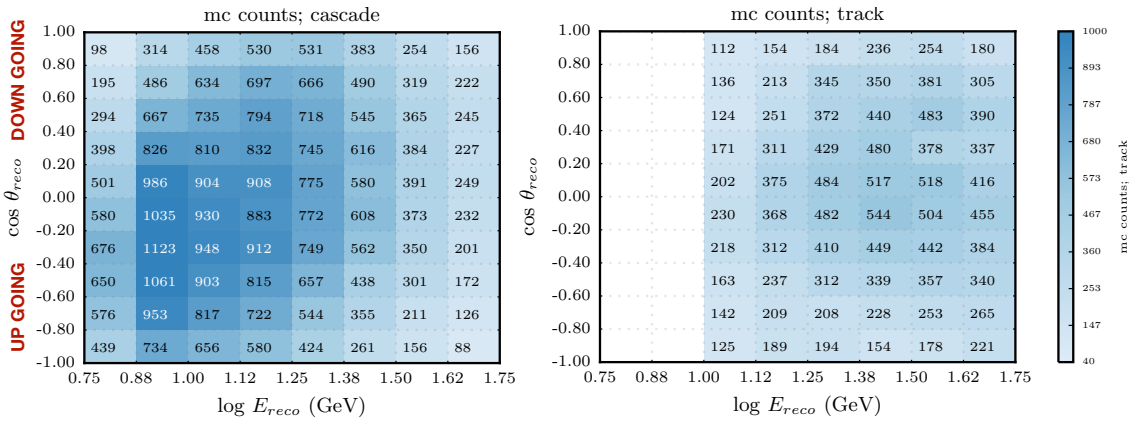

Figure 8.4: MC template before the Hyperplane treatment: (left) cascade bin with track length shorter than 50 meters and (right) track bin with track length longer than 50 meters. Events at final selection level are binned by reconstructed energy, cos zenith angle, and track length.

for this analysis. Figure 8.3 shows the separation power of reconstruction track length. Events with track lengths shorter than 50 meters are considered as cascade-like, while those with track lengths longer than 50 m are track-like events. More than 80% of each neutrino backgrounds (ν_e CC, ν_τ CC, and ν NC) are classified as cascade-like, while 34% of ν_μ CC and 46% of atmospheric μ events have track length greater than 50 meters.

Based on the above binning, events at final selection level are binned by reconstructed energy, cos zenith angle, and track length. With a total of 140 non-empty bins, the total MC template includes contributions from all six event types: ν_μ CC, ν_e CC, ν_τ CC, ν NC, atmospheric muons, and noise-triggered events. In Figure 8.4, the left and right plots are the cascade-like and track-like templates respectively. For each template, the top half of the histogram includes down going bins, whereas the bottom half contains up going events. Note that 20 bins in the track histogram are empty due to the cascade plus minimum ionizing track hypothesis in the PegLeg reconstruction algorithm. Since secondary muons from ν_μ charge current interac-

tions are expected to be minimum ionizing, their track lengths depend on the lepton. Given that a minimum ionizing muon in ice deposits roughly 1 GeV every 5 meters, events with a track longer than 50 meters must have a minimum energy above 10 GeV. As a result, no track-like events are reconstructed with energy below 10 GeV.

8.1.2 Hyperplane

The MC template in Figure 8.4 is one realization of the total expected event count per bin; the simulation sets used for building the MC template assume some base values for the optical properties of the detector. As discussed in Section 7.4, the predicted rates depend on detector properties, such as DOM efficiency, hole ice parameter, hole ice forward parameter, ice absorption, and ice scattering. These effects need to be taken into account before performing the measurement analysis.

Recall from Section 5.2.3 that rate predictions due to detector effects can be estimated by simulating different MC sets, each of which assumes a different value for one (or two) of the detector optical properties. Although only certain values are picked to produce the corresponding MC sets, the parameters related to these detector properties are continuous and should be allowed to float in a continuous space when fitting MC template to data. In an ideal world, one could generate infinite MC sets to understand the relationship between, say, DOM efficiency and predicted rate. However, with limited computational resources, only a few sets are simulated for each detector property and each event type. Each of these systematic MC sets has a unique set of detector properties that corresponds to one of the rows in Table 8.1, where the rows in red are the MC sets with base assumptions. Each MC set is processed to the final selection level, and events that pass all requirements are binned by the binning discussed in Section 8.1.1. Now, instead of one realization of MC template in Figure 8.4, there are multiple realizations of expected event counts

per bin depending on the optical properties of the detector.

However, since these detector properties are continuous and may be correlated, a continuous space across all detector-related parameters is required for a minimizer to fit the MC template to data; this is why the *Hyperplane* method is applied for each bin in the MC template. Figure 8.5 shows a simplified example of a hyperplane for one of bins in the ν_μ CC template with only DOM efficiency and hole ice parameter taken into account. The absolute expected counts of this particular bin from the systematic sets, as well as their ratios to the baseline counts, are shown in the tables on the left. The fractional counts and their error bars are plotted on the right plot; blue and red points correspond to the data points from hole ice and DOM efficiency sets respectively. Given these eleven distinct points, a plane is fitted over both detector parameters with color bar and the z axis representing the fractional counts. To verify the goodness of fit of this fitted plane, solid blue and red lines are drawn at the baseline values of DOM efficiency (1.0) and hole ice parameter (25) respectively. These two lines are projected to the dashed blue and red lines, from which a goodness of fit with the data points from the sets can be calculated. Note that the Hyperplane method does not mean a plane is always fitted to the data points; the fitted "plane" can be a plane, a mountain, a valley, a saddle, or other shapes driven by the points from different systematic sets.

For each neutrino flavor, a total of 20 systematic sets are used; thus, 20 expected counts are available, each of which corresponds to a set of discrete systematic values (i.e. each row of Table 8.1). These 20 expected counts are then divided by a reference count, which is the expected number of events in the corresponding bin calculated from the baseline set labeled in red in Table 8.1. Thus, for each bin, there are 20 points, each of which is a ratio to the baseline count, in a space across all six discrete systematics. As shown in the above example, a "plane" is then fitted to form a continuous space across all dimensions. Now that each bin has a hyper-

Table 8.1: Summary of neutrino and muon discrete sets. Baseline sets[a] are labeled in red.

	coincident fraction	DOM efficiency	hole ice p	hole ice forward $p2$	absorption scaling α_{abs}	scattering scaling α_{sca}
ν	0	1.0	25	0	1.0	1.0
	1	1.0	25	0	1.0	1.0
	0	0.88	25	0	1.0	1.0
	0	0.94	25	0	1.0	1.0
	0	0.97	25	0	1.0	1.0
	0	1.03	25	0	1.0	1.0
	0	1.06	25	0	1.0	1.0
	0	1.12	25	0	1.0	1.0
	0	1.0	15	0	1.0	1.0
	0	1.0	20	0	1.0	1.0
	0	1.0	30	0	1.0	1.0
	0	1.0	35	0	1.0	1.0
	0	1.0	25	-5	1.0	1.0
	0	1.0	25	-3	1.0	1.0
	0	1.0	25	-1	1.0	1.0
	0	1.0	25	+1	1.0	1.0
	0	1.0	25	+3	1.0	1.0
	0	1.0	25	0	0.929	0.929
	0	1.0	25	0	1.1	1.0
	0	1.0	25	0	1.0	1.1
μ	-	0.99	25	0	1.0	1.0
	-	0.693	25	0	1.0	1.0
	-	0.792	25	0	1.0	1.0
	-	0.99	15	0	1.0	1.0
	-	0.99	30	0	1.0	1.0
	-	0.99	25	-2	1.0	1.0
	-	0.99	25	-4	1.0	1.0
	-	0.99	25	0	0.929	0.929
	-	0.99	25	0	1.142	1.142
	-	0.99	25	0	0.8	1.0
	-	0.99	25	0	1.1	1.0
	-	0.99	25	0	1.0	0.8
	-	0.99	25	0	1.0	1.1

[a]Baseline sets are the MC sets generated with no deviation in discrete systematic values from what we believe in the reality.

DOM efficiency	Counts	Fraction
0.88	219	0.925
0.94	228	0.963
0.97	233	0.983
1.00	237	1.000
1.03	250	1.055
1.06	237	1.001
1.12	267	1.126

Hole Ice p	Counts	Fraction
15	246	1.040
20	248	1.048
25	237	1.000
30	238	1.004
35	233	0.985

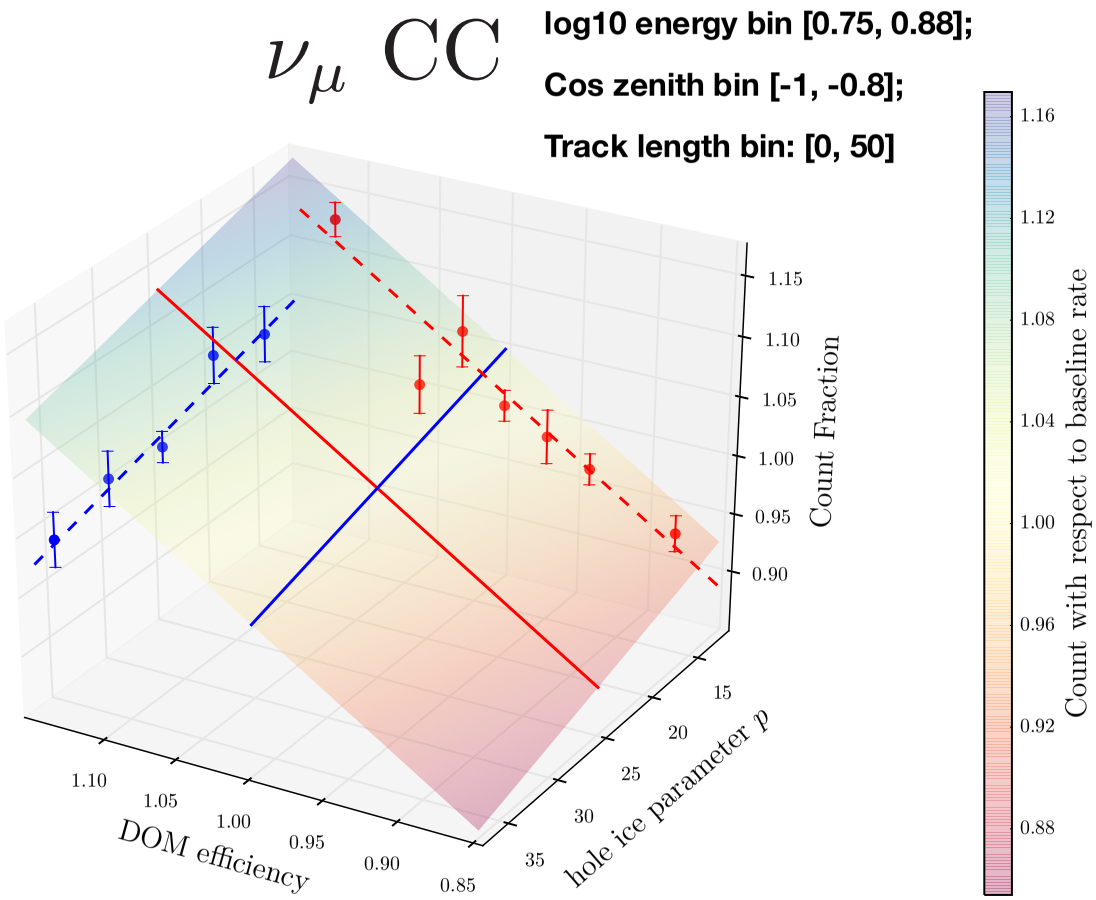

Figure 8.5: A Hyperplane example: (left) a table of counts and their ratios to the baseline count and (right) the corresponding hyperplane. This example comes from the first energy, zenith, and track length bin in the ν_μ CC template. Tables on the left show the absolute expected counts and their ratios to the baseline counts which, together with their error bars, are plotted on the right plot. Blue and red points correspond to the data points from hole ice and DOM efficiency sets respectively. A plane is fitted over the two dimensions; color bar and the z axis represent the fractional counts. Solid blue and red lines are fitted values at the corresponding baseline values, and they are projected to the dashed blue and red lines.

plane, when one specifies a set of discrete systematic values, the expected count of that bin is the baseline count multiplied by a factor returned by the hyperplane. Such process is repeated for each bin and each neutrino flavor in order to obtain the neutrino templates.

Similar procedure is used to determine the muon template but with two main differences when comparing it to the treatment of neutrino templates. First, muon hyperplanes do not include coincident fraction. For neutrinos, a coincident event is an event in which one or more muon(s) is/are seen during the time window of a neutrino interaction. Since we do not have any MC sets to predict such a rate, the coincident fraction is implemented as a systematic to estimate its effect on the shape of neutrino templates. In the case of muons, a coincident event is an event with more than one muon; by including CORSIKA events, multi-muon events are taken into account in the calculation of muon expected rates. Second, no muon systematic sets with DOM efficiency higher than 1.0 and positive hole ice forward parameter are available. It is a result of limited computational resources. Discussed in Section 5.4, neutrino sets are generated at a DOM efficiency of > 1.7 such that the number of accepted photons can be scaled down to various systematic input values. Muon sets, on the other hand, are generated with a DOM efficiency of 1.28; there are not enough total number of photons reaching a DOM to begin with for systematic sets at a DOM efficiency value greater than 1.0 and at a positive value for the hole ice forward parameter. In principle, one could regenerate muon events at a higher DOM efficiency value, which would take months to get enough statistics. However, the current systematic sets are good enough to predict an overall trend in how the muon template changes with respect to various detector parameters.

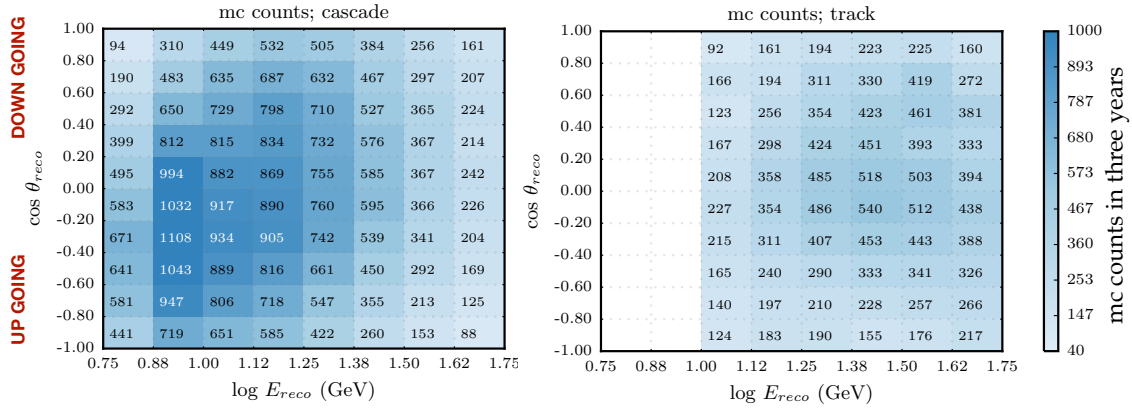

Figure 8.6: MC template after the Hyperplane treatment: (left) cascade histogram and (right) track histogram. Color bar represents expected counts in three years.

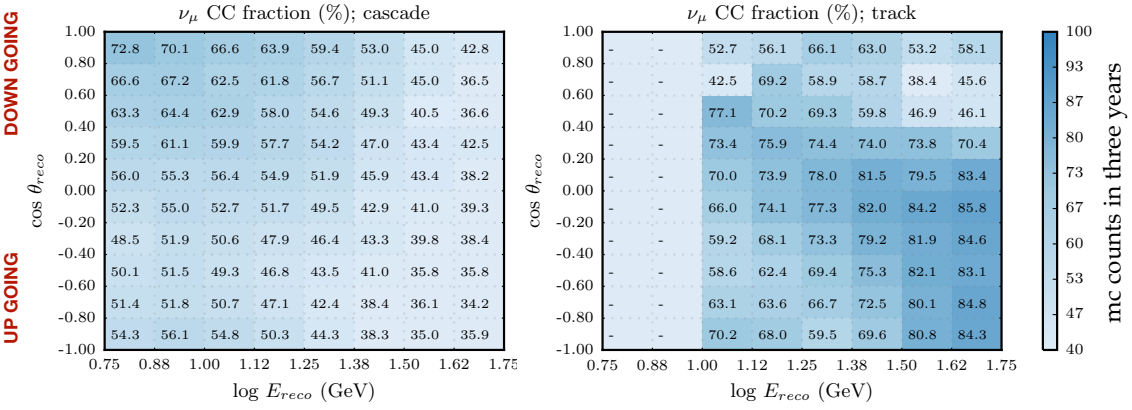

Figure 8.7: The fraction of ν_μ CC per bin in the final MC template after the Hyperplane treatment: (left) cascade histogram and (right) track histogram. Color bar represents the fractional contribution of ν_μ CC to total counts, per bin, in percentage.

8.1.3 Final Templates

After applying the Hyperplane treatment described above, a MC template is obtained for each flavor (ν_μ CC, ν_e CC, ν_τ CC, ν NC, μ, and noise[1]). Assuming the world averaged best fit values for the neutrino oscillation parameters and some base assumptions for the nuisance parameters, the final MC template, which is the sum of contributions from all flavors, is shown in Figure 8.6. Although the peak of the histogram is located at the cascade bin, Figure 8.7 shows that our ν_μ CC signal events contribute mostly in the up going track bin. It is because the cascade bin contains most of the neutrino background events, including ν_e CC, ν_τ CC, and ν NC, while the dominant background atmospheric μ concentrates in the down going region of the track bin (see Figure 8.8). With fewer up going background events that have long track lengths, the purity of ν_μ CC signal events is better in the corresponding regions of the histogram.

8.2 Modified χ^2

In this binned analysis, a χ^2 value is calculated per bin to determine how likely an observed count, labelled as μ, is a statistical fluctuation of a predicted mean count of λ. Recall that a Gaussian probability density function (PDF), f, centered at λ is given by

$$f(\mu) = \frac{1}{\sqrt{2\pi\sigma^2}}\ exp\Big[-\frac{(\mu-\lambda)^2}{\sigma^2}\Big], \tag{8.1}$$

[1]No systematic sets are generated for noise template since noise events are randomly triggered, non-physical events due to electronics.

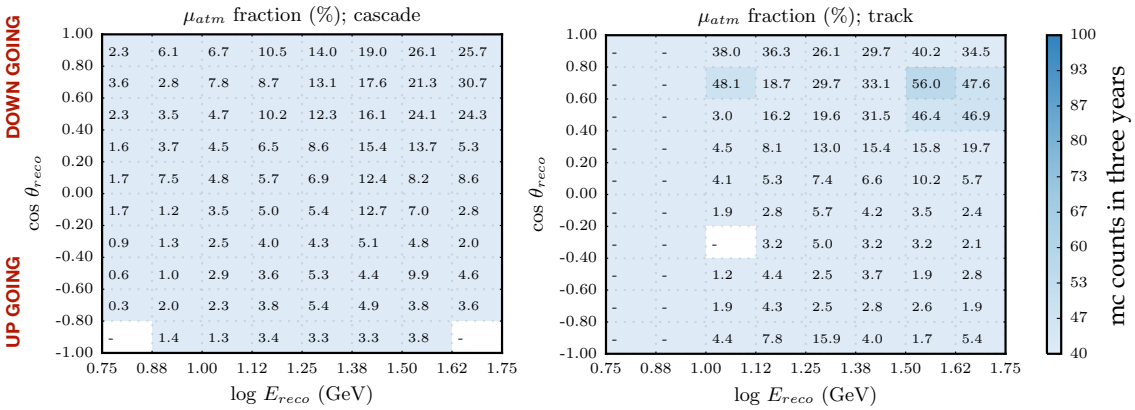

Figure 8.8: The fraction of atmospheric muon background per bin in the final MC template after the Hyperplane treatment: (left) cascade histogram and (right) track histogram. Color bar represents the fractional contribution of atmospheric muon background to total counts, per bin, in percentage.

where σ is the standard deviation of the predicted mean count of λ. Given a histogram with M bins, the total PDF is, therefore, a product of all f; that is,

$$\text{PDF from M bins} = \prod_{i}^{M} f_i(\mu_i) = \frac{1}{(2\pi)^{M/2}} \left\{ \prod_{i}^{M} \frac{1}{\sigma_i} \right\} \left\{ exp\Big[\sum_{i}^{M} -\frac{(\mu_i - \lambda_i)^2}{\sigma_i^2} \Big] \right\}. \tag{8.2}$$

We are interested in maximizing the total PDF; thus, it is easier to work with a summation instead of a product by taking its natural log;

$$\log_e \text{PDF} \propto -\sum_{i} \frac{(\mu_i - \lambda_i)^2}{\sigma_i^2}. \tag{8.3}$$

Note that maximizing the probability density function in Equation 8.3 is equivalent to minimizing its negative value. Because performing a minimization of a function is easier than doing a maximization, the total χ^2 to be minimized is defined as

$$\chi^2_{\text{total}} = \sum_{i}^{\text{all bins}} \frac{(N_{\text{mc}_i} - N_{\text{d}_i})^2}{\sigma_i^2}. \tag{8.4}$$

Here, N_{mc_i} is the predicted count in the i^{th} bin. N_{d_i} is the data count of the same bin. And, the denominator is the variance of total uncertainty of the i^{th} bin.

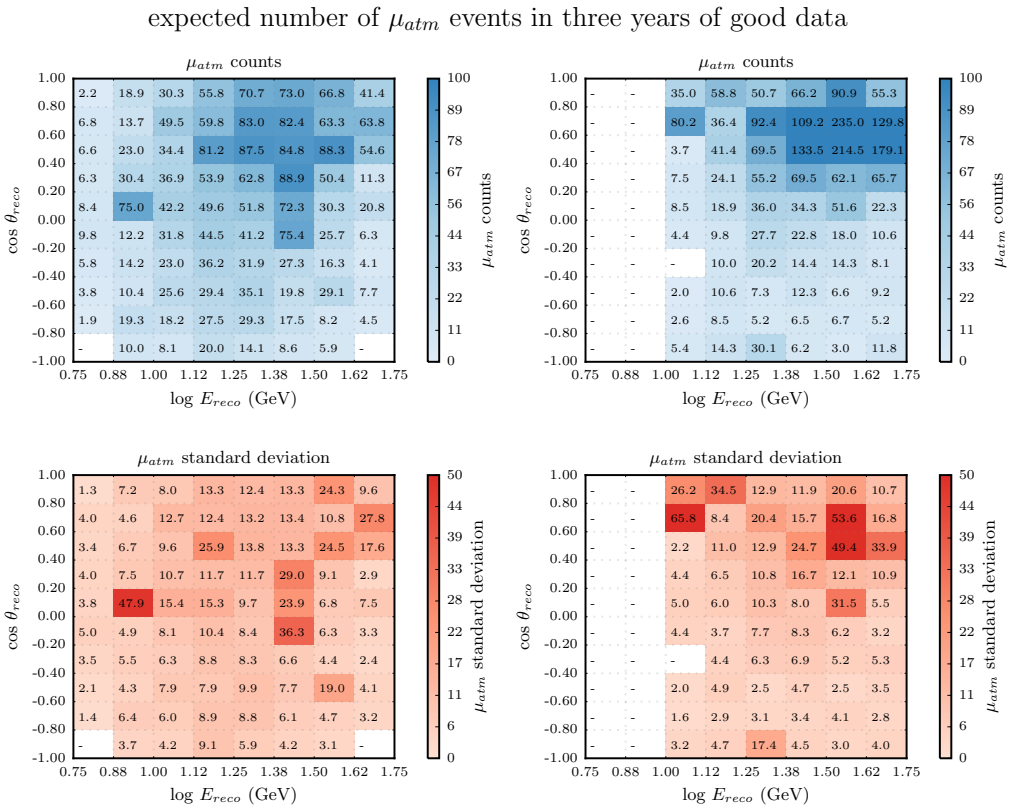

Figure 8.9: Atmospheric μ counts and the standard deviations from MC uncertainties: (top left) expected cascade counts, (bottom left) standard deviation per cascade bin, (top right) expected track counts, (bottom right) standard deviation per track bin. Only roughly a year worth of muons are available to model three years of data; hence, limited muon MC statistics cannot be ignored.

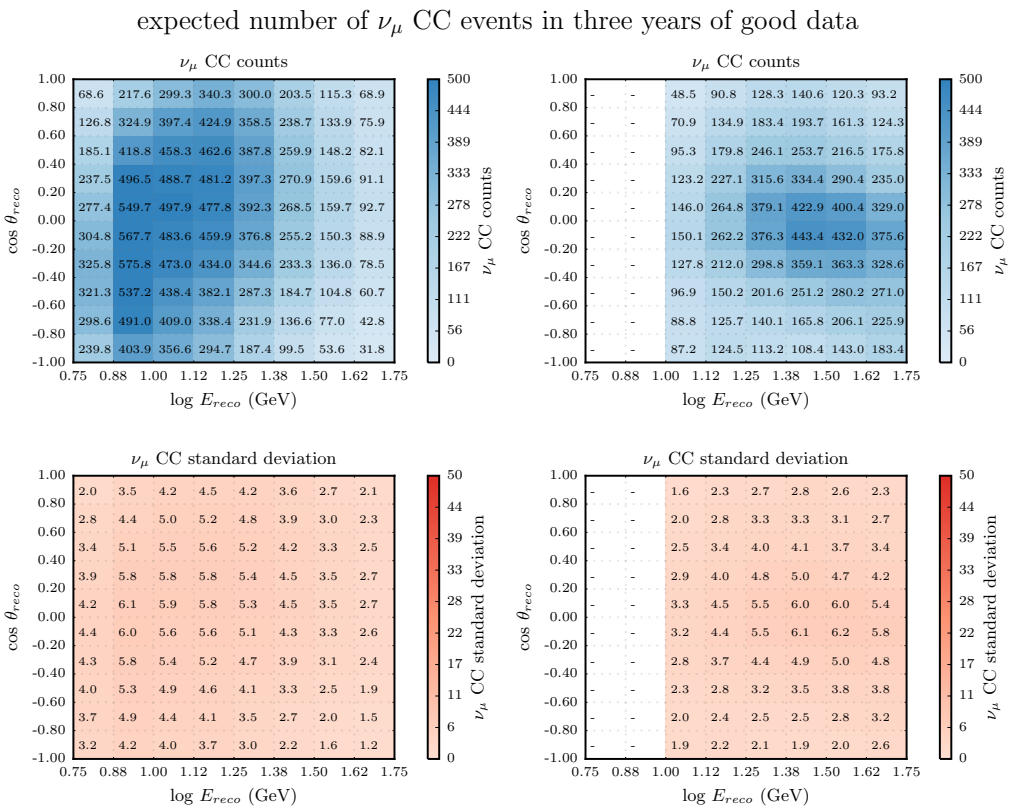

Figure 8.10: ν_μ Counts and the standard deviations from MC uncertainties: (top left) expected cascade counts, (bottom left) standard deviation per cascade bin, (top right) expected track counts, (bottom right) standard deviation per track bin. With thirty years worth of simulated events, neutrinos have small contributions to the total MC uncertainty.

The total variance of a given bin consists of a statistical error from the predicted count, $\sqrt{N_{\mathrm{mc}_i}}$, and an uncertainty, σ_{mc_i} due to finite MC statistics of that bin; thus,

$$\chi^2_i = \frac{(N_{\mathrm{mc}_i} - N_{\mathrm{d}_i})^2}{N_{\mathrm{mc}_i} + \sigma^2_{\mathrm{mc}_i}}, \tag{8.5}$$

The variance from MC uncertainty can be broken down into variances from each flavor;

$$\sigma^2_{\mathrm{mc}} = \sigma^2_{\nu_\mu \mathrm{CC}} + \sigma^2_{\nu_e \mathrm{CC}} + \sigma^2_{\nu_\tau \mathrm{CC}} + \sigma^2_{\nu \mathrm{NC}} + \sigma^2_{\mu} + \sigma^2_{\mathrm{noise}}. \tag{8.6}$$

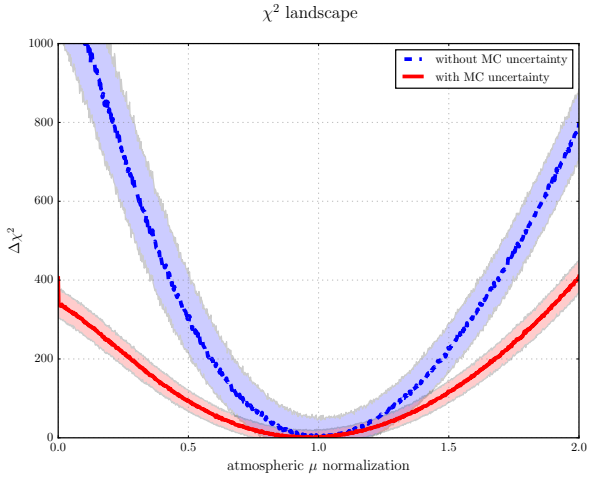

Figure 8.11: χ^2 Scan: Given an injected histogram with μ normalization of 1, solid red and dashed blue lines represent the χ^2 landscape with and without atmospheric μ MC uncertainty respectively. Shaded areas show the 1σ bands from 700 fluctuated trials. $\Delta\chi^2$ from the corresponding minima is shown to demonstrate that χ^2 space is flatter when there is a large MC uncertainty.

Out of all flavors, muon MC uncertainty contributes the most because only roughly a year worth of muons are available to model three years of data. To be specific, we have 2517 simulated muon events in total while expecting 5880 muon events given three years of exposure. Figure 8.9 shows the expected muon counts in three years, per bin, and their standard deviations σ_μ. Compared to that of ν_μ CC (see Figure 8.10) which contains more than thirty years worth of simulated events, muon MC uncertainty is more crucial in this analysis.

According to Equation 8.5, a larger MC uncertainty due to finite statistics leads to a smaller χ^2_i. Figure 8.11 shows the effect on the $\Delta\chi^2$ landscape when a large MC uncertainty term is taken into account. A μ normalization of 1 is injected as pseudo data; and, 700 fluctuated trials are performed at each μ normalization point. Representing the $\Delta\chi^2$ from its minimum when MC uncertainty term is included, the red solid line is flatter than the blue dashed line, which does not have the

MC uncertainty term. Therefore, when a minimizer lets μ normalization and other systematic parameters float to best match data, it tends to vary background muon statistics, without any penalty, as much as possible.

As a side note, Gaussian PDFs and χ^2 are used for this analysis; yet, one could also assume Poissonian PDFs given by

$$f(\mu_i) = \frac{\lambda_i^{\mu_i} e^{-\lambda_i}}{\mu_i!}. \tag{8.7}$$

By performing the same calculation from Equation 8.1 to Equation 8.4, one can obtain a Poisson log likelihood (PLLH) of

$$\text{PLLH} = 2 \times \sum_{i}^{\text{all bins}} \Big(\mu_i \; log\lambda_i - \lambda_i \Big). \tag{8.8}$$

Additional treatment is needed to take into account limited MC statistics [232]. Such a method was studied and found to have minimal impact on the measurement of atmospheric neutrino oscillation parameters.

8.3 Bayesian Priors

As discussed in Chapter 7, we have some degrees of belief in thirteen out of the sixteen nuisance parameters. These parameters include spectral indices of atmospheric neutrino (γ_ν) and muon (γ_μ) fluxes, ratio of atmospheric ν_e to ν_μ fluxes (ν_e/ν_μ), ratio of ν to $\overline{\nu}$ fluxes ($\nu/\overline{\nu}$), ratio of vertical to horizontal neutrino fluxes (up/hor), cross sections of resonance production (RES) and quasi elastic scattering (QE), ratio of ν NC to ν_μ CC (N_{NC}), fraction of neutrino coincident events (f_{coin}), DOM efficiency, hole ice parameter p, hole ice forward parameter $p2$, ice absorption scaling factor α_{abs}, and ice scattering α_{sca}.

By knowing roughly the values of the above parameters and their 1σ error bars, one can assume, for each parameter, a Gaussian PDF centered at the estimated value with the corresponding 1σ width. This prior PDF is then multiplied to the PDF in

Equation 8.2 such that the overall probability is penalized in regions where we know are less likely. Following the steps from Equation 8.2 to Equation 8.4, one realizes multiplying a prior probability to the PDF is equivalent to adding the penalty terms to the χ^2 in Equation 8.4; that is,

$$\chi^2_{\text{mod}} = \sum_{i}^{\text{all bins}} \frac{(N_{\text{mc}_i} - N_{\text{d}_i})^2}{N_{\text{mc}_i} + \sigma^2_{\text{mc}_i}} + \sum_{j}^{\text{parameters}} \frac{(\epsilon_j - \text{prior mean})^2}{(1\sigma \text{ penalty})^2}. \tag{8.9}$$

where $\sum_j$ sums over contributions from all thirteen nuisance parameters with priors centered at the prior means with 1σ penalty widths. This modified χ^2_{mod} is the χ^2 used when fitting MC to data. The numerical values for all prior means and 1σ penalties are summarized in Table 8.2.

8.4 Minimization

Minimization is a process to minimize the χ^2_{mod} by letting all nuisance and physics parameters float. Defined by Equations 8.9, χ^2_{mod} for this analysis is minimized using a standard python-based iminuit2 package [233]. While the tolerance and number of iterations are set to 1e-30 and 50000 respectively, all other settings for the iminuit minimizer are set to their default values.

During minimization, the minimizer adjusts all floating parameters to best match the MC template to data histogram by finding the smallest χ^2_{mod}. The minimizer starts the parameters at some seeded values and explores the nearby χ^2_{mod} space using the given initial step sizes (see Table 8.2). The allowed space for each parameter is defined by the lower and upper limits. When the minimizer reaches the tolerance or number of iterations set by the user, the minimizer stops and recognizes the point that returns the smallest χ^2_{mod} as a local minimum.

The local minimum may or may not be the global minimum. For most parameters, their χ^2_{mod} behave parabolically with clear minima as shown in Figure 8.11. It is, however, not the case for $\sin^2\theta_{23}$. The top plot in Figure 8.14 shows the χ^2_{mod} as a

Table 8.2: A summary of minimizer and prior information.

Parameters	Units	Minimizer Seeded Values	Minimizer Lower Limit	Minimizer Upper Limit	Minimizer Initial Step Sizes	Prior Means	1σ Penalty
Physics Parameters							
Δm^2_{31}	$\times 10^{-3}$ eV^2	2.526e-3	0.0	7e-3	0.0001	-	-
θ_{23}	(1st octant)	0.7252	0.0	0.7854	0.0001	-	-
θ_{23}	(2nd octant)	0.8456	0.7284	1.5708	0.0001	-	-
Flux Related Systematics							
γ_μ	σ	0.0	-5.0	5.0	0.1	0.0	1.0
γ_ν	-	0.0	-0.5	0.5	0.1	0.0	0.1
ν_e/ν_μ	-	1.0	0.0	4.0	0.05	1.0	0.05
$\nu/\overline{\nu}$	σ	0.0	-3.0	3.0	0.5	0.0	1.0
up / hor	σ	0.0	-3.0	3.0	0.5	0.0	1.0
coincident fraction [2]	-	0.0	0.0	1.0	0.005	0.0	0.1
Cross Section Related Systematics							
RES	σ	0.0	-3.0	3.0	0.5	0.0	1.0
QE	σ	0.0	-3.0	3.0	0.5	0.0	1.0
N_{NC}	-	1.0	0.0	4.0	0.00001	1.0	0.2
Normalization Systematics							
$N_{\nu_\mu CC}$	-	1.0	0.0	4.0	0.00001	-	-
N_μ	-	1.0	0.0	4.0	0.00001	-	-
Detector Related Systematics							
DOM efficiency	-	1.0	0.5	1.5	0.005	1.0	0.1
hole ice p	cm	25	10	40	5	25	10
hole ice forward $p2$	-	0.0	-7	7	0.01	-	-
absorption scaling α_{abs}	-	1.0	0.5	1.5	0.005	0.0	0.1
scattering scaling α_{sca}	-	1.0	0.5	1.5	0.005	0.0	0.1

As explained in Section 7.1.5, the prior of coincident fraction is a one sided Gaussian PDF because this parameter can only go from 0 (i.e. no coincident neutrino events at all) to 1 (i.e. all neutrino events are coincident).

function of $\sin^2\theta_{23}$; such a Mexican-hat landscape has two local minima. Therefore, in order to find the global minimum, two minimizations are performed for each fit: one only allows minimizer to move in the first octant ($0 \leq \sin^2\theta_{23} \leq 0.5$), while the other scans only the second octant ($0.5 < \sin^2\theta_{23} \leq 1$). The one that returns a smaller χ^2_{mod} is the global minimum.

8.5 Fluctuations and P-value Calculation

Fluctuations are taken into account by performing pseudo trials. In each trial, two sources of randomness are considered: MC and statistical fluctuations. For each bin, the MC fluctuated count of a given event type is obtained by randomly picking a value from a Gaussian PDF centered at the expected count of that event type in that bin with a width equal to the corresponding standard deviation due to finite MC statistics in that bin. The sum of MC fluctuated counts from all event types is, therefore, the total count of that bin. Then, to mimic poisson fluctuations in data counts, the final MC-fluctuated total count in the bin is randomly picked based on a Poissonian PDF with a mean value equal to the total count.

As shown on the left of Figure 8.12, a total of 800 trials is performed, from which χ^2_{mod} distribution is drawn. This distribution is then turned into a PDF, and an inverted cumulative distribution function (CDF) is determined (see the right plot of Figure 8.12). To estimate the goodness of fit from fitting to real data, the inverted CDF is used to determine the p-value. Another way to determine the goodness of fit uses reduced χ^2. Although the MC template has a total of 140 non-empty bins, and eighteen floating parameters during a fit, the number of degrees of freedom is more than 122 because thirteen nuisance parameters have priors applied. Therefore, the number of degrees of freedom is estimated to be the mean value of the χ^2 distribution on the left of Figure 8.12, which is found to be 133.

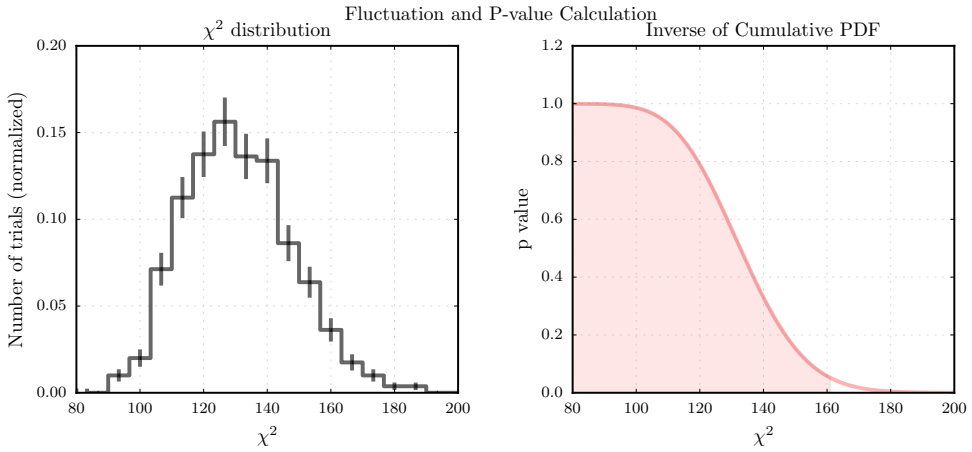

Figure 8.12: Fluctuations and p-value calculation: (left) χ^2 distribution from 800 trials and (right) inverted cumulative distribution function (CDF). χ^2 distribution from 800 trials of fluctuation is used as a PDF to determine the p-value from data. Shaded area on the right is the region where p-value is greater than 5%.

8.6 Sensitivity of Oscillation Parameter Measurements

One of the most important aspects of this measurement is the confidence level (CL) of the measured best fit oscillation parameters. In a given $\sin^2\theta_{23}$ and Δm^2_{32} space, a set of grid points are considered, each of which has a test statistic value. To determine the CL of a grid point, two approaches can be used. While Section 8.6.1 discusses the sensitivity via Wilks' Theorem, a more careful approach is presented in Section 9.2.2.

Another important aspect of this analysis is to understand how each of the sixteen nuisance parameters affects the oscillation parameter measurements. Their impacts on sensitivity are discussed in Section 8.6.2, which can be explained by their impacts on the analysis histogram. Last but not least, tests including data challenges and pseudo trials have been performed to ensure the fitting tool can

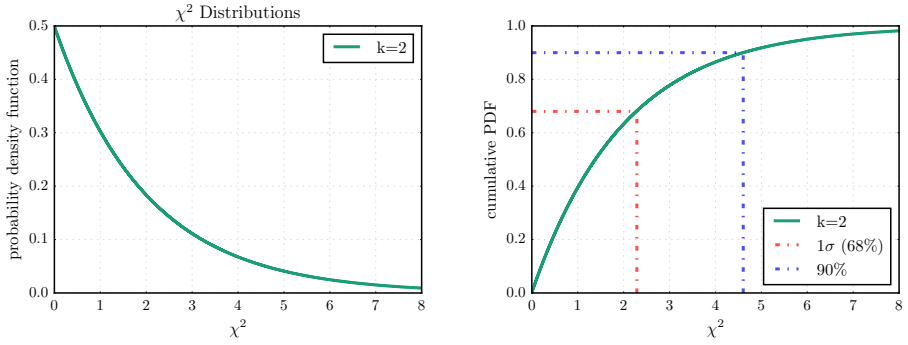

Figure 8.13: A standard χ^2 distribution with two degrees of freedom: (left) standard χ^2 distribution with two degrees of freedom and (right) cumulative distribution function (CDF) of the χ^2 distribution. From the CDF, a 68% (1σ) and 90% confidence levels are defined via the red and blue dashed dotted lines, which have χ^2 values of 2.288 and 4.605 respectively.

indeed find the true minimum, as discussed in Section 8.6.3.

8.6.1 Expected Sensitivity

The confidence level (CL) of the measured best fit oscillation parameters are determined by scanning the $\sin^2\theta_{23}$ and Δm^2_{32} space. In this two dimensional space, 45 × 45 grid points are defined within $\sin^2\theta_{23} \in (0.25, 0.75)$ and $\Delta m^2_{32} \in (2.0, 3.0)$ $\times 10^{-3}$ eV^2. At each grid point, a MC template assuming oscillation parameters equal to this grid point is fitted to data by minimizing χ^2_{mod} defined in Equation 8.9; only the sixteen nuisance parameters are allowed to float. The test statistic of this grid point is then defined to be the difference $\Delta\chi^2$ between the minimized χ^2_{mod} with fixed physics parameters and the χ^2_{mod} from the global best fit where all eighteen parameters are allowed to float.

The Wilks' Theorem states that if the sample size is large enough, the probability distribution function of a test statistic follows a standard χ^2 distribution with an effective number of degrees of freedom [234]. If this assumption is valid, a CL of

a given grid point can then be obtained by comparing its test statistic value and the standard χ^2 distribution with two degrees of freedom. The standard χ^2 distribution is shown on the left of Figure 8.13, and its cumulative distribution function (CDF) is shown on the right. From the CDF, the 68% (1σ) and 90% CLs with two degrees of freedom are defined at $\Delta\chi^2$ values of 2.288 and 4.605 respectively. Therefore, the 1σ and 90% contours are drawn around grid points where $\Delta\chi^2$ values are equal to 2.288 and 4.605.

Figure 8.14 shows the sensitivity of this analysis. Given the 2014 νfit results [1] as the injected values for Δm^2_{32} and $\sin^2\theta_{23}$, the gray solid line represents our expected 90% CL. The top and the right plots show the $\Delta\chi^2$ scans in $\sin^2\theta_{23}$ and Δm^2_{32} spaces respectively. Their 1σ widths are roughly 0.22 for $\sin^2\theta_{23}$ and 0.2e-3 eV^2 for Δm^2_{23}. Compared to measurements done by other major atmospheric oscillation experiments, our expected 90% contour shows that IceCube and DeepCore can deliver competitive results to the oscillation community. Compared to the previous IceCube result [79] represented as the blue contour, this analysis can improve Δm^2_{32} measurement by $\sim$ 30%. On the other hand, the blue contour has a smaller 90% CL in $\sin^2\theta_{23}$ compared to our sensitivity because previous IceCube reports a mixing angle near maximal (0.51) while our sensitivity is injected away from maximal mixing.

8.6.2 Impacts on Sensitivity Due to Systematics

The impact on sensitivity because of a given systematic can be studied by measuring the changes in 90% expected contours with the corresponding nuisance parameter fixed in the minimization. Figure 8.15 shows the percentage changes in the two 90% expected contours when a given systematic is turned off. Δm^2_{23} measurement is easily affected by atmospheric μ normalization, causing a 12.5%

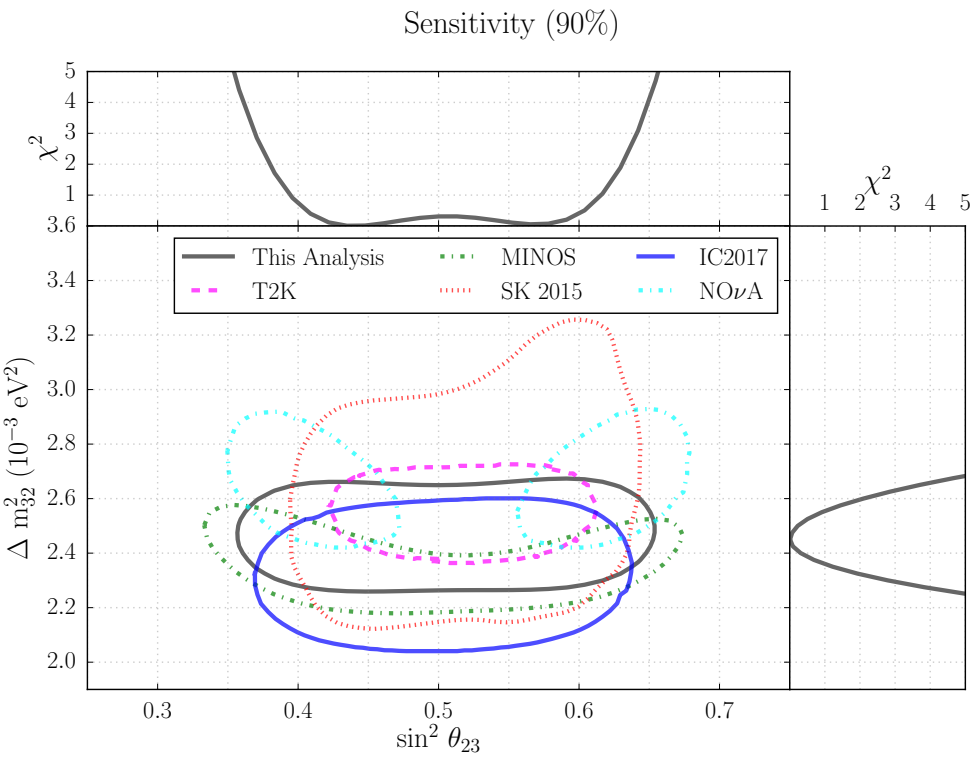

Figure 8.14: 90% Sensitivity: (bottom left) Sensitivity of 90% CL from this analysis and 90% CL contours from other experiments, (top) $\Delta\chi^2$ as a function of $\sin^2\theta_{23}$, and (right) $\Delta\chi^2$ as a function of Δm^2_{32}. Gray line represents the sensitivity of 90% confidence level from this analysis, which is competitive to other experiments.

change in the corresponding 90% range. On the other hand, $\nu/\overline{\nu}$ gives the largest change in $\sin^2\theta_{23}$ 90% CL by a slight 2%. In addition, DOM efficiency is also a relatively important systematic for both oscillation parameter measurements.

Whether a systematic is relevant to oscillation parameter measurements depends on its effects on the analysis histogram, especially in the region where signal events are dominant. Figure 8.16 shows the percentage changes in counts by varying oscillation parameters and DOM efficiency in the track bin where ν_μ CC events contribute the most. Since Δm^2_{23} drives the frequency of oscillation, lowering its value is equivalent to stretching the oscillation, which changes the peak and the dip

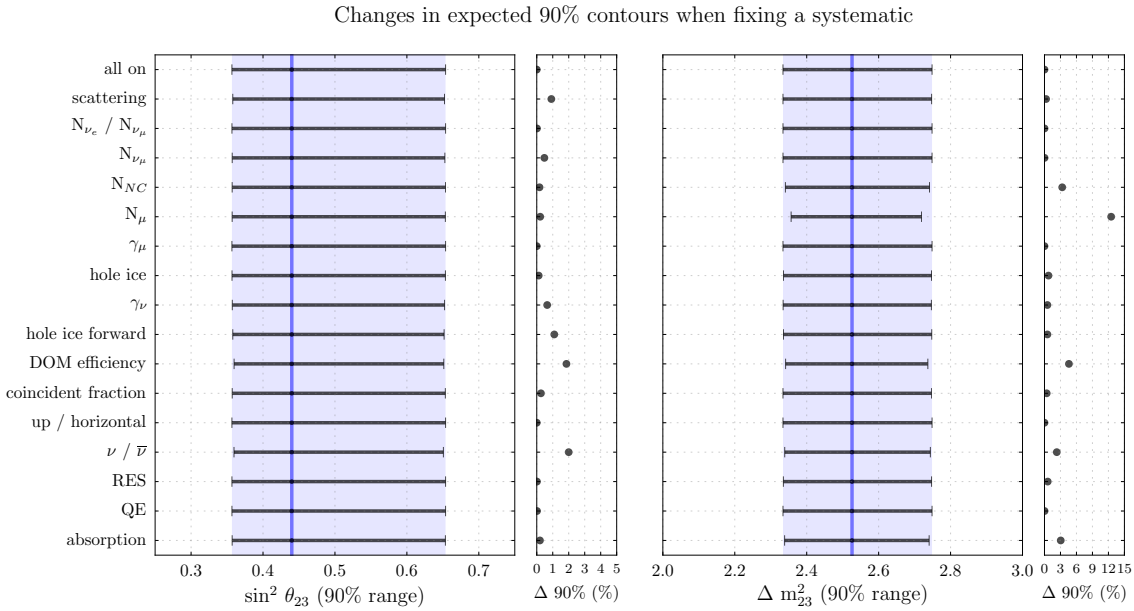

Figure 8.15: Changes in Expected 90% Contours When Fixing One Systematic: (left) Percentage change in $\sin^2\theta_{23}$ 90% CL (right) Percentage change in Δm^2_{23} 90% CL Black error bars represent the 90% CL when the corresponding systematic is turned off, whereas the shaded areas are the 90% ranges when all systematics are allowed to float. Black dots represent the percentage changes between the black error bars and the width of shaded areas. For Δm^2_{23}, fixing atmospheric μ normalization leads to the largest change in the 90% range, while the leading systematic for $\sin^2\theta_{23}$, $\nu/\overline{\nu}$, only changes its 90% range by 2%.

of the histogram. $\sin^2\theta_{23}$, on the other hand, relates to the amplitude of oscillation; given a smaller $\sin^2\theta_{23}$, less ν_μ disappear and, therefore, more events are detected, increasing the event counts in the signal region. DOM efficiency turns out to have a similar feature in the signal region of track histogram. With a less efficient DOM, less photons are seen. With less information about the event, down going muons are less likely to be removed by event selection, increasing the counts in down going bins. At the same time, having less lights in ν_μ events also lowers the resolution of event reconstruction, washing out the oscillation effects. Hence, the up going events share similar features as if the values of oscillation parameters are changed.

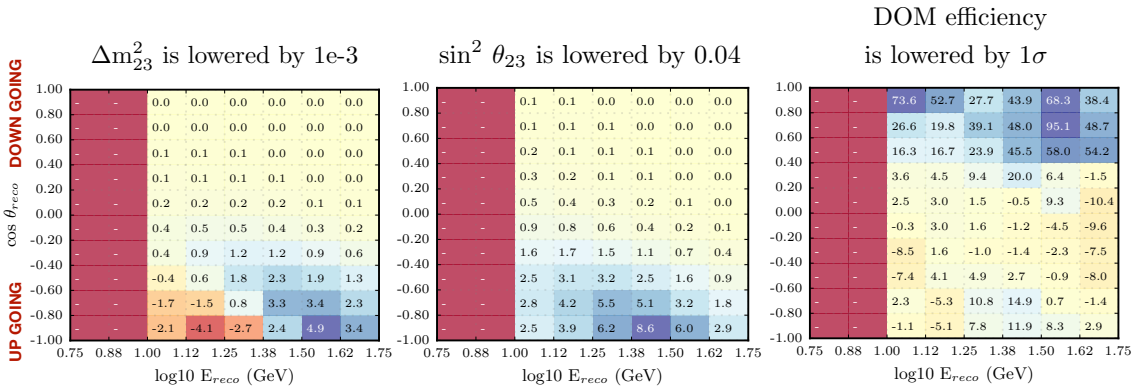

Figure 8.16: Percentage Changes in Track Event Counts When A Parameter Is Changed: (left) when Δm^2_{23} is lowered by 1e-3, (middle) when $\sin^2\theta_{23}$ is lowered by 0.04, and (right) when DOM efficiency is lowered by 1σ, which is 10%. Color axes are not in the same scale, but values of percentage changes in counts are stated. Both oscillation parameters affects event counts in the up going track bins, which can also be affected by varying DOM efficiency.

Nevertheless, since this analysis also includes down going events, the degree of pulls on DOM efficiency is modulated by its significant impact on muon template. While changing DOM efficiency to best match up going track region, the minimizer cannot overly pull DOM efficiency to an unreasonable value. Instead, together with muon normalization and other muon background related nuisance parameters, the minimizer tries to find the best pulls on different parameters to minimize the χ^2_{mod}. Given that eighteen nuisance parameters are considered during a fit, such a complex dynamical and multi-dimensional relation can be presented via a correlation matrix shown in Figure 8.17. Positive correlation means parameter X increases with parameter Y, while negative correlation means parameter X decreases with parameter Y. Thus, given its effect on the analysis histogram, DOM efficiency has a strong correlation with muon normalization and anti correlations with Δm^2 and

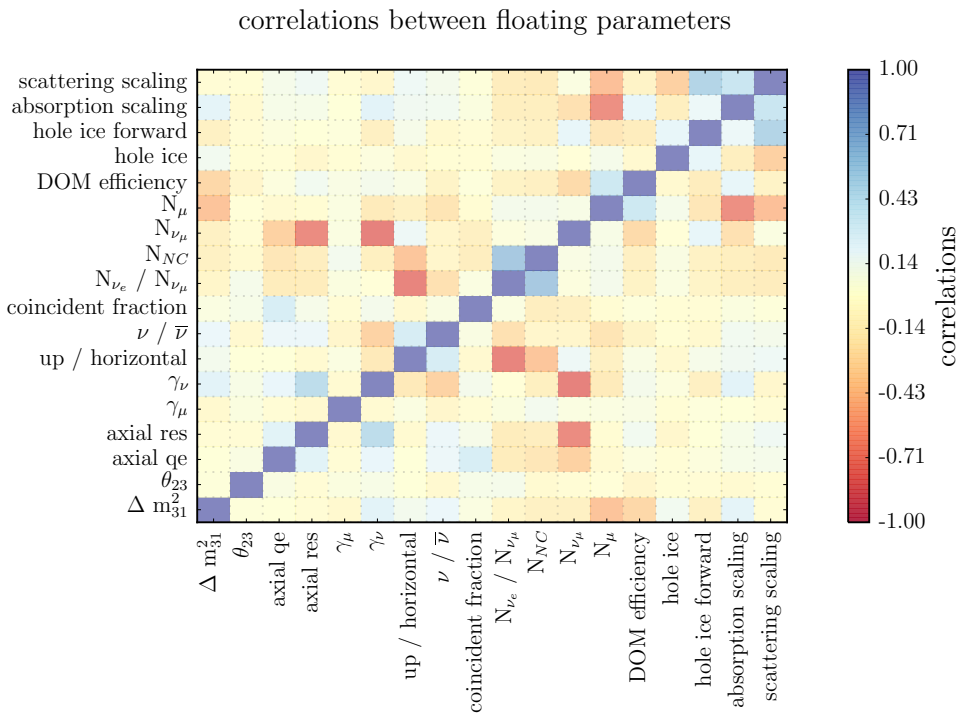

Figure 8.17: Correlation matrix among eighteen floating parameters. Color axis represents the correlations; positive correlation means Y increases with X, while negative correlation means Y decreases with X.

mildly with $\sin^2\theta_{23}$.

8.6.3 Fitter Robustness

As a final note, it is important that the fitting tool returns the true minimum; hence, two robustness tests are performed: data challenge and pseudo trials.

The purpose of a data challenge test is to ensure fitter is able to find the true minimum when minimizer starts all parameters at values away from their injected values. In this test, 81 test points are considered in the $\sin^2\theta_{23}$ and Δm^2_{32} space. At each test point, an injected histogram is built using the corresponding values of oscillation parameters; injected values of nuisance parameters are tabulated in

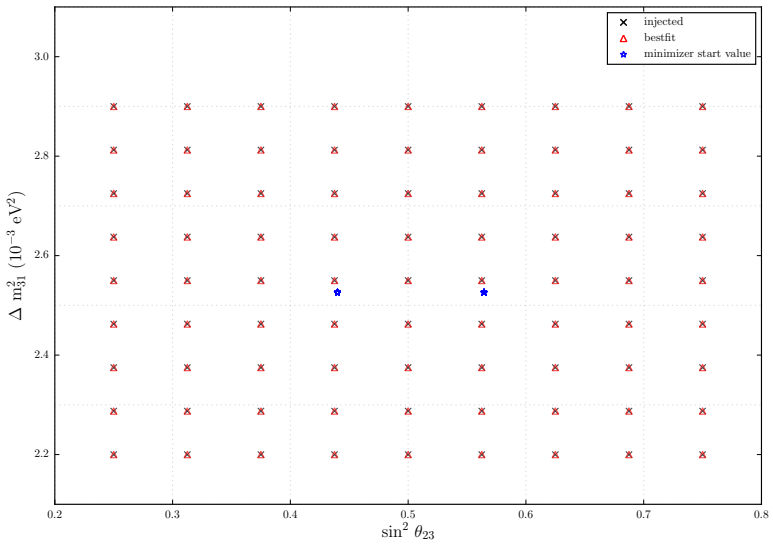

Figure 8.18: Data Challenge (Oscillation Parameter). 81 grid points are set for data challenge tests. Their Injected values of oscillation parameters are shown as black crosses. For each test, a full fit is performed, where minimizer starts at the values of blue stars. The best fits from all tests are shown as red triangles, which overlap with the black crosses. That is, the fitting tool is able to find the true minimum.

Table 8.3. Given an injected histogram at a test point, two minimizations are performed; one has minimizer starts at the first octant while the other starts at the second octant. For nuisance parameters with priors, their start values for both minimizations are set at 1σ above the injected values. Other floating parameters also start away from their injected values (see Table 8.3). Figure 8.18 shows the results in oscillation parameter spaces. 81 best fit oscillation parameters (red triangles) agree with their injected values (black crosses). The differences between injected and best fit values of all floating parameters are shown in Figure 8.19. The differences are at the order of 1e-5, which is finer than the resolution of our ability to measure the parameters. Therefore, the fitting tool is able to find the true minimum.

The above data challenge test is performed ignoring fluctuation; thus, a test with pseudo trials is needed. In this test, a distribution of best fit values for each

Table 8.3: Floating parameter setting for data challenge.

Parameters	Units	Injected Values	Minimizer Start Values
Physics Parameters			
Δm^2_{31}	$\times 10^{-3}$ eV^2	at grid point	2.526
θ_{23}	radian	at grid point	0.7252 / 0.85
Flux Related Systematics			
γ_μ	σ	0.0	1.0
γ_ν	-	0.0	0.1
ν_e/ν_μ	-	1.0	1.05
$\nu/\overline{\nu}$	σ	0.0	1.0
up / hor	σ	0.0	1.0
coincident fraction	-	0.0	0.1
Cross Section Related Systematics			
RES	σ	0.0	1.0
QE	σ	0.0	1.0
N_{NC}	-	1.0	1.2
Normalization Systematics			
$N_{\nu_\mu CC}$	-	1.0	1.1
N_μ	-	1.0	1.1
Detector Related Systematics			
DOM efficiency	-	1.0	1.1
hole ice p	cm	25	35
hole ice forward $p2$	-	0.0	1.0
absorption scaling α_{abs}	-	1.0	1.1
scattering scaling α_{sca}	-	1.0	1.1

floating parameters is obtained from 800 trials; their median values are then compared to the injected values. The percentage changes and number of σ away from their priors are stated in Figure 8.20. In particular, the median values for $\sin^2 2\theta_{23}$ and Δm^2_{32} are 0.97 and 2.57 respectively, which are both less than 2% away from their injected values. Thus, despite fluctuation, the fitting tool is still able to find the true values.

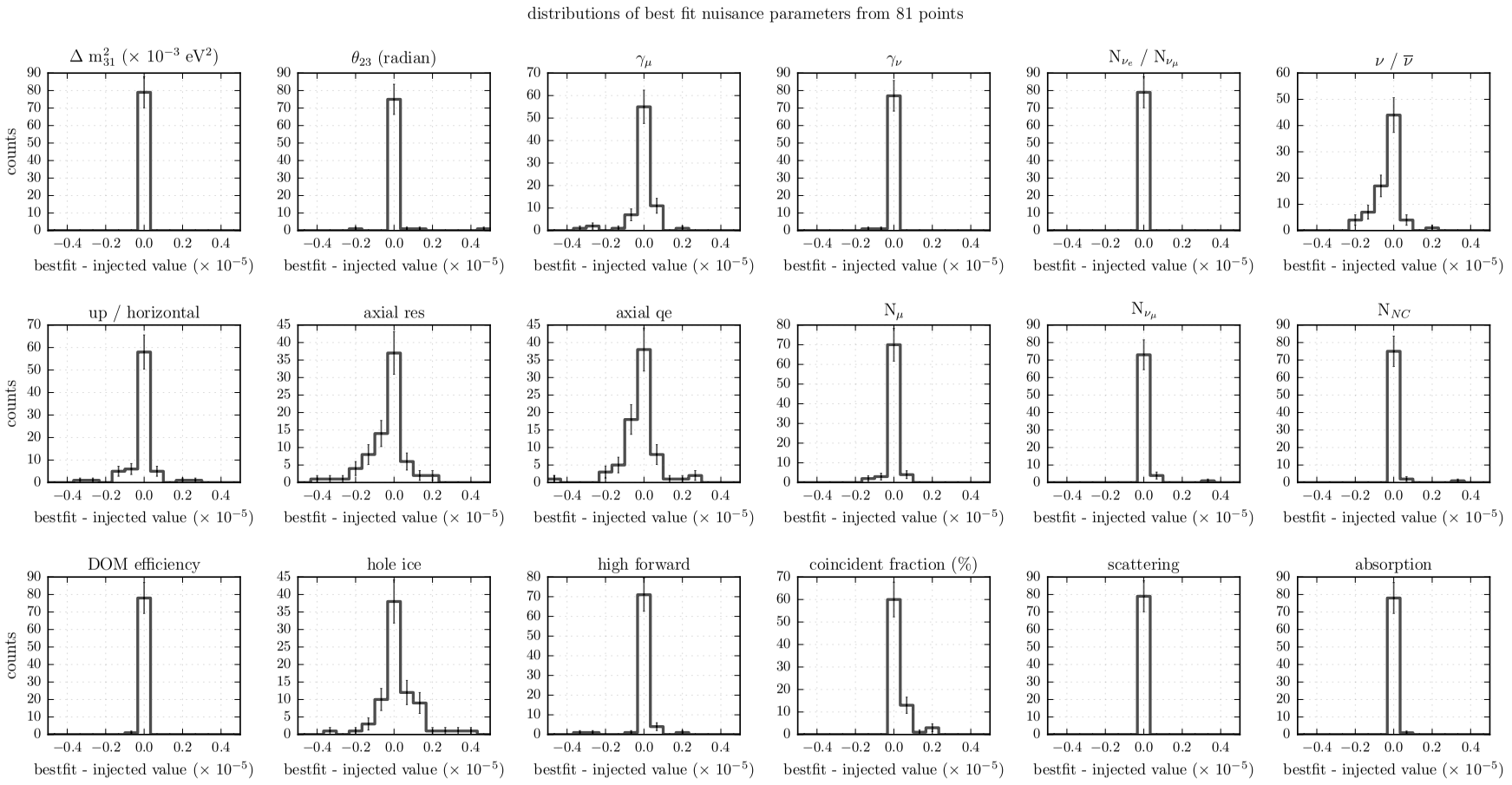

Figure 8.19: Data Challenge (Floating Parameter). 81 grid points are set for data challenge tests. For each floating parameter, its distribution of the difference between injected and best fit values are plotted from the 81 tests. The order of magnitude in the differences are 1e-5, which is smaller than the resolution of the parameters. Therefore, the fitting tool is able to find the true minimum.

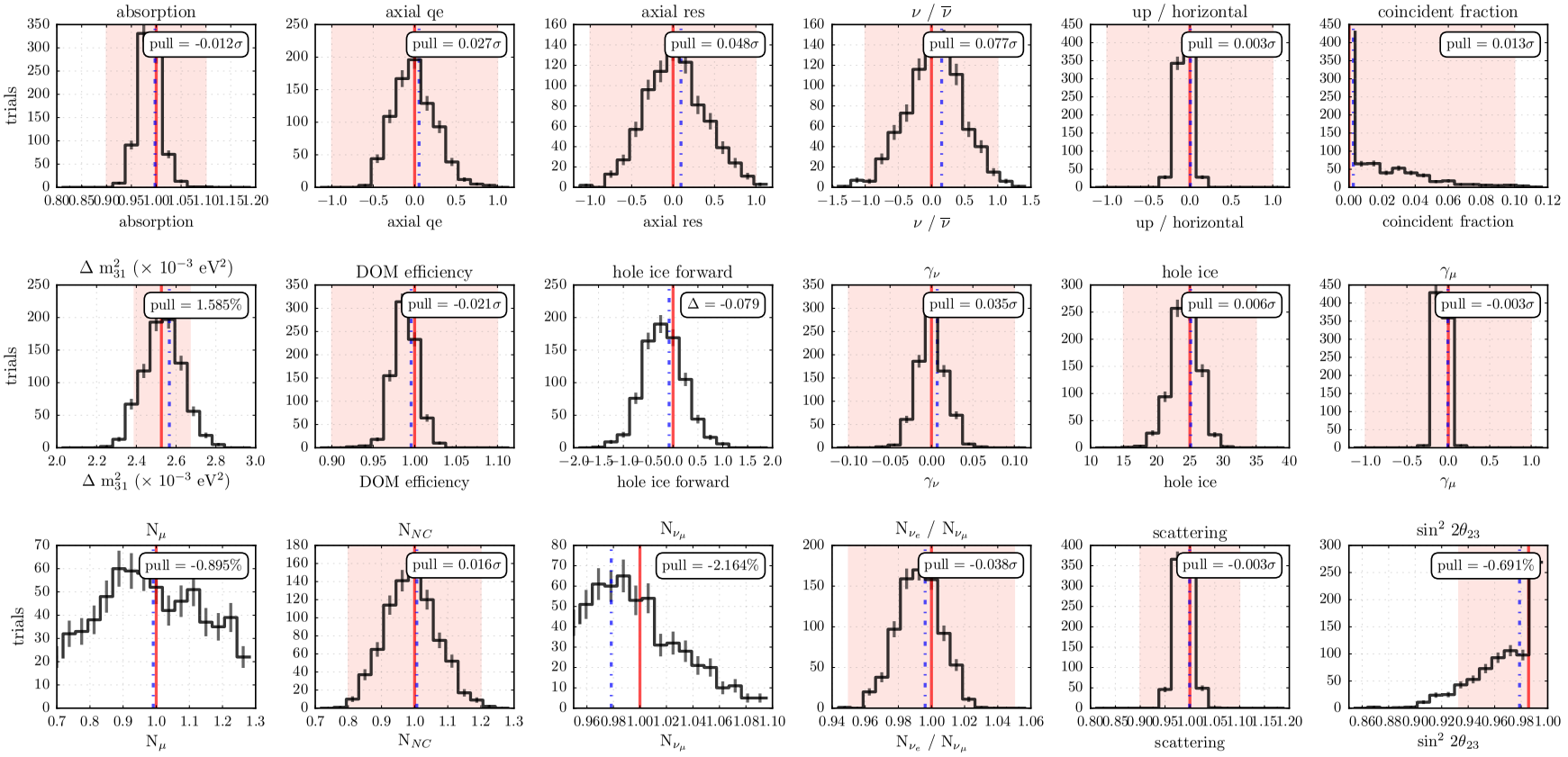

Figure 8.20: Pseudo Trials. 800 trials are performed. For each floating parameter, a median best fit value is obtained from its distribution of 800 best fit values. This median is then compared to the injected value. For parameters with priors applied, numbers of σ away from priors are calculated. For those without priors, their differences between median and injected values are shown as percentage changes.

Chapter 9: Results and Discussion

This chapter presents the final results of the measurement of atmospheric neutrino oscillation parameters. By letting all eighteen parameters float, best fit values, including the physics parameters Δm^2_{23} and $\sin^2\theta_{23}$, are presented in Section 9.1. The uncertainties on the two physics parameters are discussed in Section 9.2. Fits assuming two mass hierarchy orderings are also shown in Section 9.3. And, in Section 9.4, this measurements are compared to the recent measurements done by IceCube via different reconstructions, event selections, and analysis methods.

9.1 Best Fit from Data

Fitting with three years of data returns a χ^2_{mod}, defined in Section 8.9, of 129.44. Given 140 non-zero bins and eighteen floating parameters, 800 pseudo trials are performed, which results in an effective number of degrees of freedom of 133; the reduced χ^2 is ~ 1. To be more precise, with the probability density function from the 800 fluctuated trials in Figure 8.12, the χ^2_{mod} obtained from data corresponds to a p-value of 0.578. Therefore, the overall goodness of fit is reasonable. Figure 9.1 shows the χ^2_{mod} per bin. In general, most bins have good agreements between best fit MC and data with χ^2_{mod}s very close to 0. However, other bins, in particular in the up going region, have χ^2_{mod}'s up to ~ 9. While disagreements may come from fluctuations, better understanding of sneaky muons and ice properties in the future may improve the observed disagreement.

Table 9.1: Best Fit Values.

Parameters	Units	Best Fits	Pulls from Prior Means (σ)
Physics Parameters			
Δm^2_{23}	$\times 10^{-3}$ eV^2	$2.549^{+0.12}_{-0.11}$	-
$\sin^2\theta_{23}$	-	$0.576^{+0.04}_{-0.13}$	-
Flux Related Systematics			
γ_μ	σ	0.113	0.113
γ_ν	-	0.045	0.454
ν_e/ν_μ	-	1.031	0.619
$\nu/\overline{\nu}$	σ	-0.700	-0.700
up / hor	σ	-0.207	-0.207
coincident fraction	-	0.027	0.273
Cross Section Related Systematics			
RES	σ	-0.374	-0.374
QE	σ	-0.250	-0.250
N_{NC}/N_{CC}	-	1.016	0.079
Normalization Systematics			
$N_{\nu_\mu CC}$	-	0.948	-
N_μ	-	0.813	-
Detector Related Systematics			
DOM efficiency	-	0.980	-0.020
hole ice p	cm	30.53	0.553
hole ice forward $p2$	-	-0.839	-
absorption scaling α_{abs}	-	1.014	0.139
scattering scaling α_{sca}	-	1.033	0.333

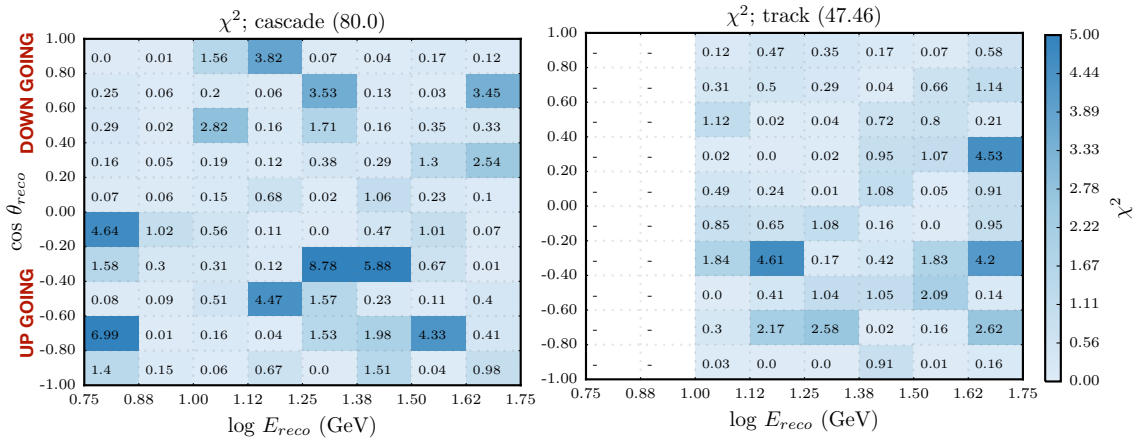

Figure 9.1: χ^2 per bin: (left) cascade bins and (right) track bins. Most bins show good agreement between data and best fit MC, but some bins have χ^2's above to ~ 3. The summed χ^2 for each cascade/track bin is stated on the top of each plot; both of them show reasonable goodness of fit.

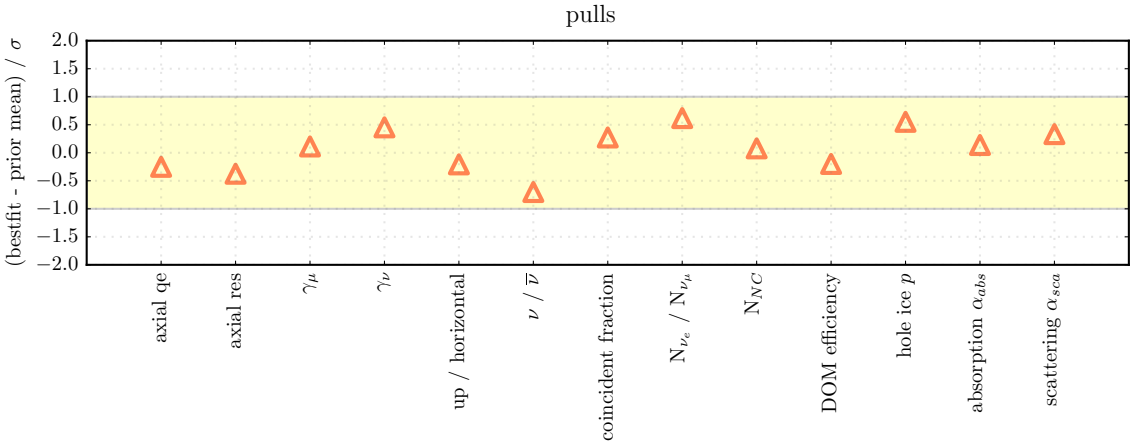

Figure 9.2: Pulls of nuisance parameters with priors applied. For each parameter with a prior applied, its pull is defined as the difference between its best fit value and the prior mean divided by its 1σ penalty. None of these parameters have a pull greater than $\pm 1\sigma$.

The best fit values of physics parameters Δm^2_{23} and $\sin^2\theta_{23}$ are $2.549^{+0.123}_{-0.114} \times 10^{-3}$ eV^2 and $0.576^{+0.042}_{-0.132}$ respectively, preferring a non maximal mixing angle away from 0.5. Best fit values for all parameters are presented in Table 9.1. Nuisance parameters without priors applied behave fairly well. For those with priors applied, their behaviors can be described by their pulls. The pull of a given parameter is defined as the difference between the best fit value and its prior mean divided by its 1σ penalty. These pulls are also presented in units of σ in Table 9.1 and shown in Figure 9.2. None of the nuisance parameters with priors applied are strongly pulled away beyond $\pm 1\sigma$.

Since the experimental parameter in the expression of oscillation probability is L/E, the effect of atmospheric neutrino oscillations can be clearly shown in L/E distributions. The bottom left plot of Figure 9.3 shows the log10 L/E histograms from both cascade and track channels. In general, the first peak of the histogram corresponds to down going events, whereas all up going events are contained in the second peak of the histogram. The saddle between two peaks is due to the stretching when taking the logarithm 10 of the propagation length. Each shaded area represents a contribution from an event type weighted by the best fit parameters from Table 9.1. These distributions are summed to obtain the total distribution as shown in the red solid line. Similarly the total distribution assuming no oscillation (null) hypothesis is shown as the blue solid line, and black points represent the log10 L/E distribution from data. The red solid lines and the data points are compared to the null hypothesis, as shown in the bottom ratio plot. For each channel, an obvious deficit is observed from data with respect to null hypothesis. The oscillation effect is especially clear in the track only channel due to the disappearance of ν_μ CC signal events.

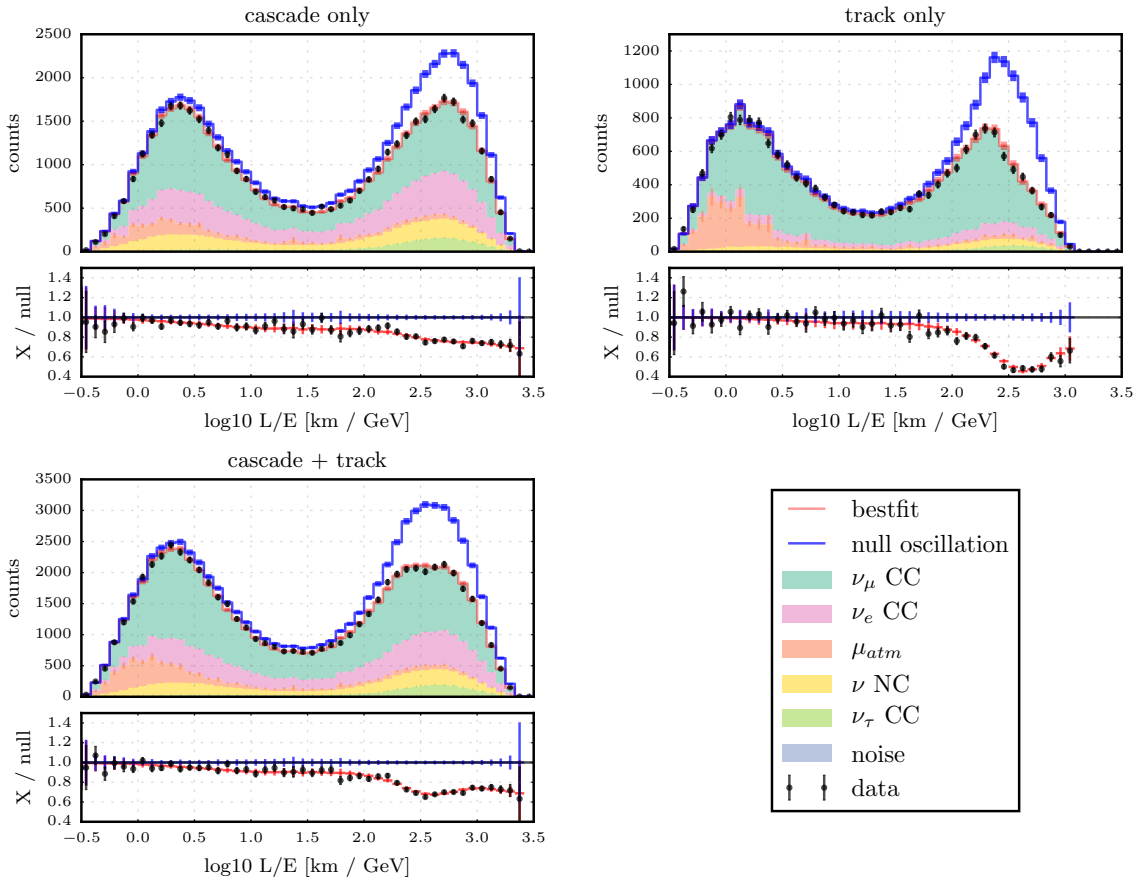

Figure 9.3: Log10 L/E distributions at best fit: (top left) cascade channel only, (right) track channel only, and (bottom left) both channels are included. For each of the three distributions, shaded areas correspond to a stacked histogram from all flavor contributions weighted by the best fit values. They are summed to the red solid line, which represents the best fit total log10 L/E distributions. This red line is comparable to the black data points. Their ratios to null hypothesis are shown in their bottom plots. Comparing data and null hypothesis, a deficit is shown in each plot. In particular, the track log10 L/E histogram show a very clear dip due to the disappearance of ν_μ CC signal events.

9.2 Contours

Based on the procedure described in Section 8.6.1, a contour is drawn to include values of Δm^2_{23} and $\sin^2\theta_{23}$ which are 90% confident. Two independent approaches are performed to determine the 90% confidence level. Section 9.2.1 discusses the contour assuming Wilk's Theorem, of which the test statistic follows a standard χ^2 distribution with two degrees of freedom. And, Section 9.2.2 presents the contour obtained via the full Feldman-Cousins approach.

9.2.1 Wilk's Theorem Assumed

As explained in Section 8.6.1, a 90% contour shown in Figure 9.4 is drawn around grid points with $\Delta\chi^2$ values greater than 4.605. With a width of 0.237 $\times 10^{-3}$ eV^2, the 1σ range of Δm^2_{23} is between 2.435 $\times 10^{-3}$ and 2.672 $\times 10^{-3}$ eV^2. On the other hand, the 1σ range of $\sin^2\theta_{23}$ goes from 0.444 to 0.618 with a width of 0.174. From the $\Delta\chi^2$ scan in $\sin^2\theta_{23}$, this analysis slightly prefers the second octant where $\sin^2\theta_{23} > 0.5$. While this observation agrees with the most recent measurements of atmospheric neutrino oscillation parameters from IceCube [79, 235, 236], none of these analyses are sensitive enough to rule out the first octant. In addition, although the most recent published result from IceCube prefers a near-maximal mixing angle of 0.51 [79], this analysis is consistent within statistical fluctuations compared to the published result; differences between the two measurements are discussed in Section 9.4. Finally, results from this analysis agree well with the latest results from long baseline experiments including T2K [70], MINOS [81], and NoνA [83].

In addition to the values of physics parameters, the behaviors of nuisance parameters are also examined in the two dimensional space of Δm^2_{23} and $\sin^2\theta_{23}$. In Figure 9.5, the plot in the top left corner presents the $\Delta\chi^2$ map from all grid

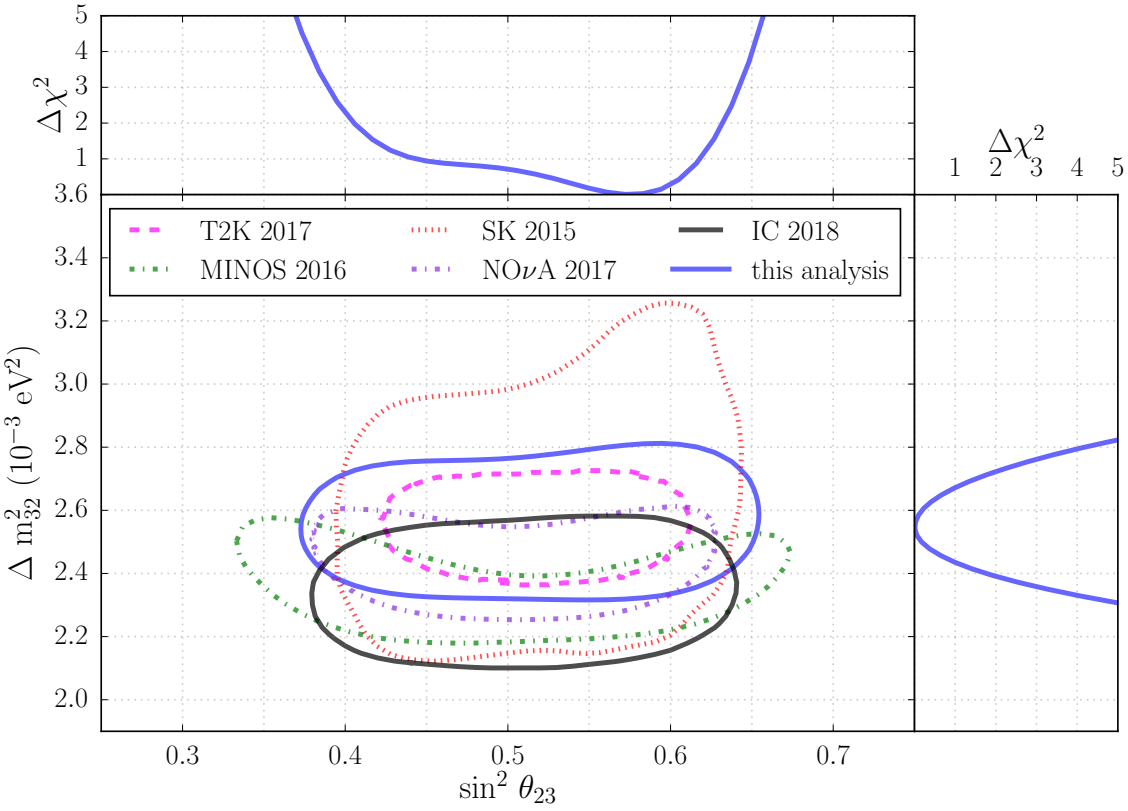

Figure 9.4: 90% contour of atmospheric neutrino oscillation parameters assuming the test statistic follows a χ^2 distribution with two degrees of freedom: (top) a scan of $\Delta\chi^2$ in $\sin^2\theta_{23}$, (right) a scan of $\Delta\chi^2$ in Δm^2_{23}, and (bottom left) the 90% contour from this analysis (solid blue) and from other oscillation experiments. Results from this analysis are comparable to previous IceCube results and other long baseline experiments. T2K, MINOS, SK, NOνA, and IC results are from [70, 79–81, 83].

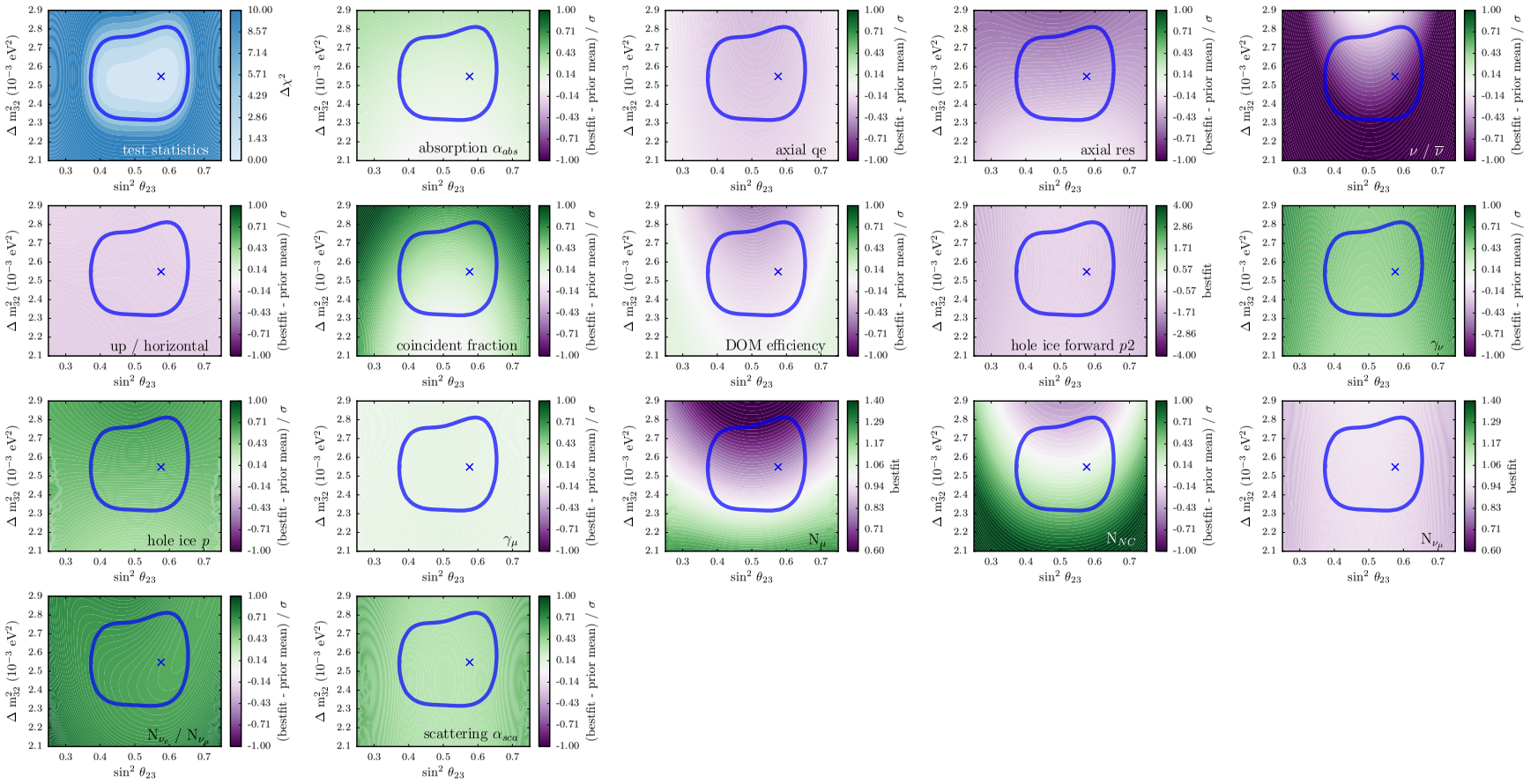

Figure 9.5: Behaviors of nuisance parameters in Δm^2_{23} and $\sin^2\theta_{23}$ space: (top left corner) the $\Delta\chi^2$ map and (the remaining) maps of best fit values of a given nuisance parameters. Best fit values of physics parameters and the 90% contour are overlaid. Green and purple color axes present either the pulls in units of σ or the best fit values of a given nuisance parameters.

points together with the best fit physics parameters and the 90% contour. Each of the remaining plots shows a map of best fit values for a given nuisance parameter; the color axes show either σ of pulls, for parameters with priors applied, or the best fit values, for those with no priors. Parameters with flatter maps, such as N_{ν_e}/N_{ν_μ} and γ_μ, have smaller effects on the measurements of physics parameters. Most parameters, however, affect the measurements to some degrees. It is the minimizer's job to find the right balance among the pulls from all nuisance parameters, and all parameters behave within expectations.

9.2.2 Feldman-Cousin Approach

An alternative assumption-free approach to determine 90% confidence level is described by Feldman and Cousin (FC) [237]. For a given Δm^2_{23} and $\sin^2\theta_{23}$ grid point, instead of assuming the test statistic distribution of $\Delta\chi^2$ follows a standard χ^2 distribution, the FC approach builds a $\Delta\chi^2$ distribution at a given grid point from many trials based on the observed p-value of that grid point.

Steps in the FC approach are described as follows. First, a global best fit is performed while letting all physics and nuisance parameters float; this returns a χ^2_{global}. Second, at a given grid point, a χ^2_{local} is obtained by running a fit with only nuisance parameters allowed to float; two physics parameters are fixed at the given grid point values. From these two χ^2s, a difference between the two test statistics is defined as $\Delta\chi^2_{\text{no-fluct}} = \chi^2_{\text{local}} - \chi^2_{\text{global}}$. The third step is to build a PDF from fluctuations around the local best fit histogram, which is given by the local fit with the χ^2_{local}. This local best fit histogram is therefore fluctuated over at least a hundred times based on the steps described in Section 8.5. For the i^{th} fluctuated trial, two fits are performed. The first fit allows all physics and nuisance parameters to float and returns a $\chi^2_{i,\text{pseudo-float}}$. The second fit fixes the physics parameters while

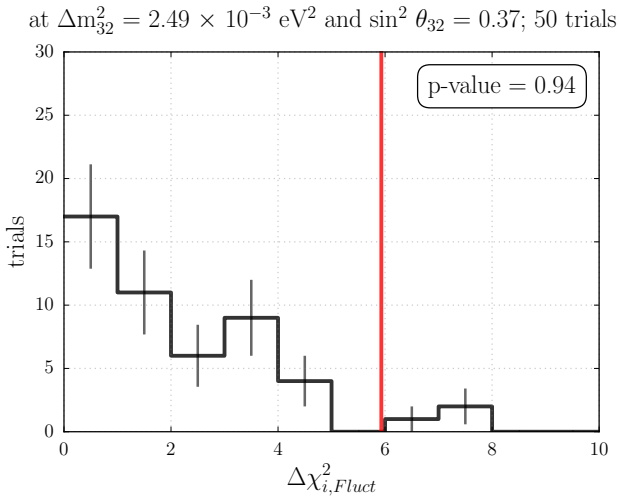

Figure 9.6: An example of Feldman-Cousin approach. At $\Delta m^2_{32} = 2.49 \times 10^{-3}$ eV^2 and $\sin^2\theta_{32} = 0.37$, 50 trials are preformed and its $\Delta\chi^2_{i,\text{fluct}}$ distribution is presented. The red line represents the value of $\Delta\chi^2_{\text{no-fluct}}$. The ratio of number of trials on the left of red line to the total trial is the p-value for this grid point.

letting nuisance parameters float, resulting in a $\chi^2_{i,\text{pseudo-fixed}}$. Then, a test statistic difference for this i^{th} trial is defined by $\Delta\chi^2_{i,\text{fluct}} = \chi^2_{i,\text{pseudo-fixed}} - \chi^2_{i,\text{pseudo-float}}$. With over a hundred trials, a distribution of $\Delta\chi^2_{i,\text{fluct}}$ is obtained. Based on where $\Delta\chi^2_{\text{no-fluct}}$ is located, a p-value is determined by the fraction of number of trials on the right of $\Delta\chi^2_{\text{no-fluct}}$ to the total number of trials performed.

An example of the FC approach is given in Figure 9.6. At a grid point (Δm^2_{23}, $\sin^2\theta_{23}$) = (2.49×10^{-3} eV^2, 0.37), 50 pseudo trials are performed[1]. With only the sixteen nuisance parameters allowed to float and the two physics parameters fixed at the given grid point, a χ^2_{local} of 135.37 is obtained. Given that the global best fit χ^2_{global} when all parameters are allowed to float is 129.44, the $\Delta\chi^2_{\text{no-fluct}}$ is 5.93, which is represented by the red solid line in Figure 9.6. For each of the 50 trials, two fits are performed, one with all parameters float and the other with only

[1]Only 50 trials are completed, and more trials will be added.

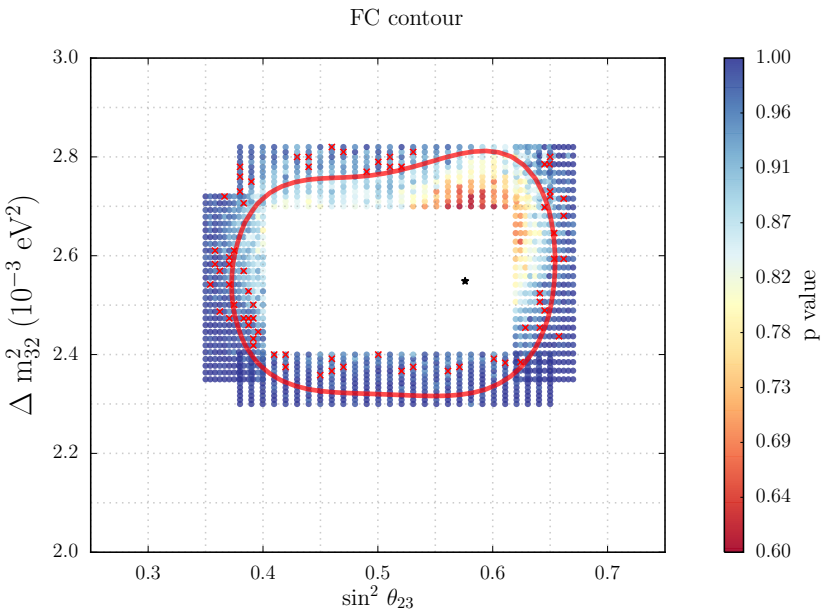

Figure 9.7: A p-value map in the Δm^2_{32} and $\sin^2\theta_{23}$ space from Feldman Cousin. Each dot represent a (Δm^2_{32}, $\sin^2\theta_{23}$) grid point, and the color represents its p-value from 50 trials. Among all the dots, those with p-values $\sim 90\%$ are shown as red crosses, which are compared to the solid red line obtained by assuming Wilk's Theorem (i.e. the blue contour in Figure 9.4).

nuisance parameters float; the difference between the two is, thus, $\Delta\chi^2_{i,\text{fluct}}$. From the 50 trials, a distribution of $\Delta\chi^2_{i,\text{fluct}}$ is plotted, and 47 entries are found to have a $\Delta\chi^2_{i,\text{fluct}}$ smaller than $\Delta\chi^2_{\text{no-fluct}}$. The p-value for this grid point is, therefore, given by the fraction of the number of trials on the left of the red line to the total number of trials, which is 94%.

A map of p-values in the Δm^2_{32} and $\sin^2\theta_{23}$ space is presented in Figure 9.7. Since the total number of fits performed is roughly the number of grid points times the number of trials, the FC approach is only performed around the 90% confidence level of the previous contour. At each grid point (a dot in Figure 9.7), its p-value (the color of the dot) from 50 trials corresponds to the percentage of getting this grid point value when the measurement is repeated many many times. A rough estimate

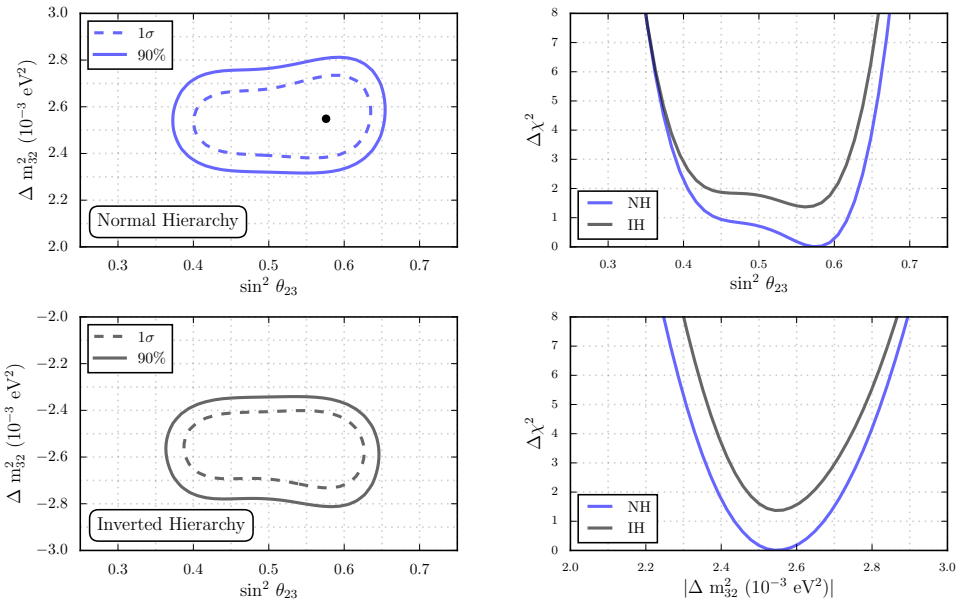

Figure 9.8: Fits with normal and inverted neutrino mass hierarchy orderings: (top left) 1σ and 90% contours assuming a normal mass ordering, (bottom left) contours assuming an inverted ordering, (top right) a $\Delta\chi^2$ scan with respect to the χ^2 from normal hierarchy assumption in $\sin^2\theta_{23}$, and (bottom right) a $\Delta\chi^2$ scan in Δm^2_{23}. This analysis prefers a normal mass ordering.

of the 90% contour is presented as the red crosses in Figure 9.7. More statistics and more grid points are under way to obtain a more accurate 90% contour from the FC approach.

9.3 Normal and Inverted Hierarchy Orderings

While all the above discussions assume a normal neutrino mass hierarchy, a full fit is also performed assuming an inverted mass hierarchy. In Figure 9.8, the 1σ and 90% confidence levels are shown for both hierarchy assumptions. Comparing the two fits, this analysis prefers a normal hierarchy with a χ^2 difference greater than 1. The $\Delta\chi^2$ scans, with respect to the χ^2_{mod} from normal hierarchy assumption, in Δm^2_{23} and $\sin^2\theta_{23}$ are also presented. While IceCube-DeepCore's sensitivity on

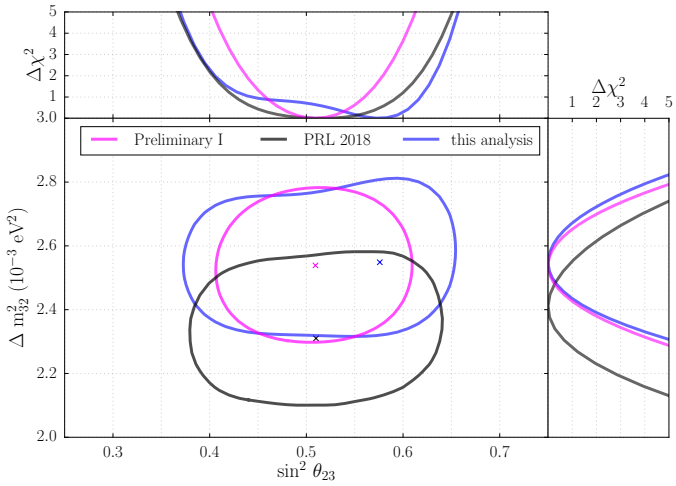

Figure 9.9: 90% contours from IceCube analyses: (top) a scan of $\Delta\chi^2$ in $\sin^2\theta_{23}$, (right) a scan of $\Delta\chi^2$ in Δm^2_{23}, and (bottom left) the 90% contours from this analysis (blue), Preliminary I (magenta), and PRL 2018 (black). Crosses represent the corresponding best fit physics parameters. With six years of data, Preliminary I has the smallest contour among the three. This analysis with only three years of data results in a similar Δm^2 measurement but away from maximal. Nonetheless, both Preliminary I and this analysis agree with the PRL 2018 result within statistical fluctuation.

mass hierarchy is limited, a more detailed study presents a 0.65σ exclusion on the inverted hierarchy hypothesis [224].

9.4 Comparison to Previous IceCube Results

With different reconstructions, event selections, analysis methods, and systematics, three recent measurements of atmospheric neutrino oscillation parameters are performed independently by the IceCube collaboration. Table 9.2 presents the differences among the three analyses. Preliminary I is an extension of an earlier publication [235], while PRL 2018 is the latest published result [79].

Different approaches are made in selection criteria; Preliminary I looks for high purity in their sample, and this analysis aims at more statistics. Since Preliminary

I applies tight cuts to select mostly ν_μ CC track events, Preliminary I reconstructs their events with a track only hypothesis, whereas this analysis assumes every event consists of a cascade and maybe track. Moreover, because of the high statistics at the final selection level, this analysis requires a more sophisticated selection method with two different BDTs to efficiently remove background muons and noise triggered events. The result from PRL 2018 is obtained from a selection with purity and statistics in between the two other analyses. One of the important features in the PRL result is the data driven background. Without enough statistics from atmospheric muon simulations, they applied an inverted cut at their near-final selection level. Data passing the inverted cut are used as their background muon template.

Moreover, the analysis techniques among the three measurements are also different. While this analysis uses reconstructed track length to identify track-like events from cascade-like events, the other two analyses compare fit results from cascade-only and track-only reconstruction hypotheses. Nonetheless, all three definitions of particle identification (PID) have fairly similar separation powers between cascade and track events. Other than PID, three analyses also have different zenith and energy binning. To archive a higher purity, Preliminary I only covers the up going region in which neutrinos pass through the Earth; for the other two analyses with more statistics, down going events are needed to better model atmospheric muon background. With less events at final level, Preliminary I uses Poisson LLH as their test statistics; with more statistics, PRL result and this analysis uses a simpler χ^2 with MC uncertainties taken into account.

Systematics are mostly the same among the three analyses. All measurements take into account γ_ν, $\nu/\bar{\nu}$, ν_e/ν_μ, up/hor, RES, ν NC / ν_μ CC, DOM efficiency, hole ice p, hole ice forward $p2$, and overall normalizations for μ_{atm} and ν_μ CC. However, this analysis also includes coincident events, muon background shape, and QE. Being the first to include systematic uncertainties due to bulk ice properties, this analysis

found that the best fit Δm^2_{32} and the contour itself are shifted up by slightly less than 0.5σ when the effects of ice absorption and scattering are considered.

Despite all the above differences, results from all three analyses are similar. As shown in Figure 9.9, three contours at 90% confidence level agree fairly well. With six years of data, Preliminary I has the smallest contour among the three, although the 90% width of Δm^2_{32} can be achieved by only three years of data. However, despite the similar 90% width of Δm^2_{23}, the best fit Δm^2_{23} from PRL 2018 [79] falls just right outside of the 90$ contour from this measurement. Other than statistical fluctuation, the small disagreement between the two analyses might be because this analysis includes bulk ice properties and a reduced charge-dependence in the reconstruction algorithm. On the other hand, this analysis prefers a non maximal mixing angle and has quite a different $\Delta\chi^2$ landscape along $\sin^2\theta_{23}$ from the other two analyses. However, all three 90% widths of $\sin^2\theta_{23}$ agree within statistical fluctuations.

Table 9.2: Comparisons among measurements of atmospheric neutrino oscillations in IceCube.

	Preliminary I	PRL 2018 [79]	This Analysis
Selections			
ν_μ CC purity	0.673	0.625 (excluded μ_{atm})	0.568
ν_μ CC events / year	4079	10287	15666
background modeling	MC	data driven	MC
selection method	straight cuts	straight cuts + 1 BDT	straight cuts + 2 BDTs
reconstruction hypothesis	track	cascade + track	cascade + track
Analysis Methods			
particle identification	$\Delta\chi^2_{\text{cascade vs track}}$	$\Delta\text{LLH}_{\text{cascade vs track}}$	track length
zenith range	up going only	all sky	all sky
log10 energy range	[0.8, 2.2]	[0.75, 1.75]	[0.75, 1.75]
test statistics	Poisson LLH	χ^2 with σ_{MC} and $\sigma_{\mu-\text{shape}}$	χ^2 with σ_{MC}
Differences in Systematics			
ν-μ_{atm} coincidence	✗	✗	✓
μ_{atm} shape	✗	✓	✓
QE	✓	✗	✓
α_{abs} and α_{sca}	✗	✗	✓
Results			
years of data	6	3	3
$\Delta m^2_{23}(\times 10^{-3}\ \text{eV}^2)$	$2.54^{+0.11}_{-0.11}$	$2.31^{+0.11}_{-0.13}$	$2.55^{+0.12}_{-0.11}$
$\sin^2\theta_{23}$	$0.51^{+0.05}_{-0.05}$	$0.51^{+0.07}_{-0.09}$	$0.58^{+0.04}_{-0.13}$
reduced χ^2	n/a	117.4/119	129.4/133
p-value to best fit	n/a	0.52	0.58

Chapter 10: Conclusion

Embedded at the heart of IceCube, DeepCore allows measurements of atmospheric neutrino oscillation parameters. Not only does IceCube act as an effective veto against atmospheric muon backgrounds, DeepCore's dense configuration of optical sensors pushes the energy sensitivity down to a few GeV. Since the amplitude of atmospheric neutrino oscillations is expected to be maximal at $\sim$ 25 GeV, IceCube-DeepCore provides a unique window to observe atmospheric neutrino oscillations at this energy scale. With over 30 megatons of exceptionally clean ice, more than 35,000 ν_μ charge current signal events are found at final level over three years of exposure. At the same time, large atmospheric muon background contemination is brought down to less than 8% in the final sample using machine learning algorithms.

With the highest statistic sample available, a binned analysis using a modified χ^2 is performed to measure the mass squared difference Δm^2_{23} and the mixing angle $\sin^2\theta_{23}$ of atmospheric neutrino oscillations. A total of sixteen nuisance parameters are considered, including atmospheric neutrino and muon fluxes, neutrino cross sections with the ice, normalization terms, and detector related systematics. Among the sixteen parameters, thirteen have priors applied, and their 1σ penalties are estimated either from previous studies or from other experiments. Uncertainties due to limited MC statistics, especially for muons, are taken into account. With 140 bins in the analysis template and 133 effective numbers of degrees of freedom, a χ^2 of 129.4 is obtained. The corresponding p-value of 0.58 and best fit values of nuisance parameters indicate a reasonable goodness of fit. The measured values of

Δm^2_{23} and $\sin^2\theta_{23}$ are $2.55^{+0.12}_{-0.11} \times 10^{-3}$ eV^2 and $0.58^{+0.04}_{-0.13}$ respectively; this analysis slightly prefers normal neutrino mass ordering and non maximal mixing. And, the 90% contour from this analysis is comparable to the latest measurements by other long baseline neutrino experiments.

Studying atmospheric neutrino oscillations using such a high statistic sample is challenging. Not only did we find disagreement between data and MC due to responses by optical sensors upon photon arrivals, this analysis is also affected by optical properties of the ice. In addition, this analysis excludes events at the very bottom of the ice near bed rock due to a discrepancy between data and MC, which is potentially caused by contamination of sneaky atmospheric muons from near the horizon or *GENIE*'s assumption of an icy Earth's core. Disagreements are also found when including high energy events beyond 100 GeV. Although we were not able to solve some of these data/MC disagreements, a huge amount of effort was made to understand our detector.

Among multiple independent approaches within the IceCube Collaboration to more precisely measure atmospheric neutrino oscillation parameters, this analysis has the highest statistics and is the first to predict atmospheric muon template via simulations despite the computational difficulties. With about one year worth of muons generated, alternative methods have been studied to carefully take into account the impacts due to limited MC statistics. In addition, new sources of systematics are also considered, investigated, and introduced.

Current atmospheric neutrino oscillation measurements by IceCube-DeepCore are limited both systematically and statistically. Not only would more data reduce statistical errors, but it would also help better model muon backgrounds, which can systematically improve sensitivities of oscillation studies. In addition, better understandings on sources of uncertainties are also important. For example, current neutrino flux related systematic implementations are based on an analysis by

Barr *et al.* [227] from 2006. Improvements can be made by direct measuring the impacts from pion to kaon ratio. Understanding our detector is also crucial to more precise oscillation parameter measurements. Previous studies assume that DOM efficiency and local ice properties due to air bubbles are independent. Although the newly introduced hyperplane method correlates different detector systematics, more simulations are required to explore off-axis points on the hyperplane.

While measurements can be improved by adding more data and better systematic controls, further works are needed on simulations, reconstructions, and analysis methods. More muon simulations are needed not only for baseline rate prediction but also for all discrete systematic sets, which would be time consuming even with *MuonGun*. On the other hand, two new reconstruction algorithms are currently under way to directly reconstruct events based on photon propagations without any track or cascade hypotheses. While performances of these reconstructions are important, great efforts are also made to improve their efficiencies. Finally, multiple analysis methods are developed. While this analysis re-calculates weights for all MC events and rebuilds the MC template at every iteration during the minimization, other analyses generate binned event distributions at a staged approach with various interpolation methods [238].

In conclusion, although this analysis does not significantly improve previous measurements of atmospheric neutrino oscillation parameters by IceCube, the 90% contour from this work supports the recently published IceCube result and represents an important cross check. Through this analysis, collaborative efforts are made to add background muon simulations, to reconstruct events with a better minimizer and hypothesis, to understand our detector, and to identify potential sources of systematics. These new modifications are valuable for improvements in future atmospheric neutrino oscillation studies by IceCube.

Bibliography

[1] M. C. Gonzalez-Garcia, M. Maltoni, and T. Schwetz. Updated fit to three neutrino mixing: status of leptonic CP violation. *JHEP*, 11:052, 2014.

[2] W. Pauli. The proposal of the neutrino. `http://microboone-docdb.fnal.gov/cgi-bin/RetrieveFile?docid=953;filename=pauli%20letter1930.pdf`, 1930.

[3] C. Sutton. *Spaceship Neutrino*. Cambridge University Press, 1 edition, 1992.

[4] J. Chadwick. Possible Existence of a Neutron. *Nature*, 129:312, 1932.

[5] E. Fermi. An Attempt of a Theory of β radiation. 1. *Z. Phys.*, 88:161–177, 1934.

[6] G. C. Hanna and B. Pontecorvo. The β-spectrum of h^3. *Phys. Rev.*, 75:983–984, Mar 1949.

[7] F. Reines and C. L. Cowan. Detection of the free neutrino. *Phys. Rev.*, 92:830–831, Nov 1953.

[8] F. Reines, C. L. Cowan, F. B. Harrison, A. D. McGuire, and H. W. Kruse. Detection of the free neutrino: A confirmation. *Science*, 124:103–104, Jul 1956.

[9] F. Reines, C. L. Cowan, F. B. Harrison, A. D. McGuire, and H. W. Kruse. Detection of the free antineutrino. *Phys. Rev.*, 117:159–173, Jan 1960.

[10] S. M. Bilenky. Bruno Pontecorvo: Mister Neutrino. In *Third NO-VE International Workshop on Neutrino Oscillations in Venice : Fifty years after the neutrino esperimental discovery : Venezia, February 7-10, 2006, Istituto Veneto di Scienze, Lettere ed Arti, Campo Santo Stefano*, pages 599–609, 2006.

[11] Raymond Davis. Attempt to detect the antineutrinos from a nuclear reactor by the $\mathrm{cl}^{37}(\overline{\nu}, e^-)\mathrm{a}^{37}$ reaction. *Phys. Rev.*, 97:766–769, Feb 1955.

[12] R. Davis. Nobel lecture: A half-century with solar neutrinos. https://www.nobelprize.org/nobel_prizes/physics/laureates/2002/davis-lecture.pdf, 2002.

[13] John N. Bahcall. Solar neutrinos. i. theoretical. *Phys. Rev. Lett.*, 12:300–302, Mar 1964.

[14] Raymond Davis. Solar neutrinos. ii. experimental. *Phys. Rev. Lett.*, 12:303–305, Mar 1964.

[15] B. Pontecorvo. Mesonium and anti-mesonium. *Sov. Phys. JETP*, 6:429, 1957. [Zh. Eksp. Teor. Fiz.33,549(1957)].

[16] M. Gell-Mann and A. Pais. Behavior of neutral particles under charge conjugation. *Phys. Rev.*, 97:1387–1389, Mar 1955.

[17] B. Pontecorvo. Inverse beta processes and nonconservation of lepton charge. *Sov. Phys. JETP*, 7:172–173, 1958. [Zh. Eksp. Teor. Fiz.34,247(1957)].

[18] G. Danby, J-M. Gaillard, K. Goulianos, L. M. Lederman, N. Mistry, M. Schwartz, and J. Steinberger. Observation of high-energy neutrino reactions and the existence of two kinds of neutrinos. *Phys. Rev. Lett.*, 9:36–44, Jul 1962.

[19] B. Pontecorvo. Neutrino Experiments and the Problem of Conservation of Leptonic Charge. *Sov. Phys. JETP*, 26:984–988, 1968. [Zh. Eksp. Teor. Fiz.53,1717(1967)].

[20] Raymond Davis, Don S. Harmer, and Kenneth C. Hoffman. Search for neutrinos from the sun. *Phys. Rev. Lett.*, 20:1205–1209, May 1968.

[21] J. N. Abdurashitov et al. Solar neutrino flux measurements by the Soviet-American Gallium Experiment (SAGE) for half the 22 year solar cycle. *J. Exp. Theor. Phys.*, 95:181–193, 2002. [Zh. Eksp. Teor. Fiz.122,211(2002)].

[22] P. Anselmann et al. Solar neutrinos observed by gallex at gran sasso. *Nuclear Physics B - Proceedings Supplements*, 31:117 – 124, 1993.

[23] J. N. Abdurashitov et al. Measurement of the solar neutrino capture rate with gallium metal. III: Results for the 2002–2007 data-taking period. *Phys. Rev.*, C80:015807, 2009.

[24] K. S. Hirata et al. Observation of ^{8}B solar neutrinos in the kamiokande-ii detector. *Phys. Rev. Lett.*, 63:16–19, Jul 1989.

[25] Q. R. Ahmad et al. Measurement of the rate of $\nu_e + d \rightarrow p + p + e^-$ interactions produced by ^8B solar neutrinos at the Sudbury Neutrino Observatory. *Phys. Rev. Lett.*, 87:071301, 2001.

[26] M. Pallavicini. Solar neutrinos: experimental review and prospectives. *Journal of Physics: Conference Series*, 598(1):012007, 2015.

[27] Y. Fukuda et al. Evidence for oscillation of atmospheric neutrinos. *Phys. Rev. Lett.*, 81:1562–1567, 1998.

[28] Super-kamiokande official website from university of tokyo. `http://www-sk.icrr.u-tokyo.ac.jp/sk/physics/atmnu.html`, 2007.

[29] R. Davis. The nobel prize in physics 2015. `https://www.nobelprize.org/nobel_prizes/physics/laureates/2015/`, 2015.

[30] Synopsis: Putting neutrino oscillations on ice. `https://physics.aps.org/synopsis-for/10.1103/PhysRevLett.120.071801`, 2018.

[31] X. Qian, C. Zhang, M. Diwan, and P. Vogel. Unitarity Tests of the Neutrino Mixing Matrix. 2013.

[32] Stephen Parke and Mark Ross-Lonergan. Unitarity and the three flavor neutrino mixing matrix. *Phys. Rev.*, D93(11):113009, 2016.

[33] S. Antusch, C. Biggio, E. Fernandez-Martinez, M. B. Gavela, and J. Lopez-Pavon. Unitarity of the Leptonic Mixing Matrix. *JHEP*, 10:084, 2006.

[34] K. Abe et al. Evidence for the Appearance of Atmospheric Tau Neutrinos in Super-Kamiokande. *Phys. Rev. Lett.*, 110(18):181802, 2013.

[35] N. Agafonova et al. Discovery of τ Neutrino Appearance in the CNGS Neutrino Beam with the OPERA Experiment. *Phys. Rev. Lett.*, 115(12):121802, 2015.

[36] Harry J. Lipkin. Quantum mechanics of neutrino oscillations: Hand waving for pedestrians. 1999.

[37] Boris Kayser. On the quantum mechanics of neutrino oscillation. *Phys. Rev. D*, 24:110–116, Jul 1981.

[38] Boris Kayser. Neutrino physics. *eConf*, C040802:L004, 2004.

[39] I. Gil-Botella. Neutrino Physics. In *Proceedings, 6th CERN - Latin-American School of High-Energy Physics (CLASHEP 2011): Natal, Brazil , March 23 - April 5, 2011*, pages 157–205, 2013.

[40] Yat-Long Chan, M. C. Chu, Ka Ming Tsui, Chan Fai Wong, and Jianyi Xu. Wave-packet treatment of reactor neutrino oscillation experiments and its implications on determining the neutrino mass hierarchy. *Eur. Phys. J.*, C76(6):310, 2016.

[41] Carlo Giunti and Chung W. Kim. Quantum mechanics of neutrino oscillations. *Found. Phys. Lett.*, 14(3):213–229, 2001.

[42] Carlo Giunti. Quantum mechanics of neutrino oscillations. In *11th International School on Particles and Cosmology Karbardino-Balkaria, Russia, April 18-24, 2001*, 2001.

[43] C. Giunti, C. W. Kim, and U. W. Lee. Remarks on the weak states of neutrinos. *Phys. Rev. D*, 45:2414–2420, Apr 1992.

[44] S. Nussinov. Solar neutrinos and neutrino mixing. *Physics Letters B*, 63(2):201 – 203, 1976.

[45] W. Grimus, S. Mohanty, and P. Stockinger. Field theoretical treatment of neutrino oscillations: The Strength of the canonical oscillation formula. In *Neutrino mixing. Festschrift in honour of Samoil Bilenky's 70th birthday. Proceedings, International Meeting, Turin, Italy, March 25-27, 1999*, pages 123–137, 1999.

[46] Yuval Grossman and Harry J. Lipkin. Flavor oscillations from a spatially localized source: A Simple general treatment. *Phys. Rev.*, D55:2760–2767, 1997.

[47] C. Giunti and C. W. Kim. Coherence of neutrino oscillations in the wave packet approach. *Phys. Rev.*, D58:017301, 1998.

[48] C. W. Walter. The Super-Kamiokande Experiment. pages 19–43, 2008.

[49] A neutrino telescope deep in the mediterranean sea. `http://cerncourier.com/cws/article/cern/50221`, 2012.

[50] Jun Cao and Kam-Biu Luk. An overview of the Daya Bay Reactor Neutrino Experiment. *Nucl. Phys.*, B908:62–73, 2016.

[51] A. Bellerive et al. The Sudbury Neutrino Observatory. *Nucl. Phys.*, B908:30–51, 2016.

[52] L. Wolfenstein. Neutrino oscillations in matter. *Phys. Rev. D*, 17:2369–2374, May 1978.

[53] S. P. Mikheev and A. Yu. Smirnov. Resonant amplification of ν oscillations in matter and solar-neutrino spectroscopy. *Il Nuovo Cimento C*, 9(1):17–26, Jan 1986.

[54] S. P. Mikheev and A. Yu. Smirnov. Resonance oscillations of neutrinos in matter. *Soviet Physics Uspekhi*, 30(9):759, 1987.

[55] A. Yu. Smirnov. The MSW effect and matter effects in neutrino oscillations. *Phys. Scripta*, T121:57–64, 2005.

[56] J. N. Bahcall and W. C. Haxton. Matter-enhanced neutrino oscillations in the standard solar model. *Phys. Rev. D*, 40:931–941, Aug 1989.

[57] A. Yu. Smirnov. Solar neutrinos: Oscillations or No-oscillations? 2016.

[58] Jiang Liu. Neutrino coherent forward scattering and its index of refraction. *Phys. Rev. D*, 45:1428–1431, Feb 1992.

[59] V. Barger, K. Whisnant, S. Pakvasa, and R. J. N. Phillips. Matter effects on three-neutrino oscillations. *Phys. Rev. D*, 22:2718–2726, Dec 1980.

[60] A. M. Dziewonski and D. L. Anderson. Preliminary reference earth model (prem). `http://ds.iris.edu/spud/earthmodel/9991844`, 1981.

[61] Ildio Lopes and Sylvaine Turck-Chize. Solar neutrino physics oscillations: Sensitivity to the electronic density in the Sun's core. *Astrophys. J.*, 765:14, 2013.

[62] J. N. Bahcall, A. M. Serenelli, and S. Basu. New solar opacities, abundances, helioseismology, and neutrino fluxes. *Astrophys. J.*, 621:L85–L88, 2005.

[63] B. Aharmim et al. Combined analysis of all three phases of solar neutrino data from the sudbury neutrino observatory. *Phys. Rev. C*, 88:025501, Aug 2013.

[64] P. Weatherly. Super-kamiokande solar neutrino results and nsi analysis. *Journal of Physics: Conference Series*, 888(1):012190, 2017.

[65] Heather L. Ray. The MiniBooNE Experiment. In *Proceedings, 34th SLAC Summer Institute on Particle Physics: The Next Frontier: Exploring with the LHC (SSI 2006): Menlo Park, California, July 17-28, 2006*, 2007.

[66] Justin Evans. The MINOS experiment: results and prospects. *Adv. High Energy Phys.*, 2013:182537, 2013.

[67] Jianming Bian. The NOνA Experiment: Overview and Status. In *Meeting of the APS Division of Particles and Fields (DPF 2013) Santa Cruz, California, USA, August 13-17, 2013*, 2013.

[68] H.S. Budd. The design and performance of the minerνa experiment. *Physics Procedia*, 37:1311 – 1318, 2012. Proceedings of the 2nd International Conference on Technology and Instrumentation in Particle Physics (TIPP 2011).

[69] K. Abe et al. The T2K Experiment. *Nucl. Instrum. Meth.*, A659:106–135, 2011.

[70] Lela Haegel. The latest T2K neutrino oscillation results. *PoS*, EPS-HEP2017:112, 2017.

[71] F. P. An et al. Observation of electron-antineutrino disappearance at Daya Bay. *Phys. Rev. Lett.*, 108:171803, 2012.

[72] P. Blasi. Recent results in cosmic ray physics and their interpretation. *Braz. J. Phys.*, 44:426–440, 2014. [,1291(2013)].

[73] J. R. Hörandel. Early cosmic-ray work published in German. In J. F. Ormes, editor, *American Institute of Physics Conference Series*, volume 1516 of *American Institute of Physics Conference Series*, pages 52–60, February 2013.

[74] M. Walter. Early cosmic ray research with balloons. *Nuclear Physics B - Proceedings Supplements*, 239-240:11 – 18, 2013. Proceedings of the 9th workshop on Science with the New Generation of High Energy Gamma-ray Experiments: From high energy gamma sources to cosmic rays, one century after their discovery.

[75] T. K. Gaisser, T. Stanev, and S. Tilav. Cosmic Ray Energy Spectrum from Measurements of Air Showers. *Front. Phys.(Beijing)*, 8:748–758, 2013.

[76] Y. Fukuda et al. Measurement of a small atmospheric muon-neutrino / electron-neutrino ratio. *Phys. Lett.*, B433:9–18, 1998.

[77] Y. Fukuda et al. Study of the atmospheric neutrino flux in the multi-GeV energy range. *Phys. Lett.*, B436:33–41, 1998.

[78] C. Patrignani et al. Review of Particle Physics. *Chin. Phys. C*, 40:100001, 2016.

[79] M. G. Aartsen et al. Measurement of atmospheric neutrino oscillations at 6˘56 gev with icecube deepcore. *Phys. Rev. Lett.*, 120:071801, Feb 2018.

[80] R. Wendell. Atmospheric results from super-kamiokande. *AIP Conference Proceedings*, 1666(1):100001, 2015.

[81] Leigh H. Whitehead. Neutrino Oscillations with MINOS and MINOS+. *Nucl. Phys.*, B908:130–150, 2016.

[82] Prabhjot Singh. Extracting Neutrino Oscillation Parameters using a Simultaneous Fit of the ν_e Appearance and ν_μ Disappearance Data in the NOνA Experiment. In *Meeting of the APS Division of Particles and Fields (DPF 2017) Batavia, Illinois, USA, July 31-August 4, 2017*, 2017.

[83] A. Radovic. Latest oscillation results from noνa. `http://nova-docdb.fnal.gov/cgi-bin/RetrieveFile?docid=25938&filename=radovicJETPFinalPublic.pdf&version=3`, Jan 2018.

[84] R. B. Patterson. Prospects for Measurement of the Neutrino Mass Hierarchy. *Ann. Rev. Nucl. Part. Sci.*, 65:177–192, 2015.

[85] S. Mertens. Direct Neutrino Mass Experiments. *J. Phys. Conf. Ser.*, 718(2):022013, 2016.

[86] M. Honda, M. Sajjad Athar, T. Kajita, K. Kasahara, and S. Midorikawa. Atmospheric neutrino flux calculation using the NRLMSISE-00 atmospheric model. *Phys. Rev.*, D92(2):023004, 2015.

[87] M. Honda, T. Kajita, K. Kasahara, S. Midorikawa, and T. Sanuki. Calculation of atmospheric neutrino flux using the interaction model calibrated with atmospheric muon data. *Phys. Rev.*, D75:043006, 2007.

[88] M. Honda, T. Kajita, K. Kasahara, and S. Midorikawa. Improvement of low energy atmospheric neutrino flux calculation using the jam nuclear interaction model. *Phys. Rev. D*, 83:123001, Jun 2011.

[89] T. K. Gaisser and M. Honda. Flux of atmospheric neutrinos. *Ann. Rev. Nucl. Part. Sci.*, 52:153–199, 2002.

[90] Anatoli Fedynitch, Julia Becker Tjus, and Paolo Desiati. Influence of hadronic interaction models and the cosmic ray spectrum on the high energy atmospheric muon and neutrino flux. *Phys. Rev. D*, 86:114024, Dec 2012.

[91] M. Thunman, Ingelman G., and Gondolo P. Charm production and high energy atmospheric muon and neutrino fluxes. *Astroparticle Physics*, 5(3):309 – 332, 1996.

[92] G. D. Barr, T. K. Gaisser, P. Lipari, Simon Robbins, and T. Stanev. A Three - dimensional calculation of atmospheric neutrinos. *Phys. Rev.*, D70:023006, 2004.

[93] V. Agrawal, T. K. Gaisser, P. Lipari, and T. Stanev. Atmospheric neutrino flux above 1-GeV. *Phys. Rev.*, D53:1314–1323, 1996.

[94] T. K. Gaisser and S. R. Klein. A new contribution to the conventional atmospheric neutrino flux. *Astropart. Phys.*, 64:13–17, 2015.

[95] T. K. Gaisser. Atmospheric Neutrinos. *J. Phys. Conf. Ser.*, 718(5):052014, 2016.

[96] J. Evans, D. G. Gamez, S. D. Porzio, S. Sldner-Rembold, and S. Wren. Uncertainties in Atmospheric Muon-Neutrino Fluxes Arising from Cosmic-Ray Primaries. *Phys. Rev.*, D95(2):023012, 2017.

[97] T. K. Gaisser. Spectrum of cosmic-ray nucleons, kaon production, and the atmospheric muon charge ratio. *Astropart. Phys.*, 35:801–806, 2012.

[98] T. K. Gaisser, R. Engel, and E. Resconi. *Cosmic Rays and Particle Physics*. Cambridge University Press, 2 edition, 2016.

[99] D. Chirkin. Fluxes of atmospheric leptons at 600-GeV - 60-TeV. 2004.

[100] W. R. Frazer, C. H. Poon, Dennis Silverman, and Harry J. Yesian. Limiting fragmentation and the charge ratio of cosmic-ray muons. *Phys. Rev. D*, 5:1653–1657, Apr 1972.

[101] Thomas K. Gaisser. Spectrum of cosmic-ray nucleons, kaon production, and the atmospheric muon charge ratio. *Astroparticle Physics*, 35(12):801 – 806, 2012.

[102] G. H. Arakelyan et al. Feynman scaling violation on baryon spectra in pp collisions at LHC and cosmic ray energies. *Phys. Atom. Nucl.*, 76:316–325, 2013.

[103] A. Ohsawa. Violation of the feynman scaling law in the forward region. *Progress of Theoretical Physics*, 92(5):1005–1018, 1994.

[104] F. Buccella and L. Popova. Violation of feynman scaling and energy dependence of multiplicity for high energy hadron interactions. *Journal of Physics G: Nuclear and Particle Physics*, 21(10):1379, 1995.

[105] P. Lipari. Lepton spectra in the earth's atmosphere. *Astroparticle Physics*, 1(2):195 – 227, 1993.

[106] T. K. Gaisser. Atmospheric Lepton Fluxes. *EPJ Web Conf.*, 99:05002, 2015.

[107] Eun-Joo Ahn et al. Cosmic ray interaction event generator SIBYLL 2.1. *Phys. Rev.*, D80:094003, 2009.

[108] S. Roesler, R. Engel, and J. Ranft. The Monte Carlo event generator DPMJET-III. In *Advanced Monte Carlo for radiation physics, particle transport simulation and applications. Proceedings, Conference, MC2000, Lisbon, Portugal, October 23-26, 2000*, pages 1033–1038, 2000.

[109] Y. Nara et al. Study of relativistic nuclear collisions at AGS energies from p + Be to Au + Au with hadronic cascade model. *Phys. Rev.*, C61:024901, 2000.

[110] S. Agostinelli et al. Geant4 simulation toolkit. *Nuclear Instruments and Methods in Physics Research Section A: Accelerators, Spectrometers, Detectors and Associated Equipment*, 506(3):250 – 303, 2003.

[111] G. Battistoni et al. The Application of the Monte Carlo Code FLUKA in Radiation Protection Studies for the Large Hadron Collider. *Prog. Nucl. Sci. Tech.*, 2:358–364, 2011.

[112] A. A. Kochanov, T. S. Sinegovskaya, and S. I. Sinegovsky. Meson cascade in the atmosphere, uncertainties in calculating the fluxes of high-energy muons, and data of direct measurements. *Physics of Atomic Nuclei*, 70(11):1913–1925, Nov 2007.

[113] Flavour universality of neutrino couplings with the z. *Physics Letters B*, 320(1):203 – 205, 1994.

[114] F. Betti. Tests of Lepton Flavour Universality with Semileptonic Decays at LHCb. 2017.

[115] *Fundamental Physics at the Intensity Frontier*, 2012.

[116] J. A. Formaggio and G. P. Zeller. From eV to EeV: Neutrino Cross Sections Across Energy Scales. *Rev. Mod. Phys.*, 84:1307–1341, 2012.

[117] J. L. Herraiz, M. C. Martínez, J. A. Caballero, and J. M. Udías. Overview of neutrino-nucleus quasielastic scattering. *AIP Conference Proceedings*, 1189(1):125–132, 2009.

[118] C. H. Llewellyn Smith. Neutrino Reactions at Accelerator Energies. *Phys. Rept.*, 3:261–379, 1972.

[119] C. F. Perdrisat, V. Punjabi, and M. Vanderhaeghen. Nucleon Electromagnetic Form Factors. *Prog. Part. Nucl. Phys.*, 59:694–764, 2007.

[120] T. Kitagaki et al. Study of $\nu d \to \mu^- p p_s$ and $\nu d \to \mu^- \Delta^{++}(1232) n_s$ using the bnl 7-foot deuterium-filled bubble chamber. *Phys. Rev. D*, 42:1331–1338, Sep 1990.

[121] T. Kitagaki et al. High-energy quasielastic $\nu_\mu n \to \mu^- p$ scattering in deuterium. *Phys. Rev. D*, 28:436–442, Aug 1983.

[122] K. L. Miller et al. Study of the reaction $\nu_\mu d \to \mu^- p p_s$. *Phys. Rev. D*, 26:537–542, Aug 1982.

[123] B. Maerkisch and H. Abele. Measurement of the Axial-Vector Coupling Constant g_A in Neutron Beta Decay. In *8th International Workshop on the CKM Unitarity Triangle (CKM 2014) Vienna, Austria, September 8-12, 2014*, 2014.

[124] D. Mund, B. Märkisch, M. Deissenroth, J. Krempel, M. Schumann, H. Abele, A. Petoukhov, and T. Soldner. Determination of the weak axial vector coupling $\lambda = g_A/g_V$ from a measurement of the β-asymmetry parameter a in neutron beta decay. *Phys. Rev. Lett.*, 110:172502, Apr 2013.

[125] B. G. Erozolimskii, I. A. Kuznetsov, I.V. Stepanenko, I.A. Kuida, and Yu. A. Mostovoi. New measurements of the electron-neutron spin asymmetry in neutron beta-decay. *Physics Letters B*, 263(1):33 – 38, 1991.

[126] J. Reich, H. Abele, M. A. Hoffmann, S. Baeßler, P. V. Bülow, D. Dubbers, V. Nesvizhevsky, U. Peschke, and O. Zimmer. A measurement of the beta asymmetry in neutron decay with PERKEO II. *Nuclear Instruments and Methods in Physics Research A*, 440:535–538, February 2000.

[127] C. Patrignani et al. Review of Particle Physics. *Chin. Phys. C*, 38:090001, 2014.

[128] M. Betancourt et al. Direct measurement of nuclear dependence of charged current quasielasticlike neutrino interactions using minerνa. *Phys. Rev. Lett.*, 119:082001, Aug 2017.

[129] R. Gran et al. Measurement of the quasielastic axial vector mass in neutrino interactions on oxygen. *Phys. Rev. D*, 74:052002, Sep 2006.

[130] K. Abe et al. Measurement of double-differential muon neutrino charged-current interactions on c_8h_8 without pions in the final state using the t2k off-axis beam. *Phys. Rev. D*, 93:112012, Jun 2016.

[131] A. A. Aguilar-Arevalo et al. Measurement of the Antineutrino Neutral-Current Elastic Differential Cross Section. *Phys. Rev.*, D91(1):012004, 2015.

[132] A. A. Aguilar-Arevalo et al. First measurement of the muon antineutrino double-differential charged-current quasielastic cross section. *Phys. Rev. D*, 88:032001, Aug 2013.

[133] J. Carlson, J. Jourdan, R. Schiavilla, and I. Sick. Longitudinal and transverse quasielastic response functions of light nuclei. *Phys. Rev.*, C65:024002, 2002.

[134] Dieter Rein and Lalit M Sehgal. Neutrino-excitation of baryon resonances and single pion production. *Annals of Physics*, 133(1):79 – 153, 1981.

[135] R. P. Feynman, M. Kislinger, and F. Ravndal. Current matrix elements from a relativistic quark model. *Phys. Rev. D*, 3:2706–2732, Jun 1971.

[136] D. Rein. Angular distribution in neutrino-induced single pion production processes. *Zeitschrift für Physik C Particles and Fields*, 35(1):43–64, Mar 1987.

[137] Ch. Berger and L. M. Sehgal. Lepton mass effects in single pion production by neutrinos. *Phys. Rev.*, D76:113004, 2007.

[138] E. Hernndez, J. Nieves, and M. J. Vicente Vacas. Single π production in neutrino-nucleus scattering. *Phys. Rev.*, D87(11):113009, 2013.

[139] M. Kabirnezhad. Single pion production in neutrino-nucleon interactions. *Phys. Rev. D*, 97:013002, Jan 2018.

[140] Krzysztof M. Graczyk and Jan T. Sobczyk. Form factors in the quark resonance model. *Phys. Rev. D*, 77:053001, Mar 2008.

[141] Joan Català-Pérez. Neutrino induced single pion production experiments review. *AIP Conference Proceedings*, 1222(1):207–211, 2010.

[142] S. Nakayama et al. Measurement of single pi0 production in neutral current neutrino interactions with water by a 1.3-GeV wide band muon neutrino beam. *Phys. Lett.*, B619:255–262, 2005.

[143] A. A. Aguilar-Arevalo et al. Measurement of ν_μ and $\overline{\nu}_\mu$ induced neutral current single π^0 production cross sections on mineral oil at $E_\nu \sim \mathcal{O}$ (1 gev). *Phys. Rev. D*, 81:013005, Jan 2010.

[144] Y. Kurimoto. SciBooNE's neutral current pi0 production measurements. *AIP Conf. Proc.*, 1189:189–194, 2009.

[145] T. Le et al. Single Neutral Pion Production by Charged-Current $\bar{\nu}_\mu$ Interactions on Hydrocarbon at $\langle E_\nu \rangle$ =3.6 GeV. *Phys. Lett.*, B749:130–136, 2015.

[146] B. Eberly et al. Charged pion production in ν_μ interactions on hydrocarbon at $\langle E_\nu \rangle$= 4.0 GeV. *Phys. Rev.*, D92(9):092008, 2015.

[147] A. De Roeck and R. S. Thorne. Structure Functions. *Prog. Part. Nucl. Phys.*, 66:727–781, 2011.

[148] J. D. Bjorken. Asymptotic sum rules at infinite momentum. *Phys. Rev.*, 179:1547–1553, Mar 1969.

[149] V. Barger, D. Marfatia, and K. Whisnant. *The Physics of Neutrinos*. Princeton University Press, 1 edition, 2012.

[150] C. H. Albright and C. Jarlskog. Neutrino production of m+ and e+ heavy leptons (i). *Nuclear Physics B*, 84(2):467 – 492, 1975.

[151] A. De Rújula, R. Petronzio, and A. Savoy-Navarro. Radiative corrections to high-energy neutrino scattering. *Nuclear Physics B*, 154(3):394 – 426, 1979.

[152] U. K. Yang and A. Bodek. Parton distributions, d/u, and higher twist effects at high x. *Phys. Rev. Lett.*, 82:2467–2470, Mar 1999.

[153] A. Bodek and U. K. Yang. Modeling deep inelastic cross-sections in the few GeV region. *Nucl. Phys. Proc. Suppl.*, 112:70–76, 2002. [,70(2002)].

[154] K. S. McFarland and S. O. Moch. Conventional physics explanations for the NuTeV sin**2theta(W). In *Electroweak precision data and the Higgs mass. Proceedings, Workshop, Zeuthen, Germany, February 28-March 1, 2003*, pages 61–83, 2003.

[155] A Bodek and U. K. Yang. Higher twist, xi(omega) scaling, and effective LO PDFs for lepton scattering in the few GeV region. *J. Phys.*, G29:1899–1906, 2003.

[156] A. Cooper-Sarkar, P. Mertsch, and S. Sarkar. The high energy neutrino cross-section in the Standard Model and its uncertainty. *JHEP*, 08:042, 2011.

[157] K. Nakamura. Review of particle physics. *Journal of Physics G: Nuclear and Particle Physics*, 37(7A):075021, 2010.

[158] M. Tzanov. Review of neutrino deep inelastic scattering results. *AIP Conference Proceedings*, 1222(1):243–247, 2010.

[159] A. Kayis-Topaksu et al. Leading order analysis of neutrino induced dimuon events in the CHORUS experiment. *Nucl. Phys.*, B798:1–16, 2008.

[160] D. Mason and others. Measurement of the nucleon strange-antistrange asymmetry at next-to-leading order in qcd from nutev dimuon data. *Phys. Rev. Lett.*, 99:192001, Nov 2007.

[161] P. Astier et al. Neutrino production of opposite sign dimuons in the nomad experiment. *Physics Letters B*, 486(1):35 – 48, 2000.

[162] J. H. Koehne, K. Frantzen, M. Schmitz, T. Fuchs, W. Rhode, D. Chirkin, and J. Becker Tjus. Proposal: A tool for propagation of charged leptons. *Computer Physics Communications*, 184(9):2070 – 2090, 2013.

[163] C. Amsler et al. Review of Particle Physics. *Physics Letters*, B667:090001, 2009.

[164] H. Bethe. Zur theorie des durchgangs schneller korpuskularstrahlen durch materie. *Annalen der Physik*, 397(3):325–400.

[165] H. Bethe. *Quantum mechanics of the one- and two-electron problems*. Martino Fine Books, 1 edition, 2014.

[166] Rossi R. *High Energy Particles*. Prentice Hall, 1 edition, 1952.

[167] P. A. Čerenkov. Visible radiation produced by electrons moving in a medium with velocities exceeding that of light. *Phys. Rev.*, 52:378–379, Aug 1937.

[168] I. M. Frank and I. E. Tamm. Coherent visible radiation of fast electrons passing through matter. *Compt. Rend. Acad. Sci. URSS*, 14(3):109–114, 1937. [Usp. Fiz. Nauk93,no.2,388(1967)].

[169] P. Askebjer et al. Uv and optical light transmission properties in deep ice at the south pole. *Geophysical Research Letters*, 24(11):1355–1358.

[170] Askebjer P. et al. Optical properties of deep ice at the south pole: absorption. *Appl. Opt.*, 36(18):4168–4180, Jun 1997.

[171] P. B. Price, K. Woschnagg, and D. Chirkin. Age vs depth of glacial ice at south pole. *Geophysical Research Letters*, 27(14):2129–2132.

[172] J. R. Petit et al. Climate and atmospheric history of the past 420,000 years from the Vostok ice core, Antarctica. *Nature*, 399:6735, Jun 1999.

[173] P. B. Price et al. Temperature profile for glacial ice at the south pole: Implications for life in a nearby subglacial lake. *Proceedings of the National Academy of Sciences*, 99(12):7844–7847, 2002.

[174] D. Chirkin. Hole ice i. `http://icecube.wisc.edu/~dima/work/WISC/new/2015/talks/holeice.ppt`.

[175] D. Chirkin. Hole ice ii. `http://icecube.wisc.edu/~dima/work/WISC/new/2015/talks/holeice-brief.ppt`.

[176] Gustav Mie. Beiträge zur optik trüber medien, speziell kolloidaler metallösungen. *Annalen der Physik*, 330(3):377–445, 1908.

[177] P. B. Price and L. Bergström. Optical properties of deep ice at the south pole: scattering. *Appl. Opt.*, 36(18):4181–4194, Jun 1997.

[178] D. Chirkin. Study of south pole ice transparency with icecube flashers. `https://icecube.wisc.edu/~dima/work/WISC/ppc/spice/paper/a.pdf`.

[179] M. G. Aartsen et al. Measurement of South Pole ice transparency with the IceCube LED calibration system. *Nucl. Instrum. Meth.*, A711:73–89, 2013.

[180] M. Ackermann et al. Optical properties of deep glacial ice at the South Pole. *J. Geophys. Res. Atmos.*, 111(D13):D13203, 2006.

[181] K. Woschnagg and P. B. Price. Temperature dependence of absorption in ice at 532 nm. *Appl. Opt.*, 40(15):2496–2500, May 2001.

[182] J. T. O. Kirk. Multiple scattering of a photon flux: implications for the integral average cosine of the underwater light field. *Appl. Opt.*, 38(15):3134–3140, May 1999.

[183] C. F. Bohren and D. R. Huffman. *Absorption and Scattering of Light by Small Particles*. WILEY VCH Verlag, 1 edition, 2007.

[184] L. G. Henyey and J. L. Greenstein. Diffuse radiation in the Galaxy. *Astrophys. J.*, 93:70–83, 1941.

[185] R. C. Bay, R. A. Rohde, P. B. Price, and N. E. Bramall. South pole paleowind from automated synthesis of ice core records. *Journal of Geophysical Research: Atmospheres*, 115(D14).

[186] T. Benson et al. Icecube enhanced hot water drill functional description. *Annals of Glaciology*, 55(68):105–114, 2014.

[187] L. Greenler, T. Benson, J. Cherwinka, A. Elcheikh, F. Feyzi, A. Karle, and R. Paulos. Modeling hole size, lifetime and fuel consumption in hot-water ice drilling. *Annals of Glaciology*, 55(68):115?123, 2014.

[188] M. G. Aartsen et al. The IceCube Neutrino Observatory: Instrumentation and Online Systems. *JINST*, 12(03):P03012, 2017.

[189] R. Abbasi et al. The Design and Performance of IceCube DeepCore. *Astropart. Phys.*, 35:615–624, 2012.

[190] M. Madsen. Icecube at icrc 2015. `https://icecube.wisc.edu/news/view/346`.

[191] R. Abbasi et al. Calibration and characterization of the IceCube photomultiplier tube. *Nuclear Instruments and Methods in Physics Research A*, 618:139–152, June 2010.

[192] M. G. Aartsen et al. Energy Reconstruction Methods in the IceCube Neutrino Telescope. *JINST*, 9:P03009, 2014.

[193] O.J. Smirnov, P. Lombardi, and G. Ranucci. Precision measurements of timing characteristics of the 8“ ETL9351 series photomultiplier. *ArXiv Physics e-prints*, March 2004.

[194] Modeling of charge response for the icecube pmt. `https://wiki.icecube.wisc.edu/index.php/Modeling_of_Charge_Response_for_the_IceCube_PMT`.

[195] Spe templates. `https://wiki.icecube.wisc.edu/index.php/SPE_templates`.

[196] R. Abbasi, Y. Abdou, T. Abu-Zayyad, J. Adams, J. A. Aguilar, M. Ahlers, K. Andeen, J. Auffenberg, X. Bai, M. Baker, et al. Calibration and characterization of the IceCube photomultiplier tube. *Nuclear Instruments and Methods in Physics Research A*, 618:139–152, June 2010.

[197] R. Abbasi et al. The IceCube Data Acquisition System: Signal Capture, Digitization, and Timestamping. *Nucl. Instrum. Meth.*, A601:294–316, 2009.

[198] Delia Tosi and Christopher Wendt. Calibrating photon detection efficiency in IceCube. *PoS*, TIPP2014:157, 2014.

[199] J. Feintzeig. *Searches for Point-like Sources of Astrophysical Neutrinos with the IceCube Neutrino Observatory*. PhD thesis, The University of Wisconsin - Madison, 2014.

[200] K. Hanson. Particle astrophysics at 90°s reports from the icecube neutrino observatory. `http://we.vub.ac.be/iap/sites/default/files2/PAI12%20-%20IceCube.pdf`.

[201] Prob 3++. `http://webhome.phy.duke.edu/~raw22/public/Prob3++/`, 2012.

[202] C. Andreopoulos, C. Barry, S. Dytman, H. Gallagher, T. Golan, R. Hatcher, G. Perdue, and J. Yarba. The GENIE Neutrino Monte Carlo Generator: Physics and User Manual. 2015.

[203] F. Finley. Weighting neutrinogenerator events with oneweight in icesim 2.0. https://docushare.icecube.wisc.edu/dsweb/Get/Document-44937/OneWeight.pdf.

[204] A. Ishihara. Neutrino generator/starting simulation at detector (finalonly mode). https://wiki.icecube.wisc.edu/index.php/Neutrino_Generator/Starting_Simulation_at_Detector_%28FinalOnly_mode%296.

[205] Clsim project. http://software.icecube.wisc.edu/documentation/projects/clsim/.

[206] Pmt response simulator. http://software.icecube.wisc.edu/documentation/projects/DOMLauncher/PMTRes.html.

[207] D. Chirkin et al. A digital optical module (dom) simulation for icecube. http://icecube.lbl.gov/PDFS/chirkin2.pdf.

[208] trigger-sim project. http://software.icecube.wisc.edu/documentation/projects/trigger-sim/.

[209] ν fit. www.nu-fit.org, 2016.

[210] J. M. Picone, A. E. Hedin, D. P. Drob, and A. C. Aikin. Nrlmsise-00 empirical model of the atmosphere: Statistical comparisons and scientific issues. *Journal of Geophysical Research: Space Physics*, 107(A12):SIA 15–1–SIA 15–16.

[211] S. Macmillan. Igrf, international geomagnetic reference field. http://nora.nerc.ac.uk/id/eprint/3981/, 2007.

[212] D. Heck, G. Schatz, T. Thouw, J. Knapp, and J. N. Capdevielle. CORSIKA: A Monte Carlo code to simulate extensive air showers. 1998.

[213] Jakob van Santen. *Neutrino Interactions in IceCube above 1 TeV: Constraints on Atmospheric Charmed-Meson Production and Investigation of the Astrophysical Neutrino Flux with 2 Years of IceCube Data taken 2010–2012*. PhD thesis, U. Wisconsin, Madison (main), 2014-11-18.

[214] G. Carminati, M. Bazzotti, S. Biagi, S. Cecchini, T. Chiarusi, A. Margiotta, M. Sioli, and M. Spurio. MUPAGE: a fast atmospheric MUon GEnerator for neutrino telescopes based on PArametric formulas. 2009.

[215] M. J. Larson. *Simulation and identification of non-Poissonian noise triggers in the IceCube neutrino detector*. PhD thesis, 2013. Copyright - Database copyright ProQuest LLC; ProQuest does not claim copyright in the individual underlying works; Last updated - 2016-06-04.

[216] M. J. Larson. *A Search or Tau Neutrino Appearance with IceCube-DeepCore*. Ph.d., Niels Bohr Institute, University of Copenhagen, 2018. Pending.

[217] M. Richman. Pybdt user manual. `http://software.icecube.wisc.edu/documentation/projects/pybdt/index.html`.

[218] The toolkit for multivariate analysis. `http://tmva.sourceforge.net/`, 2015.

[219] B. Recht and Ré C. Robust statistics in icecube initial muon reconstruction. `http://inspirehep.net/record/1413019/files/icrc2013-0807.pdf`.

[220] Software documentation of tensor of inertia. `http://software.icecube.wisc.edu/documentation/projects/tensor-of-inertia/index.html`.

[221] Software documentation of common variables. `http://software.icecube.wisc.edu/documentation/projects/CommonVariables/index.html`.

[222] Sebastian Euler. Measurement of atmospheric neutrino oscillations with icecube/deepcore in its 79-string configuration. *Physics Procedia*, 61:598 – 607, 2015. 13th International Conference on Topics in Astroparticle and Underground Physics, TAUP 2013.

[223] J. P. Yanez. Corridor cut. `https://docushare.icecube.wisc.edu/dsweb/Get/Document-62713/Yanez_CorridorCut_Oct2012.pdf`.

[224] M. Leuermann. *Testing the Neutrino Mass Ordering with Three Years of IceCube/DeepCore Data*. Ph.d., Rheinisch-Westfalische Technische Hochschule (RWTH) Aachen, 2018. Pending.

[225] M. G. Aartsen et al. Energy Reconstruction Methods in the IceCube Neutrino Telescope. *JINST*, 9:P03009, 2014.

[226] F. Feroz, M. P. Hobson, and M. Bridges. Multinest: an efficient and robust bayesian inference tool for cosmology and particle physics. *Monthly Notices of the Royal Astronomical Society*, 398(4):1601–1614, 2009.

[227] G. D. Barr, T. K. Gaisser, S. Robbins, and Todor Stanev. Uncertainties in Atmospheric Neutrino Fluxes. *Phys. Rev.*, D74:094009, 2006.

[228] Steven Wren. *Neutrino Mass Ordering Studies with IceCube-DeepCore*. PhD thesis, The University of Manchester, 8 2018.

[229] S. Mandalia and Katori T. Dis cross section uncertainties. `https://docs.google.com/document/d/1tSfKY08jZ_PBkgV6zYVoFCOjiJIRF0orw--_FlqdqJM/edit`.

[230] A. M. Dziewonski and D. L. Anderson. The nutev experiment. `https://www-e815.fnal.gov/`.

[231] M. Tzanov et al. Precise measurement of neutrino and anti-neutrino differential cross sections. *Phys. Rev.*, D74:012008, 2006.

[232] R. Barlow and C. Beeston. Fitting using finite Monte Carlo samples. *Computer Physics Communications*, 77:219–228, October 1993.

[233] Iminuit2. `https://pypi.python.org/pypi/iminuit`, 2015.

[234] G. Cowan. A goodness of fit and wilks? theorem. `www.hep.fsu.edu/~harry/statistics/Cowan_2013.pdf`, 2013.

[235] M. G. Aartsen et al. Determining neutrino oscillation parameters from atmospheric muon neutrino disappearance with three years of IceCube DeepCore data. *Phys. Rev.*, D91(7):072004, 2015.

[236] A. Terliuk and S. Blot. Six years of leesard sample. `https://events.icecube.wisc.edu/getFile.py/access?contribId=150&sessionId=22&resId=0&materialId=slides&confId=90`, Oct 2017.

[237] G. J. Feldman and R. D. Cousins. A Unified approach to the classical statistical analysis of small signals. *Phys. Rev.*, D57:3873–3889, 1998.

[238] M. G. Aartsen et al. Computational Techniques for the Analysis of Small Signals in High-Statistics Neutrino Oscillation Experiments. 2018.